



# ***Background Document***

## **Strength and Ductility of FR Welded-Bolted Connections**

**Report No. SAC/BD-98/01**

### **SAC Joint Venture**

**a partnership of:**

**Structural Engineers Association of California (SEAOC)**

**Applied Technology Council (ATC)**

**California Universities for Research in Earthquake Engineering (CUREe)**

**by**

**Sherif El-Tawil, Tameka Mikesell, Egill Vidarsson, and Sashi K. Kunnath,**

**Department of Civil and Environmental Engineering**

**University of Central Florida**

**Orlando, Florida 32816-2450**

**SAC Joint Venture**

**555 University Avenue, Suite 126**

**Sacramento, California 95825**

**916-427-3647**

**April 15, 1998**

The Background Document series has been developed as a means to disseminate information related to the mission of the Steel Project that has not been reviewed as part of the formal report series. Background Documents are provided for informational purposes only and do not necessarily represent official findings or recommendations of the Federal Emergency Management Agency (FEMA), the SAC Joint Venture and its organizations, or any other project participants.

## **THE SAC JOINT VENTURE**

SAC is a joint venture of the Structural Engineers Association of California (SEAOC), the Applied Technology Council (ATC), and California Universities for Research in Earthquake Engineering (CUREe), formed specifically to address both immediate and long-term needs related to solving the problems of the Welded Steel Moment Frame (WSMF) connection. SEAOC is a professional organization composed of more than 3,000 practicing structural engineers in California. The volunteer efforts of SEAOC's members on various technical committees have been instrumental in the development of the earthquake design provisions contained in the Uniform Building Code as well as the National Earthquake Hazards Reduction Program (NEHRP) Recommended Provisions for Seismic Regulations for New Buildings. The Applied Technology Council is a non-profit organization founded specifically to perform problem-focused research related to structural engineering and to bridge the gap between civil engineering research and engineering practice. It has developed a number of publications of national significance including ATC 3-06, which serves as the basis for the NEHRP Recommended Provisions. CUREe is a non-profit organization formed to promote and conduct research and educational activities related to earthquake hazard mitigation. CUREe's eight institutional members are: the California Institute of Technology, Stanford University, the University of California at Berkeley, the University of California at Davis, the University of California at Irvine, the University of California at Los Angeles, the University of California at San Diego, and the University of Southern California. This collection of university earthquake research laboratory, library, computer, and faculty resources is among the most extensive in the United States. The SAC Joint Venture allows these three organizations to combine their extensive and unique resources, augmented by subcontractor universities and organizations from around the nation, into an integrated team of practitioners and researchers, uniquely qualified to solve problems related to the seismic performance of WSMF structures.

## **DISCLAIMER**

This report is one of a series documenting background information related to Phase 2 of the FEMA-funded SAC Steel Project. It is being disseminated in the public interest to increase awareness of the many factors which contribute to the seismic performance of steel moment frame structures. The information contained herein is not for design use and is not applicable to specific building projects. This report has not been reviewed for accuracy, and the SAC Joint Venture has not verified any of the results presented. No warranty is offered with regard to the results, findings, and recommendations contained herein, either by the Federal Emergency Management Agency, the SAC Joint Venture and its consultants, the individual joint venture partners, their directors, members, or employees. These organizations and individuals do not assume any legal liability or responsibility for the accuracy, completeness, or usefulness of any of the information, products, or processes included in this publication. The reader is cautioned to carefully review the material presented herein.

## PREFACE

This report documents the second in a series of three detailed finite element studies in the Phase 2 Steel Project focused specifically on understanding the factors which contribute to the behavior of steel beam-column connections. The first study, performed by Gregory Deierlein, Anthony Ingrassia, and Wei-Ming Chi of Cornell University, explicitly incorporated fracture mechanics approaches in the analysis of both two-dimensional and three-dimensional meshes of various connection configurations. The primary focus was on reproducing the observed behavior of two large-scale specimens tested in the Phase 1 project, but a limited series of parametric studies was also performed using both linear and nonlinear fracture analyses to assess the influence on connection performance of factors such as: weld and base metal strength and fracture toughness; presence of weld backing bar, with and without reinforcing fillet welds; residual stresses as a result of welding; and cover plate geometry, for cover-plated connections. The results of this initial study have been published as SAC Background Document SAC/BD-97/05, entitled "Finite Element Fracture Mechanics Investigations of Welded Beam-Column Connections".

The finite element analyses described in this report focus on modeling the behavior of connections in which ductile yielding develops in the absence of fracture. An approach similar to that taken in the Cornell study is followed in which the finite element models are first calibrated against the measured behavior of a large-scale beam-column specimen tested in the Phase 1 Steel Project. This is then used as a stepping off point for a series of parametric studies investigating factors such as beam and column flange and web thicknesses, steel yield-to-ultimate-strength ratios, access hole geometry, continuity plate size, and shear transfer mechanisms. Rather than explicitly modeling the propagation of fractures in the finite element mesh as was done in the Cornell study, a series of stress and strain indices were defined at various locations in the welded connection and monitored throughout each analysis to quantify imposed demands and provide estimates of the likelihood of developing ductile fracture.

The details of the third finite element study were being finalized at the time of this writing, with the intent of building on the first two studies and the variety of investigations underway in the Phase 2 project focusing on material properties, welding and inspection, and connection performance. In particular, the final finite element study will tie together tests of T-stubs and large-scale beam-column connections of various configurations with the ultimate goal of developing straightforward, analytically-based design approaches for steel connections.

The study described in this report was performed under the auspices of the Technical Advisory Panel (TAP) for Connection Performance, chaired by Charles Roeder, and under the supervision of James Malley, SAC Project Director for Topical Investigations. Review comments were provided by members of the Connection TAP, other investigators in this team, and selected members of the TAPs for Materials and Fracture, and Joining and Inspection. The contributions from all of these individuals are greatly appreciated.

## SUMMARY

The objectives of this project are: 1) to develop a more thorough understanding of the inelastic behavior of pre-Northridge fully restrained welded-bolted connections, and 2) to lay the groundwork for the development of connection details that are not fracture critical. These objectives are addressed through detailed three-dimensional nonlinear finite element analyses of connection subassemblages. The studies reported do not account for fracture propagation. They are concerned with the potential for cracking only through the development of stress states or material conditions that would facilitate fracture if a flaw or other irregularity were introduced.

The characteristics of the analysis configurations utilized in this research are derived from the geometry of Berkeley specimen PN3, which consists of a W36x150 beam connected to W14x257 column. By changing some of the attributes of specimen PN3, different analysis configurations are created. Important geometric and material parameters are varied over the practical range of interest in order to evaluate their effect on behavior. To compare between the behavior of the different configurations analyzed in this research, and to assess the effect of the parameters of interest, a number of different stress, strain, and combined stress/strain indices are employed. These quantities are sampled at connection plastic rotations ranging from 0.0025 to 0.03 *rad*.

The following is a summary of important results concluded from the nonlinear finite element analyses conducted as part of this research:

- Stress triaxiality and plastic strains computed from the finite element analyses suggest that observed brittle fractures at the weld-column interface probably occurred due to large pre-existing flaws at the interface rather than limited ductility caused by large hydrostatic stresses. Stringent quality control is therefore key to improved connection performance.
- The finite element analyses show that the behavior of the analyzed connections is insensitive to steels with yield-to-ultimate stress ratios ( $f_y/f_u$ ) less than 0.8 for connection plastic rotations up to 0.03. The analyses further show that steel with a high yield-to-ultimate stress ratio ( $f_y/f_u = 0.95$ , for example) can result in a large reduction in the plastic hinge length of the beam, which leads to significantly greater local strains and earlier local buckling.
- Results from the finite element analyses suggest that enlarging the size of the access hole to facilitate welding could significantly increase the potential for ductile fracture at the root of the access hole.
- The finite element analyses support the FEMA-267 (1995) recommendations, which require the use of continuity plates in all connections. However, the analyses also suggest that the provisions may be relaxed with regards to required continuity plate thickness for one-sided connections such as those considered in this research.

- Comparisons between finite element results and currently recommended provisions show that panel zone strength provisions are reasonable for interior connections, but need to be modified for one-sided (exterior) connections.

This research provides extensive information on the effect of influential design variables on inelastic behavior and potential for fracture of welded-bolted connections. Further research is needed to utilize this information, as well as results from other published analytical and experimental studies, to develop more comprehensive criteria for the design of fracture-resistant connections. Finally, much research is still needed to tie results from local analyses of the sort presented in this report to global frame behavior.

## ACKNOWLEDGEMENTS

This is the final report for Sub-Task 5.3.1(b) of Phase II of the SAC Steel Project (CUREe/SAC, Subcontract No. II-36) conducted under the direction of James O. Malley, Project Director for Topical Investigations, and Charles Roeder, Team Leader for Topical Studies on Connection Performance. The SAC Joint Venture is a partnership of the Structural Engineering Association of California (SEAOC), the Applied Technology Council (ATC), and the California Universities for Earthquake Engineering (CUREe). The work forming the basis for this publication was conducted pursuant to a contract with the Federal Emergency Management Agency (FEMA). The substance of such work is dedicated to the public. The authors are solely responsible for the accuracy of the statements or interpretations contained in this publication. No warranty is offered with regards to the results, findings, and recommendations contained herein, either by FEMA, the SAC Joint Venture, the individual joint venture partners, their directors, members or employees. These organizations and individuals do not assume any legal liability or responsibility for the accuracy, completeness, or usefulness of any of the information, product or processes included in this publication.

The authors gratefully acknowledge the suggestions and review comments received from the following individuals: James Malley, Charles Roeder, Steve Mahin, Robert Dodds, Stanley Rolfe, Roger Ferch, Gregory Deierlein, Wei-Ming Chi, Donald White, and Bill Mohr.

# CONTENTS

<b>1.</b>	<b>INTRODUCTION</b>	<b>1</b>
1.1	OBJECTIVES	1
1.2	ANALYSIS CONFIGURATIONS	2
1.3	DESCRIPTION OF BERKELEY SPECIMEN PN3	3
1.4	ORGANIZATION OF REPORT	3
<b>2.</b>	<b>PREVIOUS ANALYTICAL WORK</b>	<b>4</b>
2.1	PATEL AND CHEN (1984)	4
2.2	YANG AND POPOV (1995)	4
2.3	SAC COMPETITION (SAC 1995)	5
2.4	LEON ET AL. (1996)	5
2.5	GOEL ET AL. (1997)	5
2.6	ALLEN ET AL. (1997)	6
2.7	CHI ET AL. (1997)	6
2.8	ROEDER (1997)	7
2.9	SUMMARY OF ANALYTICAL WORK	7
<b>3.</b>	<b>FINITE ELEMENT MODEL DEVELOPMENT</b>	<b>8</b>
3.1	ELEMENT TYPES	8
3.2	BOUNDARY CONDITIONS	8
3.3	GEOMETRIC NONLINEARITY	9
3.4	MATERIAL NONLINEARITY	10
3.5	FINITE ELEMENT MESHES	10
3.6	ELASTIC CONVERGENCE OF SHELL AND SOLID SUB-MODELS	11
3.6.1	IMPLICATIONS OF SUB-MODEL ANALYSES	12
3.7	INELASTIC MESH CONVERGENCE STUDIES	12
3.8	STRESS AND STRAIN INDICES	13
3.9	GLOBAL MEASURES OF DUCTILITY	15
<b>4.</b>	<b>ANALYSIS OF BERKELEY SPECIMEN PN3</b>	<b>17</b>
4.1	COMPARISON OF LOAD-DEFLECTION DATA TO TEST RESULTS	17
4.2	ANALYSIS RESULTS AT BEAM-TO-COLUMN INTERFACE	17
4.3	ANALYSIS RESULTS - OTHER LOCATIONS	19

<b>5.</b>	<b>PARAMETRIC STUDIES</b>	<b>20</b>
<b>5.1</b>	<b>YIELD-TO-ULTIMATE STRESS RATIO</b>	<b>20</b>
<b>5.2</b>	<b>ACCESS HOLE GEOMETRY</b>	<b>21</b>
5.2.1	DESIGN IMPLICATIONS OF ACCESS HOLE ANALYSES	22
<b>5.3</b>	<b>PRESENCE/ABSENCE OF CONTINUITY PLATES</b>	<b>23</b>
5.3.1	DESIGN IMPLICATIONS OF CONTINUITY PLATE ANALYSES	24
<b>5.4</b>	<b>COLUMN WEB THICKNESS</b>	<b>24</b>
5.4.1	SUMMARY OF SERIES CWT RESULTS	26
<b>5.5</b>	<b>BEAM DEPTH</b>	<b>27</b>
5.5.1	SERIES BDN	27
5.5.2	SERIES BD	28
5.5.3	SUMMARY AND IMPLICATIONS OF BEAM DEPTH ANALYSES	29
<b>5.6</b>	<b>BEAM FLANGE THICKNESS</b>	<b>30</b>
5.6.1	SUMMARY OF BEAM FLANGE THICKNESS ANALYSES	30
<b>5.7</b>	<b>COLUMN FLANGE THICKNESS</b>	<b>31</b>
<b>5.8</b>	<b>SHEAR TRANSFER IN FR WELDED-BOLTED CONNECTIONS</b>	<b>32</b>
5.8.1	SHEAR TRANSFER IN SPECIMEN PN3	32
5.8.2	EFFECT OF SHEAR TAB GEOMETRY	33
5.8.3	IMPLICATIONS OF SHEAR TAB STUDIES	34
<b>6.</b>	<b>PANEL ZONE YIELDING</b>	<b>36</b>
<b>6.1</b>	<b>EVALUATION OF CURRENT DESIGN PROVISIONS</b>	<b>37</b>
6.6.1	DESIGN IMPLICATIONS	37
<b>7.</b>	<b>SUMMARY AND CONCLUSIONS</b>	<b>40</b>
<b>7.1</b>	<b>SUMMARY</b>	<b>40</b>
<b>7.2</b>	<b>CONCLUSIONS</b>	<b>41</b>
7.2.1	STRESS CONCENTRATION AT WELD-COLUMN INTERFACE	41
7.2.2	TRIAxIAL RESTRAINT AT WELD-COLUMN INTERFACE	41
7.2.3	YIELD-TO-ULTIMATE STRESS RATIO	41
7.2.4	ACCESS-HOLE GEOMETRY	42
7.2.5	PRESENCE/ABSENCE OF CONTINUITY PLATES	42
7.2.6	COLUMN WEB THICKNESS AND PANEL ZONE STRENGTH	42
7.2.7	BEAM DEPTH	42
7.2.8	BEAM FLANGE THICKNESS	43
7.2.9	SHEAR TRANSFER	43
7.2.10	PANEL ZONE STRENGTH PROVISIONS	44
<b>7.3</b>	<b>RECOMMENDATIONS FOR FUTURE WORK</b>	<b>44</b>

## LIST OF TABLES

TABLE 1.1: AVERAGE MEASURED MATERIAL PROPERTIES	49
TABLE 2.1: SUMMARY OF RECENT ANALYTICAL WORK	49
TABLE 2.2: DETAILS OF SAC COMPETITION ANALYSES	50
TABLE 5.1: PROPERTIES OF YUSR SPECIMENS	51
TABLE 5.2: SUMMARY OF ACCESS HOLE ANALYSES	51
TABLE 5.3: PROPERTIES OF SPECIMENS OF SERIES CONT	51
TABLE 5.4: PROPERTIES OF CONFIGURATIONS IN SERIES CWT	51
TABLE 5.5: EFFECT OF PANEL ZONE STRENGTH ON STRESSES AND STRAINS	52
TABLE 5.6: PROPERTIES OF CONFIGURATIONS IN SERIES BDN ( $f_{yb}=36$ ksi, $f_{yc}=50$ ksi)	52
TABLE 5.7: PROPERTIES OF CONFIGURATIONS IN SERIES BD ( $f_{yb}=70$ ksi, $f_{yc}=45$ ksi)	52
TABLE 5.8: PROPERTIES OF CONFIGURATIONS IN SERIES BF	53
TABLE 5.9: PROPERTIES OF CONFIGURATIONS IN SERIES CFN	53
TABLE 5.10: PROPERTIES OF CONFIGURATIONS IN SERIES CFN	53
TABLE 5.11: PROPERTIES OF CONFIGURATIONS IN SERIES ST	54
TABLE 5.12: PERCENTAGE SHEAR TRANSFERRED THROUGH SHEAR TAB	54
TABLE 5.13: PERCENTAGE SHEAR TRANSFERRED THROUGH THE SHEAR TAB FOR DIFFERENT BEAM DEPTHS	54

## LIST OF FIGURES

FIGURE 1.1: TEST SETUP FOR SPECIMEN PN3	55
FIGURE 1.2: DETAILS OF CONNECTION SPECIMEN PN3	55
FIGURE 3.1: HOURGLASSING IN REDUCED INTEGRATION SHELL ELEMENTS	56
FIGURE 3.2: DETAILS OF SUPPORT CONDITIONS	56
FIGURE 3.3: EFFECT OF GEOMETRIC IMPERFECTION SIZE ON INELASTIC RESPONSE	57
FIGURE 3.4: TRUE-STRESS VS. TRUE-PLASTIC STRAIN CURVES	57
FIGURE 3.5: ALL-SHELL FINITE ELEMENT MESH	58
FIGURE 3.6: HYBRID SHELL/SOLID FINITE ELEMENT MESH	58
FIGURE 3.7: MESH WITH 4-S4R5 ELEMENTS	59
FIGURE 3.8: MESH WITH 4-C3D8R ELEMENTS	59
FIGURE 3.9: MESH WITH 16-S4R5 ELEMENTS	59
FIGURE 3.10: MESH WITH 16-C3D8R ELEMENTS	59
FIGURE 3.11: STRESS DISTRIBUTION AT INTERFACE FOR BRICK ELEMENT MODELS	60
FIGURE 3.12: STRESS DISTRIBUTION AT INTERFACE FOR SHELL ELEMENT MODELS	60
FIGURE 3.13: COMPARISON BETWEEN DIFFERENT TYPES OF ELEMENTS	61
FIGURE 3.14: DEFORMED MESH S4-6. NOTE THE BUCKLED COMPRESSION FLANGE.	61
FIGURE 3.15: INELASTIC CONVERGENCE STUDY OF SHELL MODELS	62
FIGURE 3.16: SOME LOCATIONS AT WHICH STRESSES AND STRAINS ARE EXTRACTED	62
FIGURE 3.17: GLOBAL MEASURES OF DEFORMATION	63
FIGURE 4.1: COMPARISON BETWEEN MEASURED AND COMPUTED FORCE VS. TIP DISPLACEMENT RESPONSE	64
FIGURE 4.2: COMPARISON BETWEEN MEASURED AND COMPUTED MOMENT VS. TOTAL PLASTIC ROTATION RESPONSE	64

FIGURE 4.3: DISTRIBUTION OF STRESSES ALONG INTERFACE LINE	65
FIGURE 4.4: DEVIATION OF STRESS FIELD AT ONSET OF INELASTICITY	65
FIGURE 4.5: DISTRIBUTION OF INDICES ALONG INTERFACE LINE AT FAILURE BPR (BPR=0.011)	66
FIGURE 4.6: CHANGE IN PRESSURE AND PEEQ INDICES AT BEAM FLANGE CENTER ON INTERFACE LINE	66
FIGURE 4.7: DISTRIBUTION OF INDICES ALONG BEAM HAZ LINE	67
FIGURE 4.8: DISTRIBUTION OF INDICES ALONG ACCESS HOLE LINE	67
FIGURE 5.1: EFFECT OF YIELD-TO-ULTIMATE STRESS RATIO ON PLASTIC HINGE LENGTH	68
FIGURE 5.2: ASSUMED STRESS-STRAIN CURVES WITH DIFFERENT YUSR RATIOS.	69
FIGURE 5.3: EFFECT OF YIELD-TO-ULTIMATE STRESS RATIO ON LOAD VS. TIP DEFLECTION BEHAVIOR	69
FIGURE 5.4: CONTOUR PLOTS OF THE PLASTIC EQUIVALENT STRAIN (PEEQ) FOR YUSR- 65, YUSR-85, AND YUSR-95. RESULTS PLOTTED AT CPR=0.03.	70
FIGURE 5.7: DISTRIBUTION OF PEEQ INDICES ALONG TRANSVERSE AND LONGITUDINAL LINES	71
FIGURE 5.5: DETAILS OF THE ACCESS HOLE GEOMETRY	72
FIGURE 5.6: EFFECT OF ACCESS HOLE SIZE AND GEOMETRY ON PEEQ INDICES	72
FIGURE 5.8: EFFECT OF ACCESS HOLE SIZE AND GEOMETRY ON LONGITUDINAL STRESSES. STRESSES PLOTTED ALONG TRANSVERSE LINE THROUGH ROOT OF ACCESS HOLE	73
FIGURE 5.9: DEFORMED SHAPES OF SPECIMEN WITH AND WITHOUT CONTINUITY PLATES	73
FIGURE 5.10: DEFORMED SHAPES OF SPECIMEN AT DIFFERENT LEVELS OF CPR. DISPLACEMENTS ARE MAGNIFIED 20 TIMES.	75
FIGURE 5.11: EFFECT OF CONTINUITY PLATES ON PRESSURE INDEX AT INTERFACE LINE, CPR=0.03	74
FIGURE 5.12: DISTRIBUTION OF STRESSES ALONG INTERFACE LINE	74
FIGURE 5.13: DEFORMATION CHARACTERISTICS OF CWT3 AND CWT3-N	75
FIGURE 5.14: DISTRIBUTION OF HYDROSTATIC STRESSES ALONG INTERFACE LINE	76
FIGURE 5.15: EFFECT OF PANEL ZONE TO BEAM STRENGTH RATIO ON PRESSURE INDEX AND PRINCIPAL STRESS AT MIDDLE OF INTERFACE LINE	76
FIGURE 5.16: EFFECT OF PANEL ZONE TO BEAM STRENGTH RATIO ON PEEQ INDEX AT MIDDLE OF INTERFACE AND COLUMN HAZ LINE	77
FIGURE 5.17: EFFECT OF BEAM DEPTH ON PRESSURE INDEX AT MIDDLE OF INTERFACE LINE	77
FIGURE 5.18: EFFECT OF BEAM DEPTH ON LONGITUDINAL BEAM STRESS AT MIDDLE OF INTERFACE LINE	78
FIGURE 5.19: PANEL ZONE PLASTIC ROTATION VERSUS BEAM PLASTIC ROTATION FOR SPECIMEN BDN1 (DEPTH = 18 IN) AND BDN4 (DEPTH = 40 IN)	78
FIGURE 5.20: DEFORMED SHAPES OF SPECIMEN BDN1 AND BDN4 AT DIFFERENT LEVELS OF CPR. DISPLACEMENTS ARE MAGNIFIED 20 TIMES IN THE LOWER FIGURES.	79
FIGURE 5.21: EFFECT OF BEAM DEPTH ON PEEQ INDEX AT MIDDLE OF ACCESS HOLE LINE	80
FIGURE 5.22: DEFORMED SHAPES OF SPECIMEN BD1 AND BD4 AT CPR=0.025. THE DISPLACEMENTS ARE MAGNIFIED 20 TIMES IN THE LOWER FIGURES.	80

FIGURE 5.23: DEFORMATION CHARACTERISTICS OF CONFIGURATIONS BD1 (BEAM DEPTH 18 IN) AND BD4 (BEAM DEPTH = 40 IN)	81
FIGURE 5.24: EFFECT OF BEAM DEPTH ON PRINCIPAL STRESS AT MIDDLE OF INTERFACE LINE	81
FIGURE 5.25: EFFECT OF FLANGE THICKNESS ON PRESSURE INDEX, LONGITUDINAL STRESS AT INTERFACE LINE	82
FIGURE 5.26: EFFECT OF BEAM FLANGE THICKNESS ON STRAINS	82
FIGURE 5.27: LOAD VS. PANEL ZONE PLASTIC DISTORTION	83
FIGURE 5.28: HYDROSTATIC AND PRINCIPAL STRESSES IN SERIES CF (WEAK PANEL ZONE)	83
FIGURE 5.29: DISTRIBUTION OF SHEAR AT COLUMN INTERFACE (AT 43% OF NOMINAL DESIGN LOAD - ELASTIC BEHAVIOR)	84
FIGURE 5.30: DISTRIBUTION OF SHEAR FORCE IN SHEAR TAB AS A FUNCTION OF APPLIED LOAD	84
FIGURE 5.31: EFFECT OF SHEAR TAB THICKNESS ON DISTRIBUTION OF SHEAR FORCES PER UNIT LENGTH ALONG THE SHEAR TAB (ELASTIC BEHAVIOR)	85
FIGURE 5.32: EFFECT OF SHEAR TAB HEIGHT ON DISTRIBUTION OF SHEAR FORCE ALONG SHEAR TAB	86
FIGURE 6.1: ASSUMED DEFORMED SHAPE OF WEAK PANEL ZONE	87
FIGURE 6.2: GRAVITY AND SEISMIC MOMENTS ON INTERIOR CONNECTIONS	87
FIGURE 6.3: GRAVITY AND SEISMIC MOMENTS ON EXTERIOR CONNECTIONS	88
FIGURE 6.4: COMPARISON BETWEEN FE RESULTS AND FEMA-267 (1995) PROVISIONS FOR PANEL ZONE STRENGTH – SERIES BD	89
FIGURE 6.5: COMPARISON BETWEEN FE RESULTS AND FEMA-267 (1995) PROVISIONS FOR PANEL ZONE STRENGTH – SERIES CF	90
FIGURE 6.6: COMPARISON BETWEEN FE RESULTS AND FEMA-267 (1995) PROVISIONS FOR PANEL ZONE STRENGTH – SERIES CWT	91
FIGURE 6.7: DEFORMED SHAPES OF SPECIMENS CWT1 AND CWT5	92
FIGURE 6.8: STRUCTURAL SYSTEM FOR 17 STORY BUILDING	93

# 1. INTRODUCTION

Widespread connection damage during the Northridge earthquake undermined confidence in the ductility of special moment resisting frames (SMRF), and raised many questions regarding the validity of then existing design and construction procedures for fully-restrained (FR) welded-bolted connections. An extensive research program funded by several agencies is currently underway to gain a better understanding of why FR welded-bolted connections performed poorly. Results from the research conducted so far indicate that numerous factors may have contributed to the observed failures. However, it is not yet clear how these factors interact, and to what extent they may have played a role in the observed behavior.

## 1.1 OBJECTIVES

The objectives of this project, which is a subtask of SAC/FEMA Task 5.3, are 1) to develop a more thorough understanding of the inelastic behavior of pre-Northridge FR welded-bolted connections, and 2) lay the groundwork for the development of connection details that are not fracture critical. The project builds upon previous analytical and experimental studies and attempts to establish the effect of a number of key parameters on the ductility and potential for fracture of welded-bolted connections. The research addresses these objectives through detailed three-dimensional nonlinear finite element analyses of connection subassemblages. The parameters that are addressed include:

- Key geometric parameters
  - Beam flange thickness
  - Column flange thickness
  - Beam depth
  - Column web thickness
  - Continuity plate thickness, or absence
  - Size and geometry of the weld access hole
- Variation in the material properties of the steel in the beam and column
  - Beam-to-column yield stress ratio
  - Beam yield-to-ultimate stress ratio
- Degree of panel zone deformation
- Shear tab depth, thickness, and shear span-to-depth ratio.

It must be emphasized that the studies conducted in this subtask do not address the issue of fracture propagation. This project is concerned with the potential for cracking only through the development of stress states or material conditions that would facilitate fracture if a flaw or other irregularity were introduced. The project is also concerned with conditions that clearly facilitate

yielding which shield critical areas and reduce crack potential. Fracture propagation studies were addressed in Subtask 5.3.1-a (Chi et. al. 1997).

## 1.2 ANALYSIS CONFIGURATIONS

The geometry of the analysis configurations utilized in this research is derived from the geometry of Berkeley specimen PN3 (Popov et. al. 1996) tested during Phase I of the SAC Steel Project. This particular specimen was chosen because it is representative of pre-Northridge construction practices and because it exhibited some ductility prior to failure.

Different analysis configurations are created by changing some of the attributes of specimen PN3. Important geometric and material parameters are varied over the practical range of interest in order to evaluate their effect on inelastic behavior. Non-standard sections are therefore generated in many instances. This is necessary because the use of standard sections results in the variation of several geometric properties at the same time, thus making it impossible to isolate the effect of the parameters being investigated.

The configurations that are analyzed in this work are shown in **Table A.1**, and are discussed in detail in Chapter 5. Also shown in **Table A.1** are the tip loads required to cause the configurations to reach their panel zone strength ( $P_z$ ), beam strength ( $P_b$ ), and column strength for pure bending ( $P_c$ ). The strengths shown do not include the strength reduction ( $\phi$ ) factors and are calculated according to the 1991 UBC provisions in effect prior to the Northridge earthquake. The panel zone strengths do *not* account for the 80% factor specified by the UBC code for panel zone design. These loads, as well as the ratios  $P_z/P_b$  and  $P_c/P_b$  give an indication of where inelastic deformation is expected to occur, and are useful in categorizing and evaluating results.

To compare between the behavior of the different configurations analyzed in this research, and to assess the effect of the parameters of interest, a number of different stress, strain, and combined stress/strain indices are employed. These quantities are sampled at connection plastic rotations of 0.0025 *rad* and 0.03 *rad*. The connection plastic rotation (CPR) is defined as the plastic tip displacement divided by the beam length. The former CPR is intended to represent the behavior of connections with little ductility. Many of the connections tested experimentally fractured at a connection plastic rotation that was less than 0.0025 *rad*. The larger CPR is intended to represent the behavior of connections with greater ductility. Currently recommended design provisions (FEMA 267A 1997) require a minimum plastic rotation of at least 0.03 *rad* if the rotational demands are not shown to be lower than this.

In view of the observed behavior and current test results, it is likely that most pre-Northridge type connections will *not* achieve a CPR of 0.03 *rad*. However, it is the objective of this project to identify what details or attributes contribute to such lack of ductility. This is particularly important in the event that better welding practices or other construction details, which lead to better performance, are adopted in the future.

### 1.3 DESCRIPTION OF BERKELEY SPECIMEN PN3

Specimen PN3 consists of W36x150 beam connected to W14x257 column. The specimen is detailed according to construction practices used prior to the Northridge earthquake. The web is connected through a bolted shear tab with supplementary welding, while the flanges are joined using field groove welds. The beam flanges and groove welds are 0.94 inches thick. The flange welds are made by using Flux Core Arc Welding (FCAW) procedure with E70-T4 electrodes (Lincoln Electric NS-3M). The weld-backing bars were left in place during testing. Continuity plates (1/2" x 6") were located at both sides of the column.

Details of the test setup and the specimen are shown in **Figure 1.1** and **Figure 1.2**. I-beams provide vertical and horizontal support to the column. Lateral bracing is provided as shown in **Figure 1.1**, and a hydraulic ram provides the cyclic load. The beam consists of A36 steel and the column is made of A572 Gr. 50 steel. The measured material properties are shown in **Table 1.1**. Since the properties for the E70 electrodes were not reported, the yield stress of the weld material is assumed to be 60 ksi.

### 1.4 ORGANIZATION OF REPORT

This report is organized into 7 chapters. Chapter 1 introduces the objectives and motivation for the project. The analysis configurations and the methodology employed for evaluating the analytical results are also briefly outlined. A literature review of previous analytical work on pre-Northridge type connections is presented in Chapter 2. Chapter 3 focuses on details of the finite element models utilized. The types of elements employed, as well as the meshes chosen, and mesh convergence studies are presented. The stress and strain types extracted from the finite element results are described, along with how connection, column, panel zone, and beam plastic rotations are computed. The inelastic behavior of Berkeley specimen PN3 is then presented in Chapter 4. The results of the parametric studies conducted are presented and discussed in Chapter 5, and the design implications of panel zone yielding are discussed in Chapter 6. The conclusions and findings of this study are outlined in Chapter 7. Finally, the matrix of analysis configurations is provided in Appendix A and detailed results from each finite element analysis are provided in Appendix B for reference.

## 2. PREVIOUS ANALYTICAL WORK

Considerable analytical research has already been undertaken to better understand the behavior of FR welded-bolted connections. The main features of these analyses are described below and summarized in **Table 2.1** and **Table 2.2**.

### 2.1 PATEL AND CHEN (1984)

One of the earlier finite element analyses of welded-bolted steel connections is that conducted by Patel and Chen (1984). The analyses were conducted using the program NONSAP, assuming 2-D plane stress behavior. The inelastic behavior of steel was modeled employing the Von-Mises yield criterion and using rectangular isoparametric elements. Inelastic behavior of bolts and thermal residual stresses were both accounted for, but geometric imperfections were not included in the analyses. Patel and Chen concluded that their finite element model was capable of simulating the observed behavior of welded-bolted connections in a satisfactory manner, in particular, load-deflection behavior, spread of yielded zone, and stress distribution in the panel zone. It should be noted, however, that the test program and corresponding analyses considered monotonic, gravity type loading only.

### 2.2 YANG AND POPOV (1995)

Through a simplified stress analysis, Yang and Popov (1995) showed that there were significant triaxial stresses in the beam flange-column welds. The maximum tensile stress along the beam axis (z axis) was 35% in excess of the nominal flexural stress, while the stresses in the two other global directions (x and y axes) were 58% of the nominal flexural stress. Three-dimensional *elastic* finite element analyses confirmed that the maximum tensile stress was similar to that obtained from the simplified analyses, however the stresses computed along both the x and y axes were approximately 50% of the value obtained from the simplified analyses. Shear stresses calculated by the finite element analysis were small, which lead Yang and Popov (1995) to conclude that the observed low ductility was due to limited shear slip.

Using the computer program ABAQUS, Yang and Popov (1995) also performed three-dimensional *inelastic* analyses of subassemblages that were tested as part of their research. The model employed 8 node brick elements and relied on the Von Mises yield criterion. Residual stresses and geometric imperfections were ignored in the analyses. In general they were able to obtain a good correlation between the analytically calculated load-displacement curves, and the experimentally measured ones, although the lack of residual stresses in the analytical model led to sharper changes in the response than was observed experimentally. By assuming that the unfused surface between the backing bar and the column flange causes a sharp crack, they used fracture mechanics to explain the experimentally observed behavior. They noted that the stress intensity factor for the bottom backing bar was larger than that for the top backing bar, and

surmised that that could be the reason for the preponderance of bottom flange fractures over top flange fractures. They also drew attention to the fact that the critical stress intensity factor is sensitive to small variations in temperature.

### **2.3 SAC COMPETITION (SAC 1995)**

SAC conducted a competition in which participants were asked to predict the response of an untested full size joint specimen in October 1995. Data on the test set-up, material properties, and the loading history were provided to the participants who were asked to predict the failure mode, initiation of local buckling, peak load, and other structural responses. The connection specimen was later tested at UC Berkeley EERC in November 1995, and predictions from the participants were then compared to the test results. **Table 2.2** shows a summary of the types of analyses submitted. As can be seen from the table, a wide range of models was presented, including beam-column models, and two- and three-dimensional continuum models. Although many of the entries predicted initial yielding accurately, most failed to predict initial buckling and the failure characteristics as well.

### **2.4 LEON et al. (1996)**

Leon et al. (1996) tested and analyzed 3 beam to column subassemblages with reinforced concrete top slabs acting compositely with the steel beams. Their tests showed evidence of brittle and low cycle fatigue fractures in the bottom welds of the beam flange-column interface. Detailed 3-D finite element analyses were also conducted using the program ABAQUS. Linear brick elements were used, and the top RC slab was accounted for in the analyses. To reduce the size of the finite element model, the parts of the columns that remained elastic were modeled using beam-column elements, which were linked to the brick element part. Deformation constraints were applied at the beam-column/brick element interface to ensure plane section behavior. Analysis results and data collected during the tests and from the inelastic analyses indicate that in addition to strain concentrations near the beam flange-column interface, the strains at the bottom welds are significantly higher than those in the top welds due to the presence of the slab. They suggested that these increased strains were responsible for the preponderance of the bottom weld fractures over top weld fractures.

### **2.5 GOEL et al. (1997)**

Based on observations drawn from 3-D elastic finite element analyses of a shell element model, Goel et al. (1997) noted that the stress distribution at the beam-column interface is very complex, with most of the shear force carried by the beam flanges, and not the beam web. They suggested that the flow of forces is better described by truss analogy, rather than the traditional approach whereby the web carries the shear and the flanges carry the bending moments. They proposed that the combination of triaxial stresses in the welds due to the column flange restraint in addition to the shear stresses overload the weld material, resulting in brittle failure. Truss

analogy was also used to explain the predominance of bottom weld failures since the top slab was thought to provide significant resistance to the vertical component of the force generated by the assumed truss action.

## **2.6 ALLEN et al . (1997)**

Allen et al. (1995) conducted a number of finite element analyses using the program ANSYS. The analyses employed shell and solid element models. Based on their analysis results, Allen et al. (1995) suggested that material at the beam flange-column interface is *not* constrained in such a way as to produce brittle failure. This was concluded from finite element analysis results that showed Von Mises stresses to be approximately equal to the maximum principal stresses. The suggestion is in contrast to Yang and Popov's (1995) conclusion that significant triaxial stresses at the beam-flange column interface may have been responsible for the observed low ductility. The analyses by Allen et al. (1997) also showed that there was significant stress concentration in the center of the beam flange due to the presence of the beam web. They suggested that the prying action caused by the large stress and strain gradients in the beam flanges most likely initiated fractures at the center of the weld-column interface. Their stress concentration factor was about 4.5, which was significantly higher than that obtained by Yang and Popov (1995). It should be noted however that their analyses did not include continuity plates as the analyses by Yang and Popov (1995) did. In addition, the analyzed configuration was different.

## **2.7 CHI et al. (1997)**

A series of 2-D and 3-D linear elastic fracture mechanics (LEFM) and inelastic fracture analyses of pre-Northridge type connections were conducted by Chi et al. (1997). The analyses were performed using the program FRANC, which was developed at Cornell University, and ABAQUS. The 2-D LEFM analyses utilized elastic 6-noded triangular elements with  $\frac{1}{4}$  point nodes to simulate the singularity at the crack tips. Collapsed 8-noded quadrilateral elements were used to represent inelastic crack tip blunting. Most of the elements used were plane stress, except for elements near the crack tip, which were designated as plane strain. Results from the study indicated that the weld-backing bar had an effect on the analyses only when the weld root defects were smaller than a certain size (0.1"). Moreover, placing a fillet weld at the underside of the backing bar as suggested earlier by Yang and Popov (1995) is especially beneficial for connections susceptible to brittle fracture in the elastic range. Elastic propagation studies indicated that cracks initiating at the weld-column interface would propagate into the column causing a divot-type failure. However, the crack trajectories were shown to be sensitive to a number of parameters, for example, column tension causes cracks to propagate into the column instead of just through the weld, or the trajectory taken in a divot-type failure.

## 2.8 ROEDER (1997)

Roeder (1997) conducted studies of two steel buildings that were damaged in the Northridge earthquake. A series of two- and three-dimensional frame analyses were performed to establish, among other things, the loading conditions for selected joints. The joints were then discretized using shell elements and analyzed. Results from the analyses indicated that significant stress concentrations existed in the center of the beam flange at its intersection with the column flange. Panel zone deformation was observed to cause additional stress and strain concentrations in this region. As discussed by Roeder (1997), this situation gave rise to large hydrostatic tensile stresses thereby making the region more susceptible to cracking.

## 2.9 SUMMARY OF ANALYTICAL WORK

A summary of the features of the above-described analyses is shown in **Table 2.1**. The following points can be noted **Table 2.1** and the description given above:

1. A wide spectrum of analyses are represented: two- and three-dimensional analyses, elastic and inelastic, fracture analyses, analyses based on equilibrium and compatibility, simplified analyses utilizing one-dimensional beam-column elements, etc.
2. Most of the analyses described did not account for residual stresses or geometric imperfections, probably because of the lack of knowledge about the actual residual stress distribution or size and distribution of geometric imperfections.
3. Among the computer programs employed, ABAQUS has been used most frequently.
4. The Von Mises yield criterion has been used in the majority of the analyses.
5. Mesh convergence studies were not reported in many of the analyses.
6. Finally, several of the analyses were conducted in order to either support experiments, or to study the effect of a few parameters on connection response. None of these studies systematically addressed as comprehensive a set of parameters as is planned in this subtask.

### 3. FINITE ELEMENT MODEL DEVELOPMENT

Development of the finite element models to represent specimen PN3 and the analysis configurations utilized in this research required addressing a number of modeling issues. Following is a discussion of these topics.

#### 3.1 ELEMENT TYPES

In general, second-order (quadratic interpolation) solid elements provide higher accuracy than first-order (linear interpolation) elements and are more versatile for modeling geometric features. However, second-order elements are more computationally expensive than first order solid elements and, therefore, have not been used in this research. An advantage of first order elements over second order elements is that the formers generally perform better in analyses requiring large element distortions or with large strain gradients. They are therefore more appropriate for this research because of the large plastic deformations and strain gradients expected in the connection region.

Reduced integration is used for all solid and shell element for computational efficiency. It is well known that reduced integration elements are not necessarily less accurate than fully integrated elements. However, first order, reduced integration elements may exhibit hourglassing. It is possible for them to distort in such a way that the strains calculated at the integration point are all zero, which leads to uncontrolled distortion of the mesh, see **Figure 3.1**. ABAQUS's hourglass control feature had to be calibrated to prevent this type of behavior. For the solid elements employed in this research, reduced integration implies the use of one integration point to represent the element. The number of integration points through the thickness of shell elements is taken as 5. Work by Huang (1994) indicated that while 3 integration points gave slightly inaccurate results, 7 integration points provided no real advantage.

#### 3.2 BOUNDARY CONDITIONS

It is possible to model the supports of the experimental setup shown in **Figure 1.1** in considerable detail. To determine if this is necessary, a number of analyses were conducted to study the sensitivity of the solution to the assumed boundary conditions. The analyses utilized different support models ranging from one point supports to more detailed support models. The results of the sensitivity study showed that the beam tip deflection varies by less than 6% amongst all the cases considered. Therefore, elaborate support models in which the support beam are represented are not considered because of the relative insensitivity of the subassembly response to variations in the support conditions.

The support model adopted is shown in **Figure 3.2**. In this model, the column base is assumed to be fully supported against  $y$  and  $z$ -displacements. A 7-inch high strip with a width equivalent to

the column flange width is also prevented from movement in the  $x$ -direction, simulating the lateral supporting beam. The column top is similarly supported in the lateral direction as shown in **Figure 3.2**. To prevent sidesway, lateral supports are assumed as shown in **Figure 3.2**. This boundary condition prevents movement of the connection subassembly in the  $z$ -direction and is applied through the depth of the beam. The subassembly is loaded in displacement control. The displacements are applied through three nodes at the extreme end of the subassembly. The applied tip load is back-calculated from static equilibrium using the reactions that are generated at the supports.

### 3.3 GEOMETRIC NONLINEARITY

Geometric nonlinearity (finite displacements) must be taken into consideration since the inelastic behavior of a connection subassembly may be significantly affected by it. Two assumptions are made:

1. The distribution of geometric imperfections are a linear weighted combination of the first two eigen vectors of the loaded connection configuration. The weights used for each mode shape are the maximum imperfections corresponding to that buckled shape. This approach is thought to yield the lowest ultimate load (Huang 1992, Schafer 1994, ABAQUS 1996), particularly if the eigen vectors of the model do not change significantly after the spread of plasticity.
2. The maximum value of geometric imperfection is 0.1 inches. The point with the largest eigen vector component (which is scaled down to 0.1 inches) does not exist on the beam flange but corresponds to a location on the beam web. The corresponding maximum imperfection in the beam flanges is about 0.06 inches. The ratio of this imperfection to the width of the beam flange is approximately similar to that used by Greschik et al. (1993). Further, the resulting beam flange imperfection is reasonable when compared to the total out-of-square fabrication tolerances specified in the AISC (1994) manual for W12 sections and deeper. According to the Manual, which is based upon ASTM A6, the total out-of-square tolerance for a cross-section is 5/16 inch. Assuming that this is evenly distributed between the four flange projections, the permissible imperfection is approximately  $\frac{1}{4}$  of 5/16-inch  $\approx$  0.08-inch.

The buckled shape of the connection subassembly corresponding to the first eigen vector is shown in **Figure 3.3a**. It should be noted that using imperfections not only increases the accuracy of modeling, but may actually reduce running time if geometric nonlinearity is accounted for (Schafer 1994).

To test the sensitivity of the subassembly to the size of geometric imperfections, three inelastic, geometrically nonlinear runs are conducted with different values of maximum imperfections. The maximum imperfections used are 0.05, 0.1, and 0.5-inches. Plotted in **Figure 3.3b** are the load-tip deflection curves for the three analyses. It is clear that the effect of the size of initial geometric imperfection on the response is small, even for the case with an unrealistically large imperfection of 0.5-inches. The cases with 0.05 and 0.1-inch imperfections are almost identical,

although the run with the smaller initial imperfection (0.05-inches) required more analysis steps, and hence longer running time. The buckled shape of the compression flange for one of the cases analyzed can be seen in **Figure 3.14**.

### 3.4 MATERIAL NONLINEARITY

Material nonlinearity is accounted for in the monotonic analyses through an isotropic classical plasticity model based on the Von Mises yield criterion and associated plastic flow (ABAQUS 1996). The nominal stress strain curves reported in experiments are adjusted to establish true stress vs. true plastic strain curves, such that:

$$\sigma_{true} = \sigma_{nom}(1 + \varepsilon_{nom}) \quad 3.1$$

$$\varepsilon_{pl} = \ln(1 + \varepsilon_{nom}) - \frac{\sigma_{nom}}{E} \quad 3.2$$

where,  $\sigma_{true}$  and  $\varepsilon_{pl}$  are the true stress and plastic strain respectively,  $\sigma_{nom}$  and  $\varepsilon_{nom}$  are the nominal stress and strain respectively, and  $E$  is the modulus of elasticity. The true stress vs. true plastic strain curves for A36 and A572 Gr. 50 steels are shown in **Figure 3.4**. These were derived from *nominal* stress-strain curves published in Salmon and Johnson (1996, pg. 47). For cyclic analyses pure kinematic hardening is assumed instead of isotropic hardening. In this case, the hardening stiffness is calculated as the slope of the line connecting the yield point and ultimate stress point on the stress-strain curve.

### 3.5 FINITE ELEMENT MESHES

A number of finite element meshes were utilized in this research, including all-shell meshes and hybrid shell/solid models. The all-shell models (**Figure 3.5**, for example) are computationally efficient but cannot be used to calculate some of the stress and strain quantities of interest in this research because of the assumptions inherent in shell formulations. The hybrid shell/solid models (**Figure 3.6**, for example) are used to calculate such quantities.

The shell models are comprised of 4 node reduced integration shell elements (S4R5 elements), while the hybrid finite element model is comprised of a mixture of 4-node shell (S4R5) and 8-node brick (C3D8R) reduced integration elements. The shell elements allow for finite rotations, but small strains, while the solid elements allow for finite strains and finite rotations.

The part comprised of brick elements is localized around the intersection between the beam bottom flange and the column, as shown in **Figure 3.6**. A graded shell element mesh is used to model the remainder of the subassembly. Multipoint constraints are used to enforce compatibility between the different types of finite elements. The shell elements employed have 5 degrees of freedom (DOFs) per node, of which 3 are displacement DOFs and 2 are out-of-plane

rotational DOFs. Brick elements, on the other hand, have 3 DOFs per node. The multipoint constraints employed ensure that the rotation of a line of brick element nodes to which a shell element node is connected corresponds to the rotation of the shell node. The portion of the shear tab in contact with the beam web is considered to be completely monolithic with the beam web.

### 3.6 ELASTIC CONVERGENCE OF SHELL AND SOLID SUB-MODELS

A number of elastic convergence studies are conducted on the sub-structure shown in **Figure 3.7**. The sub-structure is intended to represent the connection between the lower flange of a beam and a column without continuity plates. The plates are 10 inches by 5 inches and are 1 inch thick. A uniformly distributed load of 250 kips is applied at the right end, and the model is supported along the left vertical edge. Meshes comprised of reduced integration brick elements (C3D8R elements), 8 node brick elements with incompatible modes (C3D8I elements), 4 node reduced integration shell elements (S4R5 elements), and 9 node reduced integration shell elements (S9R5 elements) are used in the convergence studies. A number of cases representative of the different mesh densities used in the study are shown in **Figure 3.7** through **Figure 3.10**. The deformed meshes reflect the significant prying action that is present in this configuration.

Different levels of mesh refinement are referred to by the number of elements used along the beam flange. For example, a 16 element mesh has 16 elements along the width of the beam flange. Convergence is studied through examination of the stress distribution at the interface between the horizontal beam flange and the vertical column flange. The horizontal component of stress ( $s_{11}$ ) is plotted as function of location along the interface. It is clear from an examination of the stress distribution in **Figure 3.11**, for example, that a stress concentration exists at the center of the flange. This stress concentration has been observed in many other analytical studies.

The most accurate elements used in this study are the *brick elements with incompatible modes* (C3D8I elements). These elements perform well for cases involving bending. As can be seen from **Figure 3.11a**, the mesh with 16 elements produces almost converged results. The stress at the center is 58 ksi which is 3.5% greater than the stress obtained from the mesh with 24 elements. The mesh with 4 elements does not provide good results. The stress at the center computed using this mesh is much higher, and the stress distribution is different from those observed in the other finer meshes. The mesh with 8 elements results in a fairly accurate stress distribution, although the central stress is somewhat lower than that obtained in finer meshes. *Brick elements with reduced integration* (C3D8R elements) also perform very well (see **Figure 3.11b**). Even the coarsest mesh with 4 elements results in a stress distribution that compares favorably to that calculated from other more refined meshes.

The central stress does not converge with mesh refinement in meshes comprised of 4 node and 9 node shell elements. As can be seen from **Figure 3.12a**, there are no signs of convergence even though up to sixteen elements are used along the flange. This can be further seen in **Figure 3.13** which shows a comparison between the performance of the different elements for meshes with 8 and 16 elements. The stresses calculated using the S9R5 elements are considerably higher than those obtained from the S4R5 elements, and also show little signs of convergence with mesh

refinement. For example, the mesh with 8 S9R5 elements results in a central stress that is 66% higher than that computed from the mesh with S4R5 elements. The reason for non-convergence of the central stress in the shell models is the geometry of the configuration. As can be seen from **Figure 3.9**, the beam flange is supported by the column flanges and column web. Because the column web is much stiffer than the flanges, it attracts a considerable portion of the applied loads. Further, this high stiffness is concentrated at a single point at the beam flange-column flange interface. Therefore, unrealistically high stress concentrations may develop. It is therefore not advantageous to refine meshes comprised of shell elements in this vicinity since this would result in unrealistically high elastic stress concentrations.

### 3.6.1 IMPLICATIONS OF SUB-MODEL ANALYSES

The results reported above show that the longitudinal stress at the center of the weld-column interface of connections without continuity plates is sensitive to the type of finite element and mesh density. These factors must be carefully considered when evaluating the large stress concentration factors published in the literature. Also based on the studies reported above, it appears that eight C3D8R or S4R5 elements are sufficient for accurately modeling the beam flange, at least for elastic behavior. The hybrid shell/solid model described in Section 3.5, and that has been used in this research, employs 13 C3D8R elements across the beam flange width.

## 3.7 INELASTIC MESH CONVERGENCE STUDIES

A number of analyses of the connection subassembly model are conducted to study the sensitivity of the inelastic solution to mesh refinement. Three different shell meshes S4-6, S4-8, and S4-12 comprised of S4R5 elements are utilized in the study. The beam flange is discretized using 6 S4R5 elements across the width in mesh S4-6, 8 elements in mesh S4-8, and 12 elements in mesh S4-12. The material properties utilized are the measured properties for Berkeley specimen PN3 (Popov et. al. 1996).

The deformed mesh S4-6 at a tip deflection of 10 inches is shown in **Figure 3.14**. It is clear from the figure that the model underwent inelastic buckling in the top flange region that was under compression. There was also significant spread of plasticity in the panel zone and beam flange regions. The force vs. tip displacement responses of the three models are plotted in **Figure 3.15**. An examination of figure reveals that the three meshes essentially behave in the same manner. The *global behavior* of the model is therefore not sensitive to mesh refinement for the cases studied. Hence, mesh S4-6 will be utilized for further studies involving shell elements because it contains the fewest number of elements, and is therefore the most computationally expedient.

The lower beam flange in the hybrid shell/solid mesh (**Figure 3.6**) is modeled using 13 brick elements across the width, and 4 elements through the thickness. Inelastic convergence studies showed that 4 elements through the depth were sufficient for the purposes of this research (Mikesell 1998). The model is comprised of approximately 4,500 brick elements and 3,000 shell

elements, and has 40,000 degrees of freedom. An inelastic monotonic analysis ran anywhere from 2½ - 4 hours on an UltraSparc I-170E with 192 MB of RAM, running under Solaris 5.5.

### 3.8 STRESS AND STRAIN INDICES

To compare between the behavior of the different configurations analyzed in this research, and to assess the effect of the parameters of interest, a number of different stress, strain, and combined stress/strain indices are computed. The calculated stress and strain values are normalized by their corresponding yield stress or strain in order to facilitate comparison between materials with different yield strengths. The beam yield strength is used for normalization when points at the interface between the beam and column are considered. Some of the stress and strain indices employed are:

**Pressure Index:** defined as the hydrostatic stress divided by the yield stress. The pressure index is a negative number for tensile hydrostatic stresses. The hydrostatic stress is defined as follows:

$$\sigma_m = -\frac{1}{3}\text{trace}(\sigma_{ij}) \quad 3.3$$

where  $\sigma_m$  is the mean hydrostatic stress,  $\sigma_{ij}$  are the Cauchy stress components, and  $i,j$  represent the global directions,  $i=1,2,3$ , and  $j=1,2,3$ . A high tensile hydrostatic stress is usually accompanied by large principal stresses. If a crack or some other flaw exists, these high principal stresses can result in large stress intensity factors at the crack tips, which increase the potential for *brittle fracture*. Brittle fracture occurs abruptly and is not accompanied by perceptible global plastic deformations. Alternatively, a high tensile hydrostatic stress can lead to a reduction in ductility as described by LeMaitre (1996), Thomason (1990), and others. Under such conditions, high tensile triaxial stresses cause rapid damage accumulation in metals through micro-void nucleation and coalescence. Such a process is known as *ductile fracture* initiation, and is usually accompanied by plastic deformations prior to fracture. In either case, the presence of high tensile hydrostatic stresses implies a greater potential for fracture.

**Tresca Index:** defined as the maximum deviatoric stress divided by the yield stress. Although the inelastic model employed in this study is based on the von Mises yield criterion, a low Tresca index generally implies lower potential for yielding. The maximum deviatoric stress is defined as:

$$t = \text{Max}(S_{ij}) \quad 3.4$$

where  $t$  is the Tresca stress,  $S_{ij}$  are the deviatoric stress components such that  $S_{ij} = \sigma_{ij} + \sigma_m\delta_{ij}$ .

**PEEQ Index:** defined as the plastic equivalent strain divided by the yield strain. This index is a measure of local ductility. The plastic equivalent strain is defined as:

$$PEEQ = \sqrt{\frac{2}{3} \varepsilon_{ij} \varepsilon_{ij}} \quad 3.5$$

where  $\varepsilon_{ij}$  are the plastic strain components in directions  $i$  and  $j$ .

**Mises Index:** defined as the Von Mises stress divided by the yield stress. The Mises stress,  $\bar{\sigma}$ , is defined as follows:

$$\bar{\sigma} = \sqrt{\frac{3}{2} S_{ij} S_{ij}} \quad 3.6$$

where all the variables involved have been defined previously. This index is used to complement the other indices described above.

**Rupture Index:** The ratio between the hydrostatic stress and the Mises stress ( $\sigma_m / \bar{\sigma}$ ) is known as the stress triaxiality ratio. This ratio is an important quantity when considering ductile rupture of metals. High triaxiality ( $0.75 < \sigma_m / \bar{\sigma} < 1.5$ ) can cause a large reduction in the rupture strain of metals. Very high triaxiality ( $\sigma_m / \bar{\sigma} > 1.5$ ) can result in brittle behavior (LeMaitre 1996 and Barsom and Rolfe 1988). A crude, albeit effective, criterion for calculating the strain at ductile fracture is given by Hancock and Mackenzie (1976):

$$\varepsilon_f = a \exp\left(-1.5 \frac{\sigma_m}{\bar{\sigma}}\right) \quad 3.7$$

where  $\varepsilon_f$  is the failure strain,  $a$  is a material constant, and  $\sigma_m$  and  $\bar{\sigma}$  were defined previously as the hydrostatic and Mises stresses respectively. The rupture index is defined in this work as the ratio between the plastic equivalent strain index and the ductile fracture strain (calculated using Equation 3.7) multiplied by the material constant  $a$ , such that:

$$Rupture\ Index\ (RI) = a \frac{PEEQ}{\varepsilon_f} = \frac{PEEQ}{\exp\left(-1.5 \frac{\sigma_m}{\bar{\sigma}}\right)} \quad 3.8$$

Equation 3.8 can be used to compare between the potential for ductile fracture of two configurations by comparing between the rupture index at critical points. The limitation of this exercise must be realized, however (LeMaitre 1996). A ductile fracture criterion must involve a certain minimum characteristic length that represents the fracture process, which is not represented in this methodology. Further, the failure criterion depends on the direction of rolling, initial imperfections in the steel, and the strain at which ductile damage starts to accumulate, all of which are not accounted for in the above equation. However, this method presents a convenient way to compare between different analyses, keeping in mind the above limitations.

Research by Hancock and Makenzie (1976) show that this criterion is accurate for the three different types of steels they tested.

The indices described above, as well as other types of stresses and strains are computed at different locations and along different lines through the connection in order to be able to compare between the analyzed configurations. A few of the locations and lines considered are shown in **Figure 3.16**. Four lines are of particular importance and deserve a more detailed description:

1. A line in the middle of the column flange denoted by “C-HAZ” in **Figure 3.16**. This region is of interest because of the potential for lamellar flange tearing in the heat affected zone.
2. A line at the interface between the beam and column flanges, denoted by “Interface” in **Figure 3.16**. This line is important because many of the observed cracks initiated in this region. Fractographic examinations by Kaufmann and Fisher (1995) of a number of fractured connections showed that weld defects in the weld root area could be as large as 0.39 in. with a mean value of 0.19 in. The “interface” line is therefore not located at mid-height of the beam flange, but at a location where cracking is more likely to initiate. Because of modeling constraints, stresses and strains are computed along a line located at one-fourth of the height of the flange.
3. A line at the edge of the weld zone denoted by “B-HAZ” and taken nominally  $\frac{1}{2}$ ” away from the interface. This line is located at mid height of the beam flange and is of interest because of a number of fractures were observed in the beam HAZ region.
4. Finally, a line at mid-height of the beam flange, and underneath the access hole as shown in **Figure 3.16**. This region has been shown by other researchers (Leon et. al. 1996) to have significant strain concentration, which could lead to low cycle fatigue in the event of ductile behavior. Many fractures were observed at the root of the weld access hole in W-beams framing into box columns in the aftermath of the Kobe earthquake (Kuwamura 1997).

### 3.9 GLOBAL MEASURES OF DUCTILITY

The stress and strain measures described above are sampled at each load increment, however two levels of connection plastic rotation are of particular importance. Many of the connections tested experimentally fractured at a connection plastic rotation that was less than 0.0025. Currently recommended design provisions (FEMA 267A 1997) require a minimum plastic rotation of at least 0.03 if the rotational demands are not shown to be lower than this. Hence it is important to know what state of stresses and strains exist in the connections at plastic rotations of 0.0025 and 0.03, and in between.

The connection plastic rotation is computed from the finite element results in a manner similar to that used in the experiments by Popov et. al. (1996). The connection plastic rotation (*CPR*) is defined as the plastic tip displacement divided by the beam length. Therefore the *CPR* is an overall measure of connection deformation. The connection plastic rotation is further split up into three components: column plastic rotation (*CoPR*), panel zone plastic rotation (*PZPR*), and beam plastic rotation (*BPR*), as shown in Equation 3.8. These represent the contributions of the column, panel zone, and beam components to the connection plastic rotation (**Figure 3.17**).

$$CPR = CoPR + PZPR + BPR \quad 3.9$$

## 4. ANALYSIS OF BERKELEY SPECIMEN PN3

An analysis of specimen PN3, tested by Popov et al. (1996), is presented in this section. The geometry and test setup of specimen PN3 were described in Section 1.3. The inelastic analysis accounts for both geometric and material nonlinearities and is conducted using measured stress-strain properties (**Table 1.1**).

### 4.1 COMPARISON OF LOAD-DEFLECTION DATA TO TEST RESULTS

Shown in **Figure 4.1** and **Figure 4.2** are comparisons between the analytical and experimental results for Berkeley specimen PN3. The analytical results were computed using shell model S4-6 described in Section 3.7, accounting for both material and geometric nonlinearities (see Section 3.3 – 3.5). Pure kinematic hardening is assumed for this analysis. The shell model is used because it is much less computationally demanding than the hybrid shell/solid model described in Section 3.5. A close examination of the figures reveals that although the ultimate load and initial stiffness are well represented, the analytical hysteretic loops have slightly ‘sharper’ corners than the experimentally observed ones, possibly because residual stresses were not included in the analysis. Another reason for the differences in results is the possible non-uniformity of the yield strength in the column web. Test results by Shuey et. al. (1996) have shown that the yield strengths of coupons extracted from the web are sensitive to the location within the web from which the coupons were extracted. Coupons extracted close to the flanges had a significantly higher yield strength than those extracted in the middle. However, the average measured web yield strength reported by Shuey et. al. was approximately equal to the flange strength. The locations from which the coupons were extracted were *not* reported for specimen PN3, and it is not clear what the appropriate *average* properties for the column web are.

### 4.2 ANALYSIS RESULTS AT BEAM-TO-COLUMN INTERFACE

The hybrid shell/solid model (**Figure 3.6**) is analyzed under monotonically applied displacement. The maximum displacement level imposed corresponds to that observed at failure in the experiments. The distributions of some of the different stress and strain types considered in this research are plotted out at all load increments.

The distributions of stress components in the three main directions along the interface line (see Section 3.8) are shown in **Figure 4.3**. **Figure 4.3a** corresponds to elastic behavior. The applied load for this case is 35 % of the measured ultimate load. **Figure 4.3b** corresponds to a condition at the onset of inelasticity. The applied load is 79% of the experimental ultimate load and the corresponding beam plastic rotation (BPR) is 0.0005. **Figure 4.3c** corresponds to a deformation level at which specimen PN3 was observed to fracture in the experiment, at a BPR of 0.011.

The stress concentration factor for elastic conditions is 1.49. The stress concentration factor is defined as the maximum longitudinal stress at the weld-column interface divided by the average longitudinal stress. The maximum values of the longitudinal stress,  $S_{11}$ , and the vertical stress,  $S_{22}$ , both occur in the middle of the beam flange. The transverse stress  $S_{33}$  is nearly constant across the beam flange with an average value of approximately 6 ksi in tension. At the onset of inelastic behavior, the value of  $S_{33}$  at the middle of the interface line abruptly switches signs and becomes compressive. This appears to be due to rapid changes in the direction of the stress path from the beam flange to the column flange as inelastic behavior initiates. This can be visualized from **Figure 4.4**. The figure on the left shows the principal stress directions for elastic behavior. The stress field is parallel in the beam flange, but deviates to approach the stiff column web when it enters the continuity plates. This deviation actually results in a negative compressive field of transverse stresses in the continuity plates. At the onset of yielding at the center of the beam flange to column flange interface, the stress path deviates as shown on the figure on the right. This deviation generates the negative transverse stresses,  $S_{33}$ , observed in this region.

As inelasticity spreads further, the distributions of  $S_{11}$  and  $S_{22}$  flatten out, while the  $S_{33}$  distribution remains essentially unchanged. The shear stresses,  $S_{12}$ ,  $S_{13}$ , and  $S_{23}$ , were found to be rather small along the interface line. The largest calculated values for  $S_{12}$ ,  $S_{13}$ , and  $S_{23}$  are 11, 5.1, and 4 ksi. Such small deviatoric stresses imply small resultant plastic strains. This is clear in the PEEQ indices plotted in **Figure 4.5d**.

Plotted in **Figure 4.5** are pressure, Mises, Tresca, and PEEQ indices. The results are plotted out for each load increment in the analysis along the interface line. A close examination of **Figure 4.5** reveals the following:

1. For elastic behavior, the Mises, pressure, and Tresca indices are maximum at the center of the beam flange.
2. The Mises and Tresca indices keep increasing at the beam flange center as inelasticity spreads, and remain highest at the center.
3. In the presence of inelasticity, the magnitude of the hydrostatic stresses is no longer maximum at the center of the beam flange. It is actually highest a short distance away, on either side of the center. The reason for this behavior is the switch in the sign of the transverse stress,  $S_{33}$ , described above. At the onset of inelasticity, the pressure index magnitude is 0.59 at the center, with a maximum magnitude of 0.77 a short distance away. At the failure BPR observed in the experiment, the pressure index magnitude is 0.565 at the center, and 0.721 at a distance of 3 inches on either side.
4. As loading increases, the pressure index in the middle rises, then falls slightly at the onset of inelastic behavior. This can be seen in **Figure 4.6**. The reason for the drop in pressure is probably the relaxation in restraint due to localized yielding.
5. The PEEQ indices are almost zero across a large portion of the interface line. The maximum PEEQ index occurs in the middle, and has a value of 0.2 at a BPR of 0.011.

Thus there is very little inelastic deformation along the interface line. As discussed above, the reason for this is low deviatoric stresses along the interface. An examination of the Tresca index distribution along the interface shows that the Tresca stresses decrease rapidly away from the center.

As described above, the maximum hydrostatic stress encountered at the weld-column interface is 77% of the yield stress of the beam. The corresponding stress triaxiality (see Section 3.8) is 0.91, and the accompanying plastic deformation is very small (about 20% of the yield strain). This level of stress triaxiality and corresponding plastic strain implies that brittle fracture at the weld-column interface probably occurred due to large pre-existing flaws at the interface rather than limited ductility caused by large stress triaxiality. Fractographic analyses of many damaged connections by Kaufmann and Fisher (1995) support this conclusion. The fractures they encountered in their tests were all observed to initiate at relatively large flaws in the weld metal.

### 4.3 ANALYSIS RESULTS - OTHER LOCATIONS

The distributions of the pressure, Tresca, and PEEQ indices along the B-HAZ line are shown in **Figure 4.7**. In contrast to the interface line, this region exhibits significant inelastic behavior. The PEEQ index is as high as 21 at a BPR of 0.011. This maximum PEEQ index occurs at the edges of the beam flange. The large ductility is evident from the high, almost constant Tresca indices that exist along the B-HAZ line. Note that the distributions of indices are not symmetrical at higher BPR's because of slight beam buckling.

At the center of the B-HAZ line, the maximum PEEQ is reduced to approximately 14. At this location, the pressure index magnitude is highest, reaching 0.67. Stress triaxiality is 0.55, not particularly high. The distributions of the pressure, Tresca, and PEEQ indices along the access hole line are shown in **Figure 4.8**. This line is located underneath the access hole, at mid height of the beam flange. The distribution of indices along this line is similar to that observed along the B-HAZ line.

## 5. PARAMETRIC STUDIES

In this section a series of nonlinear finite element analyses are conducted in order to gain a better understanding of the behavior of pre-Northridge connections. Key geometric and material parameters are varied over the practical range of interest in order to gauge their effect on inelastic behavior. In these analyses, the weld material is assumed to have beam flange material properties, and both material and geometric nonlinearities are accounted for as discussed in Section 3.3-3.5.

### 5.1 YIELD-TO-ULTIMATE STRESS RATIO

For the subassembly in **Figure 5.1**, the applied moment varies linearly over the beam length. Assuming that the material at the beam-column interface can reach the ultimate beam strength ( $f_u$ ) without local buckling, the fully plastified length is  $\gamma L$ , such that:

$$\gamma L = (1 - \alpha\psi)L \quad 5.1$$

where,  $\psi$  is the yield-to-ultimate stress ratio, and  $\alpha$  is a factor that accounts for the effect of beam axial load and cross-section properties. Equation 5.1 suggests that the fully plastified length is a linear function of the yield-to-ultimate stress ratio ( $\psi$ ).

The plastic hinge length is comprised of the fully plastified length and the distance along which the cross-section is partially plastified. Therefore, the plastic hinge length decreases as  $\psi$  increases. Furthermore, compared to a large plastic hinge length, a smaller plastified region imposes greater inelastic strain demands in order to achieve a specified plastic rotation. This leads to greater susceptibility to low cycle fatigue. The  $\psi$  ratio can therefore significantly affect the cumulative beam plastic rotation capacity.

If the yield strength of A36 steel is assumed to be  $f_y = 36$  ksi, and the ultimate strength,  $f_u = 58$  ksi, then the yield-to-ultimate stress ratio is  $\psi = 36/58 = 0.62$ . As described by Frank (1997), recent trends in the production of A36 and A572 Gr. 50 steels have resulted in steels with much higher  $\psi$  ratios. For example, Frank (1997) cites statistical data which shows that 8% of steel could have a yield-to-ultimate stress ratio greater than 0.85. The highest ratio measured was 0.986. The strain demands in the plastic hinge region of such beams may be large, and the beam plastic rotation that can be achieved may be greatly reduced.

To study the effect of the yield-to-ultimate stress ratio on the inelastic behavior of welded-bolted connection subassemblies, three configurations are analyzed (**Table 5.1**). All three subassemblies have the geometry of Berkeley Specimen PN3. To force most of the inelastic behavior into the beam, the beam yield stress was chosen to be 50 ksi, and the column yield stress 60 ksi for all three specimens. This resulted in  $P_z/P_b = 1.3$ , and  $P_c/P_b = 2.6$ . As discussed

earlier in Section 1.2,  $P_z$ ,  $P_c$ , and  $P_b$  are the beam tip loads required to cause the subassemblage to reach its panel zone, beam, or column strength respectively, calculated according to the 1991 UBC. The only difference between the three configurations is the beam ultimate stress. This is chosen so that  $\psi = 0.65$ , 0.8, and 0.95 for specimens YUSR-65, YUSR-80, and YUSR-95 respectively (see **Table 5.1**). The constitutive relations are assumed as shown in **Figure 5.2**.

The load vs. tip deflection curves for all three specimens are plotted in **Figure 5.3**. It is clear from the figure that YUSR-65 and YUSR-80 have similar responses. Specimen YUSR-95, on the other hand, exhibited softening behavior much earlier than the other two subassemblages. The reason for this is the initiation of local buckling in the beam compression flange early on in the load history. The local buckling occurred close to the beam-column interface, where the inelastic strains were highest.

The smaller plastified zone associated with a greater yield-to-ultimate stress ratio can be clearly seen in the contour plots of the PEEQ strain in **Figure 5.4**. Note the smaller plastified length in YUSR-95 (**Figure 5.4c**) compared to YUSR-65 (**Figure 5.4a**). The greater strains associated with a high  $\psi$  ratio can also be seen in **Figure 5.5**. The figure shows the PEEQ indices at a connection plastic rotation of 0.03 plotted along transverse and longitudinal lines. The shorter plastic length associated with YUSR-95 can be clearly seen in **Figure 5.5b**. The plastic length of specimen YUSR-95 is about one half that corresponding to YUSR-65. In addition, the maximum PEEQ index for YUSR-95 is 73% greater than that associated with YUSR-65. On the other hand, the differences between YUSR-65 and YUSR-80 are relatively small, with a difference in the maximum PEEQ index of 12%. As shown in **Figure 5.5b**, even the plastified lengths for both specimens are almost equal.

## 5.2 ACCESS HOLE GEOMETRY

Many of the fractures observed in the Northridge earthquake and in laboratory tests appear to have initiated at weld defects due to incomplete fusion at the root of the groove weld, usually at mid width of the weld-column interface. These defects are caused by entrapped slag along the weld root (Kaufmann and Fisher 1995). The reduced access for welding at the beam-column interface due to the small size of the web cope increases the likelihood of the occurrence of this type of defect. The limited access also makes NDE more difficult in this area.

Increasing the size of the web cope would permit easier welding on the beam bottom flange, and possibly promote better welds. However, it is not known how such a solution will impact inelastic behavior. Tests by Lee and Lu (1989) of composite joint subassemblages indicate that larger cope holes may result in premature fracture at the root of the access hole. Engelhardt and Husain (1992), on the other hand, did not observe any such detrimental effects in their tests on connections with varying access hole sizes. It must be noted however, that most of Engelhardt and Husain's tests failed at relatively low connection plastic rotations, and the effect of increased cope size may have been masked by predominantly brittle behavior at the weld-column interface.

To investigate the effect of cope hole size and geometry on inelastic behavior, three models with the geometry of specimen PN3 are created and analyzed. The three subassemblages (A1 through A3) are identical in all respects except for the access hole geometry or size. Nominal material properties are used ( $f_{yc} = 50$  ksi, and  $f_{yb} = 36$  ksi). Details of the cope hole geometry are shown in **Figure 5.6**. Configuration A1 is that used in specimen PN3 (diameter 0.75-in). The diameter of the cope hole of A2 is double that of A1 (1.5-in). Configuration A3 is used in older construction and is no longer allowed by ASIC-LRFD (1994) for hot-rolled beams. It is included only for the purpose of comparison.

The PEEQ indices at a connection plastic rotation of 0.03 are shown in **Figure 5.7** plotted along transverse and longitudinal lines passing through the root of the access hole. The *root* of the access hole is defined as the region where the access hole transitions into the beam flange, i.e. intersection of access hole surface and beam flange top surface. It is clear from the figure that the effective plastic strains are greatest at the root of the access hole and that configuration A2 has the largest effective plastic strains. For example, the maximum PEEQ index for A2 is 60% greater than that corresponding to A1. The longitudinal *stresses* along the transverse line through the root of the access hole are plotted in **Figure 5.8**. Both A2 and A3 have almost similar maximum longitudinal stresses (165% of yield) at the root of the access hole. These elevated stresses are attributed to relatively high hydrostatic stresses and strain hardening.

Shown in **Table 5.2** is a summary of the stresses and strains at the root of the access hole. Also shown in the table is the triaxiality ratio and the rupture index (Equation 3.8). Using Equation 3.7, the rupture strain of A3 is about 30% smaller than that corresponding to A1. Although both configurations sustained the same strain at a connection plastic rotation of 0.03, the geometry of A1 is clearly better than A3 from the ductile fracture point of view. This is clearly reflected in the rupture index, which is 66 for A1, and 88 for A3. Configuration A2 has a rupture strain that is about 16% less than that of A1. Moreover, the strain at the root of the access hole of A2 is 60% greater than that corresponding to A1. The rupture index for A2 is 118, 78% greater than that corresponding to A1. Hence A2, with the larger access hole, is also more susceptible to ductile fracture than A1. It is therefore important to use a small access hole to minimize the potential for ductile crack initiation at the root of the access hole.

### 5.2.1 DESIGN IMPLICATIONS OF ACCESS HOLE ANALYSES

Increasing the size of the web cope would permit easier welding on the beam bottom flange, and possibly promote better weld quality. However, the analyses in this section suggest that it is important to use a small access hole in order to minimize the potential for ductile fracture at the root of the hole. The analyses further show that the access hole in which the web terminates perpendicular to the flange is clearly inferior to the semi-circular detail from the ductile fracture point of view.

### 5.3 PRESENCE/ABSENCE OF CONTINUITY PLATES

According to the AISC-LRFD specifications (1994), continuity plates should be provided when either the column flange is inadequate in local bending or the column web is inadequate in web crippling, local yielding, or compression buckling. Previous analysis results show that use of continuity plates may decrease the hydrostatic stress at the beam to column interface (Allen et al. 1997) and as a result may affect the cracking potential in the region (Roeder 1997). Tremblay et al. (1995) reported that connections with continuity plates were found to have fewer connection failures. Moreover, tests of cover plated connections have been most successful when continuity plates were present (Englehardt and Sabol, 1994). Based on these and other research results, currently recommended design procedures require continuity plates for all cases (FEMA 267, 1995).

To study the effect of the presence of continuity plates on inelastic behavior, the PN3 experimental subassembly with nominal material stress-strain properties ( $f_{yb}=36$  ksi and  $f_{yc}=50$  ksi) is used. The subassembly is analyzed 4 times with different continuity plate thicknesses. **Table 5.3** gives details of the specimen designations and continuity plate properties. The thicknesses considered are 0.5-in, 0.75-in, and 0.94-in. The last thickness of 0.94-in is equal to the beam flange thickness and is recommended by FEMA-267 (1995) provisions. The subassembly is also analyzed without continuity plates (Specimen CONT-N) in accordance with AISC-LRFD (1994) provisions. These provisions do not require continuity plates for this connection subassembly.

Analysis results show that there the stress and strain distributions are almost insensitive to the continuity plate thickness used. However, removal of the continuity plate resulted in large changes in behavior, especially at the weld-column interface. The deformed shapes of the solid regions for CONT-0.75 and CONT-N are shown in **Figure 5.9**. The region shown in **Figure 5.9** is the intersection between the bottom beam flange and the column, and displacements are magnified twenty times. The greater prying action and increased column flange local bending in the case without continuity plates are evident in the figure.

Results from specimens CONT-0.75 and CONT-N also show that the pressure index distribution along the interface is greatly affected by the presence of the continuity plates. As shown in **Figure 5.10**, the case without continuity plates has an abrupt drop in the pressure index in the middle of the beam flange. The case with continuity plates, on the other hand, has a more uniform pressure distribution along the interface line. The reason for this abrupt drop in hydrostatic stresses appears to be a pronounced dip in both the S22 and S33 stresses in the case without continuity plates (see **Figure 4.3d** for definition of S22 and S33). This can be clearly seen in **Figure 5.11** in which the distributions of S11, S22, and S33 stresses are plotted along the interface line for the two cases.

In general, removal of the continuity plates adversely affected the stress conditions at the interface. Some of these effects at a CPR of 0.03 are:

1. An increase in the maximum value of S22 from 33 ksi to 52 ksi (an increase of 58%).

2. An increase in the maximum pressure index from 0.76 to 0.9 (an increase of 18%).
3. An increase in the maximum principal stresses from 40.19 to 57.8 ksi (an increase of 44%).
4. An increase in the PEEQ index at the center of the B-HAZ line from 3.9 to 6 (an increase of 53%).

Behavior in some of the other regions of study show very little difference between all cases, besides slightly more uniform pressure and Mises distributions in the cases with continuity plates. There are some levels of strain produced in the C-HAZ location in the case without continuity plates which are not present in the cases including continuity plates. The maximum PEEQ indices for both the C-HAZ and the interface, however, are still much lower than the PEEQ indices along the B-HAZ and access hole lines.

### 5.3.1 DESIGN IMPLICATIONS OF CONTINUITY PLATE ANALYSES

These analyses support the FEMA-267 (1995) recommendations, which require the use of continuity plates in all connections. The analyses show that the use of continuity plates results in milder stress and strain distributions, particularly at the weld-column interface. However, the analyses also suggest that the provisions may be relaxed with regards to the required continuity plate thickness. Analyses with continuity plates of thickness less than 60% of the recommended thickness resulted in almost no change in the stress and strain conditions in the connection. Beside their increased cost, the use of overly thick continuity plates may be detrimental to connection behavior. Thicker plates require larger welds, which create additional restraint and residual stresses in the connection region. It should be noted that these results apply to one-sided connections in which the column flanges are relatively thick compared to the beam flanges. Further research is needed to verify if these conclusions apply to two-sided connections, or connections in which the column flanges are significantly thinner.

## 5.4 COLUMN WEB THICKNESS

A series comprised of 5 configurations was developed in order to study the effect column web thickness on connection response and potential for fracture. The configurations that are considered (CWT1 through CWT5) are shown in **Table 5.4**. Further details about the geometry of these configurations may be found in Appendix A. Configurations CWT3 and CWT3-N have the geometry of specimen PN3 tested at UC Berkeley. The other configurations were created by changing the column web thickness in order to change the ratio of panel zone strength to beam strength. Specimen CWT3-N is the only configuration with nominal beam and column properties:  $f_{yb}=36$  ksi,  $f_{yc}=50$  ksi. The beams of the other specimens have a yield strength of 70 ksi, which represents an upper limit for the yield strength of commercially available A36 steel. The columns have a yield strength of 45 ksi which is a lower limit for commercially available

A572 Gr. 50 steel (Frank 1997). These material properties represent a plausible situation that would result in severe demands on the panel zone region of the configurations being studied.

The tip loads required to cause the configurations to reach their panel zone strength ( $P_z$ ), beam strength ( $P_b$ ), and column strength ( $P_c$ ) are shown in **Table 5.4**. Specimens CWT1, CWT2, CWT3, and CWT4 are designed to have a weak panel zone. For example, the panel zone of CWT1 has a strength that is only 42% of the beam strength, while the ratio for CWT4 is 89%. Specimens CWT3-N and CWT5 have panel zone strengths that are greater than the beam strengths:  $P_z/P_b = 1.49$  and  $1.17$  respectively. All specimens are designed so that the columns are stronger than the panel zones and beams. Thus significant inelastic deformation is expected in the panel zone for cases CWT1 through CWT4, and in the beam for cases CWT3-N and CWT5. The connections were analyzed accounting for both material and geometric nonlinearity as described in Chapter 3.

The deformed shapes of CWT1 and CWT4 are plotted at connection plastic rotations (CPR's) of 0.03 in **Figure 5.12**. The kinks in the column flanges that accompany panel zone deformation are obvious in the deformed shape of connection CWT1 in **Figure 5.12a**. This is in contrast to the deformations of configuration CWT4 which has a stronger panel zone (**Figure 5.12b**). It is also clear that the weaker panel zone in CWT1 resulted in smaller deformations in the beam as shown in **Figure 5.12a**. The larger beam distortions in CWT4 at a CPR of 0.03 can be seen in **Figure 5.12b**.

A comparison between deformation characteristics of specimens CWT3 and CWT3-N is shown in **Figure 5.13**. The load vs. tip deflection curves are shown in **Figure 5.13a**. The contribution of the panel zone to the plastic rotation (CWTPR) vs. the total connection plastic rotation (CPR) is shown in **Figure 5.13b**. It is clear that the panel zone deformations dominate the response of CWT3.

A comparison between the distribution of pressure indices along the interface line for connections CWT1 and CWT4 is shown in **Figure 5.14**. The dotted lines correspond to a CPR of 0.0025 while the thick solid lines correspond to a CPR of 0.03. The thin solid lines correspond to the different load increments. Most notable is the difference in the shape of the distributions. The hydrostatic stresses are greatest at the center of the interface line in CWT1. On the other hand, the distribution of hydrostatic stresses for CWT4 dips in the middle because of reasons described in Section 4.2.

The pressure indices at the middle of the interface line are plotted vs. the  $P_z/P_b$  ratio in **Figure 5.15a**. At low connection plastic rotations (CPR=0.0025), the magnitude of the pressure index decreases as the panel zone strength decreases (**Figure 5.15**). At this level of deformation, kinking in the column flange is not yet pronounced, and the stresses are generally lower. However, as inelasticity spreads, the hydrostatic stresses increase more rapidly in the connections with weaker panel zones and end up higher than in connections with stronger panel zones because of the kinks in the column flanges. For instance, the magnitude of the pressure index at the middle of the interface line for CWT1 increases from 0.42 to 0.80 (91% increase) as the CPR increases from 0.0025 to 0.03 while a corresponding change of 0.53 to 0.57 (7.6%

increase) was observed in specimen CWT5. Interestingly, the magnitude of the pressure index for CWT1 is smaller than that for CWT2. This is due to smaller longitudinal stresses in the beam in CWT1 compared to CWT2 since the weaker panel zone absorbs most of the connection deformation shielding the beam from rapidly increasing stresses at higher deformation levels.

The maximum principal stresses normalized by the beam yield stress at the middle of the interface line are plotted vs. the  $P_z/P_b$  ratio in **Figure 5.15b**. It is clear from the figure that the principal stresses are highest in connection CWT1 compared to the other specimens at a CPR of 0.03. At this level of connection deformation, the ratio of the maximum principal tensile stress to the beam yield stress is 1.19 for CWT5 and 1.36 for CWT1. This corresponds to an increase in the principal stress ratio of 14.3%. At a CPR of 0.03, the beam plastic rotation of CWT1 is 0.001 while that corresponding to CWT4 is 0.01. It is therefore clear that although the plastic rotation demand on the beam is much smaller in CWT1, the stress conditions are more critical and hence more conducive to cracking in the event of a flaw. In spite of the kinks in the connections with weaker panel zones, the PEEQ indices are lower at the middle of the interface line in connections with weaker panel zones compared to connections with stronger panel zones (**Figure 5.16a**). On the other hand, inelastic deformation at the middle of the column HAZ line is much more pronounced in the connections with a weaker panel zone, especially at higher CPR's (**Figure 5.16b**).

The stress and strain conditions at the corner between the beam and column flanges are also examined (see **Table 5.5**). These stresses and strains are extracted at the integration point of a column element at the center of the column flange, immediately underneath the beam. Because of the presence of the corner, there are large stress and strain concentrations in this region. It is clear that the panel zone strength strongly influences the stresses and strains in this area. For example, the hydrostatic stresses are 66% higher in CWT1 (weakest panel zone) compared to CWT5 (strongest panel zone). This is accompanied by an increase in stress triaxiality from 0.85 in CWT5 to 1.33 (a 56% increase) in CWT1. Moreover, the rupture index for CWT5 is only 19 compared to 145 (a 7-fold increase) for CWT1 at a connection plastic rotation of 0.03. Therefore connection CWT1 is much more susceptible to ductile fracture in this region compared to CWT5. Connection CWT1 is also more likely to undergo brittle fracture if a defect or flaw exists at the beam-column interface region. The principal stress in this case is 34.4% higher than that corresponding to CWT5, reaching 91.7 ksi. This is almost twice the yield stress of the column steel. The reason for the occurrence of such high principal stresses is the presence of large hydrostatic stresses in the corner area.

#### 5.4.1 SUMMARY OF SERIES CWT RESULTS

The primary effect of varying the column web thickness is to vary the ratio of panel zone strength to beam strength. At low connection plastic rotations (CPR=0.0025), the connections with smaller column webs, and therefore weaker panel zones, show milder overall stress conditions than the connections with stronger panel zones. However, as the connection plastic rotation increases, the hydrostatic and principal stresses at the middle of the weld-column interface increase much more rapidly, becoming significantly higher in connections with weaker

panel zones. At a CPR of 0.03, the principal stress at the middle of the weld-column interface of the connection with weakest panel zone (CWT1) is 14.3% more than the corresponding stresses in the connection with strongest panel zone (CWT5). Stress triaxiality and inelastic strains are also significantly greater in CWT1 compared to CWT5 at a CPR of 0.03. However, at this level of connection deformation, the beam plastic rotation of CWT1 is 0.001 while that corresponding to CWT5 is 0.013. It is therefore clear that although the plastic rotation demand on the beam is much smaller in CWT1, the stress and strain conditions are more conducive to crack initiation.

## 5.5 BEAM DEPTH

Statistical analyses by Roeder and Foutch (1996) suggest that beam depth may have a strong influence on the beam flexural ductility that may be achieved prior to connection failure. To study the influence of beam depth on connection ductility, two series of beam-to-column connections (series BD and BDN) are created and analyzed.

Series BDN has nominal material properties ( $f_{yb}=36$  ksi and  $f_{yc}=50$  ksi) and is comprised of 4 connections. Configuration BDN3 has the geometry of specimen PN3. The other configurations in this series are created by changing the beam depth as shown in **Table 5.6**. Further details about the geometry of these configurations may be found in Appendix A. In order to minimize the effect of panel zone deformation, the ratio  $P_z/P_b$  is kept approximately constant by adjusting the column web thickness. Shown in **Table 5.6** are the tip loads required to cause the configurations to reach their panel zone strength ( $P_z$ ), beam strength ( $P_b$ ), and column strength ( $P_c$ ) as described in Section 1.2. It is clear from the table that most of the inelastic deformation is expected to occur in the beam. The second series, called BD, is also comprised of 4 connections (**Table 5.7**). However, the material properties are chosen to reflect a more critical situation in which the beam has a yield strength that is higher than the nominal design stress, and the column has a yield stress that is lower than the design stress ( $f_{yb}=70$  ksi,  $f_{yc}=45$  ksi). As discussed in the panel zone analyses above, these material properties represent a plausible situation that would result in severe demands on the panel zone region of the configurations being studied. It is clear from **Table 5.7** that, unlike series BDN, significant inelastic deformation is expected to occur in the panel zone in series BD.

### 5.5.1 SERIES BDN

The effect of beam depth on hydrostatic stresses at the middle of the interface line for configurations in Series BDN is shown in **Figure 5.17a**. The pressure index magnitude is 0.66 for the 18 inch beam and 0.52 for the 40 inch beam at a CPR of 0.025. In other words, the hydrostatic stress drops by 21.2% as the beam depth increases from 18 to 40 inches. The longitudinal stress at the middle of the interface line also drops from 38.5 ksi for the 18 inch beam to 34.9 ksi for the 40 inch beam at a CPR of 0.025 (**Figure 5.18a**). This corresponds to a drop of approximately 9%. The reason for the increase in stresses with decreasing beam depth seems to be due to increased deformation in the panel zone of connections with shallower beams. This can be clearly seen in **Figure 5.19**, where the panel zone plastic distortions for specimens

BDN1 and BDN4 are plotted versus beam plastic rotations. For example, connection BDN1 has a panel zone plastic rotation of  $0.0067 \text{ rad}$  which is almost three times the corresponding value for BDN4 at a beam plastic rotation of  $0.03 \text{ rad}$ . The increased panel zone deformation and column flange kinking in Specimen BD1 compared to BD4 can be clearly seen in **Figure 5.20**. Based on these figures alone, it is not clear that deeper beams are more susceptible to brittle cracking compared to shallower beams.

The variation of PEEQ indices with beam depth at the middle of the access hole line (underneath the root of the access hole) are shown in **Figure 5.21a**. At a low level of connection plastic rotation (CPR = 0.0025), the PEEQ index in BDN4 is 2.3 times the PEEQ index in BDN1. The difference between the PEEQ index of deeper sections compared to shallower sections decreases at higher connection plastic rotations. For example, at a CPR of 0.03, the PEEQ index in BDN1 is 18.1 versus 21.6 for BDN4 at the middle of the access hole line. This corresponds to a 19% increase compared to a 130% increase at a CPR of 0.0025 as discussed above. Assuming that the ratio of plastic strength to yield strength is 1.15 on average for rolled sections, and knowing that the moment distribution is linear, then the length of the inelastic zone of the beam is approximately 13% of the beam length. Also assuming a similar curvature distribution along the plastified zone, it follows that deeper beams have greater flange strains in general than shallower beams at the same level of beam plastic deformation. This increased strain is accompanied by earlier local buckling as shown in **Figure 5.20b**. Thus, the deeper beam, BDN4, is more susceptible to low-cycle fatigue and may have a reduced cumulative ductility compared to BDN1.

### 5.5.2 SERIES BD

Shown in **Figure 5.22** are plots of the deformed shapes of the solid element region for specimens BD1 and BD4 at a CPR of 0.03. The beam is more highly distorted in BD4 (depth = 40 inch) than in BD1 (depth = 18 in) which implies significantly greater plastic rotation in the beam of BD4 compared to BD1. **Figure 5.23a** shows the relationship between beam plastic rotation and connection plastic rotation for configurations BD1 and BD4. It is clear that there is little inelastic beam participation in BD1 compared to BD4. For instance, at a CPR of 0.03, the beam plastic rotation is  $0.0015 \text{ rad}$  for BD1 versus  $0.0045 \text{ rad}$  for BD4. Most of the inelastic deformation is concentrated in the panel zone in both cases as can be seen in **Figure 5.23b**.

Although the trends in series BD (weak panel zone) were similar in many respects to those observed in series BDN (strong panel zone), there were some significant differences. The pressure index magnitude at the middle of the interface line is 0.72 for the 18 inch beam and 0.64 for the 40 inch beam at a CPR of 0.025. It is clear that the hydrostatic stress indices are higher in this series than in the BDN series in which the panel zone does not undergo as much inelastic action. Analyses of configurations in series CWT showed a similar trend. The analyses also show that the maximum principal stress at the middle of the interface line decreases as the beam depth increases. For example, the maximum principal stress decreases from 94.5 ksi to 84.7 ksi (11.5% decrease) as the beam depth increases from 18 to 40 inches at a CPR of 0.025 (**Figure 5.24**). However, an opposite trend is observed in the longitudinal stresses in the beam because the

weaker panel zone absorbs most of the inelastic action shielding the beam from rapidly increasing longitudinal stresses. The longitudinal stress increases from 56 ksi to 67.9 ksi (21.2% increase) as the beam depth increases from 18 to 40 inches at a CPR of 0.025 (**Figure 5.18b**).

The variation of PEEQ indices with beam depth at the middle of the access hole line is shown in **Figure 5.21b**. At a low level of connection plastic rotation (CPR = 0.0025), the PEEQ index for all specimens is almost zero signifying that little inelastic deformation is taking place in the beam. At this low level of connection deformation, the panel zone is contributing most to the connection plastic rotation. At higher levels of connection plastic rotation (CPR = 0.03), the panel zone strain hardens in configurations BD3 and BD4 resulting in greater inelastic deformation in the beams. On the other hand inelastic deformation remains limited in the beams of specimens BD1 and BD2. The deeper beams therefore sustain significantly more inelastic strains, especially at higher connection plastic rotations than the shallower beams. For example, at a CPR of 0.03, the PEEQ index in BD1 is 0.3 versus 6.1 for BDN4 at the middle of the access hole line. Thus, the deeper beam, BD4, is gain more susceptible to low-cycle fatigue and may have a reduced ductility compared to BD1.

### 5.5.3 SUMMARY AND IMPLICATIONS OF BEAM DEPTH ANALYSES

The results of series BDN in which the panel zone strength is 49% greater than the beam strength indicate that the shallower beams have slightly higher stresses at the beam-column interface compared to deeper beams. For example, the hydrostatic stresses at the middle of the interface line dropped by 21% as the beam depth increased from 18 to 40 inches. The longitudinal stresses at the same location also dropped by 9% as the beam depth increased. However, the PEEQ indices in the beam flange of deeper sections were significantly higher compared to shallower sections. At a CPR of 0.0025, the PEEQ index in BDN4 is 2.3 times the PEEQ index in BDN1 at the middle of the access hole line. Thus, deeper beams appear to be more susceptible to low-cycle fatigue and may have a reduced cumulative ductility compared to shallower beams. The increased strain in deeper beams is also accompanied by earlier local buckling.

The results of series BD in which the panel zone strength is about 32% lower than the beam strength indicate that stress conditions at the weld column-interface are generally higher than those observed in corresponding connections in Series BDN at the same level of connection plastic rotation. Connections with smaller beam depth were found to have higher principal stresses at the center of the interface line than connections with deeper beams. However, the plastic strains in the beam flanges are much higher in the deeper beams compared to shallower beams at high connection plastic rotations. The same conclusions drawn for series BDN are therefore applicable.

## 5.6 BEAM FLANGE THICKNESS

To study the effect of beam flange thickness on inelastic behavior, five different configurations are created and analyzed. The geometry of specimen PN3 is adopted as the base configuration and other analysis models are created by varying the beam flange thickness. The flange thickness in this study varies from 0.79 in. to 3.0 in, representing the practical range of thicknesses found in W36 sections. Nominal material properties are employed for all specimens: beam yield stress is 36 ksi and column yield stress is 50 ksi. The configurations that are analyzed are shown in **Table 5.8** and are described in more detail in **Table A.1**. By increasing the beam flange thickness, greater demands are placed on the panel zone. Therefore, in order to avoid introducing panel zone deformation as another variable in this series, the column web thickness is varied in order to maintain a somewhat constant  $P_z/P_b$  ratio. An examination of **Table 5.8** shows that the beam is weaker than both the column and panel zone and hence most of the inelastic deformation is expected to take place in the beam.

The maximum pressure index at the interface is plotted as a function of the beam flange thickness in **Figure 5.25a**. The indices are plotted out at CPR's of 0.0025 and 0.03. An increase in thickness from 0.79 to 3.0 inches results in a corresponding increase in the maximum pressure index magnitude at the interface from 0.67 to 0.90 for the low CPR and 0.6 to 0.89 for a CPR of 0.03. The increase in pressure index is accompanied by a corresponding increase in longitudinal stress, S11, as shown in **Figure 5.25b**. For example, the maximum value of S11 increased from 33.6 ksi for the thinnest flange to 42.1 ksi for the thickest flange (an increase of 26%). Clearly, increasing the beam flange thickness adversely affects the stress conditions at the beam-to-column interface.

Another effect of increasing the flange thickness is an increase in the stresses in general, and the hydrostatic stresses in particular at the column HAZ line. Since the column flange thickness is held constant in these analyses, the greater flange thickness affects a larger portion of the column flange. This increases the probability of exacerbating the conditions at preexisting flaws in the column HAZ. Further, thicker flanges require larger full penetration welds, which lead to a larger heat-affected zone. It is noteworthy to mention that with increasing flange thickness, greater inelastic strains were observed at both the interface and column HAZ lines (**Figure 5.26**). The maximum PEEQ index however, was less than 1.6 at a CPR of 0.025 and was still much lower than the PEEQ indices along the beam HAZ and access hole lines, which were in the range of 20-25.

### 5.6.1 SUMMARY OF BEAM FLANGE THICKNESS ANALYSES

Increasing the beam flange thickness resulted in greater triaxial restraint and larger longitudinal stresses at the beam-to-column interface. For example, the maximum longitudinal stresses increased by 26% as the beam flange thickness increased from 0.79-in to 3.0-in. The analyses also show that a greater beam flange thickness affects a larger portion of the column flange. This increases the probability of exacerbating the conditions at preexisting flaws in the column HAZ.

## 5.7 COLUMN FLANGE THICKNESS

To study the effect of column flange thickness on the inelastic behavior of welded-bolted connections, two series of configurations are created. The configurations of the first series (Series CFN) are designed to have strong panel zones, while subassemblages of the second series (Series CF) had weak panel zones. Specimens of series CFN had nominal material properties, in which the yield strength of the column is 50 ksi, and the yield strength of the beam is 36 ksi. The corresponding yield strengths for series CF are 45 and 70 ksi respectively. The dimensions and properties of the different subassemblages are shown in Appendix A and **Table 5.9** and **Table 5.10**. Configurations CFN3 and CF3 have the geometry of specimen PN3 tested at UC Berkeley. The other configurations were created by changing the column flange thickness over the practical range of dimensions for W 14 sections. In order to maintain a similar ratio of panel zone to beam strength, the column web thickness was modified as shown in **Table 5.9** and **Table 5.10**.

The relationships between the applied tip load and the panel zone plastic distortion for series CFN (strong panel zone) are plotted out in **Figure 5.27a**. It is clear from the figure that Specimen CFN4 underwent some panel zone plastic distortion (0.0066 *rad*) in spite of the fact that the panel zone is much stronger than the beam ( $P_z/P_b = 1.51$ ). Specimen CFN1, on the other hand, underwent much less inelastic panel zone deformation. **Figure 5.27** also suggests that although all the specimens have the same  $P_z/P_b$  ratio, the specimens with thicker column flanges underwent earlier panel zone plastic deformation compared to specimens with thinner flanges. Another conclusion that can be drawn is that all 4 subassemblages have approximately the same strength. There is a 3.5% difference between the strengths of subassemblage CFN1 and CFN4. The reason for this is that the strength of the subassemblage is governed by the beam strength.

Similar plots for series CF (weak panel zone) are shown in **Figure 5.27b**. The differences among the configurations in both strength and deformational characteristics are greater in this series. Although CF1 and CF4 have the same  $P_z/P_b$  ratio ( $P_z/P_b = 0.69$ ), the strength of CF1 calculated from the finite element model is 12.7% greater than that of CF4. Specimen CF4 also underwent much earlier panel zone plastic deformation compared to CF1.

The larger panel zone deformation in CFN4 resulted in greater hydrostatic stresses at middle of the interface line compared to the other specimens. For example, the pressure index magnitude rose from 0.55 for CFN1 to 0.77 for CFN4, a 40% increase. Also, the maximum principal stress at the middle of the interface line increased by approximately the same ratio. The earlier panel zone deformations in CF4 resulted in a smaller initial maximum principal stress at the interface between the beam and column compared to CF1. For example, the maximum principal stress at the middle of the interface line increased from 52 to 76 ksi for CF4 (28.6% increase) as the connection plastic rotation increased from 0.0025 to 0.03 *rad*. In specimen CF1, the corresponding stresses were 71.4 and 74.7 ksi, an increase of only 4.6 %. The maximum principal stresses in specimen CF4 were slightly higher at a CPR of 0.03 *rad* compared to CF1, reflecting the effect of greater panel zone deformation. Similar trends were observed for the hydrostatic stresses at the interface, as depicted in **Figure 5.28**.

## 5.8 SHEAR TRANSFER IN FR WELDED-BOLTED CONNECTIONS

Current design procedures require welded-bolted steel connections to be designed assuming that 1) beam flanges transmit moments, 2) beam web transmits shear forces, and 3) the assumed mechanisms for shear and moment transfer are uncoupled. Recent finite element analyses by Goel et al. (1997) have shown that forces in the vicinity of the beam to column interface are transferred in diagonal bands, which results in much of the shear forces being transferred through the beam flanges. This observation led Goel et al. (1997) to theorize that high shear forces in the flanges could have contributed to the observed failures in the Northridge earthquake. Goel's analyses, however, were based on linear elastic behavior, and did not consider the effect of spread of plasticity. In this section, elastic and inelastic shear distributions in the shear tab and flanges are investigated. The effect of shear tab thickness and height are also evaluated through parametric finite element analyses.

In evaluating the following results, the limitations of the analyses and assumptions involved must be kept in mind. The portion of the shear tab in contact with the beam web is considered to be completely monolithic with the beam web. Thus bolt deformations, including possible slip are not considered. Local bearing deformations in the shear tab due to the bolts bearing against the plates are not included. In addition, the supplemental welding between the shear tab and the beam web is not modeled. In spite of these approximations, these analyses can be used in identifying important trends in behavior, and in pointing out areas of research that need to be pursued further using more refined models.

### 5.8.1 SHEAR TRANSFER IN SPECIMEN PN3

The shell element model (S4-6) described in Section 3.5 is selected for this analysis. The model represents specimen PN3 and accounts for inelastic material behavior, but not geometric nonlinearities. The measured stress-strain properties for specimen PN3 are utilized.

The shear forces at 43% of the nominal design load are extracted from the finite element model and plotted in **Figure 5.29**. The behavior at this load level is essentially elastic. Based on the shown distributions, the total shear force transferred through the shear tab is 57% of the applied tip load. The remainder of the applied force is transferred through the top and bottom flanges. An examination of **Figure 5.29** reveals that the central portion of the shear tab is actually under small negative shear forces, while shear stresses are concentrated at the top and bottom of the tab. The shear distribution does not resemble the parabolic distribution predicted by classical beam theory on which the design assumptions are based. Diagonal action as described by Goel et al. (1997) was observed for these conditions. Also shown on **Figure 5.29a** is the shear distribution at a section  $\frac{1}{4}$  of the beam span away from the column face. The shear distribution in this case follows the elastic distribution predicted using classical beam theory.

The observed shear stress distribution along the shear tab is clearly due to the influence of the boundary conditions. The beam cross-section adjacent to the column tends to warp due to the high shear forces. However, the column provides resistance that reduces cross-section warping at

the beam to column interface. The resistance to warping imposed by the column appears to have resulted in the observed distribution of stresses (Goel et. al. 1997).

As inelasticity spreads, the percentage shear transferred through the shear tab gradually increases, and the distribution of shear stresses changes significantly. The change in the shear distribution in the shear tab as a function of the applied load is shown in **Figure 5.30**. Diagonal action is no longer clearly defined at large plastic rotations.

## 5.8.2 EFFECT OF SHEAR TAB GEOMETRY

This section investigates the effect of shear tab thickness and length on shear transfer and inelastic behavior of FR welded-bolted connections. Six connection configurations comprising three different beam sections are analyzed in this series (Series ST). The properties of these configurations are summarized in **Table 5.11**. Two shear tab heights are considered for each beam section. The first corresponds to the maximum length permitted by the geometry of the connections, and the second corresponds to the minimum specified by the AISC-LRFD specifications to accommodate the required bolts. The number appended to the letters ST in the connection designations represent the nominal beam depth, whereas the last letter, S or L, indicates whether the shear tab is short or long. Connection ST36-L has the geometry of Berkeley specimen PN3. All other connection configurations have the same beam and column lengths as ST36-L. The measured stress-strain properties for specimen PN3 are utilized.

### 5.8.2.1 Effect of Shear Tab Thickness

The base connection configuration used in this study is ST36-L which corresponds to Berkeley specimen PN3. The shear tab of this connection is 30 inches long and 0.625 inches thick. Four different shear tab thicknesses are considered: 0.75, 1.0, 1.5, and 2.0 times the thickness of the shear tab of ST36-L. The percentage shear transferred through the different shear tabs is calculated for elastic conditions and at two other levels of inelastic behavior. The load at the first level of inelastic behavior causes the connection to reach its nominal design strength. The nominal design strength is computed assuming nominal material properties ( $f_{yb}=36$  ksi,  $f_{yc}=50$  ksi) and accounts for the strength reduction factor ( $\phi$ ). At this load level, the beam tip displacement is approximately 1.0 inch, and beam has undergone some inelastic behavior. The second level of inelastic behavior corresponds to an applied load that is 150% of the nominal design load. This is not unrealistically high, since the assumed yield strength of the beam (measured properties of specimen PN3) is significantly higher than the nominal yield strength. This level of loading corresponds to a beam plastic rotation of approximately 0.03.

Shown in **Table 5.12** is the percentage shear transferred through the shear tabs of different thicknesses at the different load levels considered. An examination of **Table 5.12** reveals that the shear transferred through the shear tab is almost insensitive to the shear tab thickness. For example, the percentage shear transferred through the shear tab for elastic conditions changes from 56.4% to 57.6% as the shear tab thickness changes from 0.75 to twice the thickness of the

tab of the base configuration. A similar trend in behavior can be seen at the other load levels. The distributions of shear force transferred through the shear tab for elastic behavior are shown in **Figure 5.31**. It is clear that the shear tab thickness has almost no effect on the distribution of shear forces. Similar trends were observed for the other two levels of inelastic behavior.

### 5.8.2.2 Effect of Tab Height

A comparison between elastic distributions of shear force along the shear tab for ST36-L and ST36-S is shown in **Figure 5.32a**. The shear distribution is similar in both cases with maximum shear stresses occurring at the extreme ends of the tabs. The shear stresses at mid-height are higher in the shorter tab compared to the longer tab. As seen in **Table 5.13**, the percentage shear going through the shorter tab (49.1%) is slightly smaller than that going through the deeper tab (56.8%) for elastic behavior. At the nominal design load level (**Figure 5.32c**), the shear stresses are still maximum at the ends of both shear tabs, and the stresses at mid-height of the smaller tab are higher than those at mid-height of the larger tab. However, the stresses at mid-height in both tabs are higher than the corresponding stresses for elastic behavior. At a BPR of 0.03 (**Figure 5.32d**), the difference in the distribution of shear is large. While the longer tab is still under small shear stresses at mid-height, the shear stresses are highest at mid-height of the smaller shear tab, and the tab has actually yielded in shear at this point. The trends for the ST30 and ST24 configurations are similar to what was observed in the ST36 connections. The percentage shear going through the shear tab for all cases is shown in **Table 5.13**.

It is interesting to note that the span to depth ratio has no clear effect on the shear transferred for the three cases considered. For example, ST24-L has a larger span to depth ratio compared to ST30-L, yet the shear transferred through the shear tab for elastic conditions is slightly smaller. An opposite trend is observed when comparing between ST36-L and ST30-L.

### 5.8.3 IMPLICATIONS OF SHEAR TAB STUDIES

The studies described above show that the shear tab thickness has almost no effect on the percentage and distribution of shear forces transferred through the shear tab. The results also show that for elastic behavior, shear stresses are concentrated at the ends of welded shear tabs of different lengths. Under these conditions, approximately  $\frac{1}{2}$  the shear force is transmitted through the tab, while the remainder goes through the flanges. Moreover, forces in the vicinity of the connection appear to be transmitted in diagonal bands. At low levels of beam plastic rotation, the shear stresses are still maximum at the ends of shear tabs of different lengths, but the stresses at mid-height of the shorter tabs are much higher than those at mid-height of the longer tabs. At high beam plastic rotations (BPR = 0.03), the difference in the distribution of shear in long and short tabs is large. While the longer tabs are generally under small shear stresses at mid-height, the shear stresses are largest at mid-height of the smaller shear tabs. Diagonal action is no longer pronounced at this level of beam plastic rotation.

The finite element analyses suggest that when large beam plastic rotations are attained, the majority of shear force is transferred through the shear tab. Therefore, it appears reasonable to design the shear tab for the full shear when using LRFD. This is warranted for unreinforced connections such as the ones analyzed in this research, in which a plastic hinge is expected to form adjacent to the column. However, current design philosophy encourages shifting the plastic hinge away from the column face. Dog-bone connections and reinforced connections are good examples of such a design philosophy. For these connections, the behavior at the beam column interface remains mostly elastic, and the assumption that “web carries shear while flanges carry moment” may not accurately represent the force transfer mechanism in the vicinity of the connection.

## 6. PANEL ZONE YIELDING

Panel zone yielding has been long recognized as an efficient way to dissipate seismic energy and to provide good over all hysteretic behavior (Krawinkler 1978). Currently recommended design provisions and provisions in effect prior to the Northridge earthquake (for example, UBC 1991) are based on this premise. These provisions allow the panel zone to deform inelastically prior to reaching its design strength. The idea is allow some level of controlled inelastic deformation in the joint panel and therefore force the panel zone to participate in energy dissipation.

Krawinkler (1978) and Popov (1987) have pointed out that large panel zone deformations lead to local kinking in the beam and column flanges which contribute to premature fracture at the beam-to-column weld. Therefore, although the panel zone region itself can undergo large inelastic excursions under reversed loading without strength degradation, a weak panel zone may have a substantial detrimental effect on the ductility that may be achieved by the beams framing into the steel connection. Statistical analyses by Foutch and Roeder (1995) of many cyclic tests conducted on rigid steel connections clearly confirm this observation. Fracture analyses by Chi et al. (1997) have shown that panel zone yielding could result in a moderate increase in toughness demand on a flaw at the weld-column interface. They did not, however, come to a firm conclusion regarding the effect of panel zone strength on toughness demands because their comparisons were not made for the same level of connection deformation.

As described by Frank (1997), new trends in the production of A36 steel have resulted in actual yield strengths that could far exceed the nominal capacity. Therefore, A36 beams designed using nominal steel properties would be much stronger than assumed, and would deliver greater shear forces to the panel zone. Overloading the panel zone in this manner results in greater inelastic deformations than intended by design specifications, and may have played a role in the observed Northridge failures.

The finite element analyses reported in Sections 5.4, 5.5, and 5.7 shed more light on the effects of inelastic panel zone deformation on connection behavior and fracture potential. The following are general observations regarding the effects of weak panel zones:

1. At low connection plastic rotations, connections with weaker panel zones show milder overall stress conditions compared to connections with stronger panel zones.
2. As the connection plastic rotation increases, the hydrostatic and principal stresses at the weld-column interface increase more rapidly and end up higher in connections with weaker panel zones. The potential for brittle fracture is therefore greater in such connections if there are flaws or other irregularity at the beam-column interface.
3. Stress triaxiality and inelastic strains in the column flange in the vicinity of the weld-column interface are significantly greater in connections with weak panel zones. The

potential for ductile fracture initiation in the column flanges is greater in such connections

4. Beam plastic rotation demands are smaller in connections with weak panel zones.

These results clearly show that although beam plastic rotation demands are smaller in connections with weak panel zones, the stress conditions are more critical at higher connection plastic rotations. Therefore, while the panel zone can effectively contribute to overall connection ductility, a weak panel zone can also lead to a greater potential for brittle and/or ductile fracture at higher connection plastic rotations.

## 6.1 EVALUATION OF CURRENT DESIGN PROVISIONS

As discussed by Popov (1987) there are three main philosophies for the design of steel panel zones in seismic regions. The first ensures that the panel zone remains as rigid as possible, forcing all inelastic deformation to occur in the beams framing into the joint (for example, AISC 1980). This design philosophy is thought to be rather uneconomical. In this approach, the shear resistance of the panel zone is:

$$V_n = 0.55F_y t_c d_c \quad 6.1$$

where,  $F_y$  is the yield strength of the column,  $t_c$  is the thickness of the panel zone, and  $d_c$  is the depth of the column.

The second approach concentrates all inelastic deformation in the panel zone region, thus preventing plastic hinges from forming in the beams (Kawano 1984). This philosophy may adversely affect connection ductility as evinced by the analyses presented in Chapter 5, and is counter to current thinking. There is growing consensus amongst structural engineers that excessive panel zone deformation may be detrimental to overall connection ductility (FEMA 267A 1997).

The third approach allows some level of controlled inelastic deformation in the joint panel (Krawinkler 1978 and FEMA 267A 1997), thereby forcing the beams and the panel zone to participate in energy dissipation. This method is therefore a compromise between methods one and two, and is currently recommended for panel zone design. In this approach, the shear resistance of the panel zone is:

$$V_n = 0.55F_y t_c d_c \left( 1 + \frac{3b_{cf} t_{cf}^2}{d_b d_c t_c} \right) \quad 6.2$$

where,  $F_y$ ,  $t_c$ , and  $d_c$ , are as defined previously;  $t_{cf}$  is the column flange thickness,  $b_{cf}$  is the column flange width, and  $d_b$  is the depth of the beam. The term in the brackets accounts for the contribution of the column flanges. The equation was derived assuming that the sides of the panel zone remain straight after panel zone deformation, and that design strength is reached at a

panel zone plastic distortion of  $4\delta_y$ , where  $\delta_y$  is the elastic panel zone distortion (Krawinkler 1978). As a result of the panel zone sides remaining straight, plastic hinges or ‘kinks’ form in the column flanges (**Figure 6.1**).

The shear strength of the panel zone calculated according to Equation 6.2 is not required to exceed 80% of the shear corresponding to the plastic moment capacity of the beams framing into the joint (FEMA 267A 1997). For such conditions, the design strength of the panel zone may be thought of as:

$$V_n = \frac{0.55F_y t_c d_c}{0.8} \left( 1 + \frac{3b_{cf} t_{cf}^2}{d_b d_c t_c} \right) \quad 6.3$$

The 80% factor accounts for the presence of gravity moments acting on an interior joint (Popov 1987). Although the moments caused by an earthquake on either side of an interior joint have the same sense, the moments caused by gravity loading have opposite senses, and tend to decrease the total moment acting on a connection (**Figure 6.2**); hence the reduction factor.

While the 80% factor may be argued successfully for interior joints, it may result in overloading in the case of exterior joints similar to the ones considered in this study. When only one beam frames into a joint, the gravity moment may act in the same sense as the moment caused by the earthquake (**Figure 6.3**). In spite of this, current design provisions do not differentiate between interior and exterior joints, and exterior connections can be designed taking advantage of this provision.

The relationship between panel zone distortion and applied tip loads computed from the finite element models are plotted in **Figure 6.4** to **Figure 6.6**. The relationships are plotted out for Series BD, CF, and CWT. These connection configurations were designed to have a weak panel zone, and exhibited significant inelastic panel zone deformation. Also plotted on the same figure are the tip loads causing the panel zones to reach their design strengths calculated using Equations 6.1 through 6.3 (without  $\phi$  factors). The vertical lines plotted in the figures correspond to a panel zone plastic distortion of  $4\delta_y$ . As assumed by Krawinkler (1978), the panel zones are assumed to reach their “design” strength at this level of plastic distortion.

It is clear from **Figure 6.4** that Equation 6.2 reasonably predicts the strength at a panel zone plastic distortion of  $4\delta_y$  for connections with different beam depths. Equation 6.3, on the other hand, appears to be consistently asymptotic with the force-deformation response. However, significant inelastic panel zone deformation must occur before the panel zone strength according to Equation 6.3 can be achieved. Equation 6.1 closely predicts strength at the onset of inelastic panel zone deformation for specimens with different beam depths.

An examination of **Figure 6.5** shows that Equation 6.2 is also able to reasonably predict the strength for connections CF1 through CF3. In addition, Equation 6.3 appears to be asymptotic with the force deformation response for these three cases. However, Equation 6.2 appears to slightly overestimate the strength for case CF4, the configuration with the thickest column flanges ( $t_{cf} = 3.2$ -in respectively). Krawinkler (1978) noted that Equation 6.2 may not work well

for cases with very thick column flanges. However, no such limitation exists in current design provisions. Equation 6.1 closely predicts the strength at the onset of inelastic panel zone deformation for specimens with different column flange thicknesses. In evaluating these results note that the column web thickness is varied in order to maintain a similar ratio of beam to panel zone strength in the different configurations.

**Figure 6.6** implies that significant panel zone distortions can be expected for cases with  $P_z/P_b > 1.0$ . For example, connection CWT5 underwent a panel zone plastic distortion of 0.013 *rad* even though  $P_z/P_b = 1.17$ . It is important to note that these large inelastic panel zone deformations occur in CWT5 at the load level specified by Equation 6.1 (**Figure 6.6e**). However, as described in Section 5.4, this is not accompanied by a large increase in principal and hydrostatic stresses as in cases with weaker panel zones. The stresses are not as large as in cases with weaker panel zones because the local kinks in the column flange are not pronounced. This can be clearly seen in **Figure 6.7b**. Note that the sides of the panel zones do not remain straight as assumed in the derivation of Equation 6.2. The local kinks, however, can be seen in the deformed shape of Specimen CWT1 (**Figure 6.7a**). The sides of the deformed panel zone of CWT1 are also straighter than in CWT5. The source of inelastic panel zone deformation in CWT5 appears to be reverse curvature bending of the panel zone region (**Figure 6.7b**). Hence, while this case may have a lower potential for fracture than connections with weaker panel zones, it may still lead to large frame deformations, and problems with frame stability.

### 6.1.1 DESIGN IMPLICATIONS

The large bending deformations in CWT5 occur because of the relatively large aspect ratio (depth/width  $\cong 2.2$ ) and large shear to bending strength ratio of the panel zone. These bending deformations suggest that designing such panel zones for pure shear may be inadequate. Provisions that account for axial-shear-bending interaction may be warranted.

The 80% provision is also of concern. As discussed above, this factor can lead to greater inelastic deformation than assumed by Equation 6.2 in *exterior* (one-sided) connections. This effect can be clearly seen in **Figures 6.4** through **6.6**, where the strength according to Equation 6.3 is reached *only* after significant panel zone distortion. These analyses suggest that while this factor appears reasonable for interior (two-sided) connections, it could be detrimental to the performance of exterior (one-sided) connections. This is a very important point when considering pre-Northridge construction practices in which moment resistance is provided by a few moment resisting frames. In a previous study conducted by the first author (**Figure 6.8**), one-sided moment connections accounted for approximately 2/3 of the moment resisting connections in a 17 story building that was damaged in Northridge (Chi et. al. 1997).

## 7. SUMMARY AND CONCLUSIONS

### 7.1 SUMMARY

The main objectives of this project have been: 1) to develop a more thorough understanding of the inelastic behavior of pre-Northridge FR welded-bolted connections, and 2) to lay the groundwork for the development of connection details that are not fracture critical. These objectives have been addressed through detailed three-dimensional nonlinear finite element analyses of connection subassemblages.

The characteristics of the analysis configurations utilized in this research were derived from the geometry of Berkeley specimen PN3 which consists of a W36x150 beam connected to W14x257 column. Different analysis configurations were created by changing some of the attributes of specimen PN3. Important geometric and material parameters were varied over the practical range of interest in order to evaluate their effect on inelastic behavior. The parameters that have been addressed include:

- Key geometric parameters
  - Beam flange thickness
  - Column flange thickness
  - Beam depth
  - Column web thickness
  - Continuity plate thickness, or absence
  - Size and geometry of the weld access hole
- Variation in the material properties of the steel in the beam and column
  - Beam-to-column yield stress ratio
  - Beam yield-to-ultimate stress ratio
- Degree of panel zone deformation
- Shear tab depth, thickness, and shear span-to-depth ratio.

To compare between the behavior of the different configurations analyzed in this research, and to assess the effect of the parameters of interest, a number of stress, strain, and combined stress/strain indices were employed. These included hydrostatic stress, Mises stress, longitudinal stress, maximum principal stress, and effective plastic strain. These stresses and strains were sampled at connection plastic rotations of 0.0025 and 0.03 *rad*. The former CPR was intended to represent the behavior of connections with little ductility whereas the larger CPR was intended to represent the behavior of connections with greater ductility as specified by currently recommended provisions.

The studies conducted in this research did not address the issue of fracture propagation. This project was concerned with the potential for cracking only through the development of stress states or material conditions that would facilitate fracture if a flaw or other irregularity were introduced.

## **7.2 CONCLUSIONS**

The key findings and conclusions from this research are listed below. Unless noted otherwise, these conclusions apply to one-sided connections with configuration and general dimensions similar to those for specimen PN3 tested at UC Berkeley.

### **7.2.1 STRESS CONCENTRATION AT WELD-COLUMN INTERFACE**

The results reported in Section 3.6 show that the longitudinal stress at the center of the weld-column interface of connections without continuity plates is sensitive to the finite element type and mesh density. These factors must be carefully considered when evaluating the large stress concentration factors that have been published in the literature.

### **7.2.2 TRIAXIAL RESTRAINT AT WELD-COLUMN INTERFACE**

The maximum hydrostatic stresses encountered at the weld-column interface occurred in configuration CONT-N (specimen without continuity plates, Section 5.3). In this case, the hydrostatic stresses reached 92% of the yield stress of the beam. The corresponding stress triaxiality (see Section 3.8) was 1.07, and the accompanying plastic strains were very small. These levels of stress triaxiality and plastic strains imply that observed brittle fracture at the weld-column interface probably occurred due to large pre-existing flaws at the interface rather than limited ductility caused by large hydrostatic stresses. Stringent quality control is therefore key to improved connection performance.

### **7.2.3 YIELD-TO-ULTIMATE STRESS RATIO**

The cases analyzed in Section 5.1 show that the behavior of the analyzed connections is insensitive to steels with yield-to-ultimate stress ratios ( $f_y/f_u$ ) less than 0.8 for connection plastic rotations up to 0.03. The analyses further show that steel with a high yield-to-ultimate stress ratio ( $f_y/f_u = 0.95$ ) can result in a large reduction in the plastic hinge length of the beam. For example, the plastified length of the beam with  $f_y/f_u = 0.95$  was about  $\frac{1}{2}$  the corresponding length of the beam with  $f_y/f_u = 0.80$ . The smaller plastified length leads to increased local strains which in turn promote earlier local buckling. The increase in strains result in a greater susceptibility to low cycle fatigue.

#### **7.2.4 ACCESS-HOLE GEOMETRY**

Increasing the size of the web cope would permit easier welding on the beam bottom flange, and possibly promote better weld quality. However, the analyses in Section 5.2 suggest that it is important to use a small access hole in order to minimize the potential for ductile fracture at the root of the hole. The analyses further show that the access hole in which the web terminates perpendicular to the flange is clearly inferior to the semi-circular detail from the ductile fracture point of view.

#### **7.2.5 PRESENCE/ABSENCE OF CONTINUITY PLATES**

These analyses support the FEMA-267 (1995) recommendations, which require the use of continuity plates in all connections. The analyses show that the use of continuity plates results in milder stress and strain distributions, particularly at the weld-column interface. However, the analyses also suggest that the provisions may be relaxed with regards to the required continuity plate thickness. Analyses with continuity plates whose thickness is less than 60% of the recommended thickness resulted in almost no change in the stress and strain conditions in the connection. Beside their increased cost, the use of overly thick continuity plates may be detrimental to connection behavior. Thicker plates require larger welds, which create additional restraint and residual stresses in the connection region. It should be noted that these results apply to one-sided connections in which the column flanges are relatively thick compared to the beam flanges. Further research is needed to verify if these conclusions apply to two-sided connections, or connections in which the column flanges are significantly thinner.

#### **7.2.6 COLUMN WEB THICKNESS AND PANEL ZONE STRENGTH**

The primary effect of varying the column web thickness is to vary the ratio of panel zone strength to beam strength. At low connection plastic rotations ( $CPR=0.0025$ ), the connections with smaller column web thickness, and hence weaker panel zones, show milder overall stress conditions than the connections with stronger panel zones. However, as the connection plastic rotation increased, the hydrostatic and principal stresses at the middle of the weld-column interface increased much more rapidly and ended up much higher in connections with weaker panel zones. Stress triaxiality and inelastic strains at the corner of the weld-column interface are also significantly greater in connections with weak panel zones. The analyses further showed that although the plastic rotation demand on the beam is smaller in connections with weak panel zones, the stress conditions are more critical and hence more conducive to cracking in the event of a flaw.

#### **7.2.7 BEAM DEPTH**

The results of series BDN in which the panel zone strength is 49% greater than the beam strength indicate that the shallower beams have slightly higher stresses at the beam-column interface

compared to deeper beams. However, the inelastic strains in the beam flange of deeper sections were significantly higher compared to shallower sections. Thus, deeper beams appear to be more susceptible to low-cycle fatigue and may have a reduced cumulative ductility compared to shallower beams. The increased strain in deeper beams is also accompanied by earlier local buckling.

The results of series BD in which the panel zone strength is about 32% lower than the beam strength indicate that stress conditions at the weld column-interface are generally higher than those observed in corresponding connections in Series BDN at the same level of connection plastic rotation. Connections with smaller beam depth were found to have higher principal stresses at the center of the interface line than connections with deeper beams. However, the plastic strains in the beam flanges are much higher in the deeper beams compared to shallower beams at high connection plastic rotations. The same conclusions drawn for series BDN are therefore applicable.

### **7.2.8 BEAM FLANGE THICKNESS**

Increasing the beam flange thickness resulted in greater triaxial restraint and larger principal stresses at the beam-to-column interface. For example, the maximum longitudinal stresses increased by 26% as the beam flange thickness increased from 0.79-in to 3.0-in. The analyses also show that a greater beam flange thickness affects a larger portion of the column flange. This increases the probability of exacerbating the conditions at preexisting flaws in the column HAZ.

### **7.2.9 SHEAR TRANSFER**

The studies described in Section 3.8 are subject to the modeling assumption that the shear tab is monolithic with the beam web. These studies show that the shear tab thickness has almost no effect on the percentage and distribution of shear forces transferred through the shear tab in the cases analyzed. The results also show that for elastic behavior, shear stresses are concentrated at the ends of welded shear tabs of different lengths. Under these conditions, approximately  $\frac{1}{2}$  the shear force is transmitted through the tab, while the remainder goes through the flanges. Moreover, forces in the vicinity of the connection appear to be transmitted in diagonal bands. At low levels of beam plastic rotation, the shear stresses are still maximum at the ends of shear tabs of different lengths, but the stresses at mid-height of the shorter tabs are much higher than those at mid-height of the longer tabs. At high beam plastic rotations ( $BPR = 0.03$ ), the difference in the distribution of shear in long and short tabs is large. While the longer tabs are generally under small shear stresses at mid-height, the shear stresses are largest at mid-height of the smaller shear tabs. Diagonal action is no longer pronounced at this level of beam plastic rotation.

The finite element analyses suggest that when large beam plastic rotations are attained, the majority of shear force is transferred through the shear tab. Therefore, it appears reasonable to design the shear tab for the full shear when using the LRFD methodology. This is warranted for unreinforced connections such as the ones analyzed in this research, in which a plastic hinge is

expected to form adjacent to the column. However, current design philosophy encourages shifting the plastic hinge away from the column face. Dog-bone connections and reinforced connections are good examples of such a design philosophy. For these connections, the behavior at the beam column interface remains mostly elastic, and the assumption that “web carries shear while flanges carry moment” may not accurately represent the force transfer mechanism in the vicinity of the connection.

#### **7.2.10 PANEL ZONE STRENGTH PROVISIONS**

Comparisons between analysis results and currently recommended panel zone provisions show that Equation 6.2 reasonably predicts the strength of panel zones with different beam depths, but slightly overestimates strength of connections with very thick column flanges. Furthermore, significant inelastic panel zone deformation must occur before the panel zone strength according to Equation 6.3 can be achieved. Equation 6.1, on the other hand, closely predicts strength at the onset of inelastic panel zone deformation for specimens with different beam depths and column flange thicknesses.

Large bending deformations were observed in specimen CWT5. These are attributed to the relatively large aspect ratio (depth/width  $\cong 2.2$ ) and large shear to bending strength ratio of the panel zone. These bending deformations suggest that designing such panel zones for pure shear may be inadequate. Provisions that account for axial-shear-bending interaction may be warranted.

Finally, while the 80% factor in currently recommended panel zone provisions is reasonable for interior connections, the analyses conducted as part of this research suggest that this factor should not be used for the design of exterior connections.

### **7.3 RECOMMENDATIONS FOR FUTURE WORK**

The analyses presented in this report have provided extensive data for evaluating the effect of important design variables on the potential for fracture of welded-bolted connections. The analyses also raised specific questions regarding the appropriateness of some of the current design recommendations for flange-welded, web-bolted connections. In particular, provisions for shear transfer at the beam-column interface, panel zone strength, and continuity plates need to be reexamined. It is envisioned that detailed finite element analyses similar to the ones presented in this report can be used to support further experimental work and to calibrate fracture-resistant design models.

Furthermore, the studies conducted in this research have focused on unreinforced pre-Northridge type connections in which the beam plastic hinge is expected to form adjacent to the column. It is important to extend analyses of this sort to other type of connections such as dog-bones and reinforced connections in which the plastic hinge is shifted away from the beam-column

interface. Such analyses would provide information that would help clarify the inelastic behavior of these connections and would also facilitate the development of new fracture resistant details.

Finally, much research is still needed to tie results from local analyses of the sort presented in this research to global frame behavior.

## REFERENCES

- ABAQUS (1996), *User's Manual - Version 5.6*, Hibbit, Karlsson, and Sorenson, Inc, 1080 Main Street, Pawtucket, RI 02860.
- AISC, Specifications for the Design, Fabrication, and Erection of Structural Steel for Buildings, With Commentary. *Manual of Steel Construction*, 1980, 8<sup>th</sup> Edition, Chicago, Illinois, AISC.
- AISC-LRFD, (1994). *Load and Resistance Factor Design Specification for Structural Steel Buildings*. American Institute of Steel Construction (AISC), Chicago, IL.
- Allen, J., Partridge, J., Radau, S., and Richard, R. (1997), *Ductile Connection Designs for Welded Steel*, Technical Report, Seismic Structural Design Associates (SSDA), Inc.
- Barsom, J. M. and Rolfe. S. T. (1987), *Fracture and Fatigue Control in Structures*, Prentice-Hall, Englewood Cliffs, NJ 07632.
- Chi, W., El-Tawil, S., Deierlein, G. G., and Abel, J. F., "Inelastic Analyses of a 17 Story Framed Building Damaged During Northridge," *Engineering Structures*, Vol. 20, Nos. 4-6, pp. 481-495, (1998).
- Chi, W., Deierlein, G. G., and Ingrassia, A. R. (1997), Finite Element Fracture Mechanics Study of Welded Beam-Column Connections, *Draft SAC Report 97-xx*, SAC Joint Venture.
- Engelhardt, M. D. and Husain, A. S. (1992), Cyclic Tests on Large Scale Steel Moment Connections, *Report No. PMFSEL 92-2*, Phil M. Ferguson Structural Lab, Dept. of Civil Engineering, University of Texas at Austin.
- Engelhardt, M. D. and Hussain, A. S. (1993), "Cyclic-Loading Performance of Welded Flange-Bolted Web Connections," *Journal of Structural Engineering*, ASCE, Vol. 119, No. 12, pp. 3537-3549.
- Engelhardt, M. D. and Sabol, T. A., *Testing of Welded Steel Moment Connections in Response to the Northridge Earthquake*, Progress Report to the AISC Advisory Subcommittee on Special Moment Resisting Frame Research, October 1994.
- FEMA-267 (1995), *Interim Guideline: Evaluation, Repair, Modification, and Design of Welded Steel Moment Frame Structures*, Report No. SAC-95-02, SAC Joint Venture.
- FEMA-267A (1995), *Interim Guideline: Advisory No. 1, Supplement to FEMA-267*, Report No. SAC-96-03, SAC Joint Venture.
- Frank, K. H., The Physical and Metallurgical Properties of Structural Steels, *Background Reports*, SAC 95-09, 1997, 1-1 to 1-22.

- Goel, S. C., Stojadinovic, B., and Lee, K. (1997), *A New Look at Steel Moment Connections*, Report, Department of Civil and Env. Engineering, University of Michigan, Ann Arbor, MI 48109-2125.
- Greschick, G., White, D. W., McGuire, W., and Abel, J. F. (1993), "On the Correlation of Analysis and Tests of the Inelastic Flexural Behavior of Wide-Flange Steel Beams," *Computers and Structures*, Vol. 48, No. 3, pp. 511-622.
- Hancock, J. W. and Mackenzie, A. C. (1976), "On the Mechanism of Ductile Fracture in High-Strength Steels Subjected to Multi-Axial Stress-States," *Journal of Mech. Phys. Solids*, Vol. 24, pp. 147-169.
- Huang, P. (1994), *Finite Element Analysis of Structural Steel Beams and Bridge Girders*, PhD thesis, School of Civil and Environmental Engineering, Cornell University, Ithaca, NY 14853.
- Kaufmann, E. J. and Fisher, J. W. (1995), "Fracture Analysis of Failed Moment Frame Weld Joints Produced in Full-Scale Laboratory Tests and Buildings Damaged in the Northridge Earthquake," *Technical Report SAC 95-08*, SAC Joint Venture, pp. 1-1 to 1-8.
- Kawano, A. (1984), "Inelastic Behavior of Low-Rise Steel Frame Based on a Weak Beam-to-Column Connection Philosophy to Earthquake Motion," *Proceedings, Eighth World Conference on Earthquake Engineering*, Vol. IV, San Francisco, California, USA, pp. 519-526.
- Krawinkler, H. (1978), "Shear in Beam-Column Joints in Seismic Design of Steel Frames," *Engineering Journal, AISC*, Vol. 3, 82-91.
- Kuwamura, H. (1997), "Transition Between Fatigue and Ductile Fracture in Steel," *Journal of Structural Engineering*, ASCE, Vol. 123, No. 7, pp. 864-870.
- Lee, S-J. and Lu, L-W. (1989), "Cyclic Tests of Full-Scale Composite Joint Subassemblages," *Journal of Structural Engineering*, ASCE, Vol. 115, No. 8, pp. 1977-1998.
- Leon, R. T., Hajjar, J. F., and Shield, C. K. (1996), "The Effect of Composite Floor Slabs on the Behavior of Steel Moment-Resisting Frames in the Northridge Earthquake," *Composite Construction in Steel and Concrete III*, New York: American Society of Civil Engineers.
- Lemaitre, J. (1996), *A Course on Damage Mechanics*, Springer-Verlag, Berlin, Germany.
- Mikesell, T. D. (1997), *Strength and Ductility of Welded-Bolted Steel Connections*, MS Thesis, Department of Civil and Environmental Engineering, University of Central Florida, Orlando, FL 32816.
- Patel, K. V. and Chen, W. F (1984), "Nonlinear Analysis of Steel Moment Connections," *Journal of Structural Engineering*, ASCE, Vol. 110, No. 8, pp. 1861-1874.

- Popov, E. P., Blondet, M., Stepanov, L., and Stojadinovic, B. (1996), "Full-Scale Beam-Column Connection Tests," *Experimental Investigations of Beam-Column Subassemblages*, Technical Report CAS 96-01, Part 2.
- Popov, E. P. (1987), "Panel Zone Flexibility in Seismic Moment Joints," *Journal of Constructional Steel Research*, 1987, Vol. 8, 91-118.
- Roeder, C. W. and Foutch, D. A. (1996), "Experimental Results for Seismic Resistant Steel Moment Frame Construction," *Journal of Structural Engineering, ASCE*, Vol. 122, No. 6, pp. 581-588.
- Roeder (1997), "An Evaluation of Cracking Observed in Steel Moment Frames," *ASCE Structures Congress*, Portland, April 1997, pp. 767-771.
- SAC Competition (SAC 1995), Correspondence with Jim Malley.
- Salmon, C. G. and Johnson, J. E. (1996), *Steel Structures – Design and Behavior*, Harper Collins College Publishers.
- Schafer, B. (1995), *Behavior and Design of Cold Formed Steel Members With Intermediate Stiffeners*, MS Thesis, School of Civil and Environmental Engineering, Cornell University, Ithaca, NY 14853.
- Shuey, B. D., Engelhardt, M. D., and Sabol, T. A. (1996), "Testing of Repair Concepts for Damaged Steel Moment Connections," *Experimental Investigations of Beam-Column Subassemblages*, Technical Report CAS 96-01, Part 2.
- Thomason, P. F. (1990), *Ductile Fracture of Metals*, Pergamon Press.
- Tremblay, R., Timler, P., Bruneau, M., and Filiatault, A. (1995), "Performance of Steel Structures During the 1994 Northridge Earthquake," *Canadian Journal of Civil Engineering*, Vol. 22, pp. 338-360.
- UBC (1991), *Uniform Building Code*, International Conference of Building Officials, Whittier, California, USA.
- Yang, T. and Popov E. P. (1995), "Behavior of Pre-Northridge Moment Resisting Steel Connections," Report No. UCB/EERC-95/08, August 1995.

TABLE 1.1 AVERAGE MEASURED MATERIAL PROPERTIES

Properties	<i>Beam (W36x150)</i>		<i>Column (W14x257)</i>	
	Flange	Web	Flange	Web
E (ksi)	30100	28100	28900	29000
Yield Strength (ksi)	40.3	48.6	48.6	70*
Ultimate Strength (ksi)	57.4	60.1	67.2	76

\*BASED ON 0.2% OFFSET

TABLE 2.1: SUMMARY OF RECENT ANALYTICAL WORK

Research Group	Analysis Types	Yield Criterion	Element Type	Program	Comments
Patel and Chen (1985)	2-D, plane stress, inelastic	Von. Mises	Rectangular, isoparametric	NONSAP	Residual stresses included
SAC Competition	See Table 2.2 for Details				
Yang and Popov (1995)	3-D, inelastic	Von Mises	8-node brick elements	ABAQUS	
Leon et. al. (1996)	3-D, inelastic	Von Mises	Mixture of beam-column and solid elements	ABAQUS	
Richard et. al. (1995) and Allen et. al. (1997)	3-D, inelastic	Von Mises	Mixture of plate bending and solid elements	ANSYS	
Goel et. al. (1997)	3-D, elastic and inelastic	Von Mises	Plate elements	ABAQUS	
Chi et. al. (1997)	3-D, LEFM and inelastic fracture mechanics	Von Mises	Plane stress & strain elements and special singular elements	FRANC, ABAQUS	Residual stresses included
Roeder (1997)	3-D, inelastic	Unknown	Shell elements	Unknown	

TABLE 2.2: DETAILS OF SAC COMPETITION ANALYSES

Research Group	Analysis Type	Yield Criterion	Element Type	Program	Comments
Dameron, ANATECH	3-D, inelastic	Damage model	Quadratic shell	ABAQUS	
McCullen, LL National Labs	3-D, inelastic	Unknown	Shell	NIKE3D	
Manheim, TM Engineers	N/A	N/A	N/A	N/A	Used plasticity theory, compatibility, and equilibrium
Way et. al., BIC	2-D, inelastic	N/A	2-D beam-column	DRAIN-2D	
MacRae, U. Washington	2-D, inelastic	N/A	2-D beam-column	DRAIN-2DX	
Ju, UCLA	2-D, inelastic	Von Mises	4-node quadrilateral	FEAP	Damage modeling
Balan et. al., UC Berkeley	3-D, inelastic	Von Mises	4-node thin shell	MIRAGE/PC	
Maison et, al., Lehigh U.	2-D, inelastic	N/A	2-D beam-column	PC-ANSR	
Warmka et. al., Washington U.	3-D, inelastic	Unknown	20-node brick elements	ABAQUS	Did not present analysis results
Nofal et. al., UC Irvine	3-D, inelastic	Unknown	Shell	NIKE3D	
Ingraffea et. al., Cornell U.	2-D, fracture	Von Mises	Singular elements, plane strain & stress elements	FRANC	Included residual stresses due to welding process
Hart et. al., Hart Consultants	2-D, inelastic	Unknown	Fiber beam-column	DRAIN-3DX	Included residual stresses in sections
Zekioglu et. al., OAP	3-D, inelastic	Unknown	Shell	ANSYS	

TABLE 5.1: PROPERTIES OF YUSR SPECIMENS

Name	$\psi$ (%)	$P_z/P_b$	$P_c/P_b$
YUSR-65	65	1.3	2.6
YUSR-80	80	1.3	2.6
YUSR-95	95	1.3	2.6

TABLE 5.2: SUMMARY OF ACCESS HOLE ANALYSES

Configuration	A1	A2	A3
PEEQ Index	28.2	45.1	29
Longitudinal Stress (ksi)	51.1	59.1	58.9
Triaxiality Ratio	0.57	0.64	0.74
Rupture Index	66	120	88

TABLE 5.3: PROPERTIES OF SPECIMENS OF SERIES CONT

Specimen	CONT-0.5	CONT-0.75	CONT-0.94	CONT-N
Continuity Plate Thickness (in)	0.5	0.75	0.94	None

TABLE 5.4: PROPERTIES OF CONFIGURATIONS IN SERIES CWT

Name	$t_{wc}$ (in)	$P_b$ (kips)	$P_z$ (kips)	$P_c$ (kips)	$P_z/P_b$	$P_c/P_b$
CWT1	0.6	299	125	398	0.42	1.33
CWT2	0.8	299	153	404	0.51	1.35
CWT3	1.18	299	206	417	0.69	1.39
CWT3-N	1.18	154	229	464	1.49	3.01
CWT4	1.6	299	266	432	0.89	1.44
CWT5	2.2	299	350	452	1.17	1.51

TABLE 5.5: EFFECT OF PANEL ZONE STRENGTH ON STRESSES AND STRAINS AT CORNER

Connection	$P_z/P_b$	Hydrostatic Stress (ksi)	Triaxiality	PEEQ Index	Max. Principal Stress (ksi)	Rupture Index
CWT1	0.41	63.6	1.33	19.6	91.7	145
CWT2	0.51	62.8	1.33	18.3	90.7	135
CWT3	0.69	51.7	1.13	8.3	80.2	46
CWT4	0.89	41.7	0.92	5.3	71.4	21
CWT5	1.17	38.3	0.85	5.2	68.2	19

TABLE 5.6: PROPERTIES OF CONFIGURATIONS IN SERIES BDN ( $f_{yb}=36$  ksi,  $f_{yc}=50$  ksi)

Name	$d$ (in)	$t_{cw}$ (in)	$P_b$ (kips)	$P_z$ (kips)	$P_c$ (kips)	$P_z/P_b$	$P_c/P_b$
BDN1	18	0.8	62	92	381	1.46	6.1
BDN2	24	1	90	134	409	1.48	4.53
BDN3	35.9	1.18	154	229	464	1.48	3.01
BDN4	40	1.2	179	266	485	1.49	2.71

TABLE 5.7: PROPERTIES OF CONFIGURATIONS IN SERIES BD ( $f_{yb}=70$  ksi,  $f_{yc}=45$  ksi)

Name	$d$ (in)	$t_{cw}$ (in)	$P_b$ (kips)	$P_z$ (kips)	$P_c$ (kips)	$P_z/P_b$	$P_c/P_b$
BD1	18	0.8	122	83	343	0.68	2.82
BD2	24	1	176	121	368	0.68	2.09
BD3	35.9	1.18	299	206	417	0.68	1.39
BD4	40	1.2	348	239	436	0.68	1.25

TABLE 5.8: PROPERTIES OF CONFIGURATIONS IN SERIES BF

Name	$t_{wc}$ (in)	$t_{bf}$ (in)	$P_b$ (kips)	$P_z$ (kips)	$P_c$ (kips)	$P_z/P_b$	$P_c/P_b$
BF1	1.05	0.79	139	210	459	1.51	3.31
BF2	1.18	0.94	154	229	464	1.49	3.01
BF3	1.45	1.18	179	272	474	1.52	2.65
BF4	1.95	1.73	234	350	493	1.50	2.1
BF5	3.1	3.0	355	530	537	1.49	1.51

TABLE 5.9: PROPERTIES OF CONFIGURATIONS IN SERIES CFN

Name	$t_{wc}$ (in)	$t_{fc}$ (in)	$P_b$ (kips)	$P_z$ (kips)	$P_c$ (kips)	$P_z/P_b$	$P_c/P_b$
CFN1	1.35	1.3	154	232	361	1.51	2.35
CFN2	1.18	1.89	154	229	464	1.49	3.01
CFN3	0.95	2.5	154	228	560	1.48	3.64
CFN4	0.65	3.2	154	232	661	1.51	4.29

TABLE 5.10: PROPERTIES OF CONFIGURATIONS IN SERIES CFN

Name	$t_{wc}$ (in)	$t_{fc}$ (in)	$P_b$ (kips)	$P_z$ (kips)	$P_c$ (kips)	$P_z/P_b$	$P_c/P_b$
CF1	1.35	1.3	299	209	325	0.70	1.09
CF2	1.18	1.89	299	231	417	0.69	1.39
CF3	0.95	2.5	299	205	504	0.69	1.68
CF4	0.65	3.2	299	209	595	0.70	1.99

TABLE 5.11: PROPERTIES OF CONFIGURATIONS IN SERIES ST

Configuration	Beam	Column	Shear Tab Height
ST36-L	W36x150	W14x257	30
ST36-S	W36x150	W14x257	22'
ST30-L	W30x99	W14x257	24
ST30-S	W30x99	W14x257	18
ST24-L	W24x68	W14x257	18
ST24-S	W24x68	W14x257	12

\*Because of modeling constraints, this height is slightly smaller than the minimum specified by the AISC-LRFD specifications to accommodate the required bolts.

TABLE 5.12: PERCENTAGE SHEAR TRANSFERRED THROUGH SHEAR TAB

Load Level	Shear tab thickness			
	0.75t	t	1.5t	2t
Elastic	56.4%	56.8%	57.2%	57.6%
Nominal Design	75.9%	76.0%	76.1%	76.5%
BPR* = 0.03	93.5%	94.6%	94.7%	95.5%

\*BPR : Beam Plastic Rotation

TABLE 5.13: PERCENTAGE SHEAR TRANSFERRED THROUGH THE SHEAR TAB FOR DIFFERENT BEAM DEPTHS

Load level	W36x150		W30x99		W24x68	
	STH' = 22"	STH' = 30"	STH' = 18"	STH' = 24"	STH' = 12"	STH' = 18"
Elastic	49.1%	56.8%	60.2%	70.3%	62.1%	68.2%
Design load	77.9%	76.0%	87.4%	84.5%	86.1%	77.9%

\*STH = Shear Tab Height

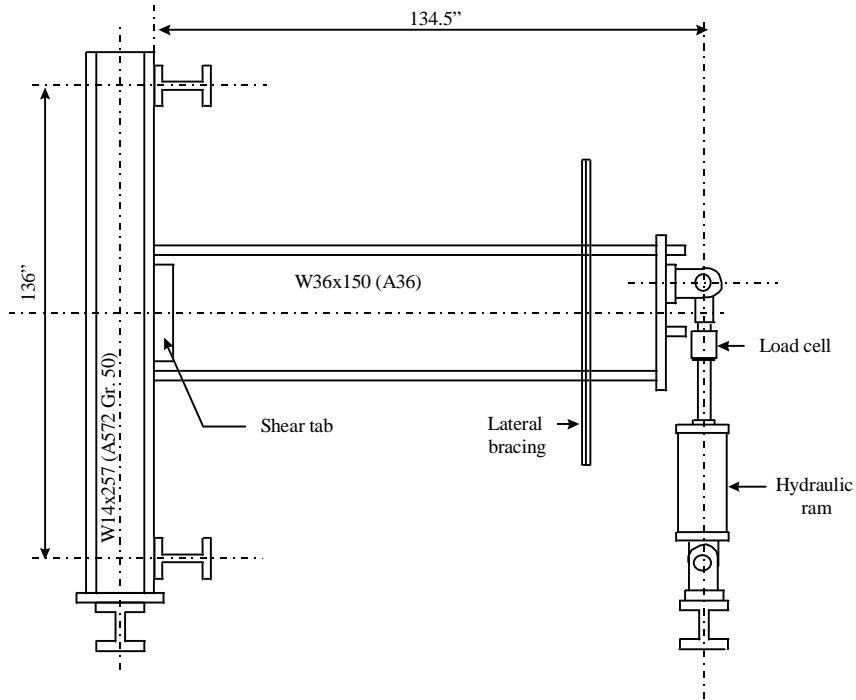
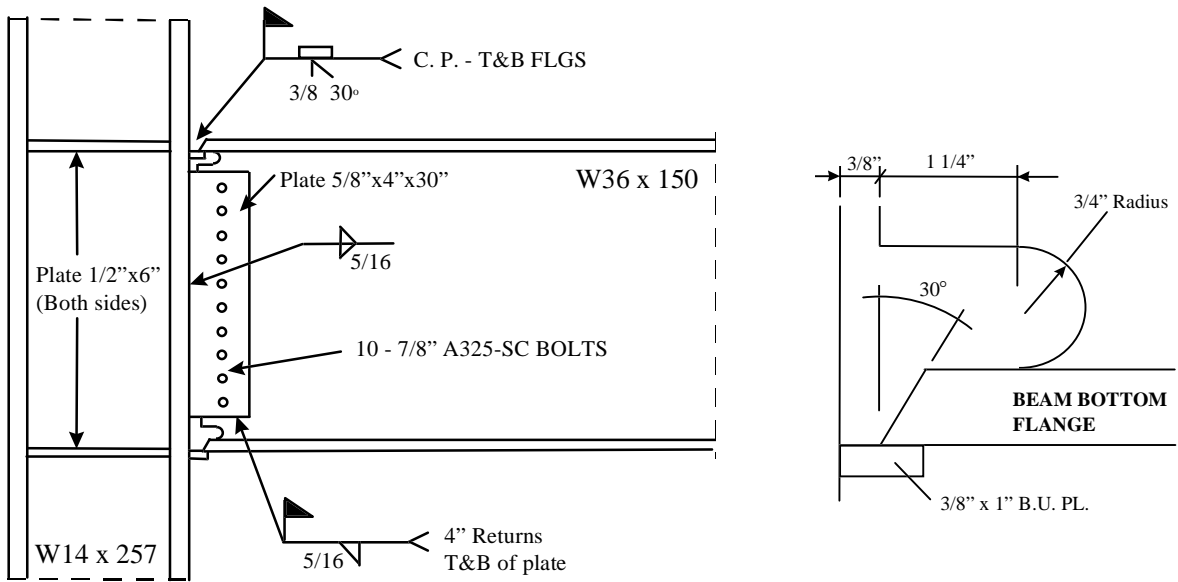


FIGURE 1.1: TEST SETUP FOR SPECIMEN PN3



a- Specimen PN3

b- Details of lower access hole

FIGURE 1.2: DETAILS OF CONNECTION SPECIMEN PN3

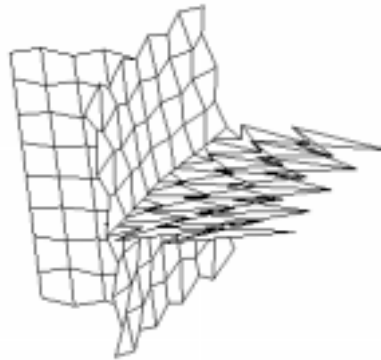


FIGURE 3.1: HOURGLASSING IN REDUCED INTEGRATION SHELL ELEMENTS

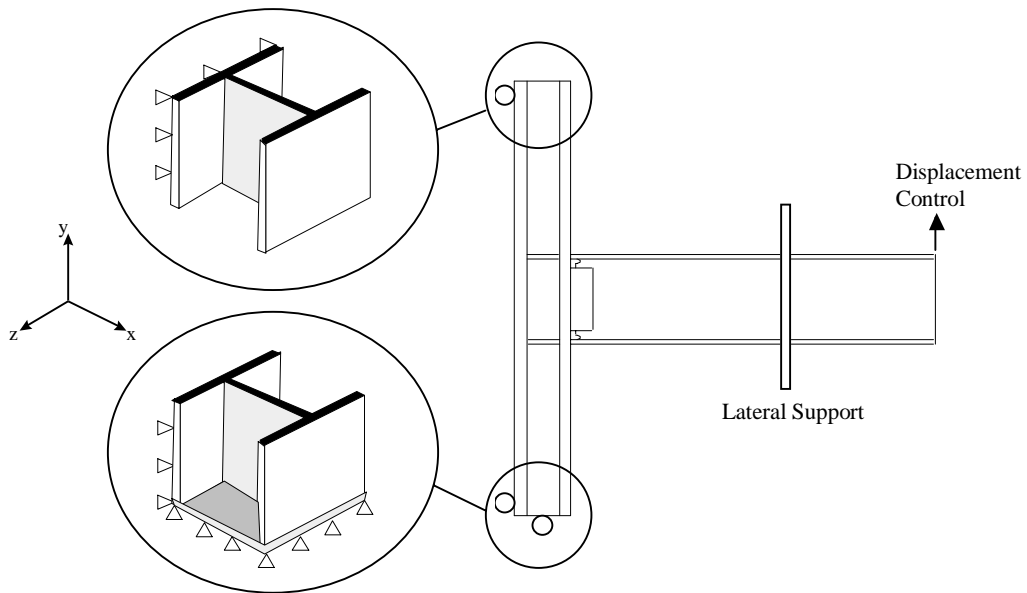


FIGURE 3.2: DETAILS OF SUPPORT CONDITIONS

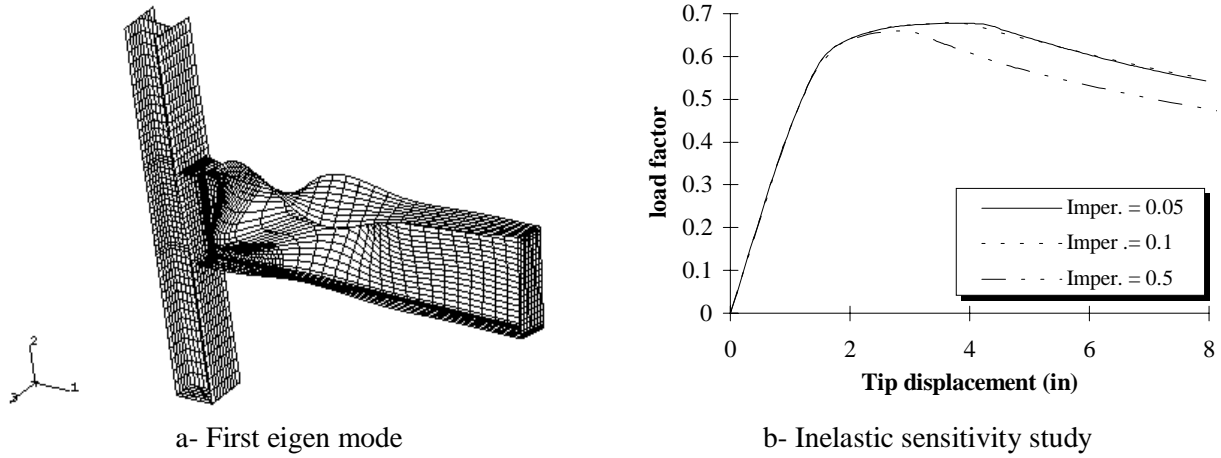


FIGURE 3.3: EFFECT OF GEOMETRIC IMPERFECTION SIZE ON INELASTIC RESPONSE

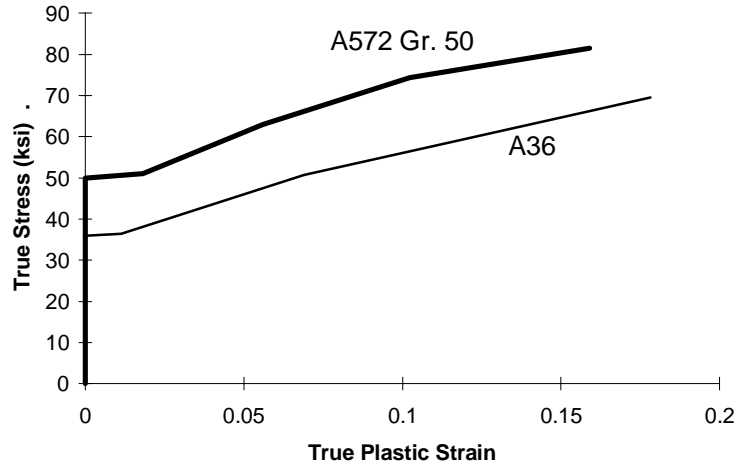


FIGURE 3.4: TRUE-STRESS VS. TRUE-PLASTIC STRAIN CURVES FOR A36 AND A572 GR. 50 STEELS. DERIVED FROM *NOMINAL* STRESS-STRAIN CURVES PUBLISHED IN SALMON AND JOHNSON (1996, pg. 47).

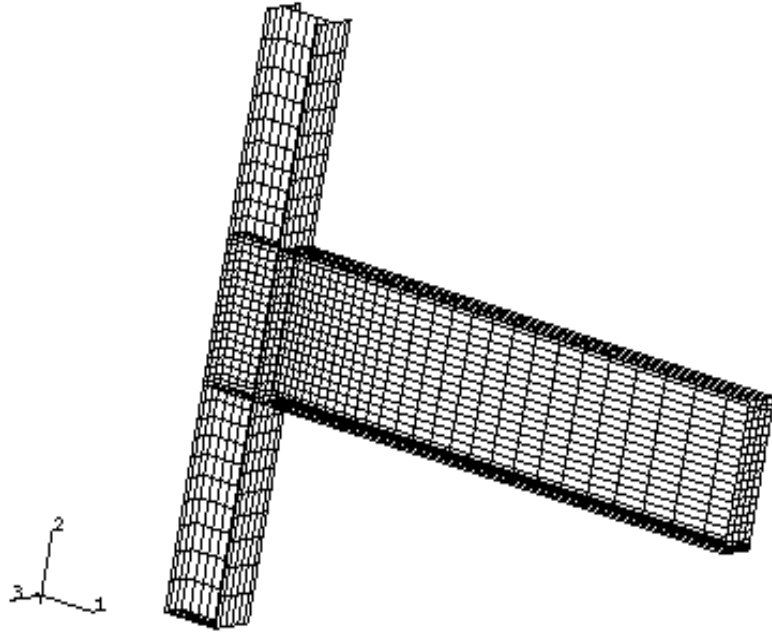


FIGURE 3.5: ALL-SHELL FINITE ELEMENT MESH

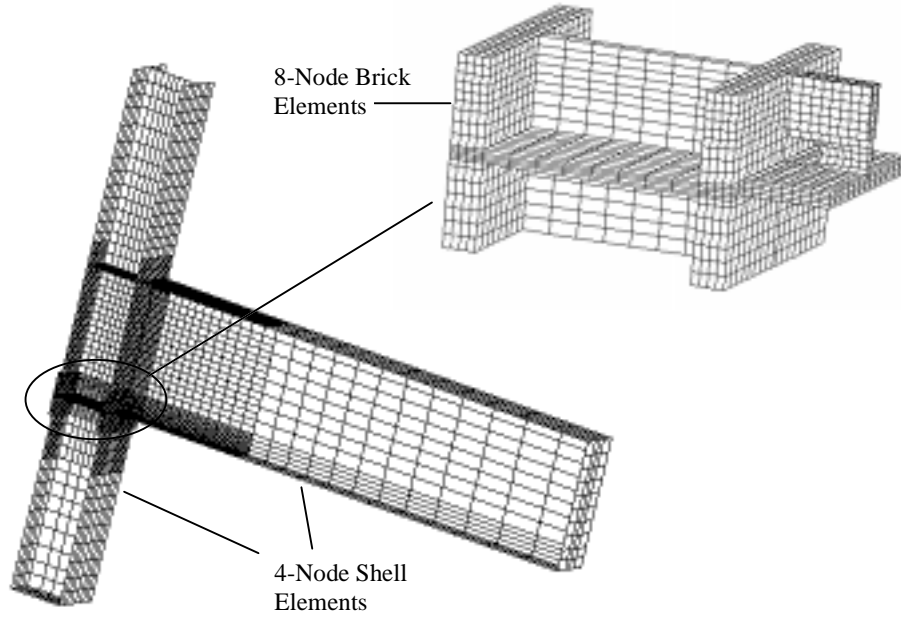


FIGURE 3.6: HYBRID SHELL/SOLID FINITE ELEMENT MESH

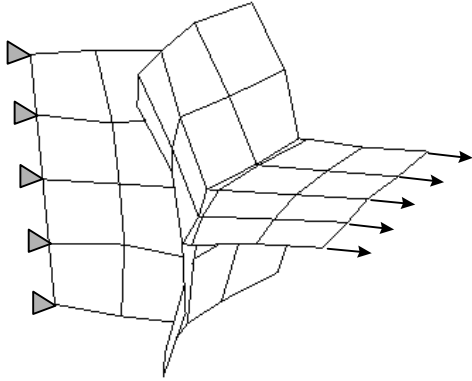


FIGURE 3.7: MESH WITH 4-S4R5 ELEMENTS

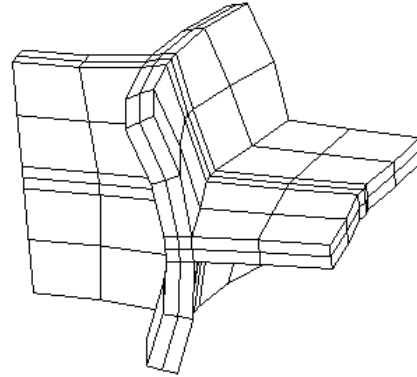


FIGURE 3.8: MESH WITH 4-C3D8R ELEMENTS

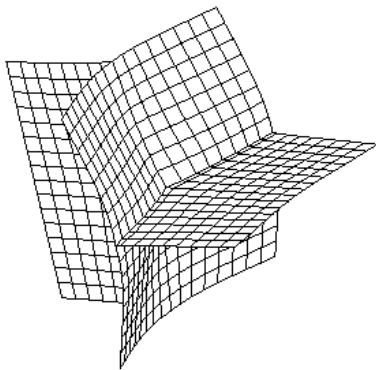


FIGURE 3.9: MESH WITH 16-S4R5 ELEMENTS

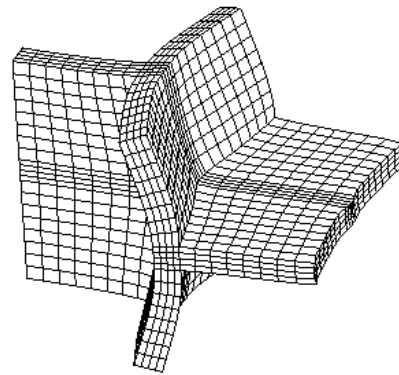
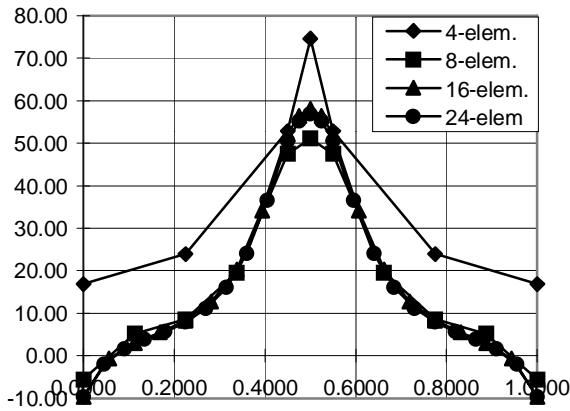
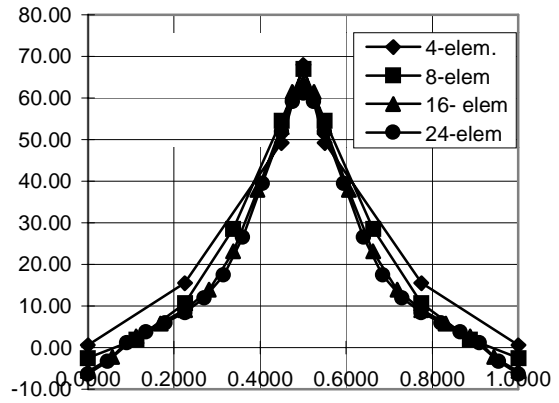


FIGURE 3.10: MESH WITH 16-C3D8R ELEMENTS

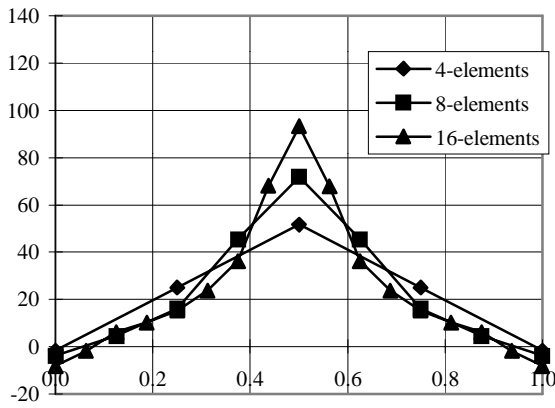


(a) Bricks with incompatible modes (C3D8I)

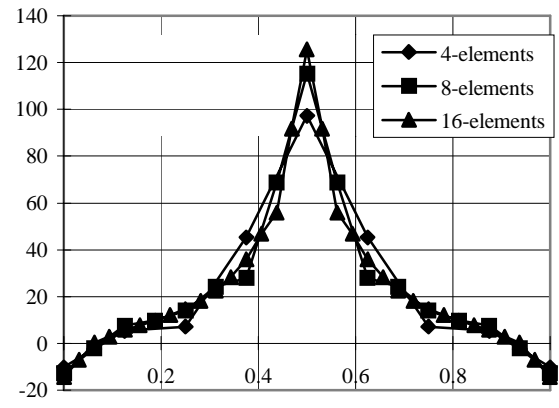


(b) Bricks with reduced integration (C3D8R)

FIGURE 3.11: STRESS DISTRIBUTION AT INTERFACE FOR BRICK ELEMENT MODELS

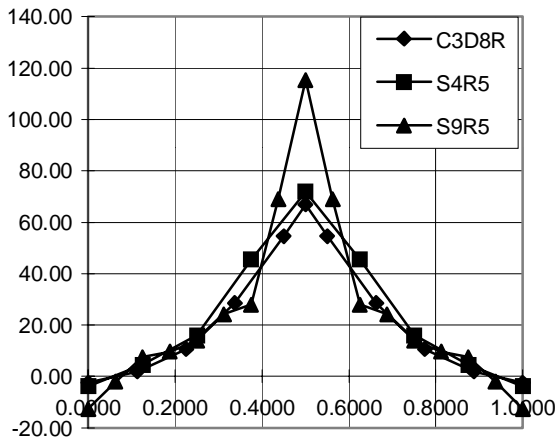


(a) Four node quadrilateral elements (S4R5)

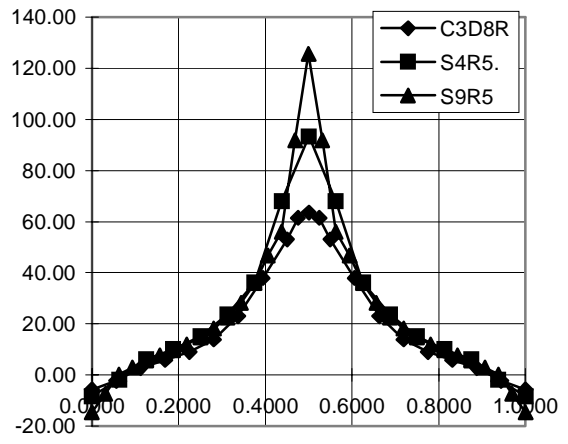


(b) Nine node quadrilateral elements (S9R5)

FIGURE 3.12: STRESS DISTRIBUTION AT INTERFACE FOR SHELL ELEMENT MODELS

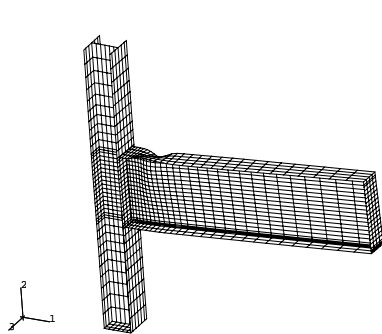


(a) Eight elements along flange

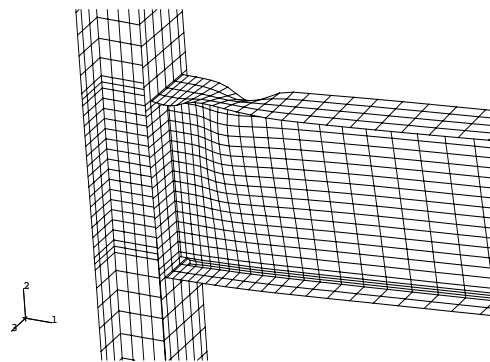


(b) Sixteen elements along flange

FIGURE 3.13: COMPARISON BETWEEN DIFFERENT TYPES OF ELEMENTS



(a) Full View



(b) Zoom view

FIGURE 3.14: DEFORMED MESH S4-6. NOTE THE BUCKLED COMPRESSION FLANGE.

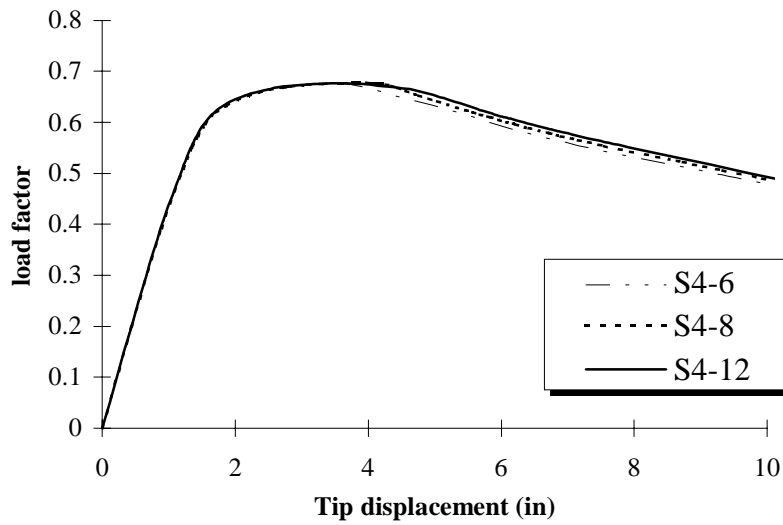


FIGURE 3.15: INELASTIC CONVERGENCE STUDY OF SHELL MODELS

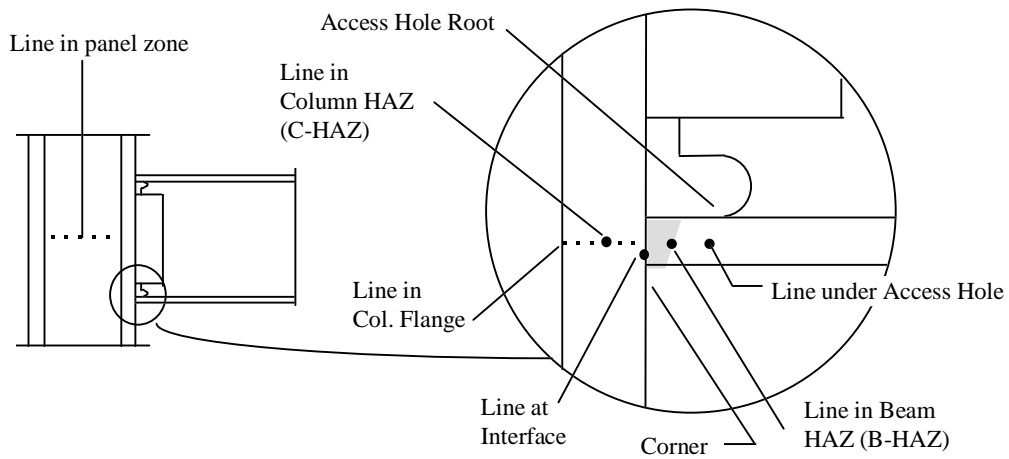


FIGURE 3.16: SOME LOCATIONS AT WHICH STRESSES AND STRAINS ARE EXTRACTED

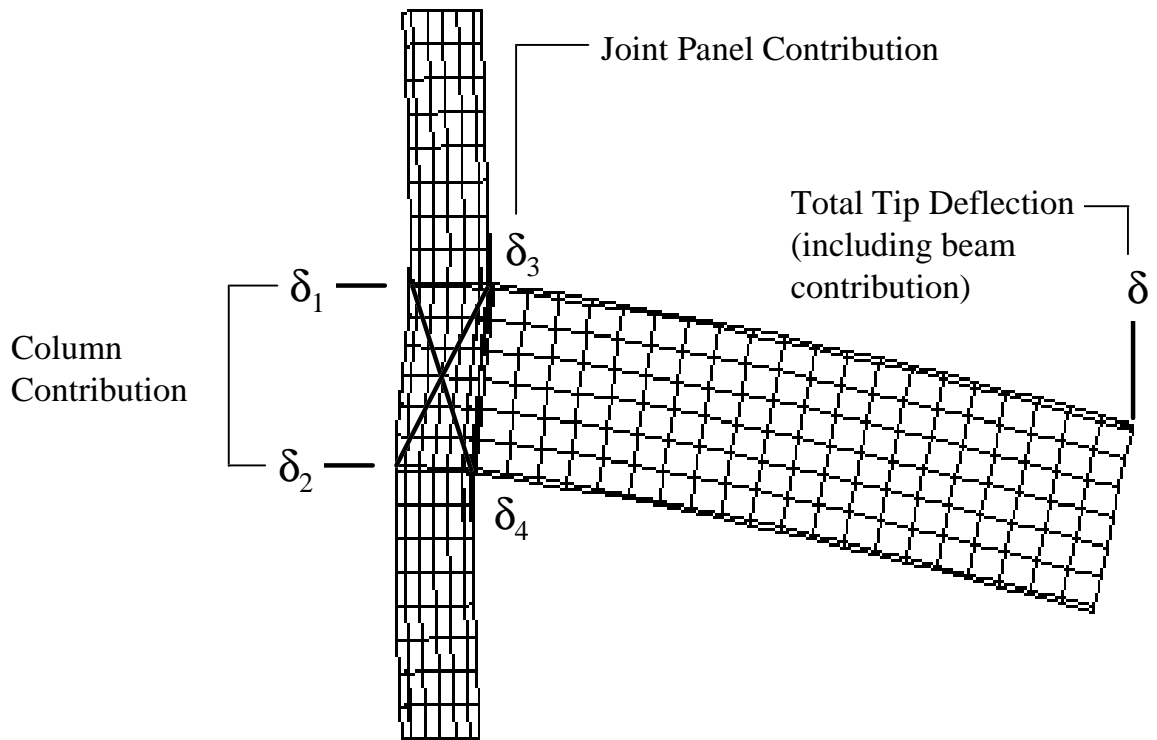
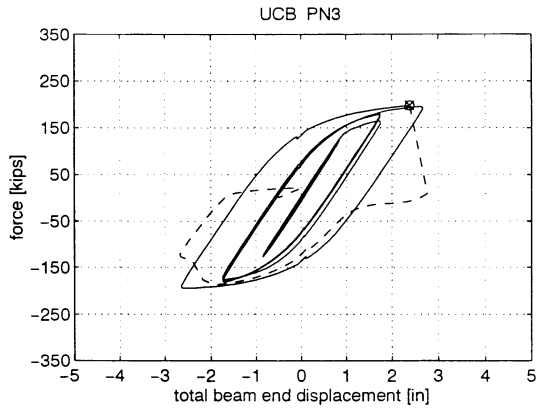
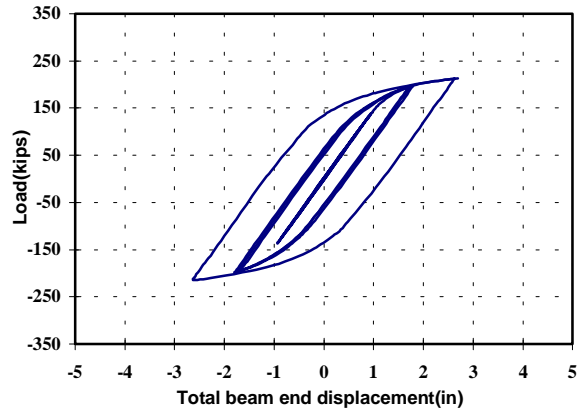


FIGURE 3.17: GLOBAL MEASURES OF DEFORMATION

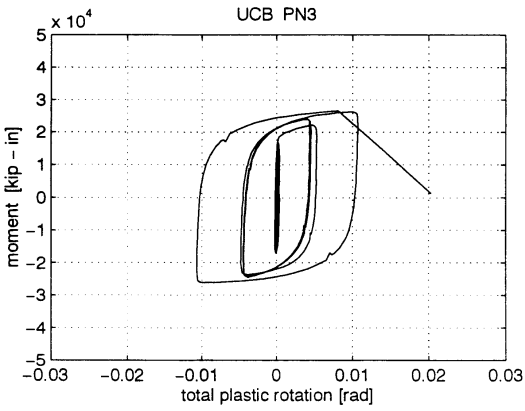


(a) Measured response

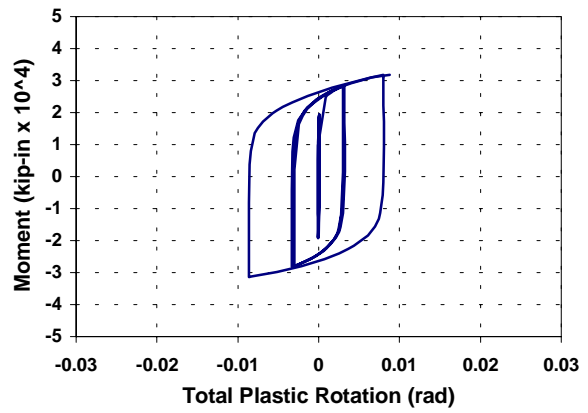


(b) Computed Response

FIGURE 4.1: COMPARISON BETWEEN MEASURED AND COMPUTED FORCE VS. TIP DISPLACEMENT RESPONSE

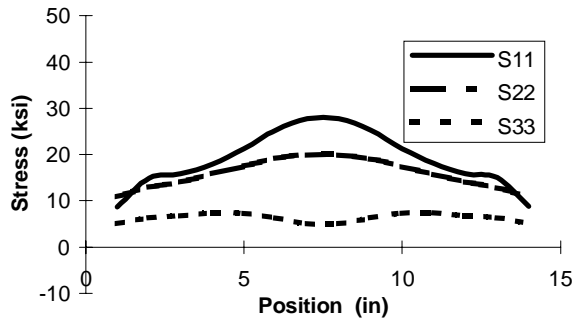


(a) Measured response

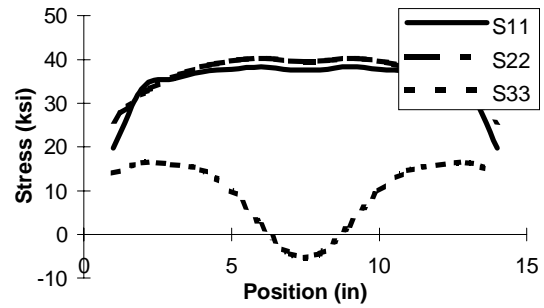


(b) Computed Response

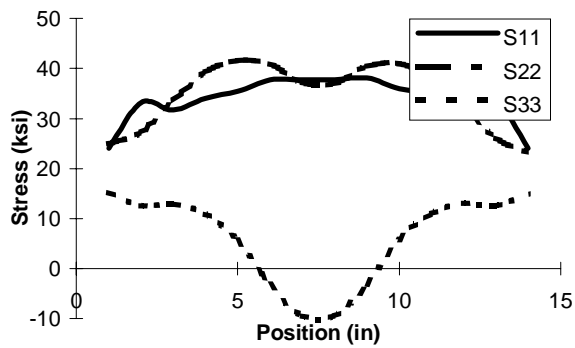
FIGURE 4.2: COMPARISON BETWEEN MEASURED AND COMPUTED MOMENT VS. TOTAL PLASTIC ROTATION RESPONSE



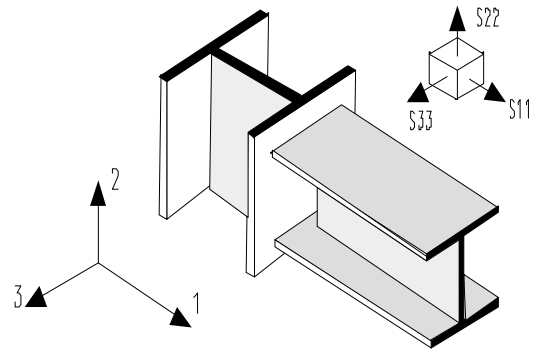
a - Elastic behavior, BPR = 0.0



b - BPR = 0.0005



c - BPR = 0.011



d - Stress Directions

FIGURE 4.3: DISTRIBUTION OF STRESSES ALONG INTERFACE LINE

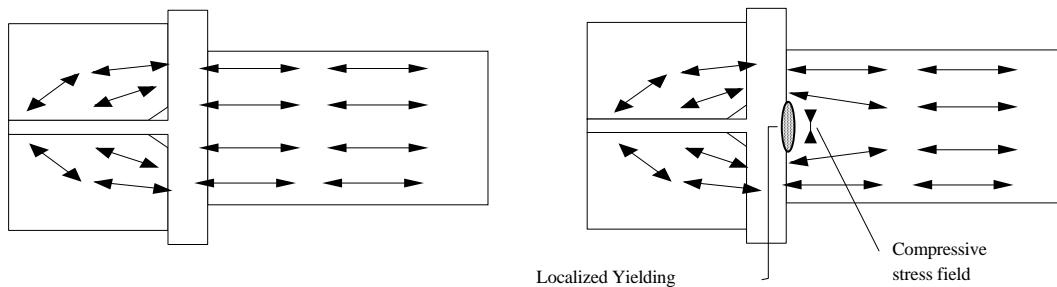


FIGURE 4.4: DEVIATION OF STRESS FIELD AT ONSET OF INELASTICITY

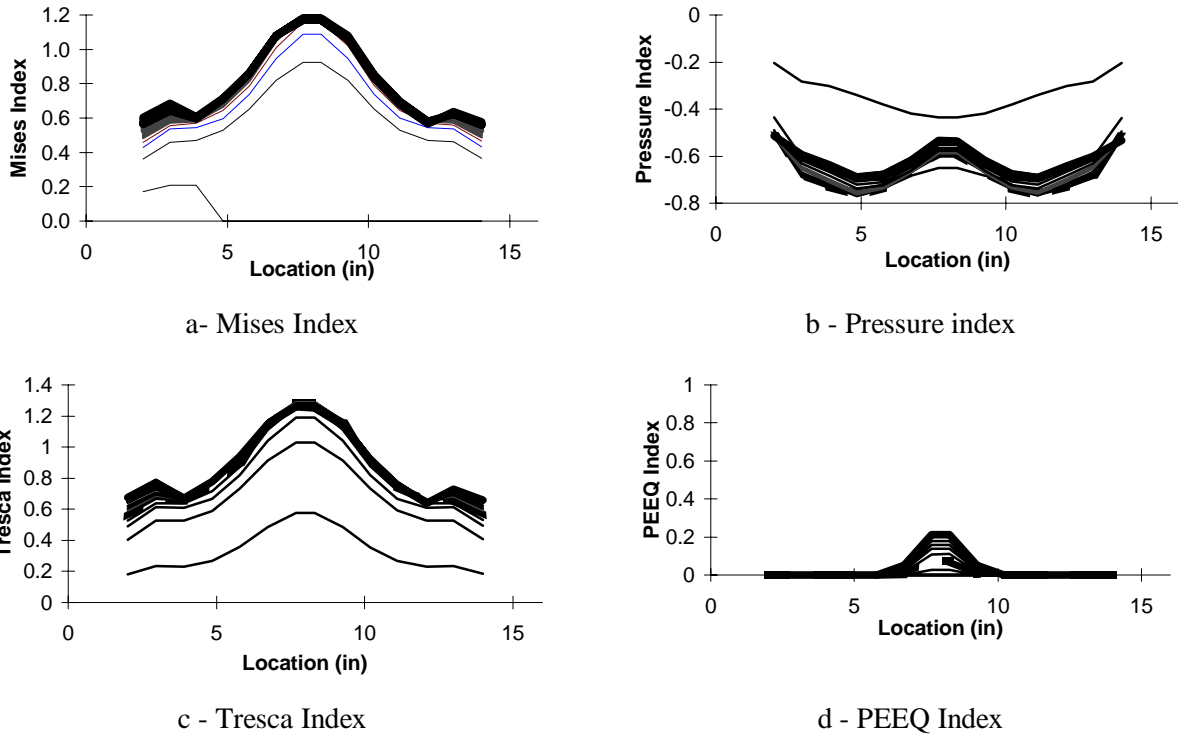


FIGURE 4.5: DISTRIBUTION OF INDICES ALONG INTERFACE LINE AT FAILURE BPR (BPR=0.011)

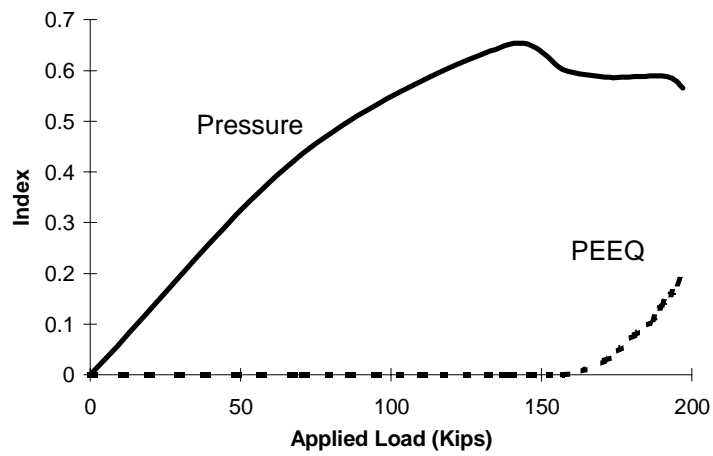


FIGURE 4.6: CHANGE IN PRESSURE AND PEEQ INDICES AT BEAM FLANGE CENTER ON INTERFACE LINE

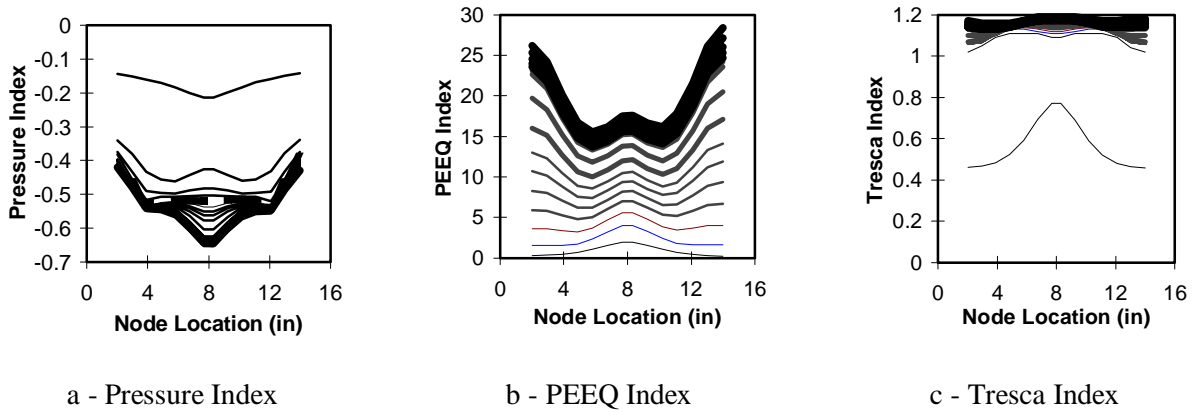


FIGURE 4.7: DISTRIBUTION OF INDICES ALONG BEAM HAZ LINE

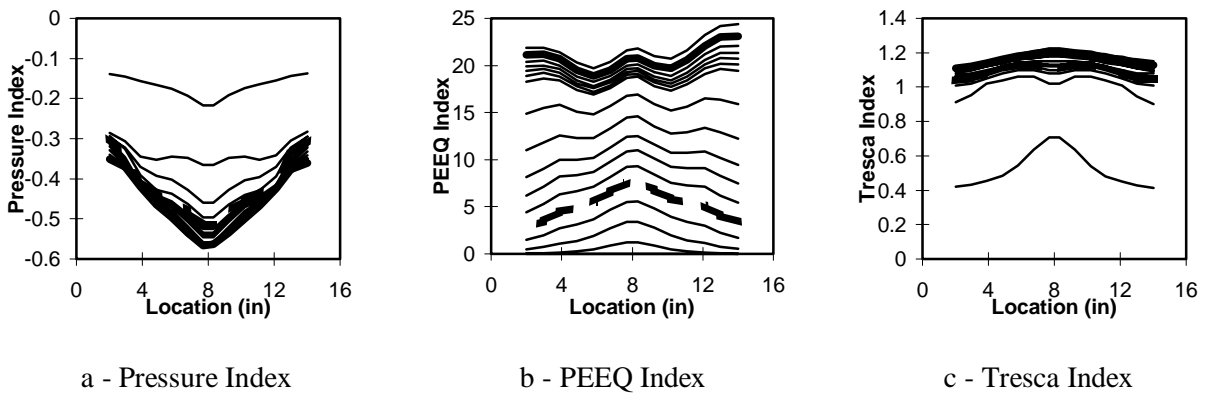


FIGURE 4.8: DISTRIBUTION OF INDICES ALONG ACCESS HOLE LINE

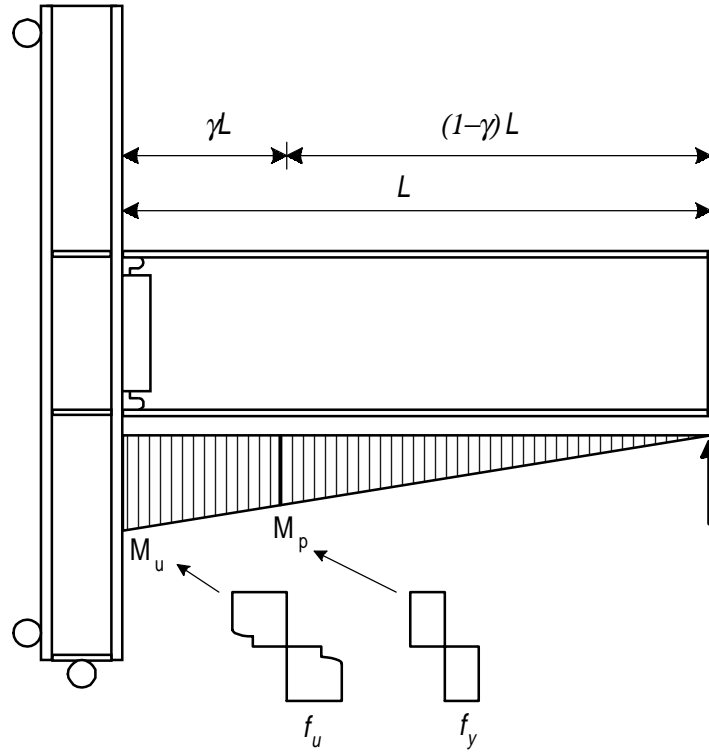


FIGURE 5.1: EFFECT OF YIELD-TO-ULTIMATE STRESS RATIO ON PLASTIC HINGE LENGTH

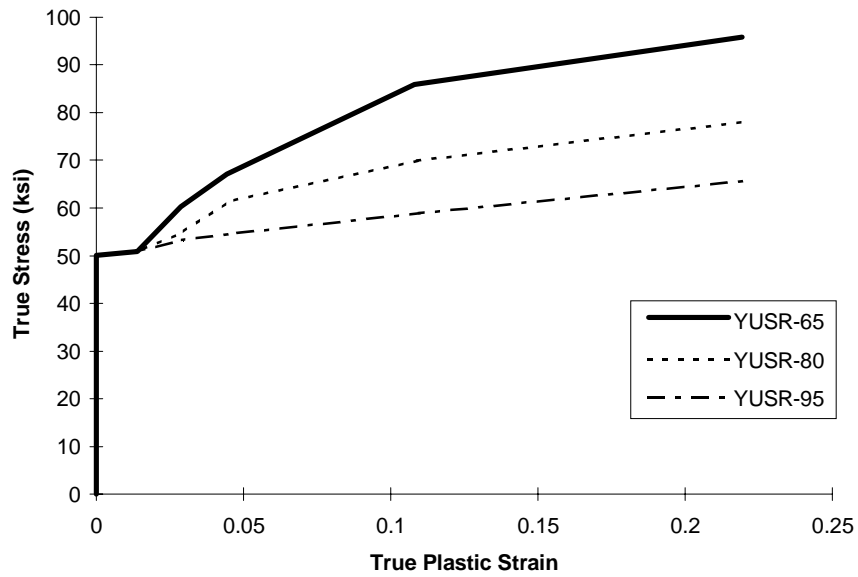


FIGURE 5.2: ASSUMED STRESS-STRAIN CURVES WITH DIFFERENT YUSR RATIOS.

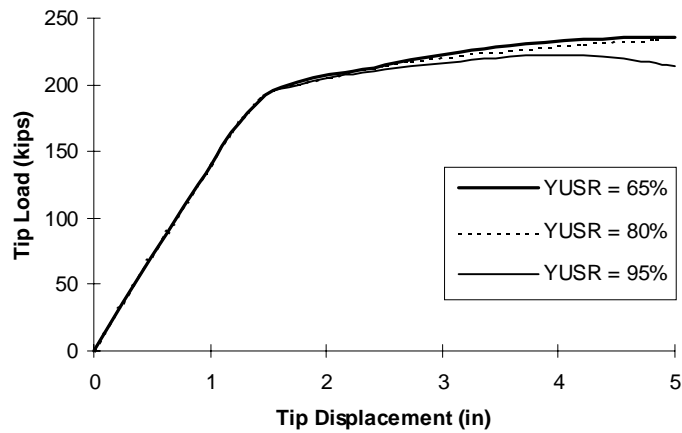
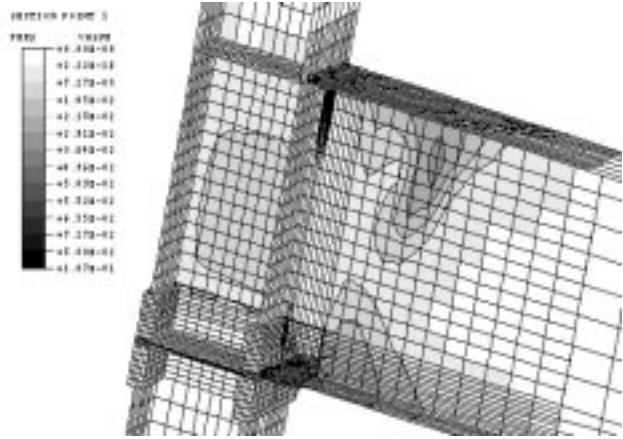
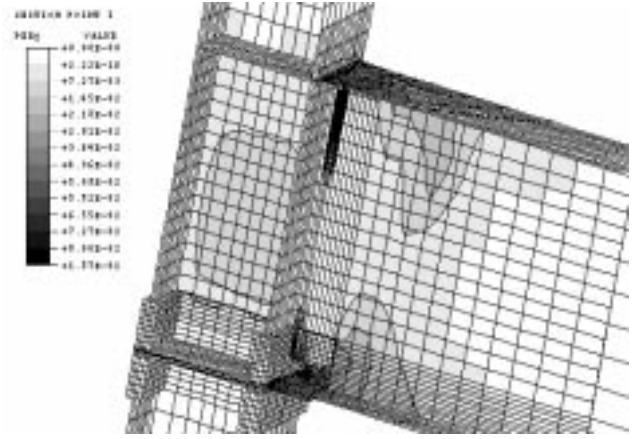


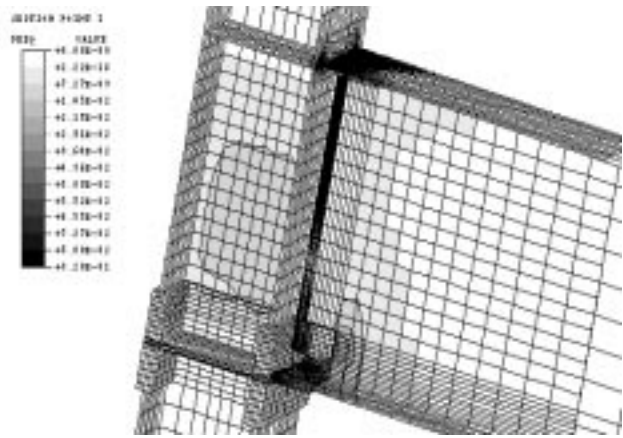
FIGURE 5.3: EFFECT OF YIELD-TO-ULTIMATE STRESS RATIO ON LOAD VS. TIP DEFLECTION BEHAVIOR



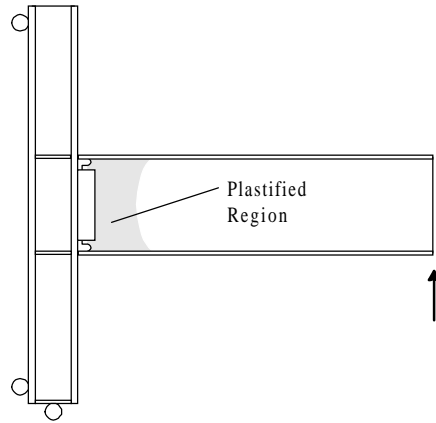
a - YUSR-65



b- YUSR-80



c - YUSR-95



d - Location of plastic hinge

FIGURE 5.4: CONTOUR PLOTS OF THE PLASTIC EQUIVALENT STRAIN (PEEQ) FOR YUSR-65, YUSR-85, AND YUSR-95. RESULTS PLOTTED AT CPR=0.03.

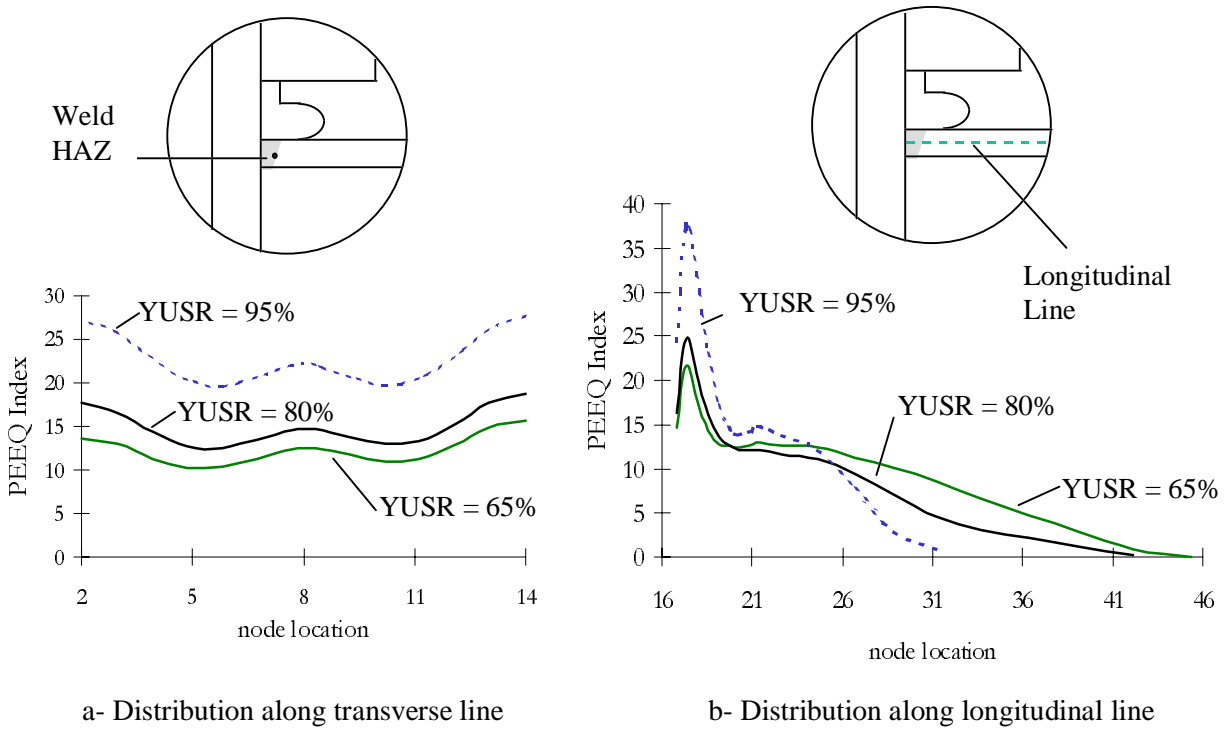


FIGURE 5.5: DISTRIBUTION OF PEEQ INDICES ALONG TRANSVERSE AND LONGITUDINAL LINES

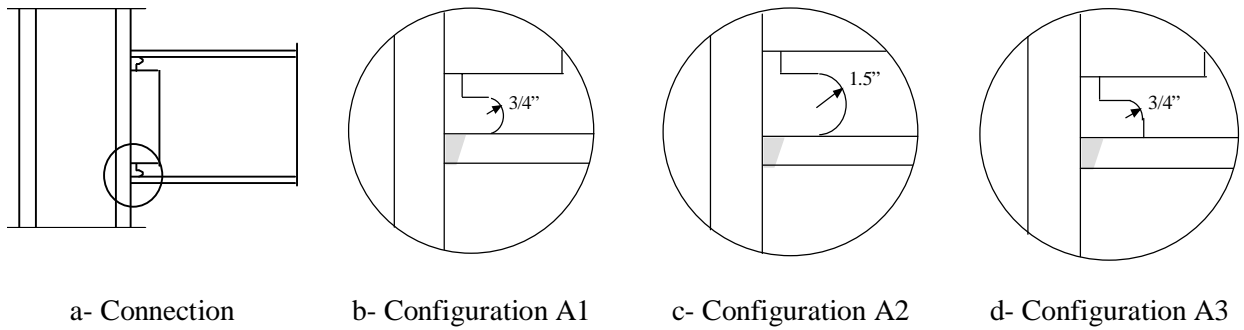


FIGURE 5.6: DETAILS OF THE ACCESS HOLE GEOMETRY

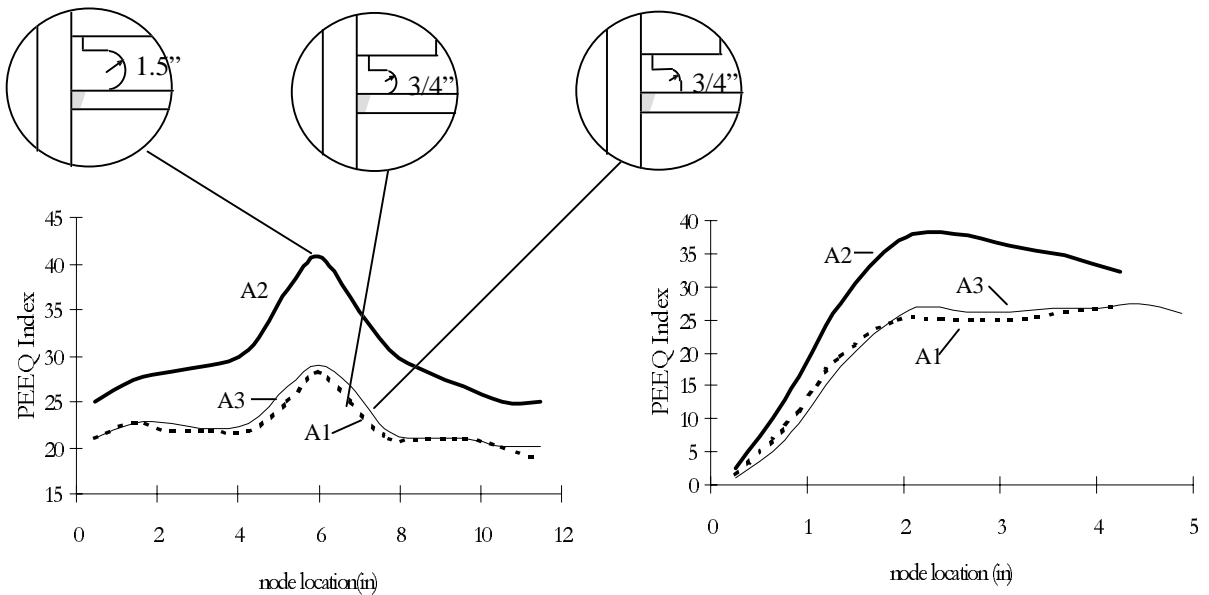


FIGURE 5.7: EFFECT OF ACCESS HOLE SIZE AND GEOMETRY ON PEEQ INDICES

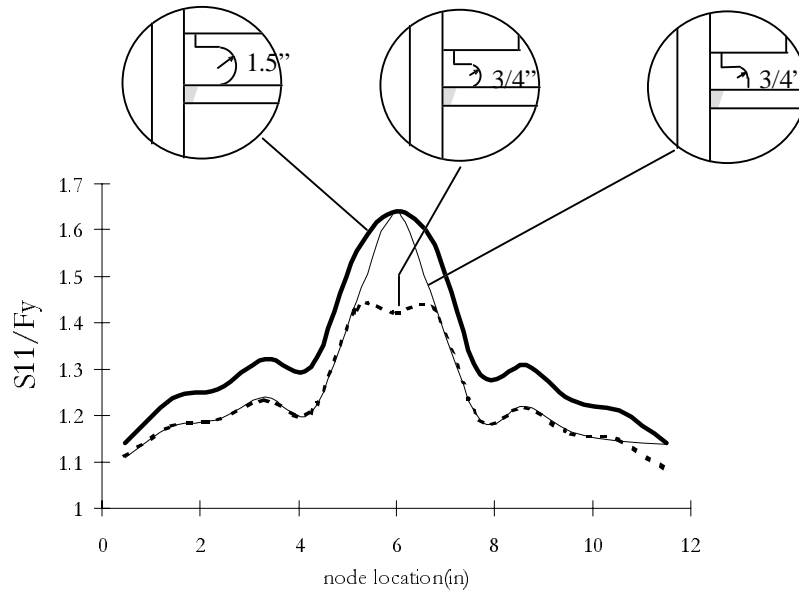
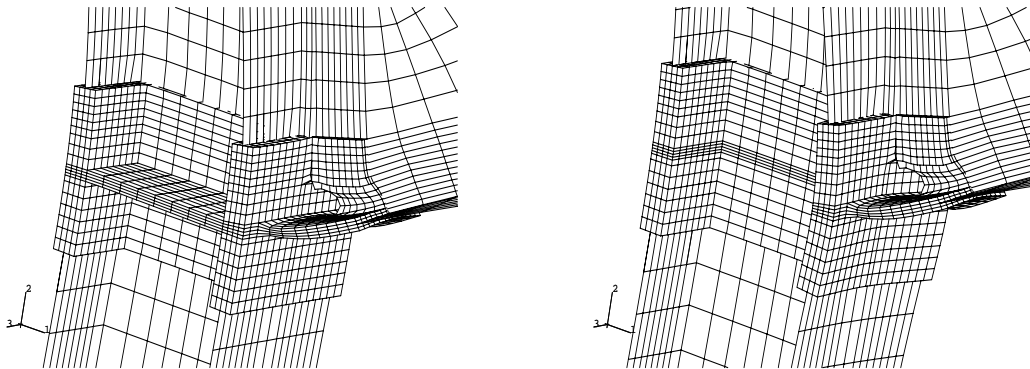


FIGURE 5.8: EFFECT OF ACCESS HOLE SIZE AND GEOMETRY ON LONGITUDINAL STRESSES. STRESSES PLOTTED ALONG TRANSVERSE LINE THROUGH ROOT OF ACCESS HOLE



(a) Specimen CONT-0.75

(b) Specimen CONT-None

FIGURE 5.9: DEFORMED SHAPES OF SPECIMEN WITH AND WITHOUT CONTINUITY PLATES

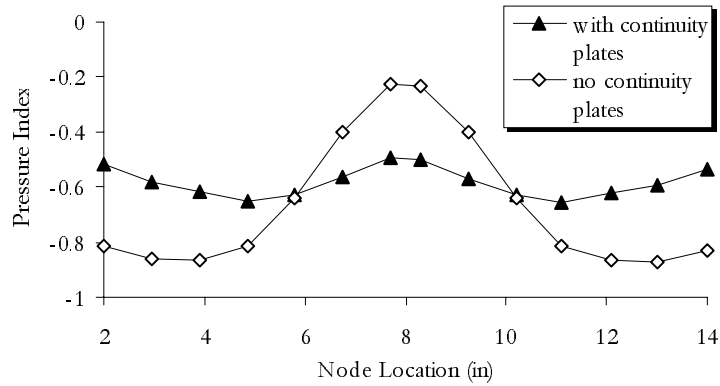
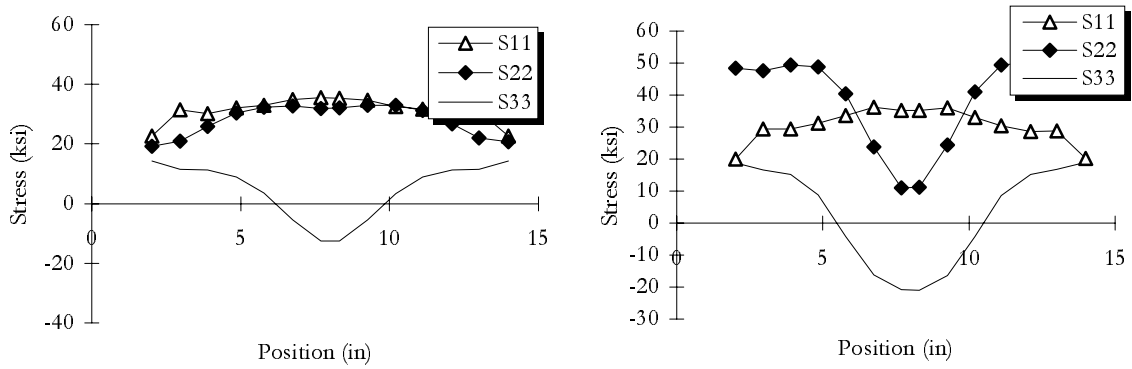


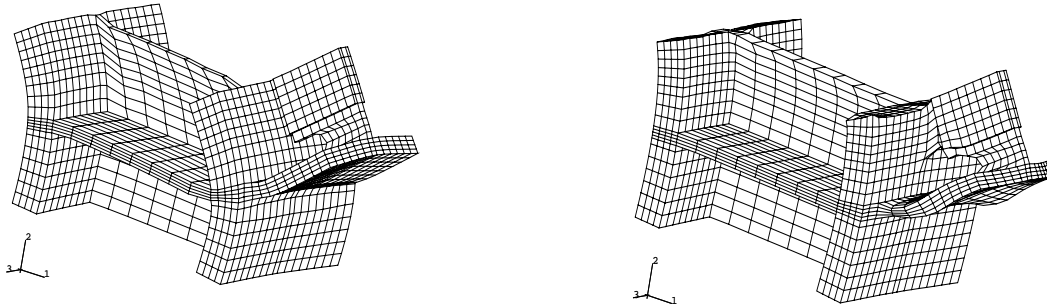
FIGURE 5.10: EFFECT OF CONTINUITY PLATES ON PRESSURE INDEX AT INTERFACE LINE, CPR=0.03



(a) With Continuity Plates, BPR = 0.022

(b) Without Continuity Plates, BPR = 0.022

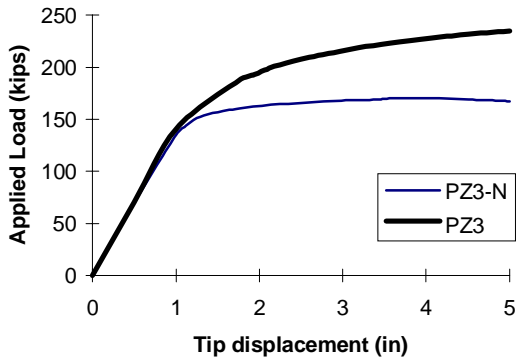
FIGURE 5.11: DISTRIBUTION OF STRESSES ALONG INTERFACE LINE



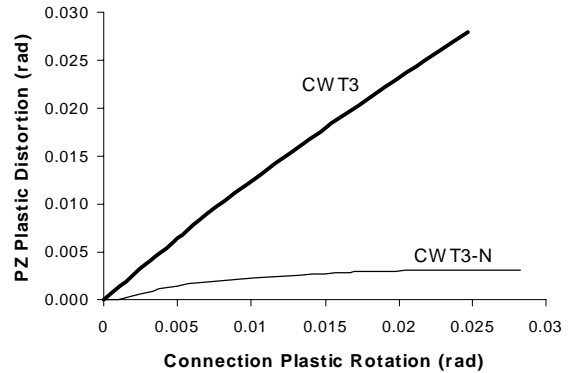
a - Deformed shape of CWT1 at CPR = 0.03

b - Deformed shape of CWT4 at CPR = 0.03

FIGURE 5.12: DEFORMED SHAPES OF SPECIMEN AT DIFFERENT LEVELS OF CPR. DISPLACEMENTS ARE MAGNIFIED 20 TIMES.

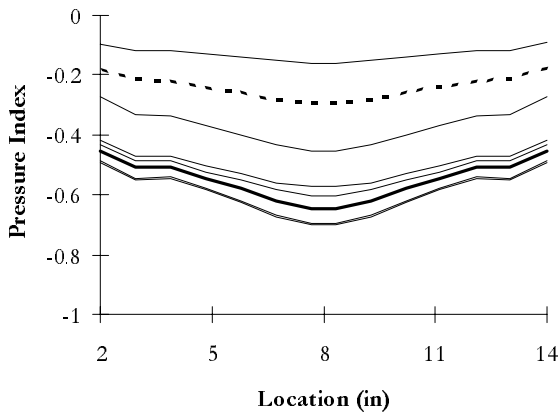


a - Load - deflection curve

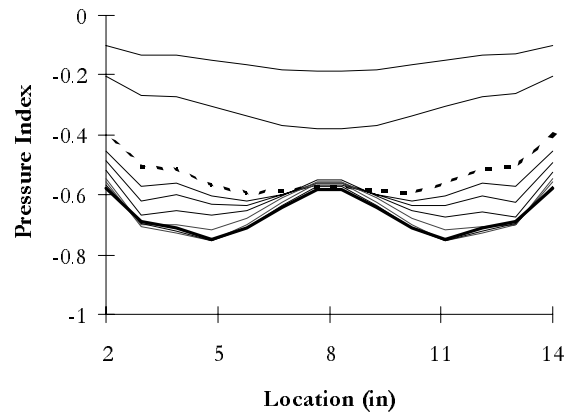


b - CPR vs. CWTPR

FIGURE 5.13: DEFORMATION CHARACTERISTICS OF CWT3 AND CWT3-N

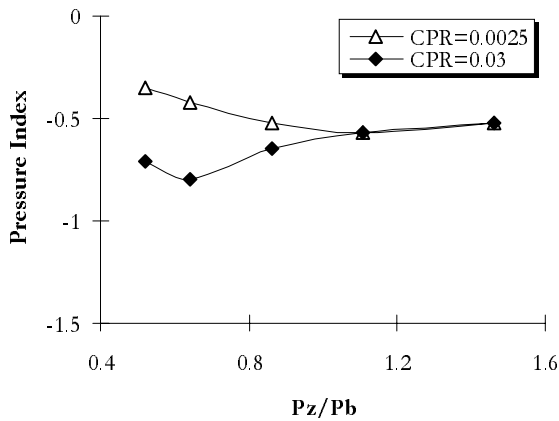


a – Connection CWT1

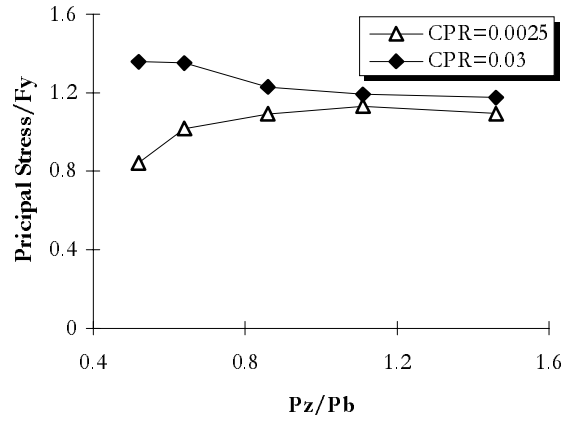


b - Connection CWT4

FIGURE 5.14: DISTRIBUTION OF HYDROSTATIC STRESSES ALONG INTERFACE LINE

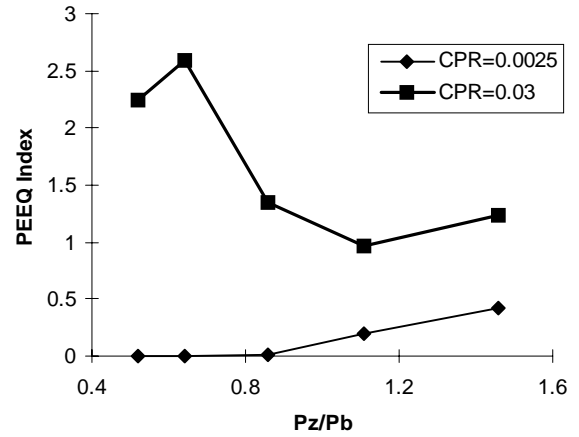
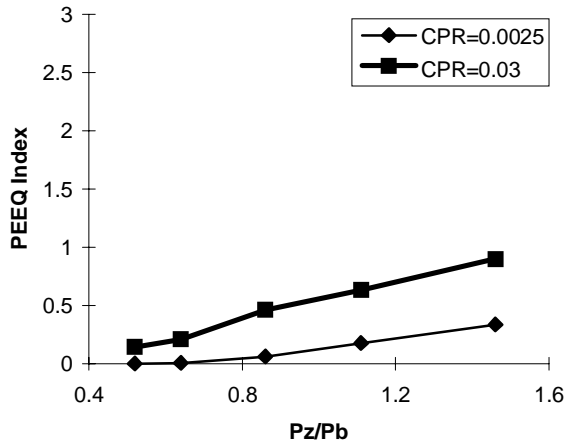


a - Pressure index at middle of interface line



b - Principal stress index at middle of interface

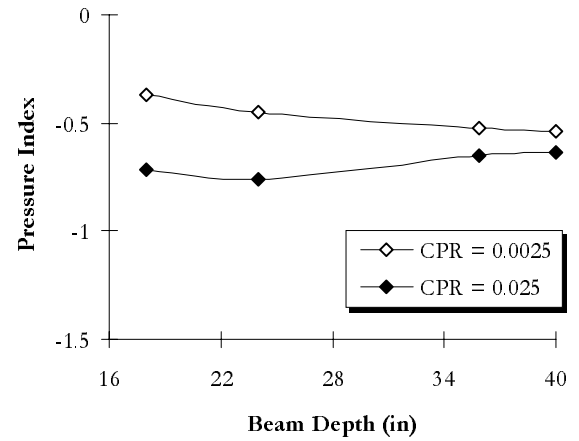
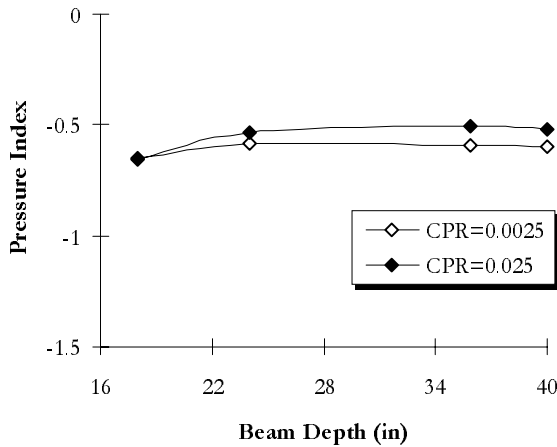
FIGURE 5.15: EFFECT OF PANEL ZONE TO BEAM STRENGTH RATIO ON PRESSURE INDEX AND PRINCIPAL STRESS AT MIDDLE OF INTERFACE LINE



a – PEEQ index at middle of interface line

b - PEEQ index at middle of column HAZ line

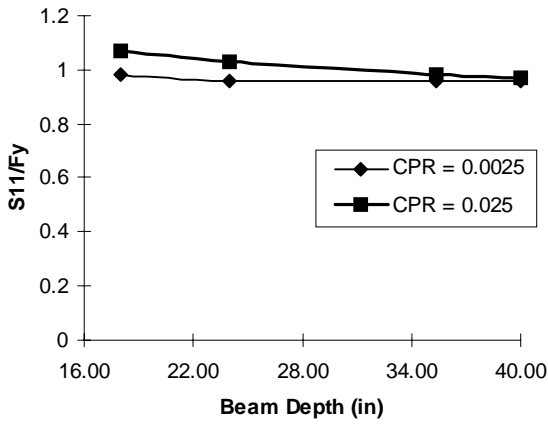
FIGURE 5.16: EFFECT OF PANEL ZONE TO BEAM STRENGTH RATIO ON PEEQ INDEX AT MIDDLE OF INTERFACE AND COLUMN HAZ LINE



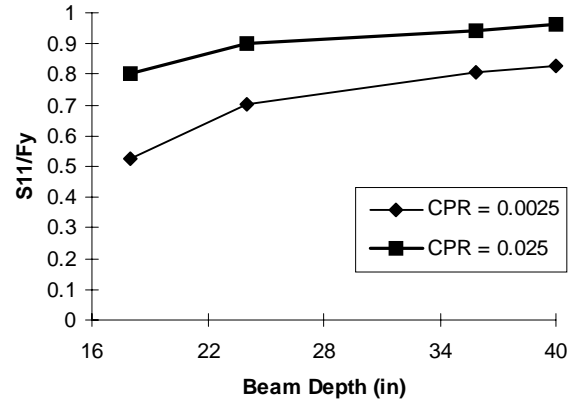
a - Series BDN (strong panel zone)

b - Series BD (weak panel zone)

FIGURE 5.17: EFFECT OF BEAM DEPTH ON PRESSURE INDEX AT MIDDLE OF INTERFACE LINE



a – Series BDN (strong panel zone)



b - Series BD (weak panel zone)

FIGURE 5.18: EFFECT OF BEAM DEPTH ON LONGITUDINAL BEAM STRESS AT MIDDLE OF INTERFACE LINE

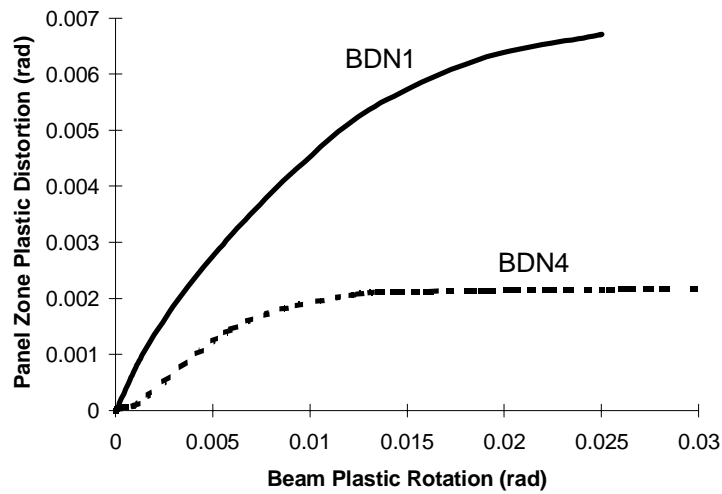
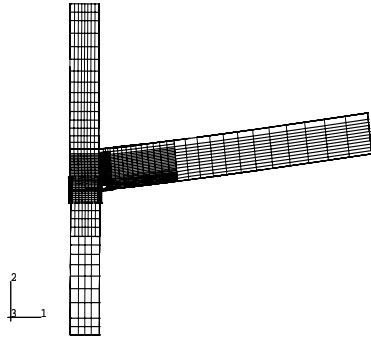
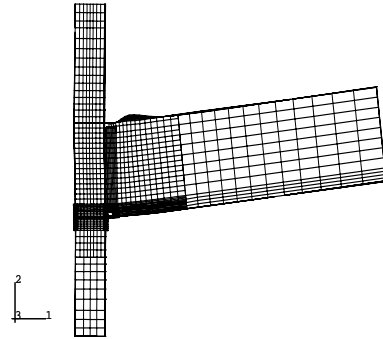


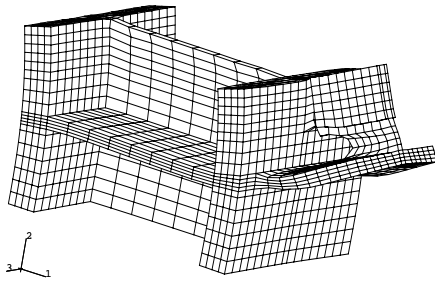
FIGURE 5.19: PANEL ZONE PLASTIC ROTATION VERSUS BEAM PLASTIC ROTATION FOR SPECIMEN BDN1 (DEPTH = 18 IN) AND BDN4 (DEPTH = 40 IN)



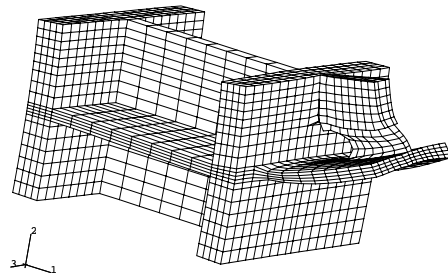
a - BDN1 (full view)



b - BDN4 (full view)

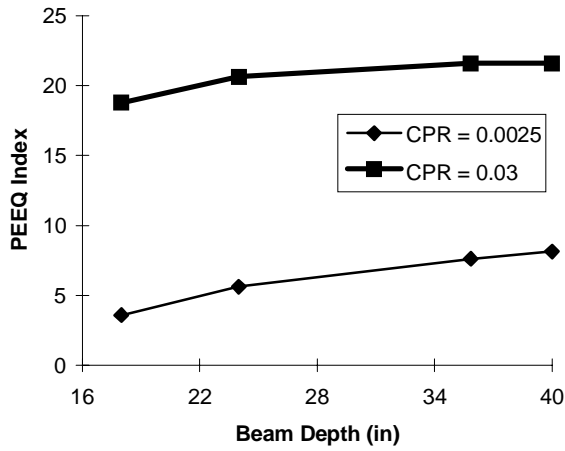


c - BDN1 (deformed shape of solid region)

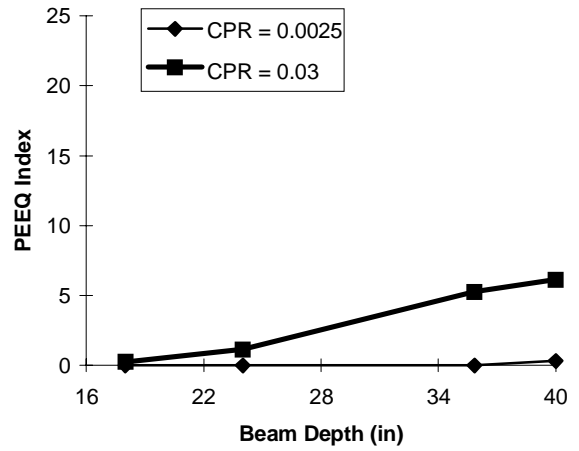


d - BDN4 (deformed shape of solid region)

FIGURE 5.20: DEFORMED SHAPES OF SPECIMEN BDN1 AND BDN4 AT DIFFERENT LEVELS OF CPR. DISPLACEMENTS ARE MAGNIFIED 20 TIMES IN THE LOWER FIGURES.

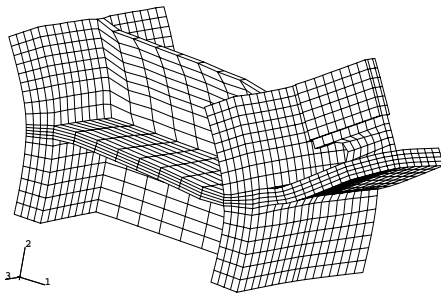


a - Series BDN (strong panel zone)

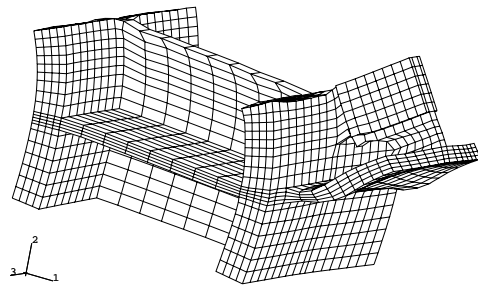


b - Series BD (weak panel zone)

FIGURE 5.21: EFFECT OF BEAM DEPTH ON PEEQ INDEX AT MIDDLE OF ACCESS HOLE LINE

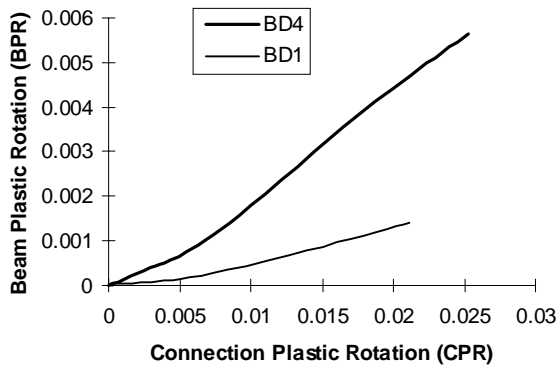


c - BD1 (deformed shape of solid region)

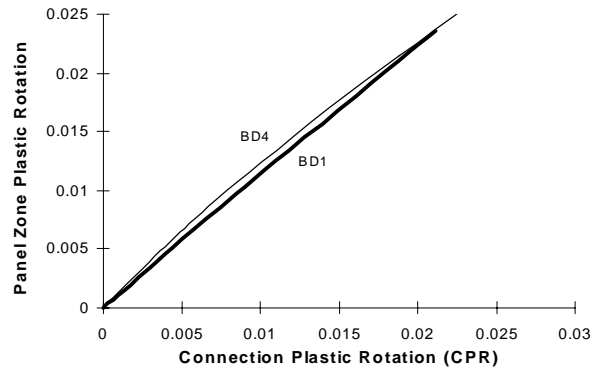


d - BD4 (deformed shape of solid region)

FIGURE 5.22: DEFORMED SHAPES OF SPECIMEN BD1 AND BD4 AT CPR=0.025. THE DISPLACEMENTS ARE MAGNIFIED 20 TIMES IN THE LOWER FIGURES.



a - BPR



b - CWTPR

FIGURE 5.23: DEFORMATION CHARACTERISTICS OF CONFIGURATIONS BD1 (BEAM DEPTH 18 IN) AND BD4 (BEAM DEPTH = 40 IN)

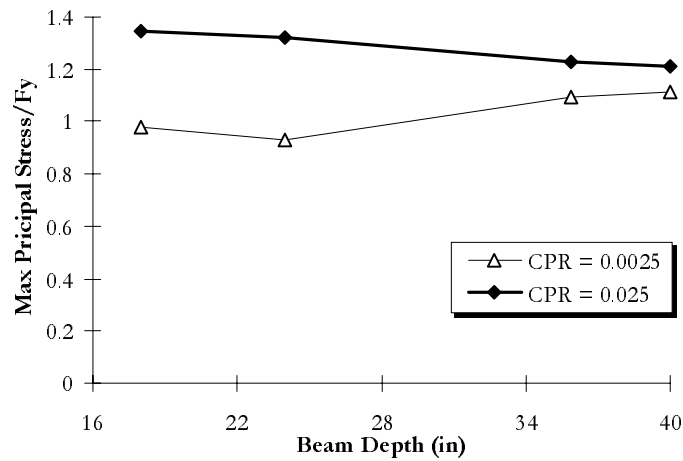
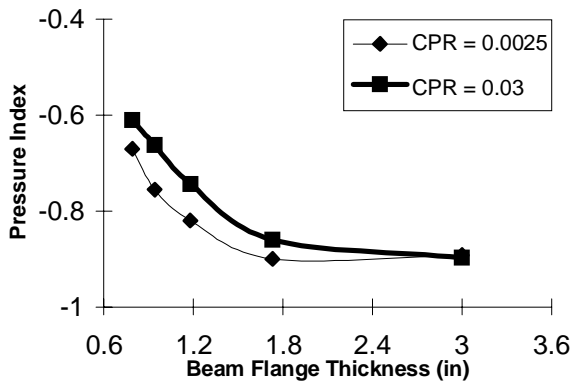
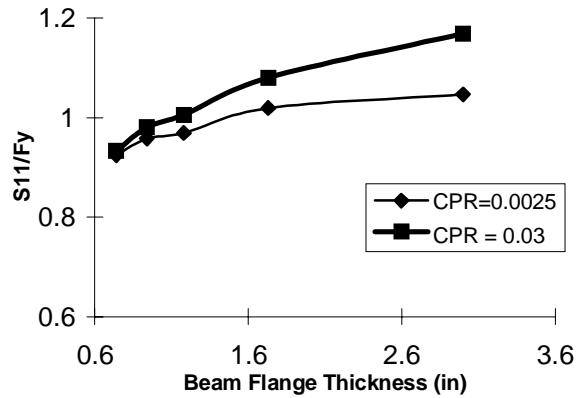


FIGURE 5.24: EFFECT OF BEAM DEPTH ON PRINCIPAL STRESS AT MIDDLE OF INTERFACE LINE

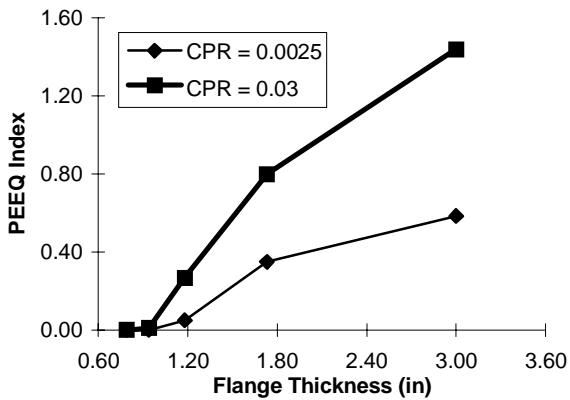


a - Maximum pressure index

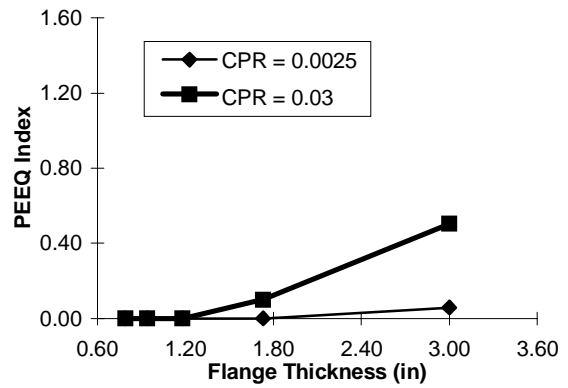


b- Longitudinal stress at center

FIGURE 5.25: EFFECT OF FLANGE THICKNESS ON PRESSURE INDEX, LONGITUDINAL STRESS AT INTERFACE LINE

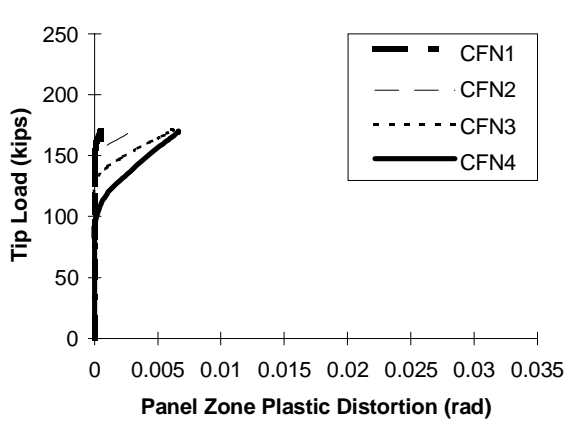


a - PEEQ at Center of Interface Line

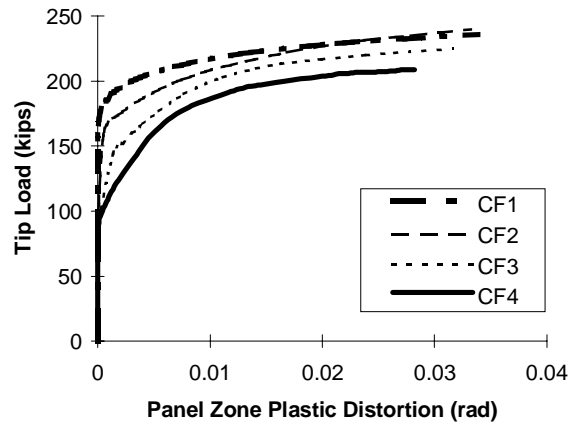


b - PEEQ at Center of C-HAZ line

FIGURE 5.26: EFFECT OF BEAM FLANGE THICKNESS ON STRAINS

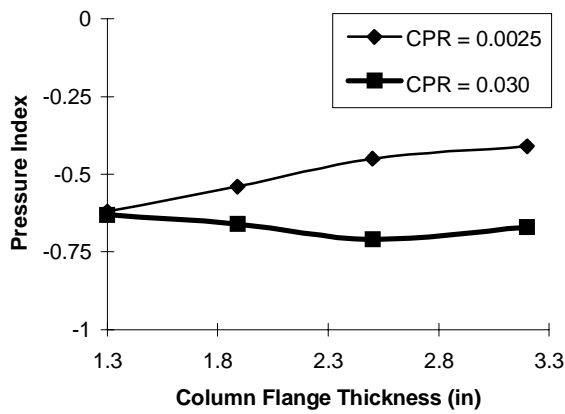


a- Strong Panel Zone (Series CFN)

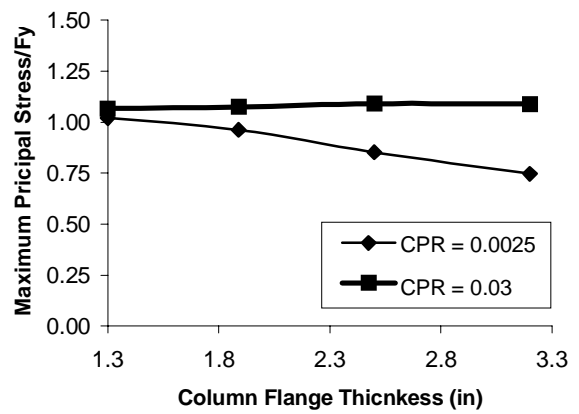


b- Weak Panel Zone (Series CF)

FIGURE 5.27: LOAD VS. PANEL ZONE PLASTIC DISTORTION

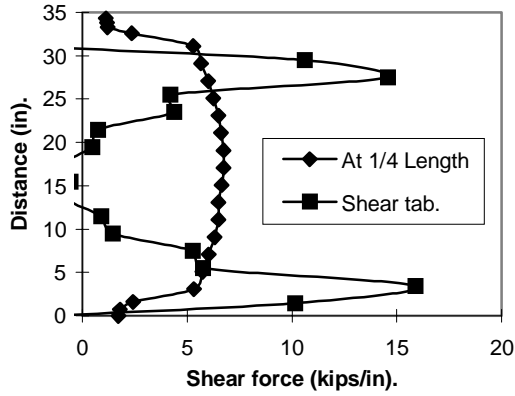


a- Hydrostatic Stresses

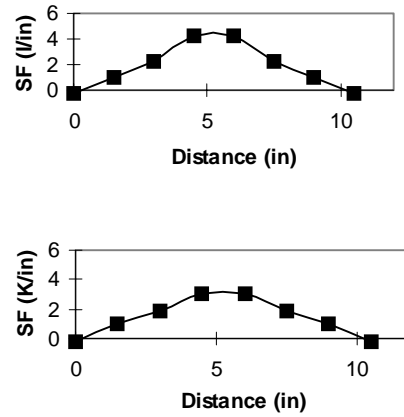


b- Principal Stresses

FIGURE 5.28: HYDROSTATIC AND PRINCIPAL STRESSES IN SERIES CF (WEAK PANEL ZONE)

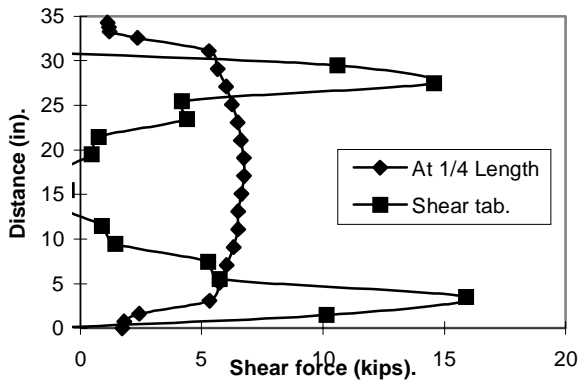


(a) Shear distribution in shear tab at column flange interface

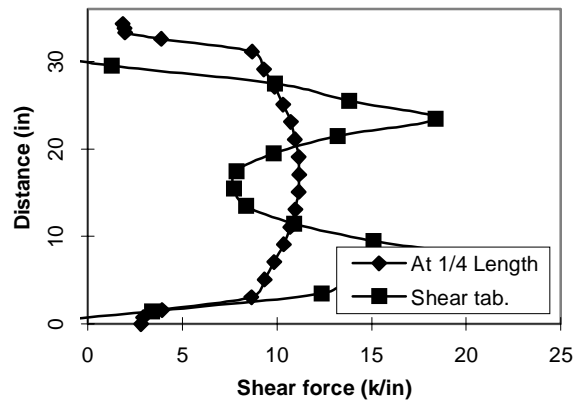


(b) shear distribution in top and bottom flanges at column flange interface

FIGURE 5.29: DISTRIBUTION OF SHEAR AT COLUMN INTERFACE (AT 43% OF NOMINAL DESIGN LOAD - ELASTIC BEHAVIOR)



a) 75% of nominal design capacity



b) 123 % of nominal design capacity

FIGURE 5.30: DISTRIBUTION OF SHEAR FORCE IN SHEAR TAB AS A FUNCTION OF APPLIED LOAD

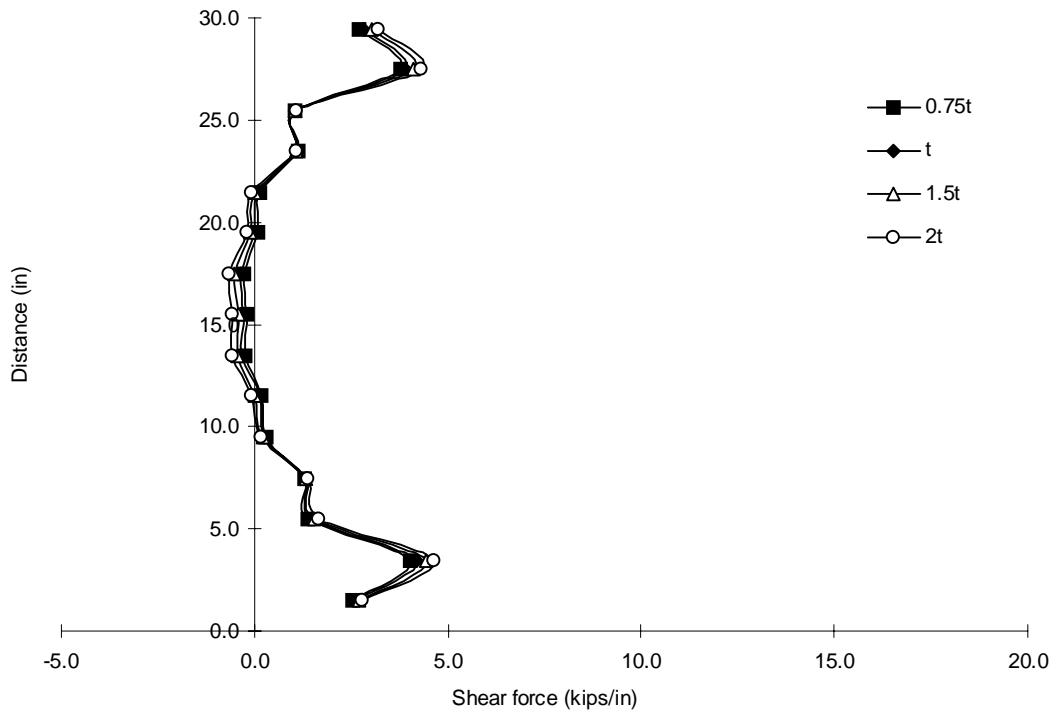
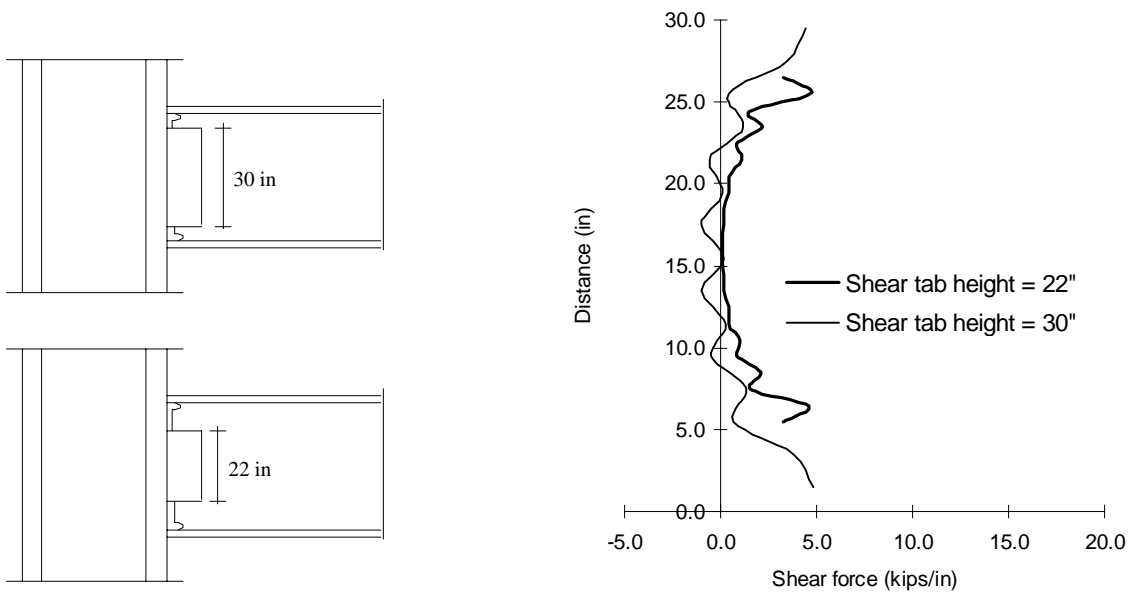
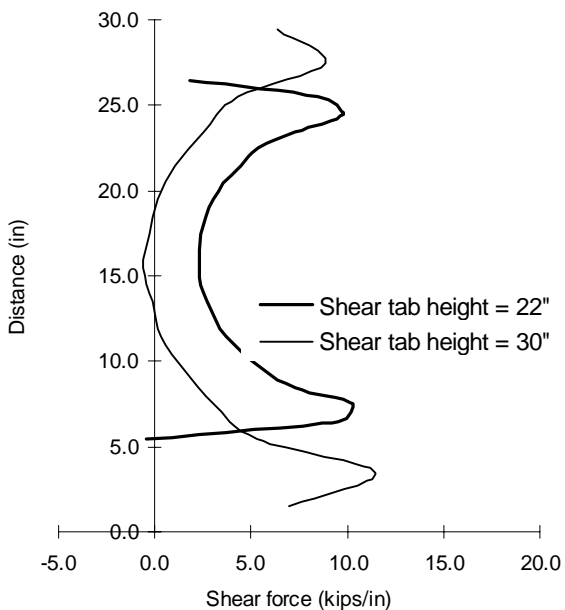


FIGURE 5.31: EFFECT OF SHEAR TAB THICKNESS ON DISTRIBUTION OF SHEAR FORCES PER UNIT LENGTH ALONG THE SHEAR TAB (ELASTIC BEHAVIOR)

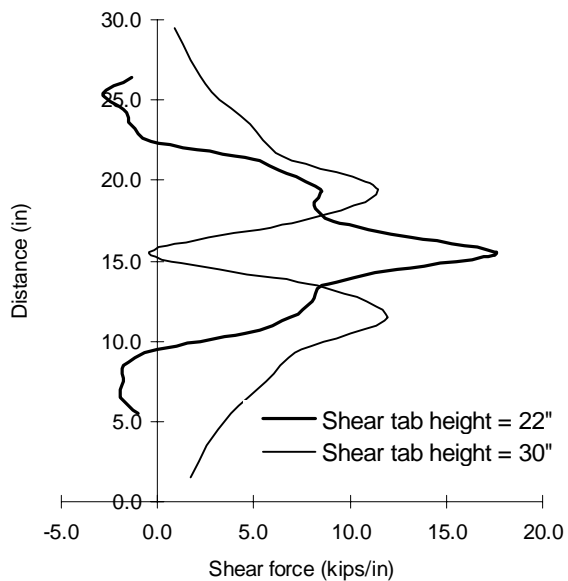


a- Shear tab heights

b- Elastic Behavior



c - Nominal Design Load



d - BPR = 0.03

FIGURE 5.32: EFFECT OF SHEAR TAB HEIGHT ON DISTRIBUTION OF SHEAR FORCE ALONG SHEAR TAB

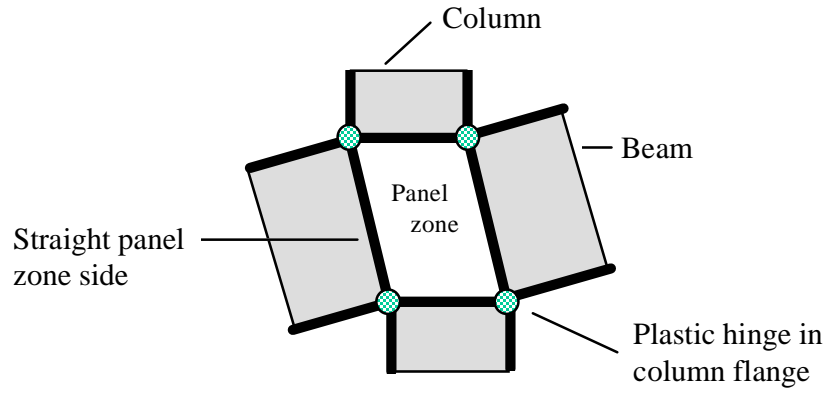


FIGURE 6.1: ASSUMED DEFORMED SHAPE OF WEAK PANEL ZONE

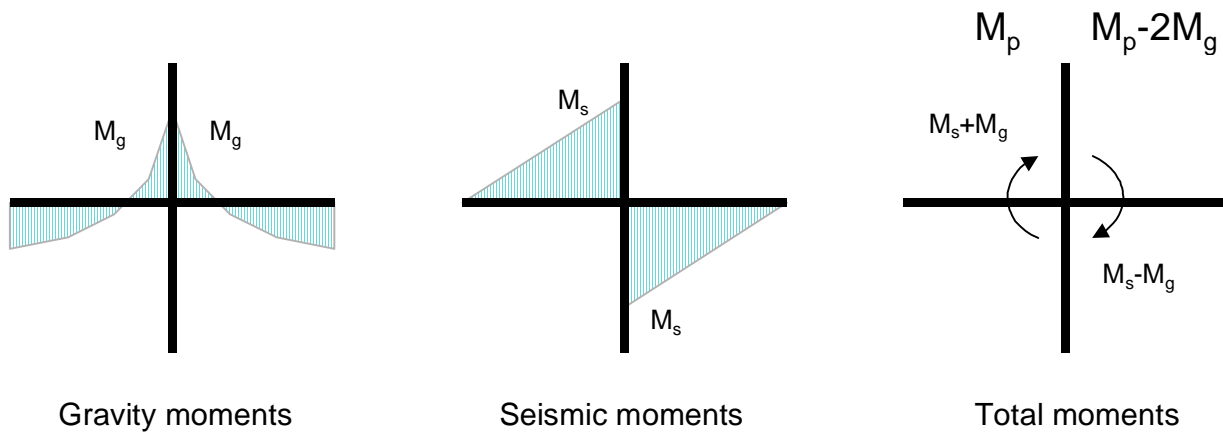


FIGURE 6.2: GRAVITY AND SEISMIC MOMENTS ON INTERIOR CONNECTIONS

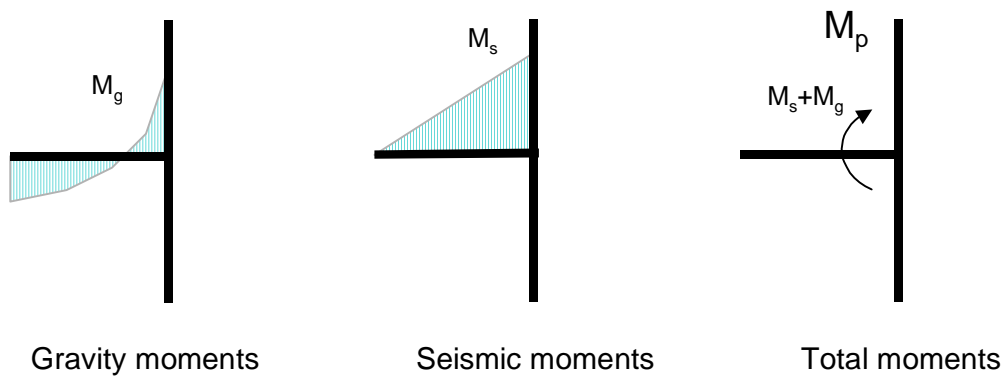
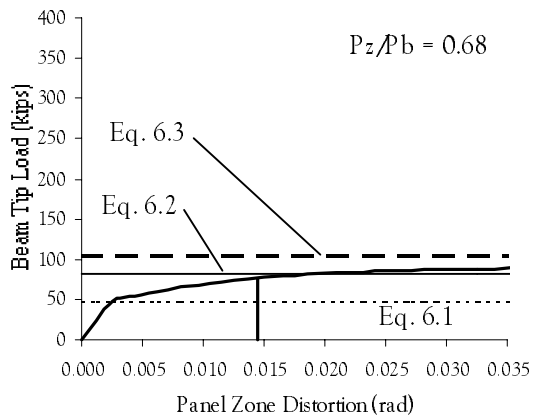
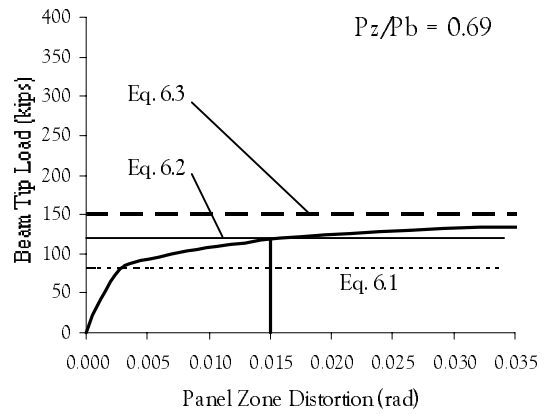


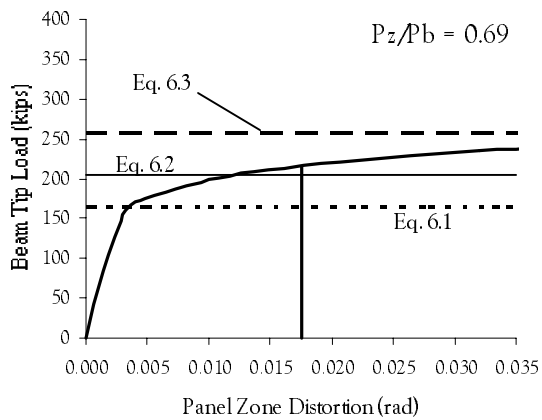
FIGURE 6.3: GRAVITY AND SEISMIC MOMENTS ON EXTERIOR CONNECTIONS



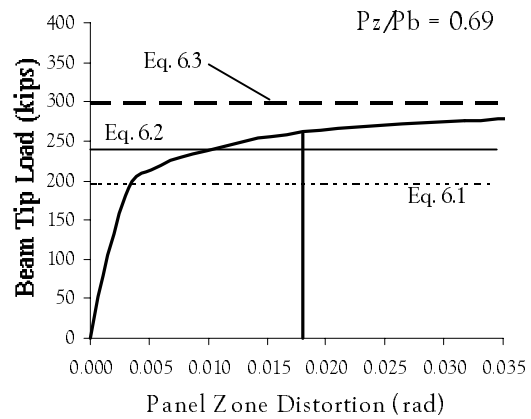
a) Specimen BD1 (beam depth 18 in)



b) Specimen BD2 (beam depth 24 in)

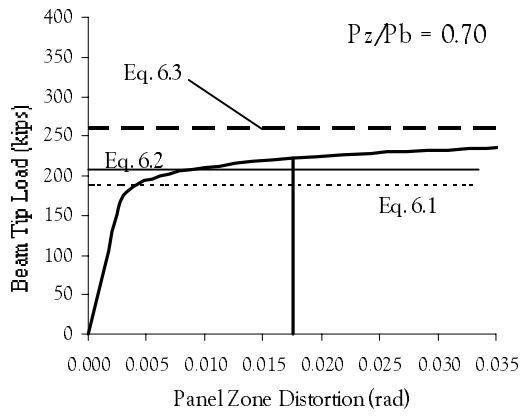


c) Specimen BD3 (beam depth 36 in)

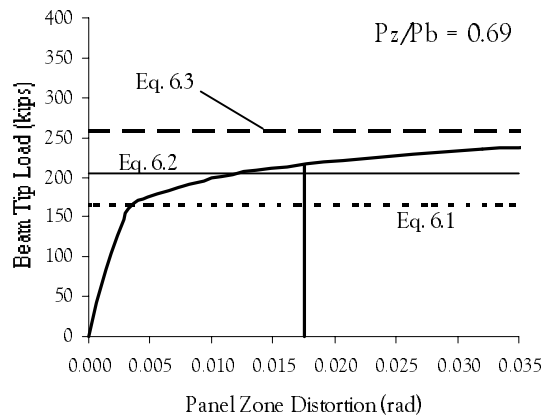


d) Specimen BD4 (beam depth 40 in)

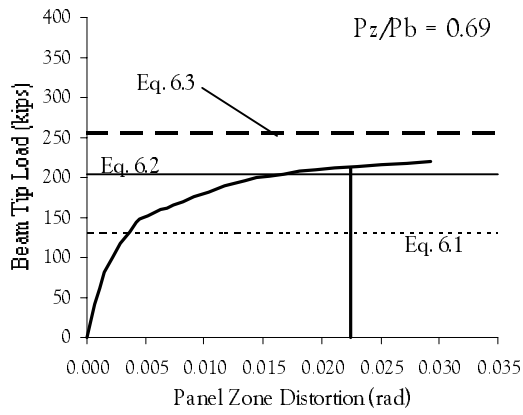
FIGURE 6.4: COMPARISON BETWEEN FE RESULTS AND FEMA-267 (1995) PROVISIONS FOR PANEL ZONE STRENGTH – SERIES BD



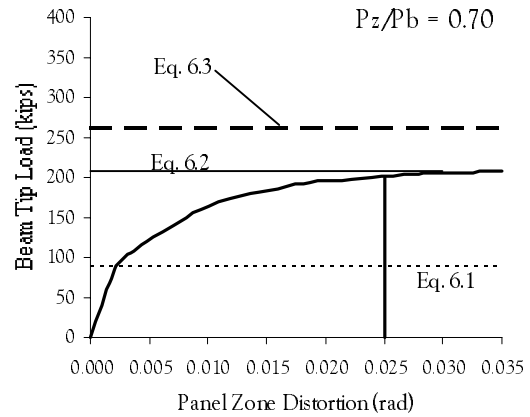
a) Specimen CF1 ( $t_{cf} = 1.3$  in)



b) Specimen CF2 ( $t_{cf} = 1.89$  in)



c) Specimen CF3 ( $t_{cf} = 2.5$  in)



d) Specimen CF4 ( $t_{cf} = 3.2$  in)

FIGURE 6.5: COMPARISON BETWEEN FE RESULTS AND FEMA-267 (1995) PROVISIONS FOR PANEL ZONE STRENGTH - SERIES CF

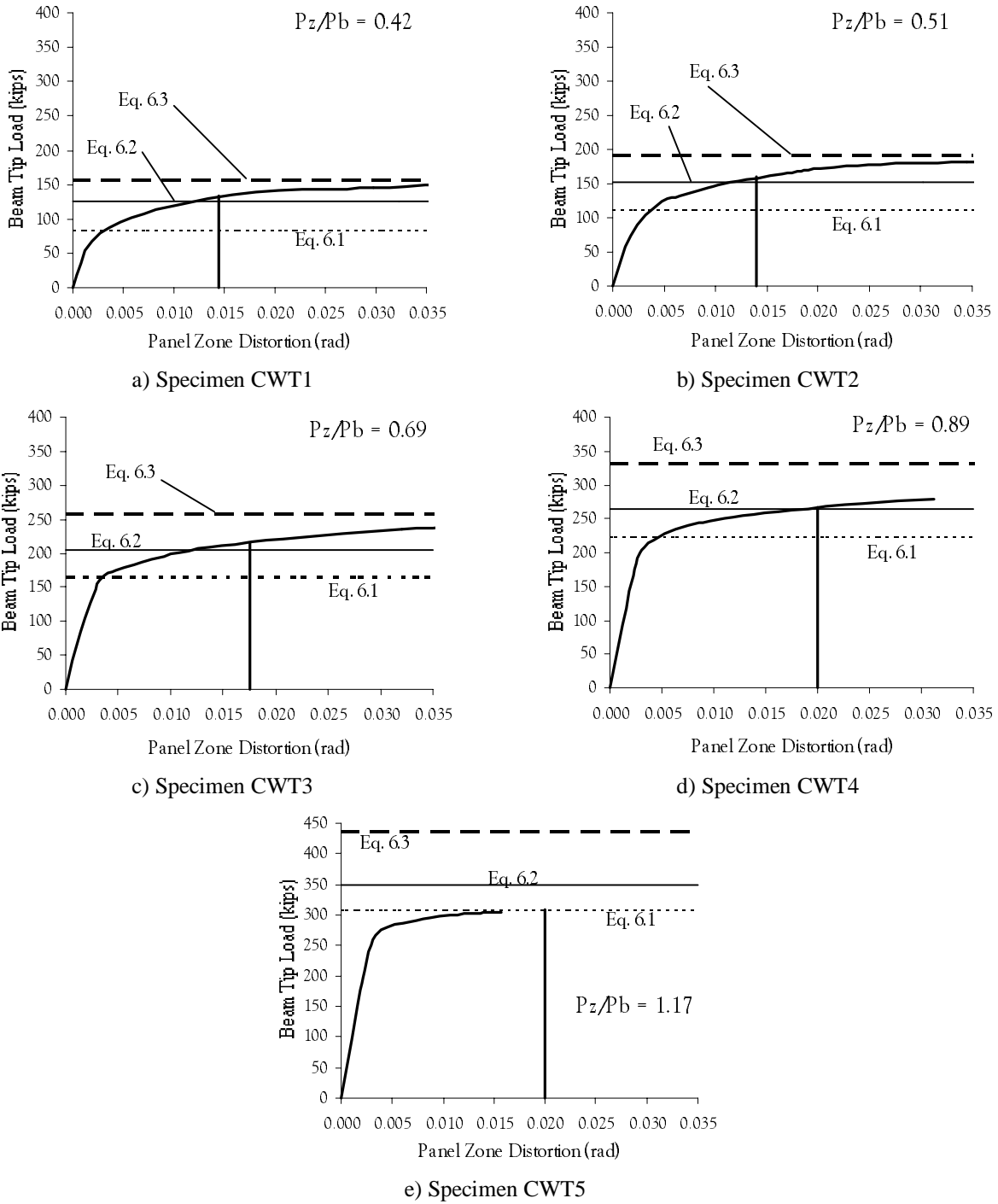
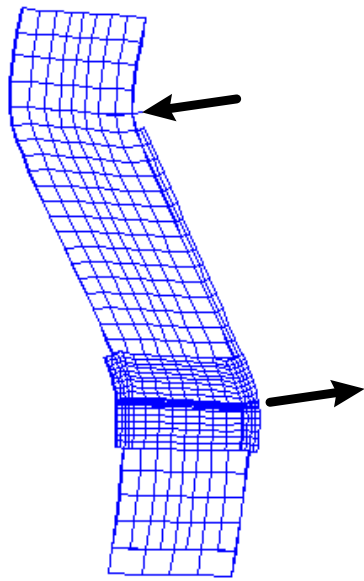
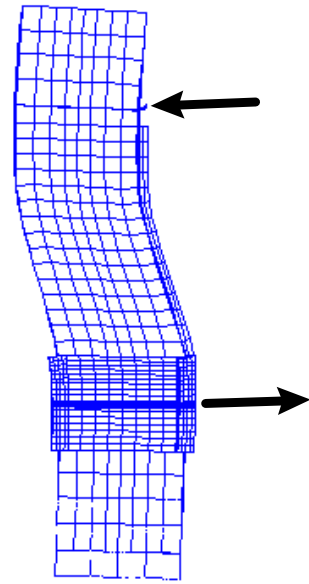


FIGURE 6.6: COMPARISON BETWEEN FE RESULTS AND FEMA-267 (1995) PROVISIONS FOR PANEL ZONE STRENGTH - SERIES CWT



(a) Specimen CWT1



(b) Specimen CWT5

FIGURE 6.7: DEFORMED SHAPES OF SPECIMENS CWT1 AND CWT5 AT A CONNECTION PLASTIC ROTATION OF 0.03 RAD

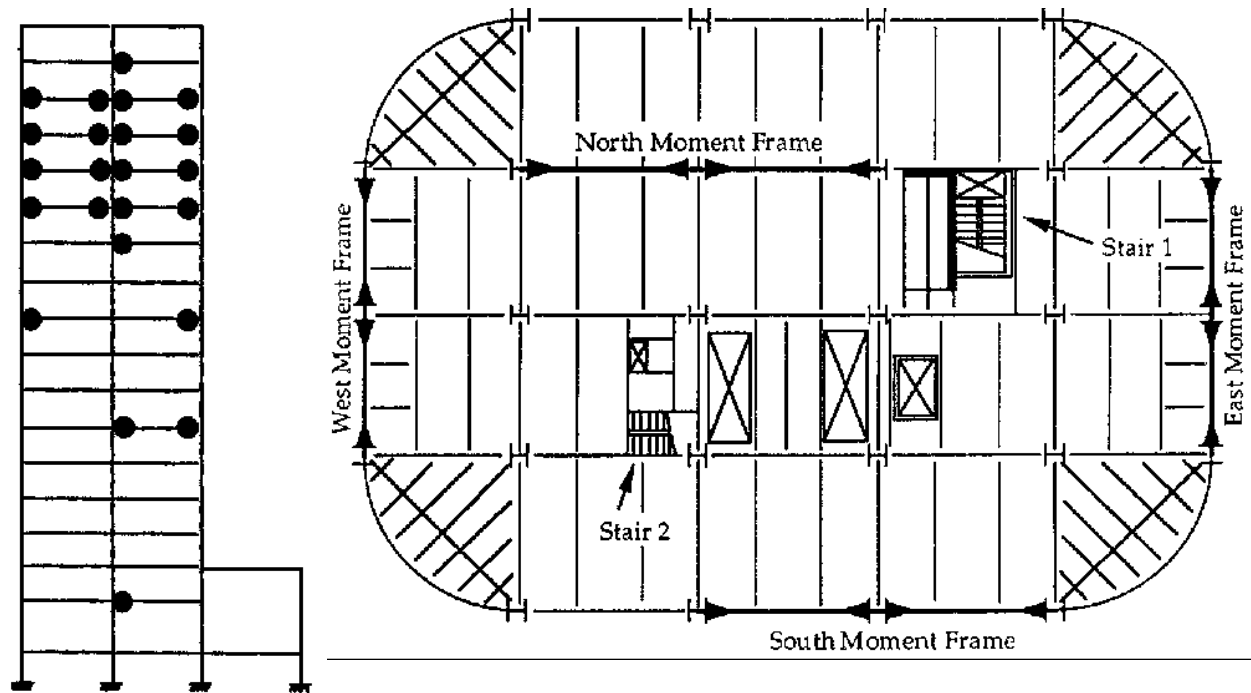


FIGURE 6.8: STRUCTURAL SYSTEM FOR 17 STORY BUILDING DAMAGED IN NORTHRIDGE (CHI et al. 1997). NOTE THE LARGE PERCENTAGE OF EXTERIOR (ONE-SIDED) CONNECTIONS.

## APPENDIX A - MATRIX OF ANALYSIS CONFIGURATIONS

The characteristics of the analysis configurations utilized in this research were derived from the geometry of Berkeley specimen PN3 (Figure A.1). Different analysis configurations were created by changing some of the attributes of Specimen PN3. Configuration dimensions are given in Table A.1, where the variables used are as follows:

- $d$  Beam or column depth.
  - $t_w$  Beam or column web thickness.
  - $b_f$  Beam or column flange width.
  - $t_f$  Beam or column flange thickness.
  - $P_b$  Beam tip load required to cause configuration to reach beam strength.
  - $P_z$  Beam tip load required to cause configuration to reach panel zone strength.
  - $P_c$  Beam tip load required to cause configuration to reach column strength.
- Subscripts  $b$  and  $c$  corresponds to beam and column respectively.

The beam tips loads shown in the table do not include the strength reduction ( $\phi$ ) factors and are calculated according to the 1991 UBC provisions in effect prior to the Northridge earthquake. The panel zone strengths do *not* account for the 80% factor specified by the UBC code for panel zone design (see Equation A.2). These loads, as well as the ratios  $P_z/P_b$  and  $P_c/P_b$  give an indication of where inelastic deformation is expected to occur, and are useful in categorizing and evaluating the results. The tip loads are calculated as follows:

$$P_b = \frac{M_{pb}}{L_b} \tag{A.1}$$

$$P_z = 0.55F_{yc}d_c t_{wc} \frac{\left(1 + 3 \frac{b_f t_f^2}{d_c d_b t_{wc}}\right)}{\left(\frac{L_b}{0.95d_b} - \frac{L_b + d_c / 2}{L_c}\right)} \tag{A.2}$$

$$P_c = \frac{2M_{pc}}{\left(\frac{L_b + d_c / 2}{L_c}\right)(L_c - d_b)} \tag{A.3}$$

where:

$L_b$  Beam length (see Figure A.1)

$L_c$  Column length (see Figure A.2)

$M_p$  is the plastic moment capacity of the beam or column cross-section

Other variables and subscripts are as defined above

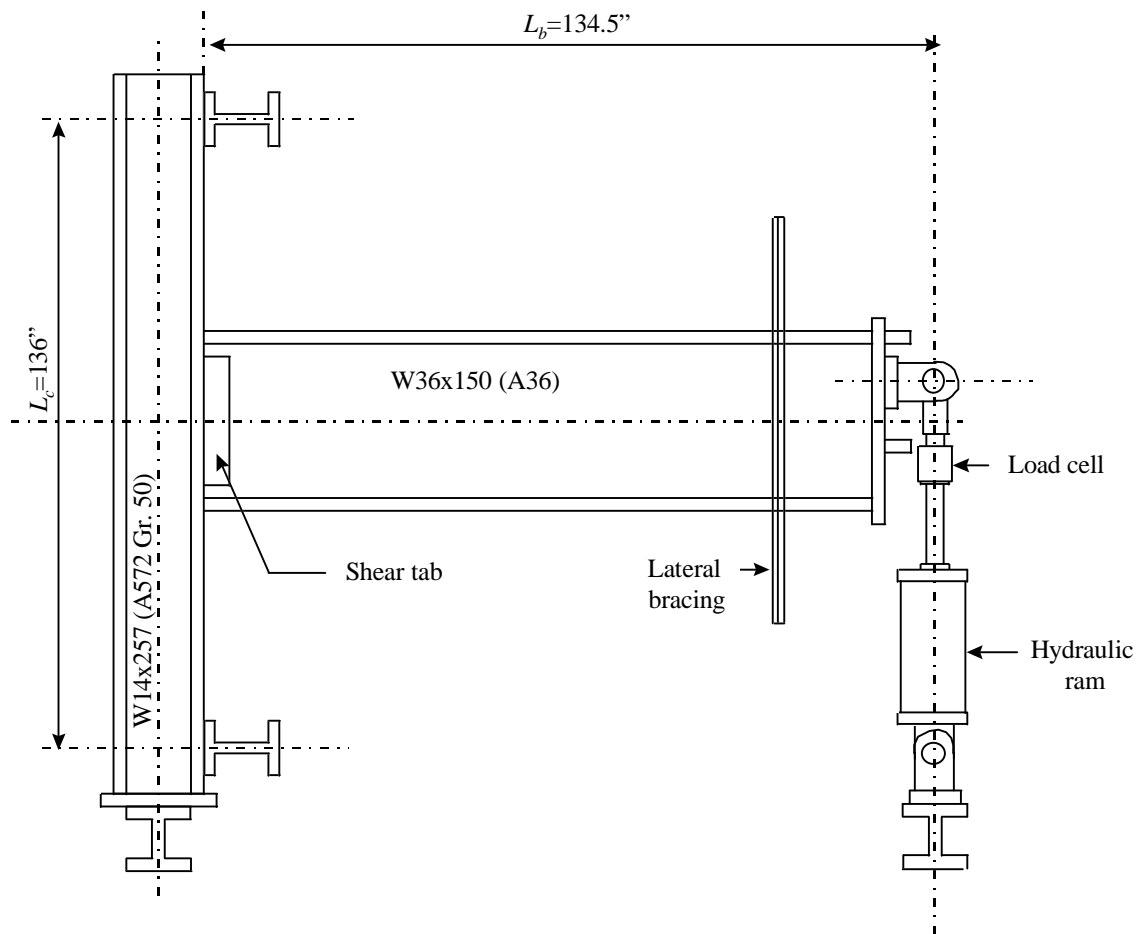


FIGURE A.1: DIMENSIONS OF SPECIMEN PN3

TABLE A.1: PROPERTIES OF ANALYSIS CONFIGURATIONS

Member	$d$ (in)	$t_w$ (in)	$b_f$ (in)	$t_f$ (in)	$P_b$ (kip)	$P_z$ (kip)	$P_c$ (kip)	$P_z/P_b$	$P_c/P_b$
<b>Series BF</b> <i>Beam Flange Thickness (<math>f_{yb} = 36</math> ksi, <math>f_{yc} = 50</math> ksi)</i>									
BF1-Column	16.38	1.05	16.00	1.89					
BF1-Beam	35.90	0.63	11.98	0.79	139	210	459	1.51	3.31
BF2-Column	16.38	1.18	16.00	1.89					
BF2-Beam	35.85	0.63	11.98	0.94	154	229	464	1.49	3.01
BF3-Column	16.38	1.45	16.00	1.89					
BF3-Beam	35.90	0.63	11.98	1.18	179	272	474	1.52	2.65
BF4-Column	16.38	1.95	16.00	1.89					
BF4-Beam	35.90	0.63	11.98	1.73	234	350	493	1.50	2.10
BF5-Column	16.38	3.10	16.00	1.89					
BF5-Beam	35.90	0.63	11.98	3.00	355	530	537	1.49	1.51
<b>Series BDN</b> <i>Beam Depth (<math>f_{yb} = 36</math> ksi, <math>f_{yc} = 50</math> ksi)</i>									
BDN1-Column	16.38	0.80	16.00	1.89					
BDN1-Beam	18.00	0.63	11.98	0.94	62	92	381	1.46	6.10
BDN2-Column	16.38	1.00	16.00	1.89					
BDN2-Beam	24.00	0.63	11.98	0.94	90	134	409	1.48	4.53
BDN3-Column	16.38	1.18	16.00	1.89					
BDN3-Beam	35.85	0.63	11.98	0.94	154	229	464	1.49	3.01
BDN4-Column	16.38	1.20	16.00	1.89					
BDN4-Beam	40.00	0.63	11.98	0.94	179	266	485	1.48	2.71

TABLE A.1 (CONT.): PROPERTIES OF ANALYSIS CONFIGURATIONS

Member	$d$ (in)	$t_w$ (in)	$b_f$ (in)	$t_f$ (in)	$P_b$ (kip)	$P_z$ (kip)	$P_c$ (kip)	$P_z/P_b$	$P_c/P_b$
<b>Series BD</b>		<b>Beam Depth (<math>f_{yb} = 70</math> ksi, <math>f_{yc} = 45</math> ksi)</b>							
BD1-Column	16.38	0.80	16.00	1.89					
BD1-Beam	18.00	0.63	11.98	0.94	122	83	343	0.68	2.82
BD2-Column	16.38	1.00	16.00	1.89					
BD2-Beam	24.00	0.63	11.98	0.94	176	121	368	0.69	2.09
BD3-Column	16.38	1.18	16.00	1.89					
BD3-Beam	35.85	0.63	11.98	0.94	299	206	417	0.69	1.39
BD4-Column	16.38	1.20	16.00	1.89					
BD4-Beam	40.00	0.63	11.98	0.94	348	239	436	0.69	1.25
<b>Series CFN</b>		<b>Column Flange Thickness (<math>f_{yb} = 36</math> ksi, <math>f_{yc} = 50</math> ksi)</b>							
CFN1-Column	16.38	1.35	16.00	1.30					
CFN1-Beam	35.85	0.63	11.98	0.94	154	232	361	1.51	2.35
CFN2-Column	16.38	1.18	16.00	1.89					
CFN2-Beam	35.85	0.63	11.98	0.94	154	229	464	1.49	3.01
CFN3-Column	16.38	0.95	16.00	2.50					
CFN3-Beam	35.85	0.63	11.98	0.94	154	228	560	1.48	3.64
CFN4-Column	16.38	0.65	16.00	3.20					
CFN4-Beam	35.85	0.63	11.98	0.94	154	232	661	1.51	4.29

TABLE A.1: (CONT.) PROPERTIES OF ANALYSIS CONFIGURATIONS

Member	$d$ (in)	$t_w$ (in)	$b_f$ (in)	$t_f$ (in)	$P_b$ (kip)	$P_z$ (kip)	$P_c$ (kip)	$P_z/P_b$	$P_c/P_b$
<b>Series CF</b>		<b>Column Flange Thickness (<math>f_{yb} = 70</math> ksi, <math>f_{yc} = 45</math> ksi)</b>							
CF1-Column	16.38	1.35	16.00	1.30					
CF1-Beam	35.85	0.63	11.98	0.94	299	209	325	0.70	1.09
CF2-Column	16.38	1.18	16.00	1.89					
CF2-Beam	35.85	0.63	11.98	0.94	299	206	417	0.69	1.39
CF3-Column	16.38	0.95	16.00	2.50					
CF3-Beam	35.85	0.63	11.98	0.94	299	205	504	0.69	1.68
CF4-Column	16.38	0.65	16.00	3.20					
CF4-Beam	35.85	0.63	11.98	0.94	299	209	595	0.70	1.99
<b>Series CWT</b>		<b>Column Web Thickness (<math>f_{yb} = 70</math> ksi, <math>f_{yc} = 45</math> ksi)</b>							
CWT1-Column	16.38	0.60	16.00	1.89					
CWT1-Beam	35.85	0.63	11.98	0.94	299	125	398	0.42	1.33
CWT2-Column	16.38	0.80	16.00	1.89					
CWT2-Beam	35.85	0.63	11.98	0.94	299	153	404	0.51	1.35
CWT3-Column	16.38	1.18	16.00	1.89					
CWT3-Beam	35.85	0.63	11.98	0.94	299	206	417	0.69	1.39
CWT3N-Col.*	16.38	1.18	16.00	1.89					
CWT3N-Beam	35.85	0.63	11.98	0.94	154	229	464	1.49	3.01
CWT4-Column	16.38	1.60	16.00	1.89					
CWT4-Beam	35.85	0.63	11.98	0.94	299	266	432	0.89	1.44
CWT5-Column	16.38	2.20	16.00	1.89					
CWT5-Beam	35.85	0.63	11.98	0.94	299	350	452	1.17	1.51

\*Nominal properties are used for this particular configuration, ( $f_{yb} = 36$  ksi,  $f_{yc} = 50$  ksi)

## APPENDIX B - FINITE ELEMENT RESULTS

The indices plotted in this appendix are extracted from the finite element results along the following lines through the connection:

1. A line in the middle of the column flange denoted by “C-HAZ” in Figure B.1.
2. A line at the interface between the beam and column flanges, denoted by “Interface” in Figure B.1.
3. Finally, a line at mid-height of the beam flange, and underneath the access hole as shown in Figure B.1.

The indices that are plotted are the Mises, pressure and PEEQ indices. The Mises index is the von Mises stress divided by the corresponding yield stress. The pressure index is ratio between the hydrostatic stress and the corresponding yield stress. The pressure index is a negative number for tensile hydrostatic stresses. The PEEQ index is the ratio between the effective plastic strain and the corresponding yield strain. The beam yield stress and strain are used for normalization of quantities at the interface between the beam and column.

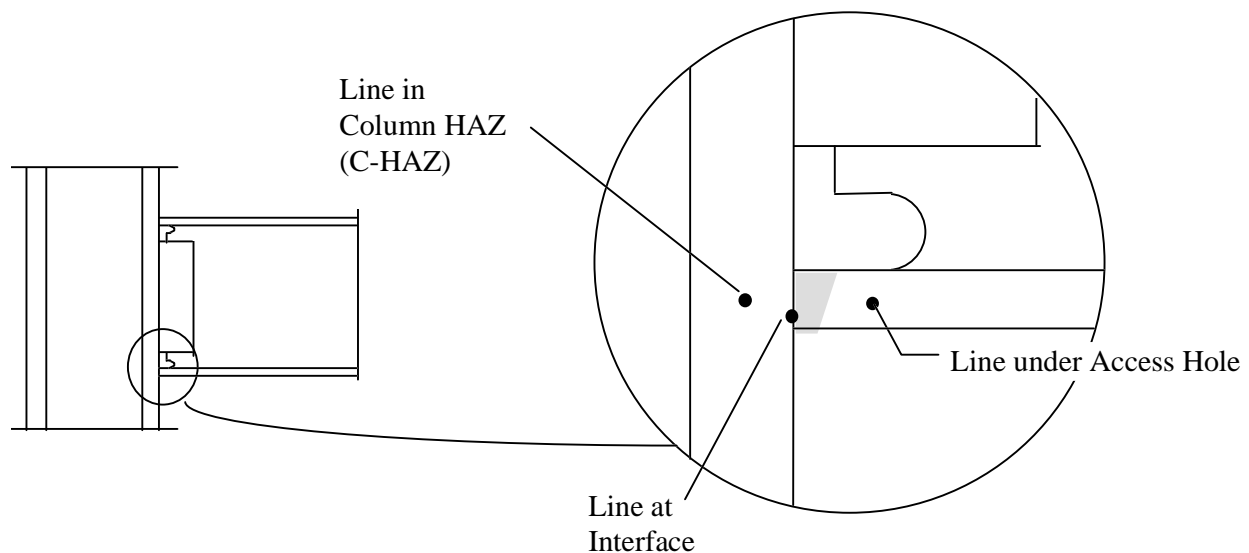
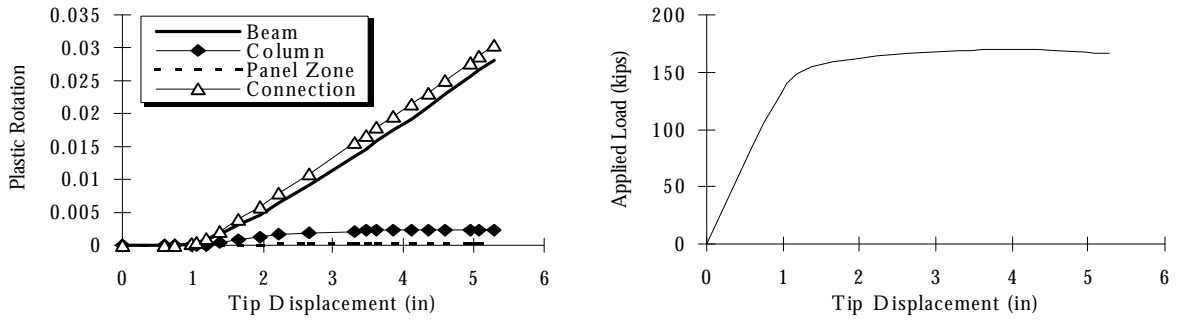


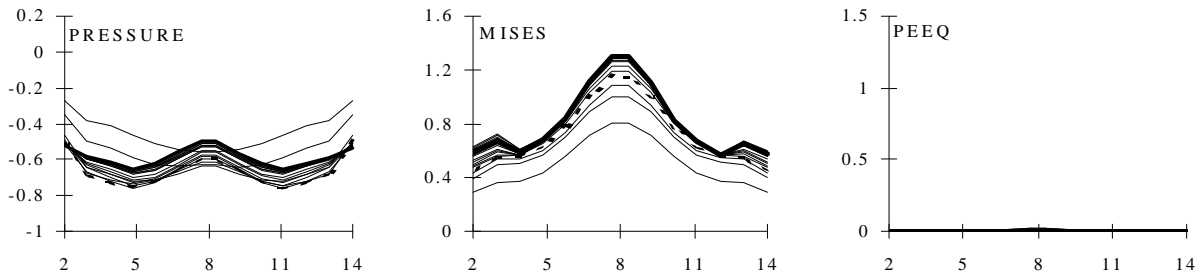
FIGURE B.1: LOCATIONS AT WHICH INDICES ARE EXTRACTED

FIGURE B.1. SPECIMEN BF2. ALSO BDN3, CFN2, A1 & CWT3, ( $f_{yb}=36\text{ksi}$ ,  $f_{yc}=50\text{ksi}$ ). THIS SPECIMEN HAS GEOMETRY OF PN3.

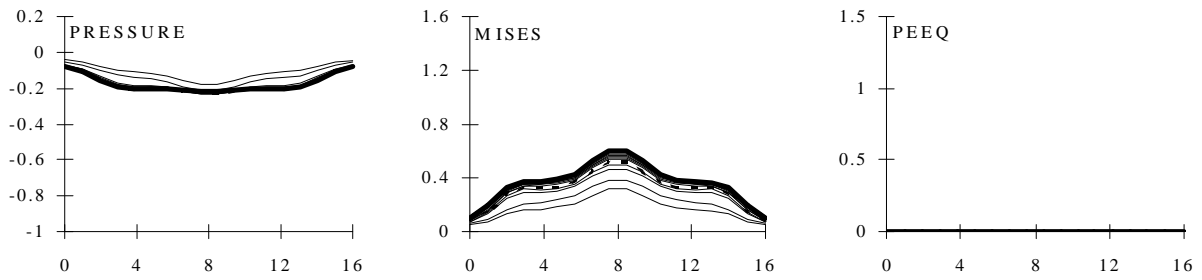


(a) Plasticity vs. Applied Tip Displacement

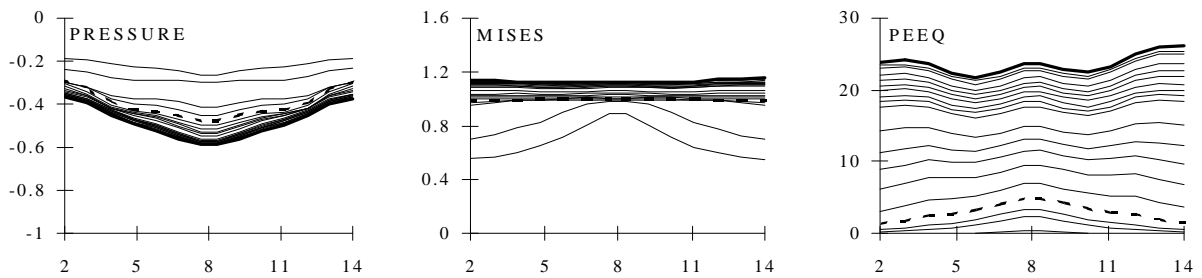
(b) Load vs. Applied Tip Displacement



(c) Pressure, Mises, and PEEQ at interface

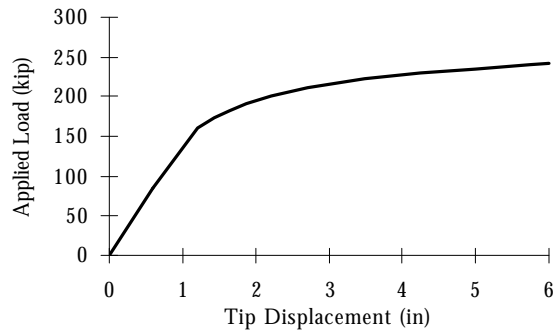
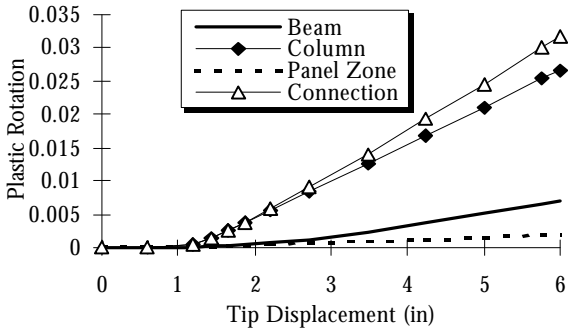


(d) Pressure, Mises, and PEEQ in column flange



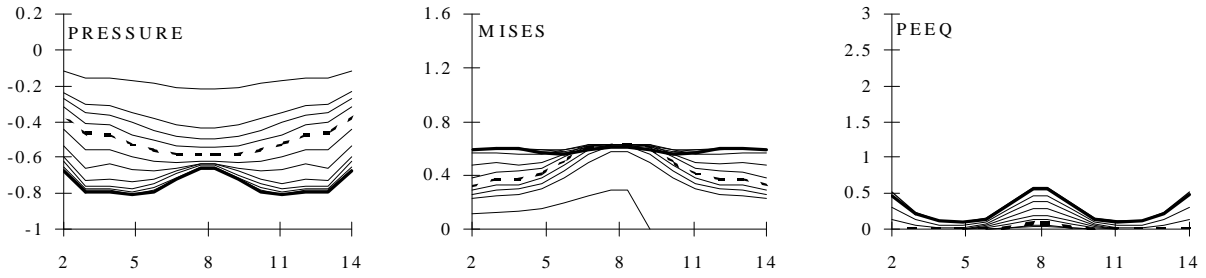
(e) Pressure, Mises, and PEEQ below access hole

FIGURE B.2. SPECIMEN BD3. ALSO CF2 & CWT3, ( $f_{yb}=70\text{ksi}$ ,  $f_{yc}=45\text{ksi}$ ).  
THIS SPECIMEN HAS GEOMETRY OF PN3.

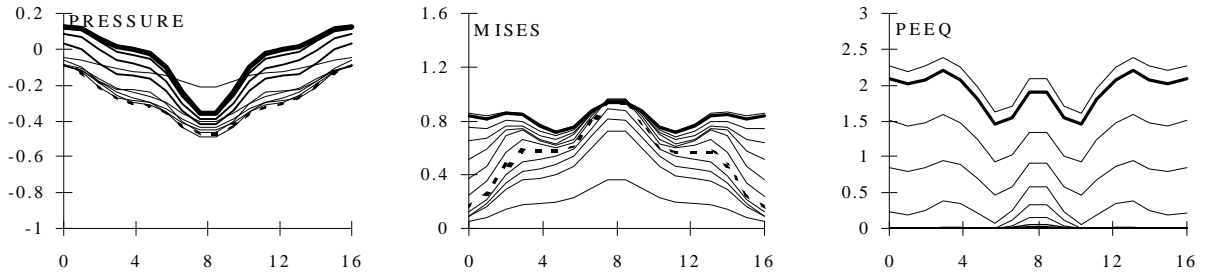


(a) Plasticity vs. Applied Tip Displacement

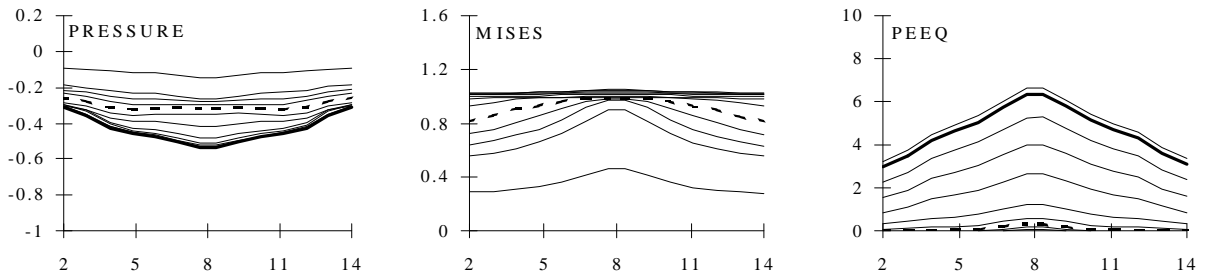
(b) Load vs. Applied Tip Displacement



(c) Pressure, Mises, and PEEQ at interface

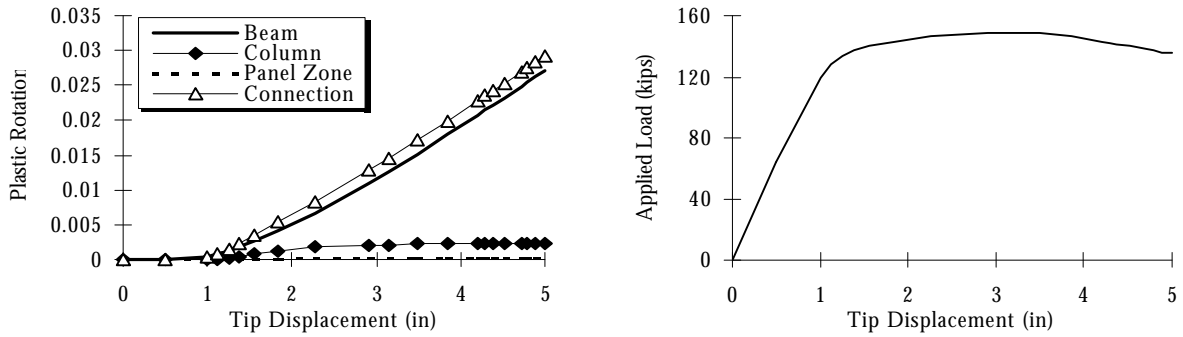


(d) Pressure, Mises, and PEEQ in column flange



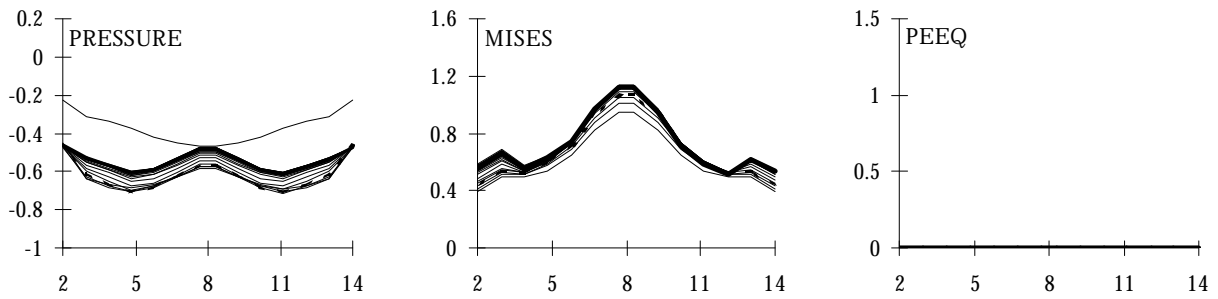
(e) Pressure, Mises, and PEEQ below access hole

FIGURE B.3. SPECIMEN BF1. ( $f_{yb}=36\text{ksi}$ ,  $f_{yc}=50\text{ksi}$ ).

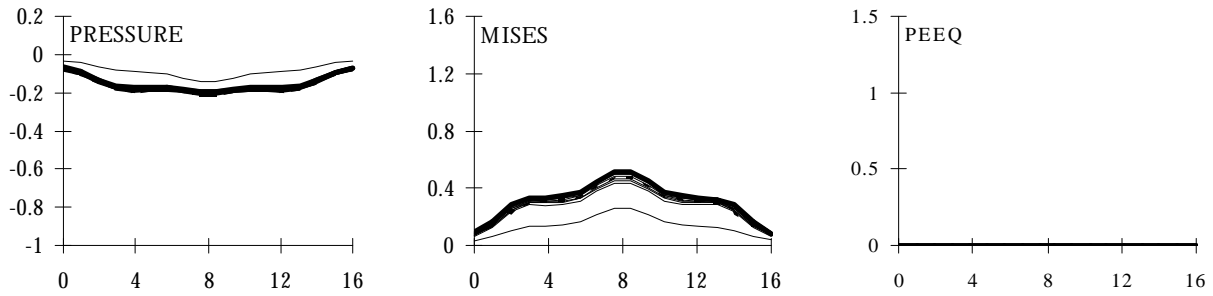


(a) Plasticity vs. Applied Tip Displacement

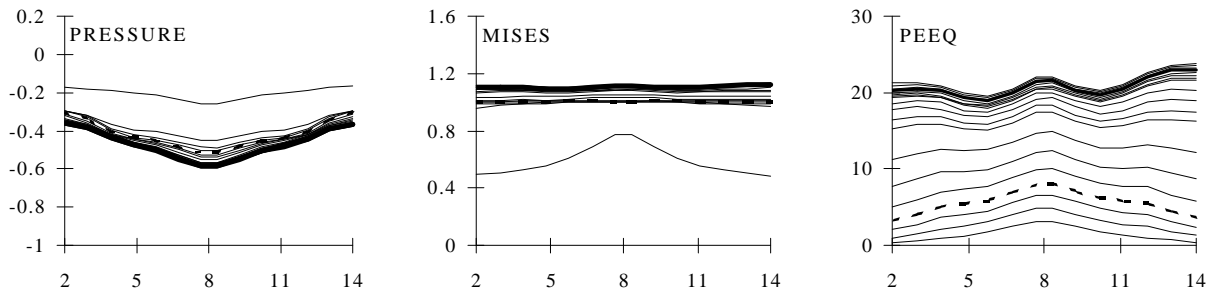
(b) Load vs. Applied Tip Displacement



(c) Pressure, Mises, and PEEQ at interface

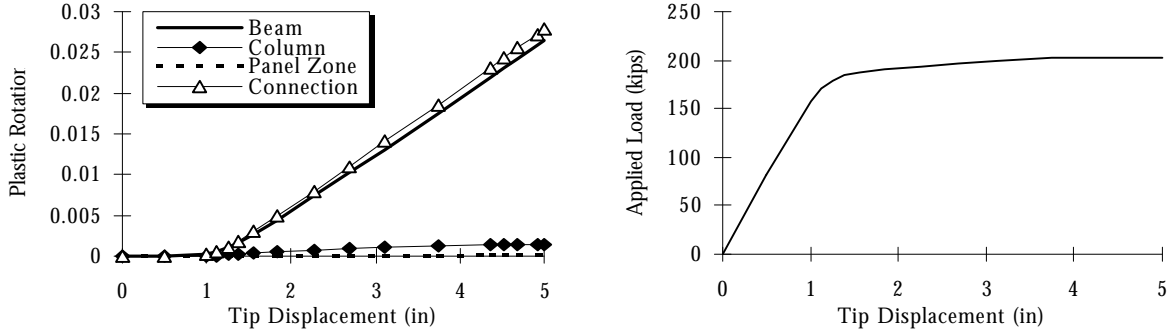


(d) Pressure, Mises, and PEEQ in column flange



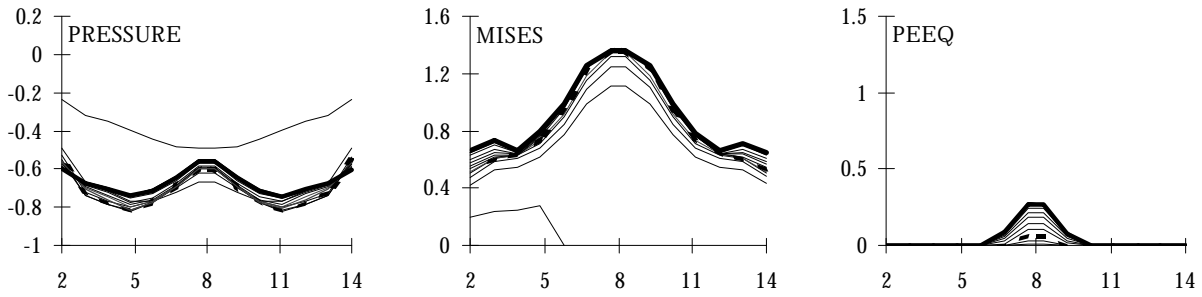
(e) Pressure, Mises, and PEEQ below access hole

FIGURE B.4. SPECIMEN BF3. ( $f_{yb}=36\text{ksi}$ ,  $f_{yc}=50\text{ksi}$ ).

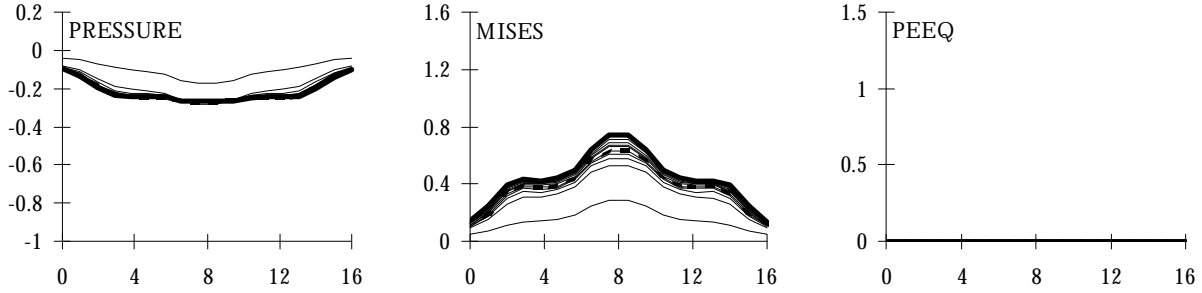


(a) Plasticity vs. Applied Tip Displacement

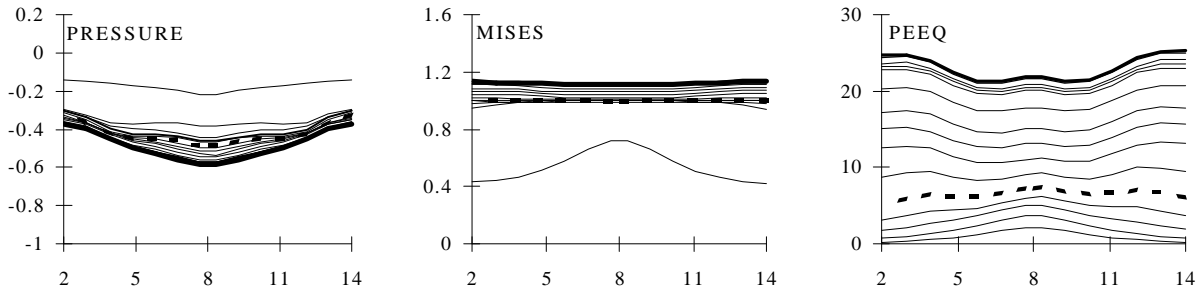
(b) Load vs. Applied Tip Displacement



(c) Pressure, Mises, and PEEQ at interface

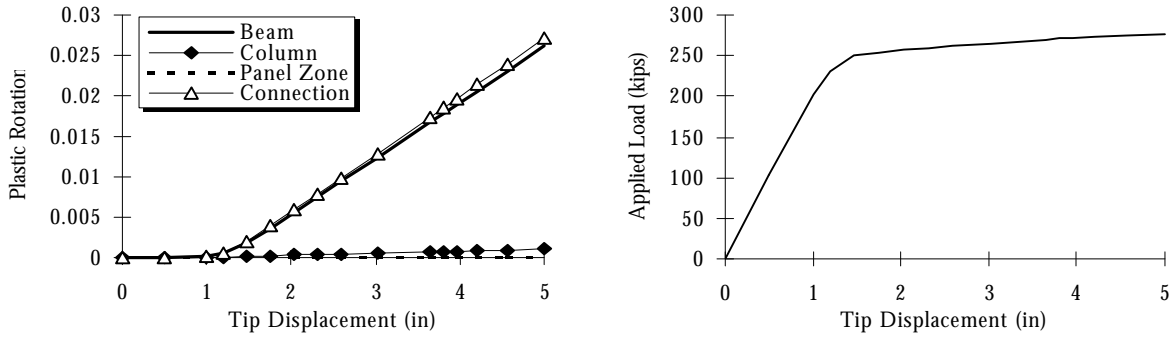


(d) Pressure, Mises, and PEEQ in column flange



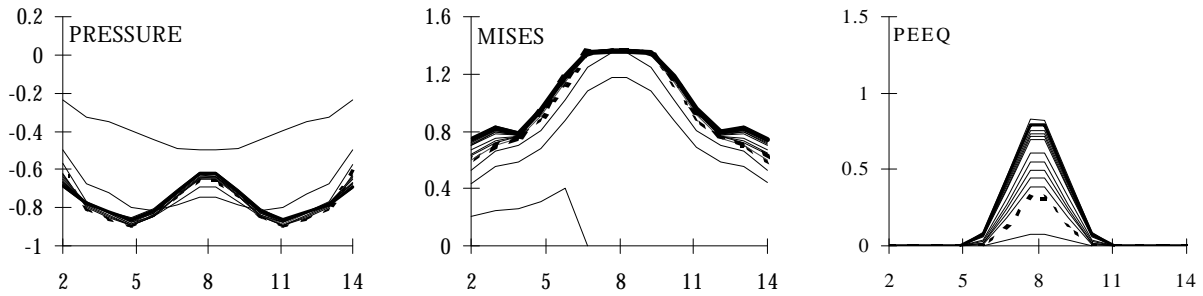
(e) Pressure, Mises, and PEEQ below access hole

FIGURE B.5. SPECIMEN BF4. ( $f_{yb}=36\text{ksi}$ ,  $f_{yc}=50\text{ksi}$ ).

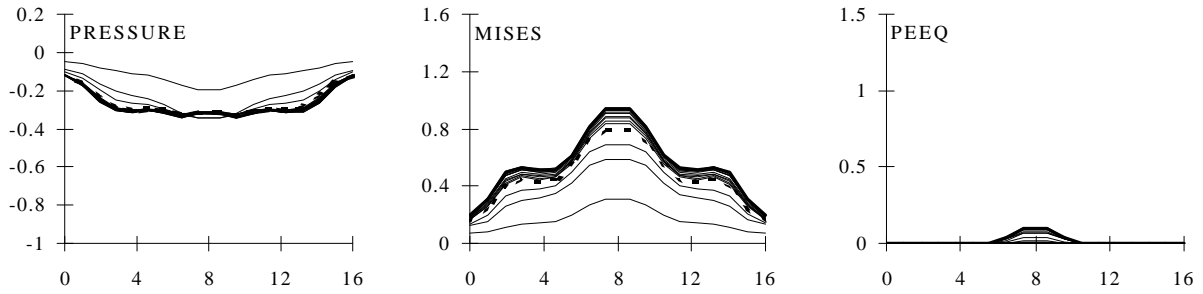


(a) Plasticity vs. Applied Tip Displacement

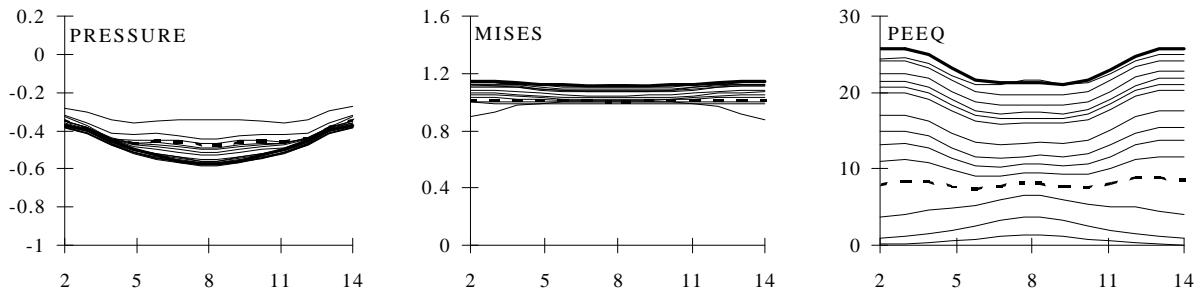
(b) Load vs. Applied Tip Displacement



(c) Pressure, Mises, and PEEQ at interface

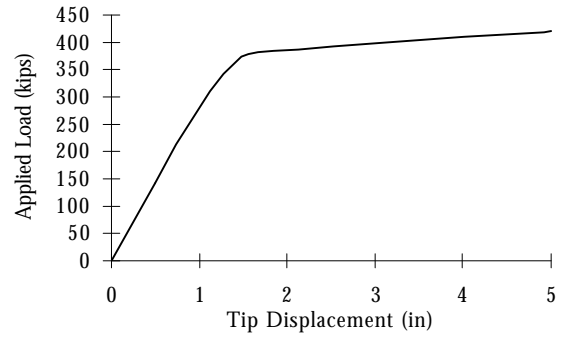
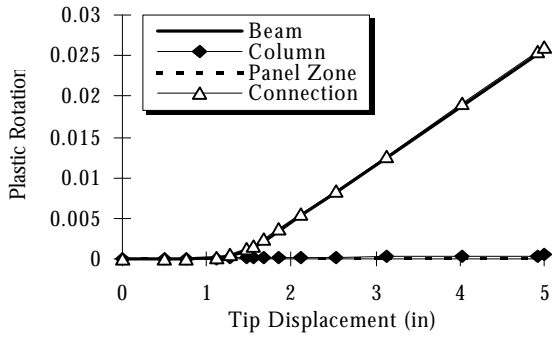


(d) Pressure, Mises, and PEEQ in column flange



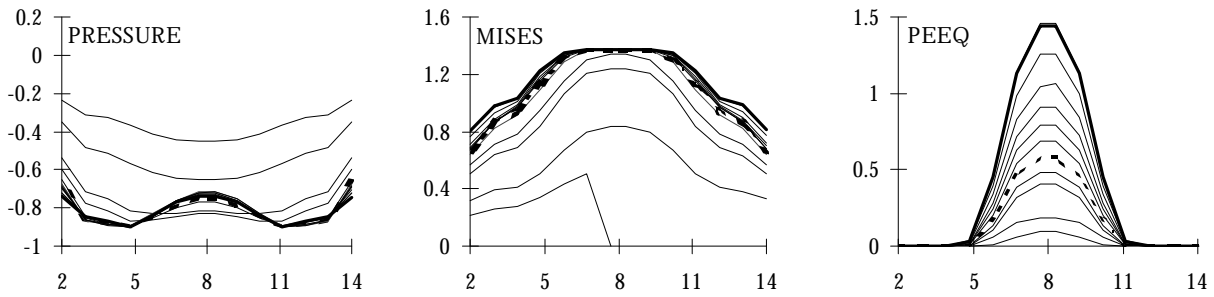
(e) Pressure, Mises, and PEEQ below access hole

FIGURE B.6. SPECIMEN BF5. ( $f_{yb}=36\text{ksi}$ ,  $f_{yc}=50\text{ksi}$ ).

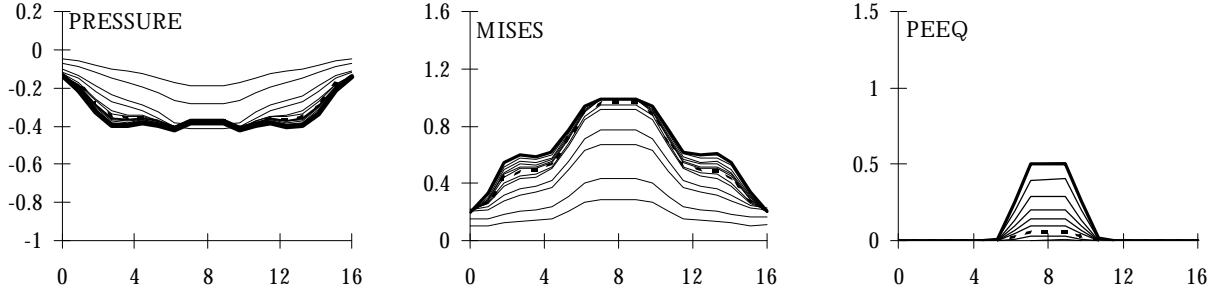


(a) Plasticity vs. Applied Tip Displacement

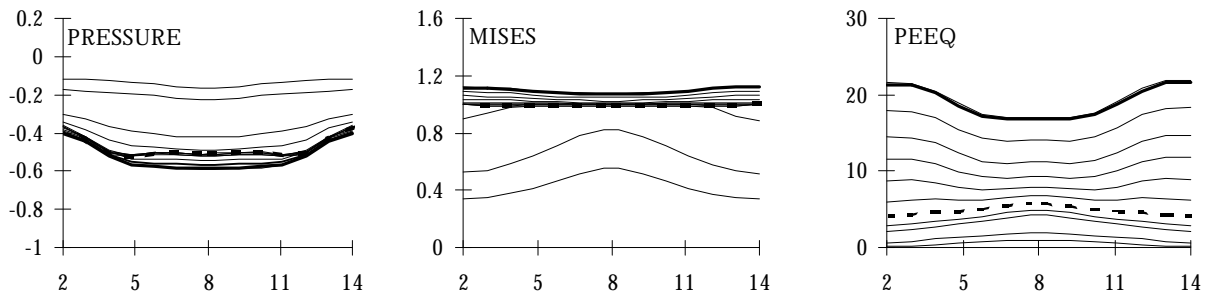
(b) Load vs. Applied Tip Displacement



(c) Pressure, Mises, and PEEQ at interface

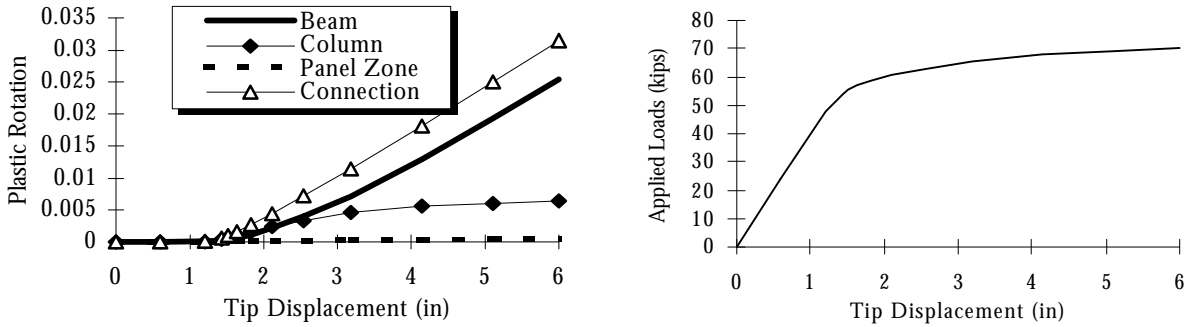


(d) Pressure, Mises, and PEEQ in column flange



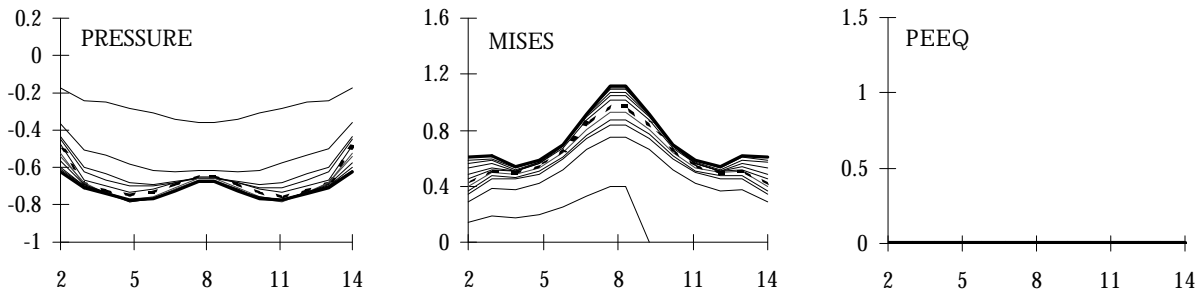
(e) Pressure, Mises, and PEEQ below access hole

FIGURE B.7. SPECIMEN BDN1. ( $f_{yb}=36\text{ksi}$ ,  $f_{yc}=50\text{ksi}$ ).

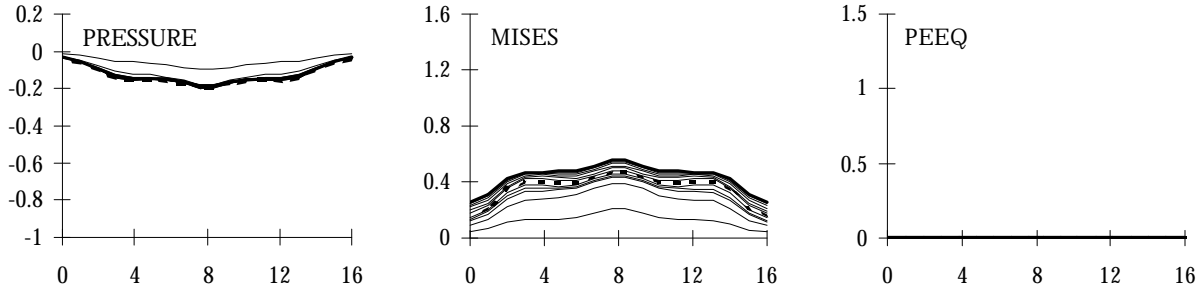


(a) Plasticity vs. Applied Tip Displacement

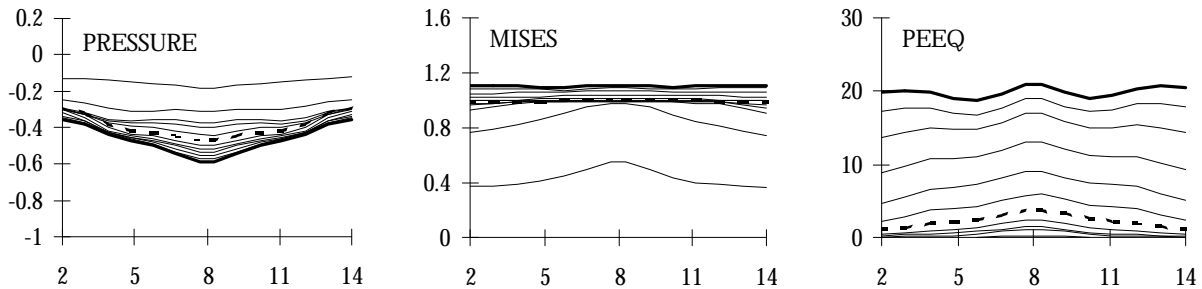
(b) Load vs. Applied Tip Displacement



(c) Pressure, Mises, and PEEQ at interface

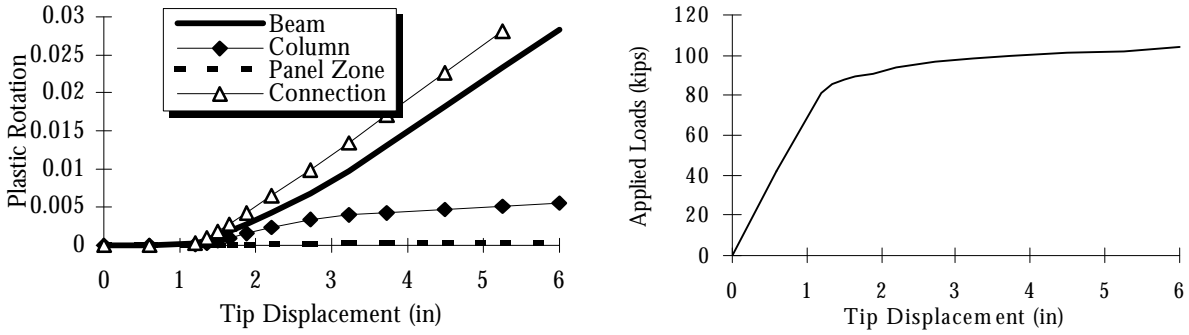


(d) Pressure, Mises, and PEEQ in column flange



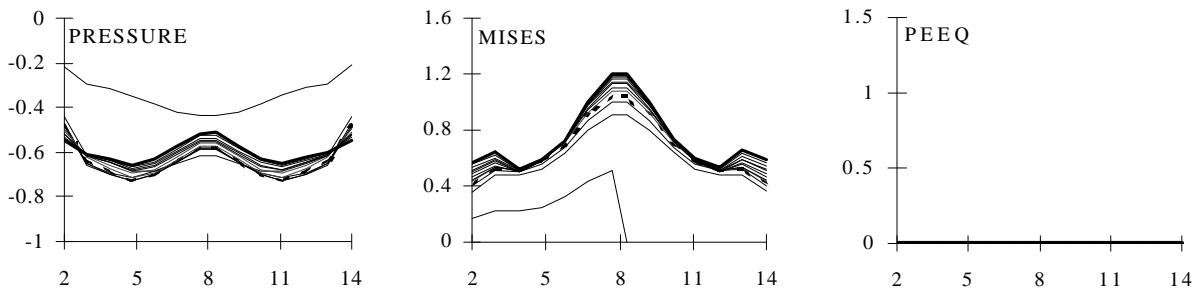
(e) Pressure, Mises, and PEEQ below access hole

FIGURE B.8. SPECIMEN BDN2. ( $f_{yb}=36\text{ksi}$ ,  $f_{yc}=50\text{ksi}$ ).

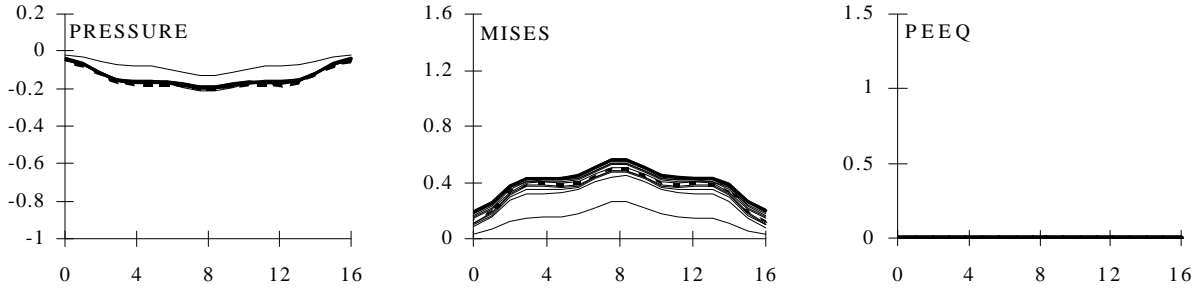


(a) Plasticity vs. Applied Tip Displacement

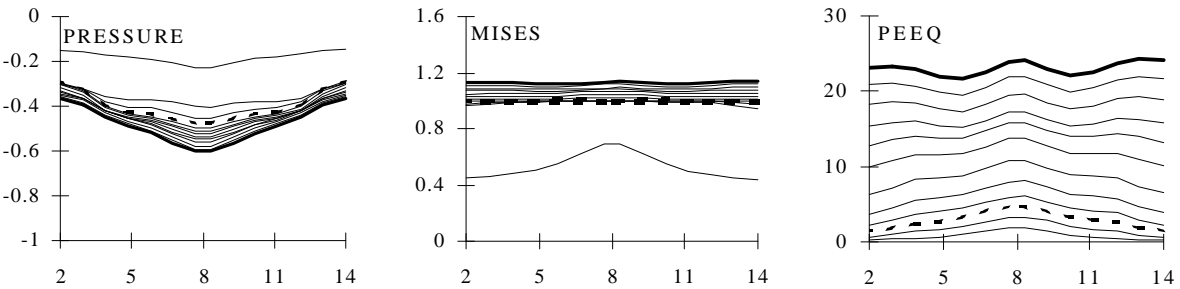
(b) Load vs. Applied Tip Displacement



(c) Pressure, Mises, and PEEQ at interface

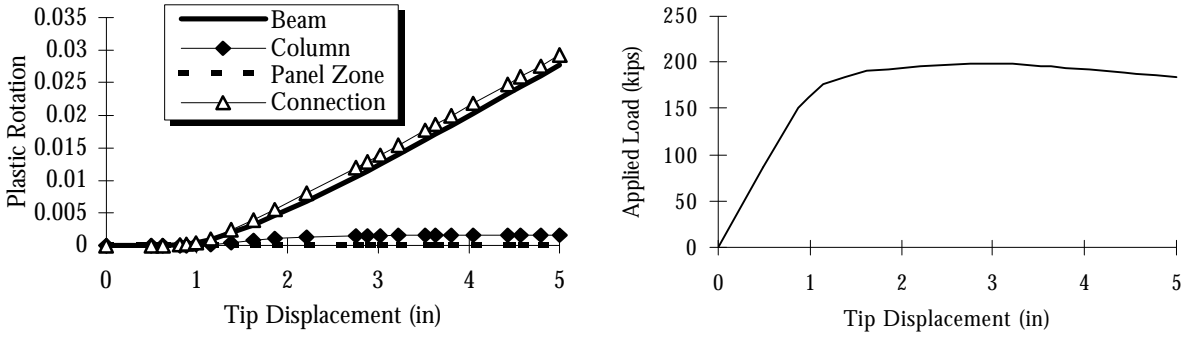


(d) Pressure, Mises, and PEEQ in column flange



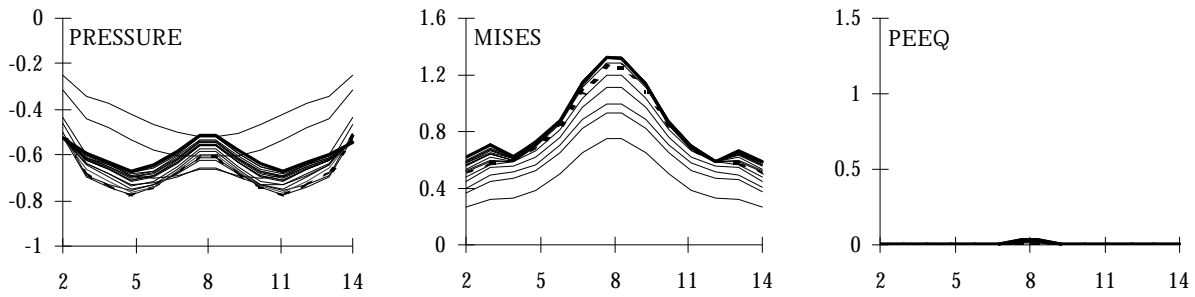
(e) Pressure, Mises, and PEEQ below access hole

FIGURE B.9. SPECIMEN BDN4. ( $f_{yb}=36\text{ksi}$ ,  $f_{yc}=50\text{ksi}$ ).

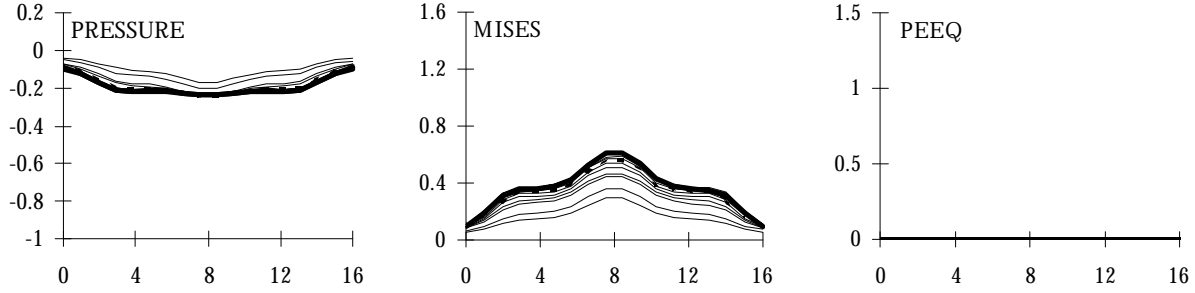


(a) Plasticity vs. Applied Tip Displacement

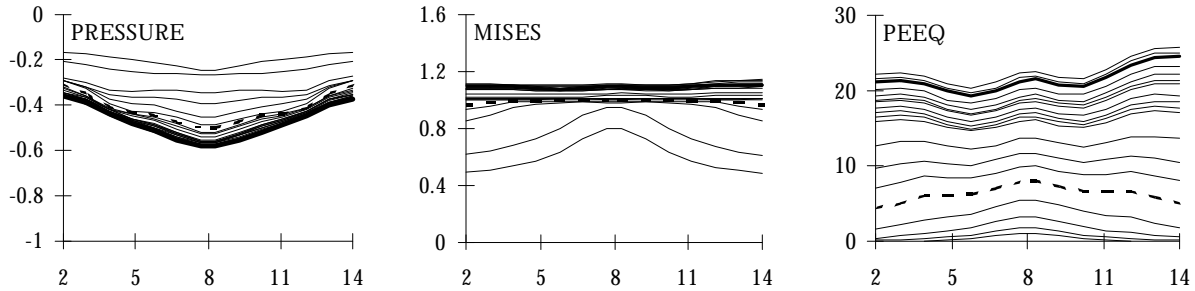
(b) Load vs. Applied Tip Displacement



(c) Pressure, Mises, and PEEQ at interface

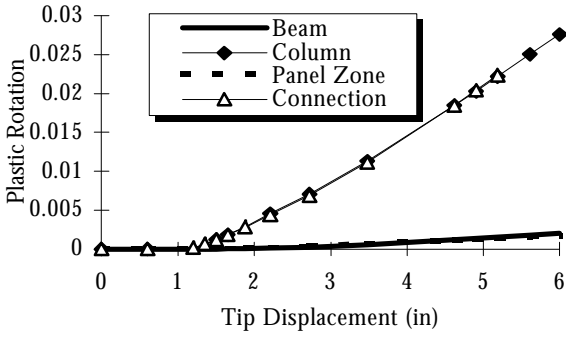


(d) Pressure, Mises, and PEEQ in column flange

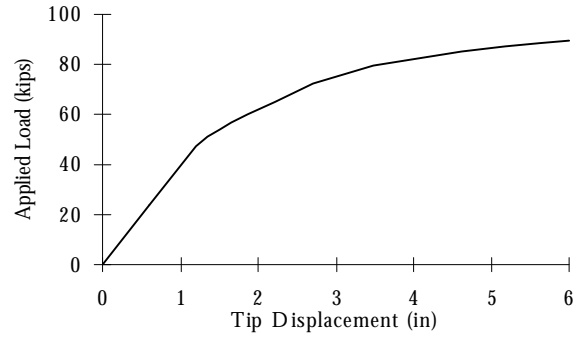


(e) Pressure, Mises, and PEEQ below access hole

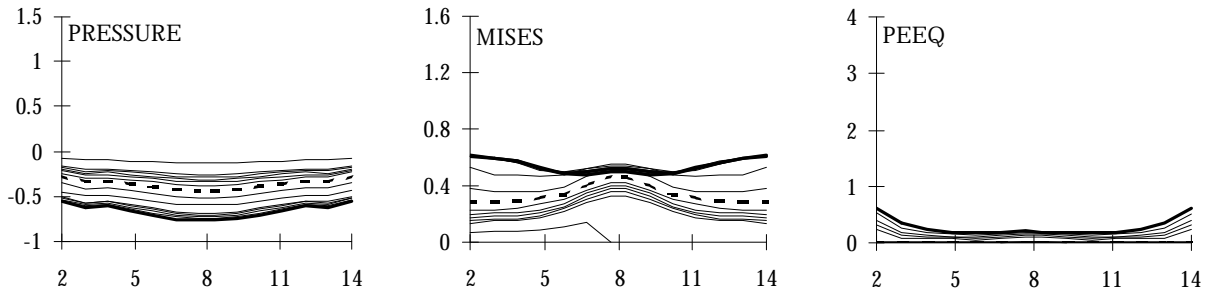
FIGURE B.10. SPECIMEN BD1. ( $f_{yb}=70\text{ksi}$ ,  $f_{yc}=45\text{ksi}$ ).



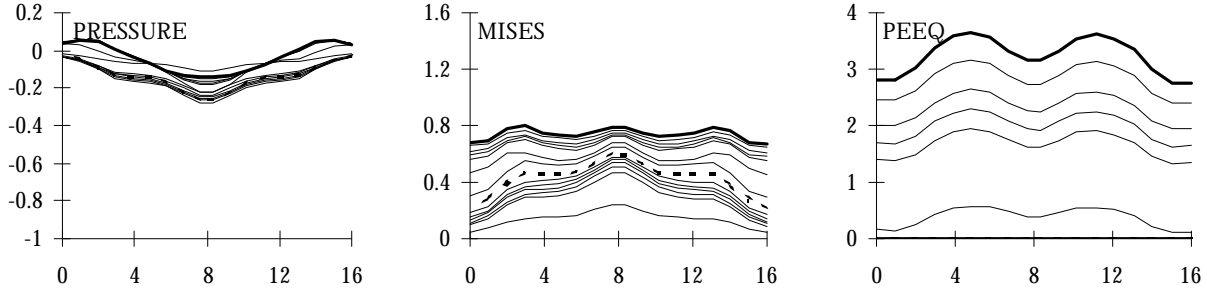
(a) Plasticity vs. Applied Tip Displacement



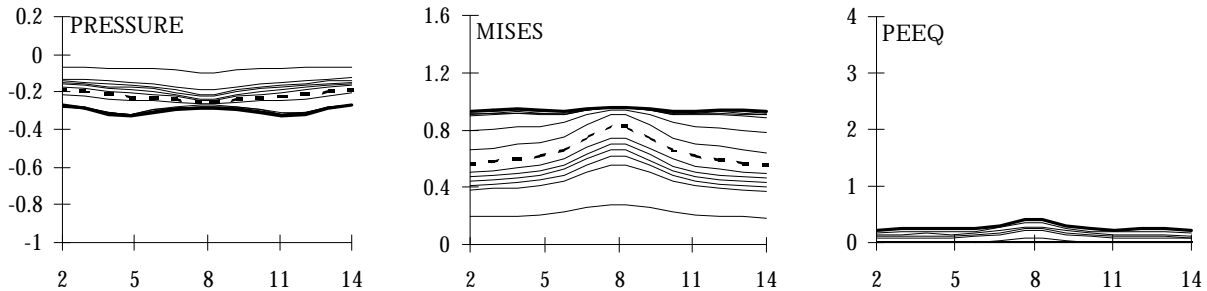
(b) Load vs. Applied Tip Displacement



(c) Pressure, Mises, and PEEQ at interface

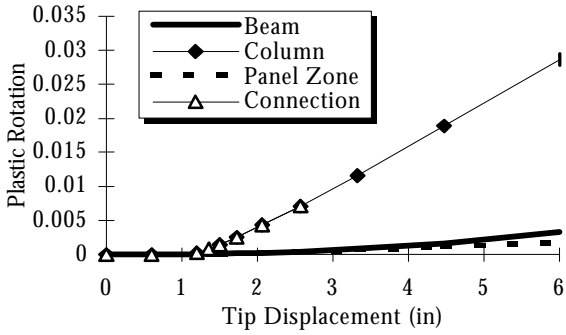


(d) Pressure, Mises, and PEEQ in column flange

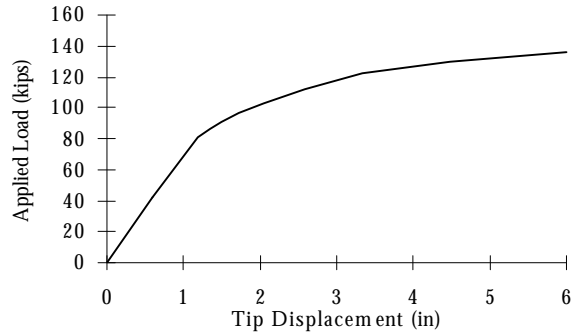


(e) Pressure, Mises, and PEEQ below access hole

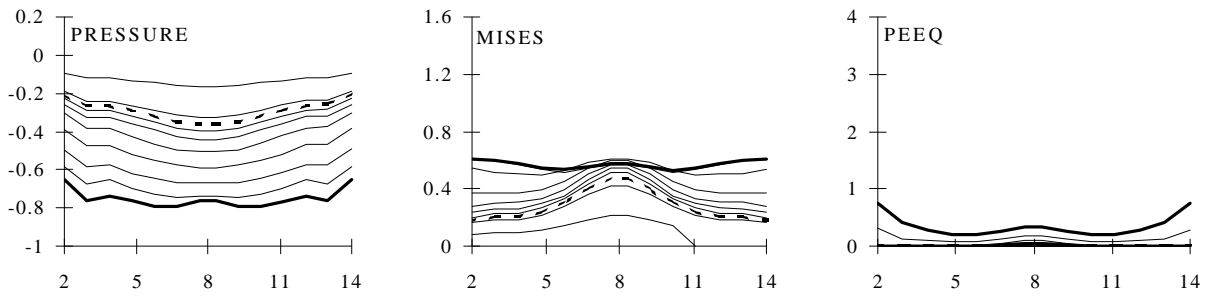
FIGURE B.11. SPECIMEN BD2. ( $f_{yb}=70\text{ksi}$ ,  $f_{yc}=45\text{ksi}$ ).



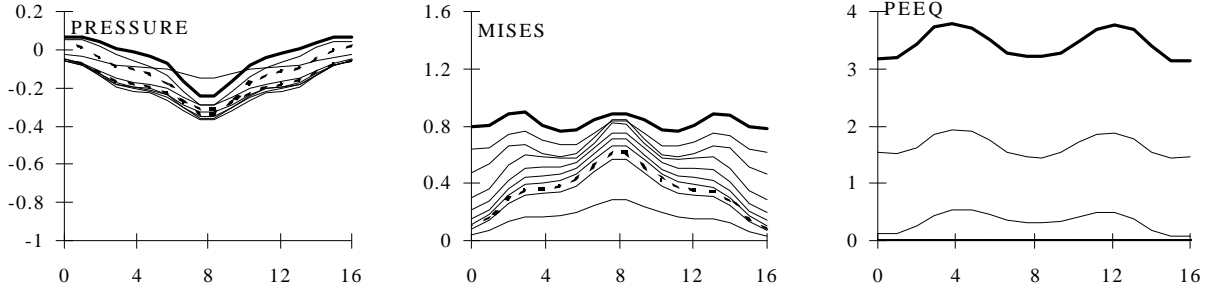
(a) Plasticity vs. Applied Tip Displacement



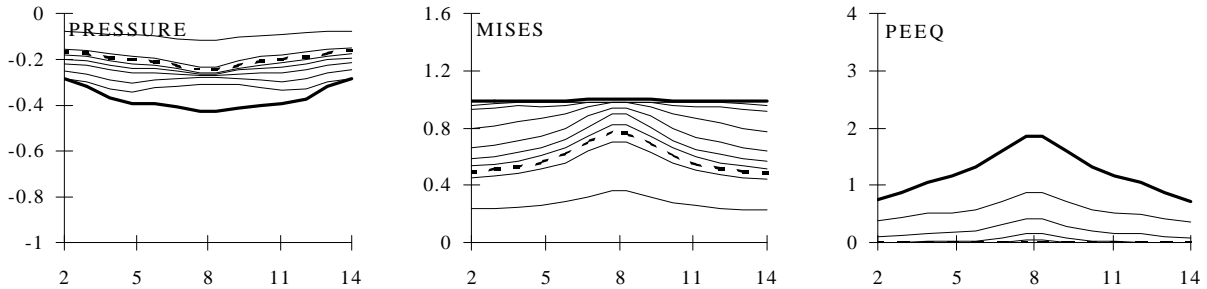
(b) Load vs. Applied Tip Displacement



(c) Pressure, Mises, and PEEQ at interface

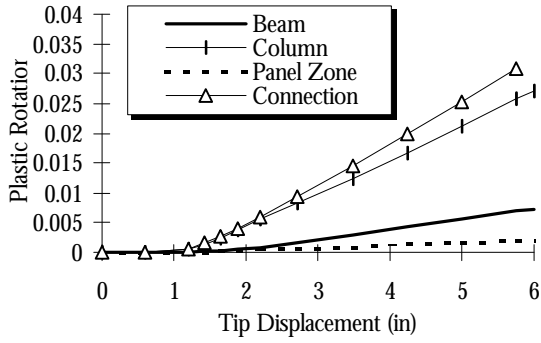


(d) Pressure, Mises, and PEEQ in column flange

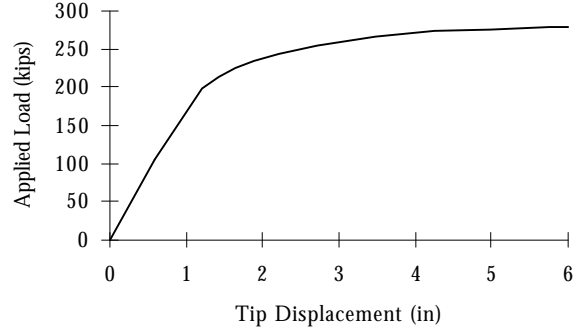


(e) Pressure, Mises, and PEEQ below access hole

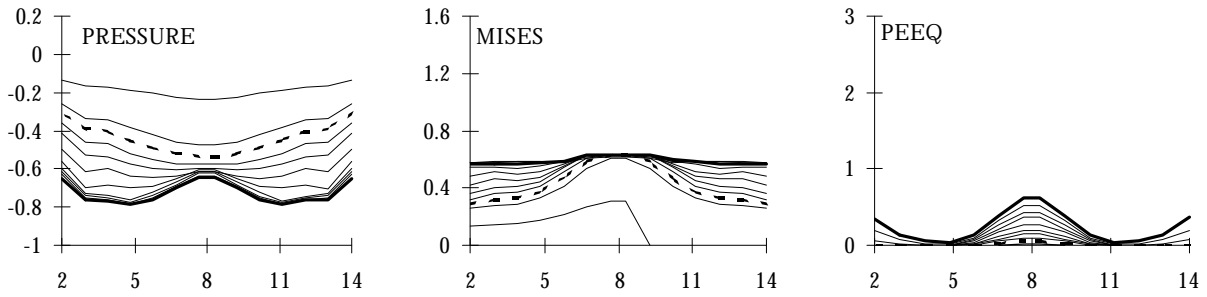
FIGURE B.12. SPECIMEN BD4. ( $f_{yb}=70\text{ksi}$ ,  $f_{yc}=45\text{ksi}$ ).



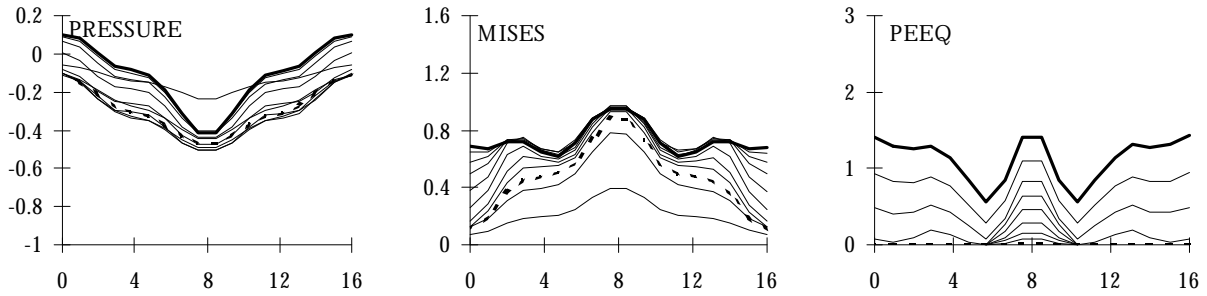
(a) Plasticity vs. Applied Tip Displacement



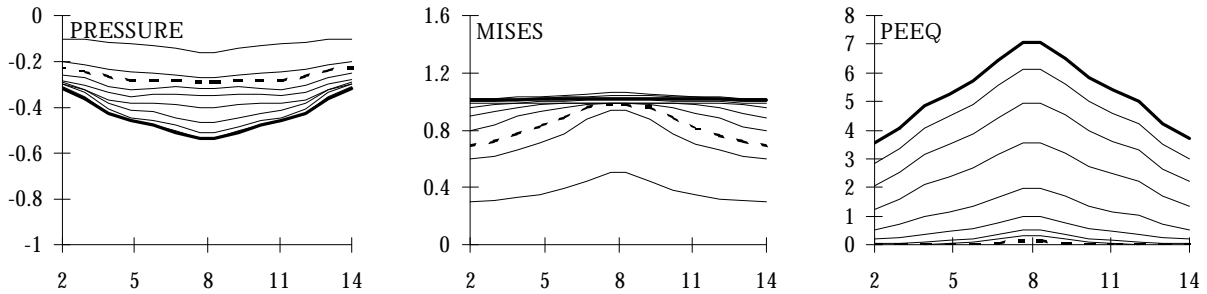
(b) Load vs. Applied Tip Displacement



(c) Pressure, Mises, and PEEQ at interface

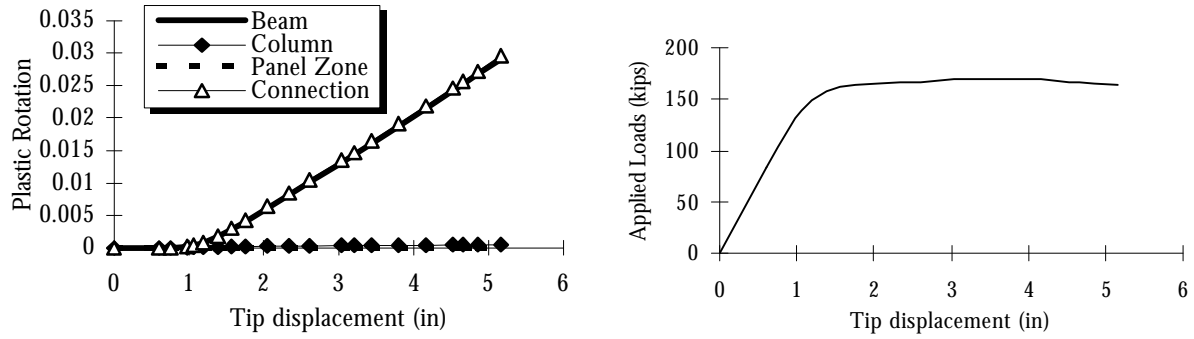


(d) Pressure, Mises, and PEEQ in column flange



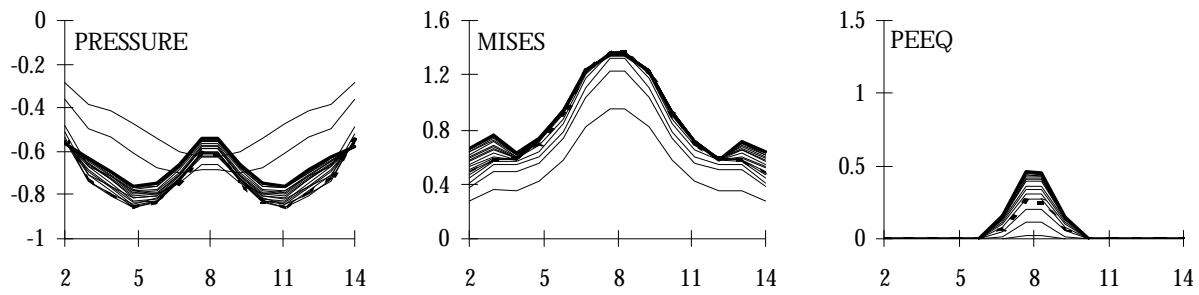
(e) Pressure, Mises, and PEEQ below access hole

FIGURE B.13. SPECIMEN CFN1. ( $f_{yb}=36$  ksi,  $f_{yc}=50$  ksi).

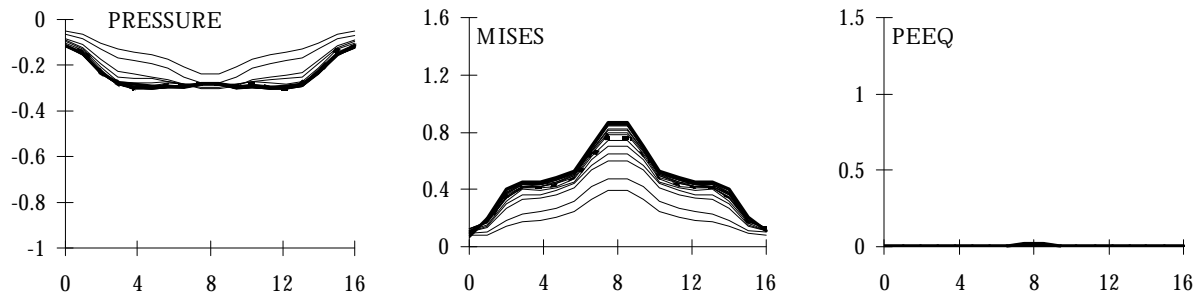


(a) Plasticity vs. Applied Tip Displacement

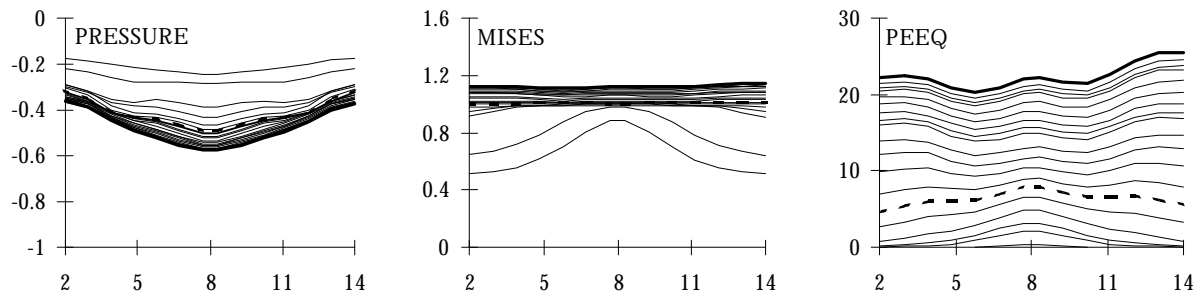
(b) Load vs. Applied Tip Displacement



(c) Pressure, Mises, and PEEQ at interface

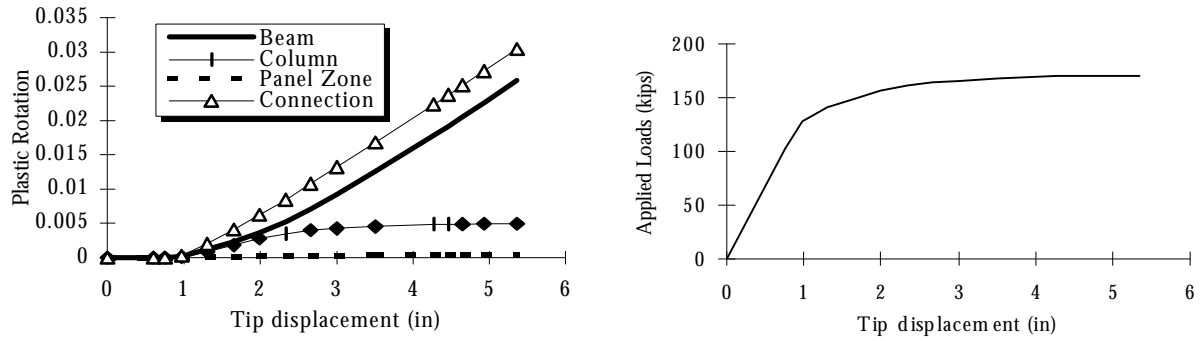


(d) Pressure, Mises, and PEEQ in column flange



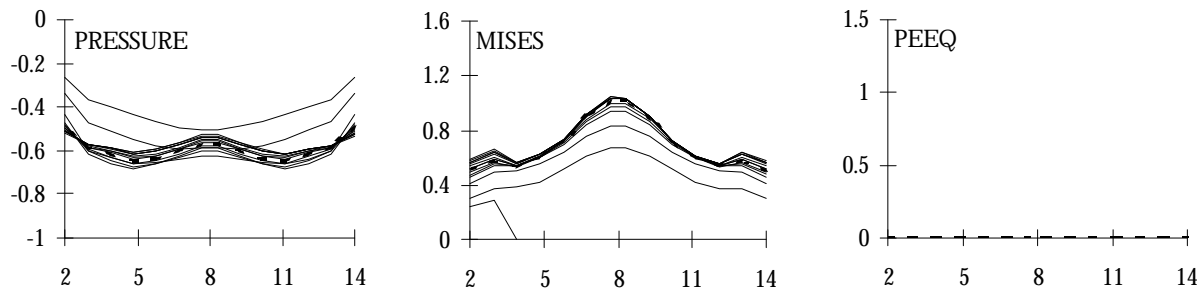
(e) Pressure, Mises, and PEEQ below access hole

FIGURE B.14. SPECIMEN CFN3. ( $f_{yb}=36$  ksi,  $f_{yc}=50$  ksi).

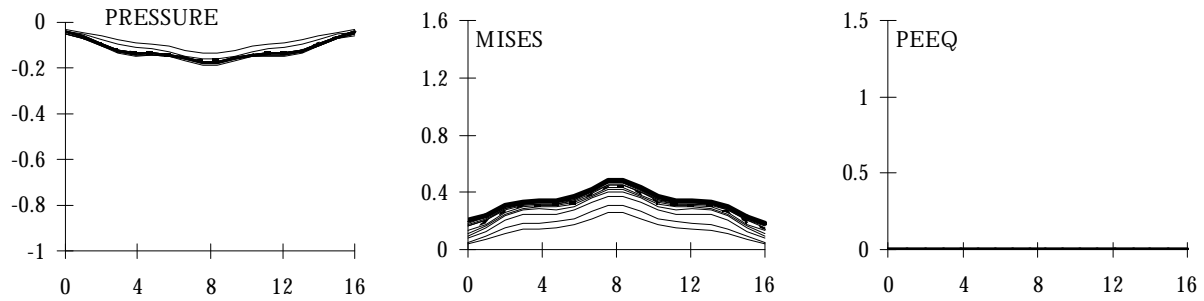


(a) Plasticity vs. Applied Tip Displacement

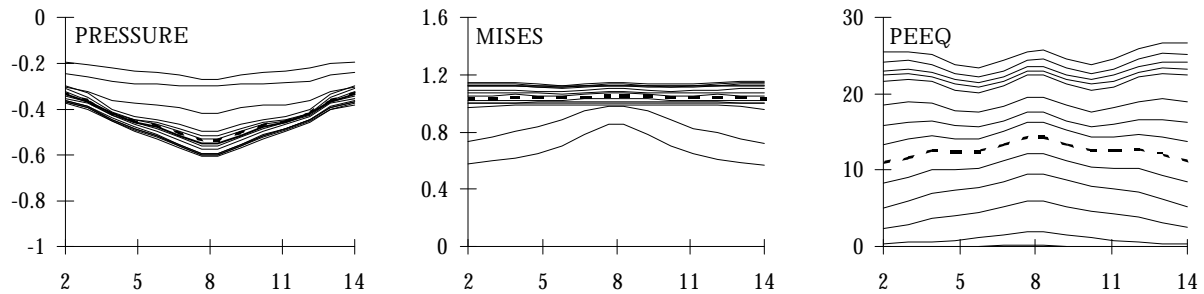
(b) Load vs. Applied Tip Displacement



(c) Pressure, Mises, and PEEQ at interface

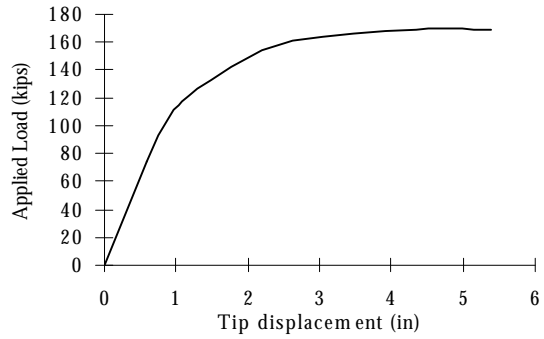
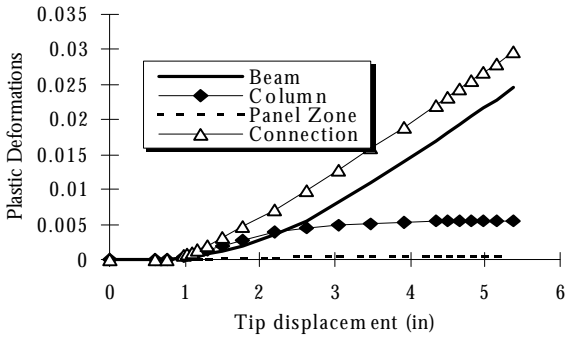


(d) Pressure, Mises, and PEEQ in column flange



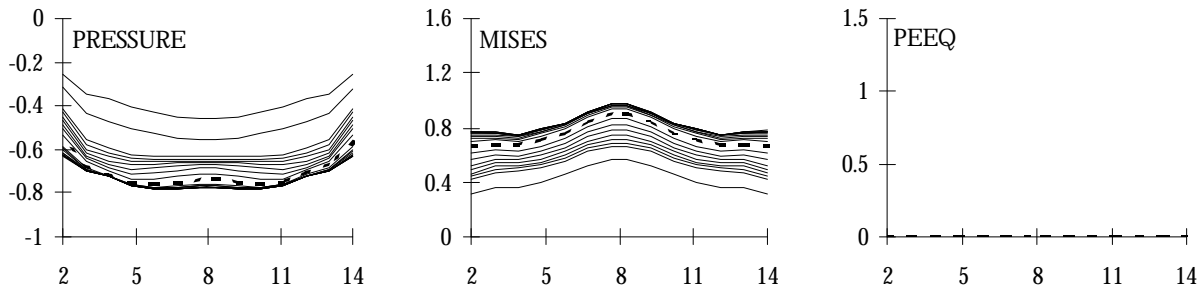
(e) Pressure, Mises, and PEEQ below access hole

FIGURE B.15. SPECIMEN CFN4, ( $f_{yb}=36$  ksi,  $f_{yc}=50$  ksi)

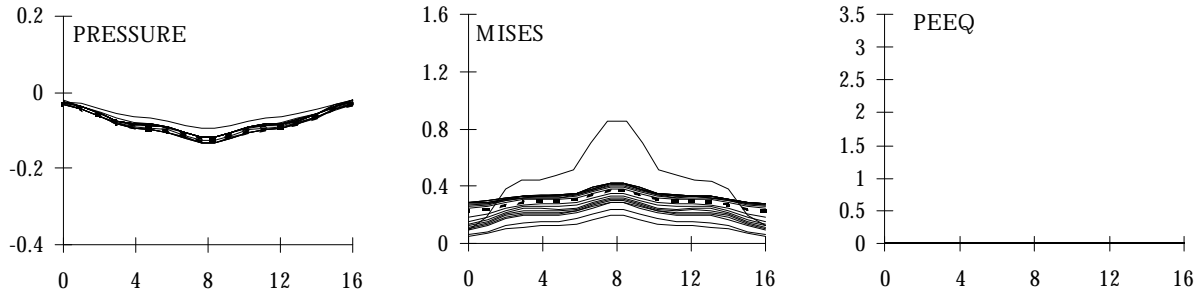


(a) Plasticity vs. Applied Tip Displacement

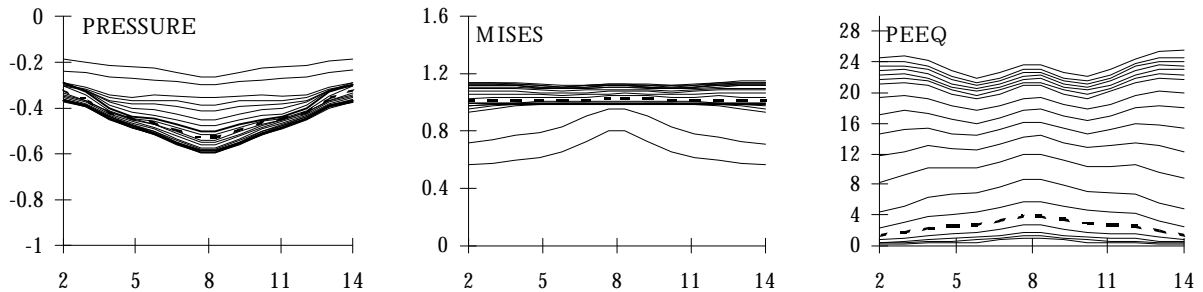
(b) Load vs. Applied Tip Displacement



(c) Pressure, Mises, and PEEQ at interface

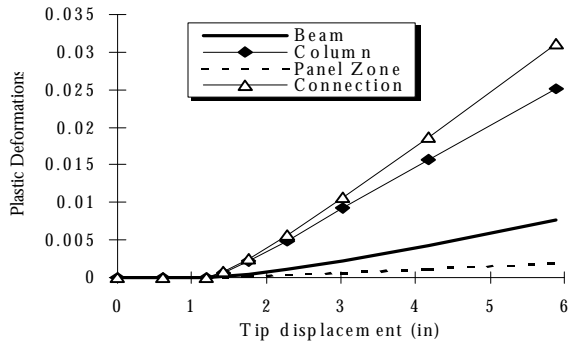


(d) Pressure, Mises, and PEEQ in column flange

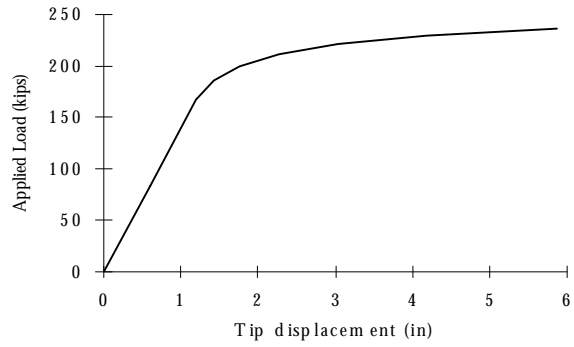


(e) Pressure, Mises, and PEEQ below access hole

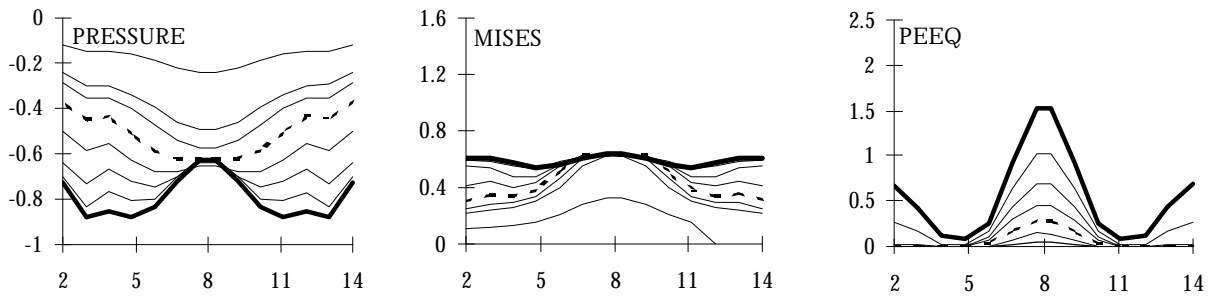
FIGURE B.16. SPECIMEN CFS1, ( $f_{yb}=70$  ksi,  $f_{yc}=45$  ksi)



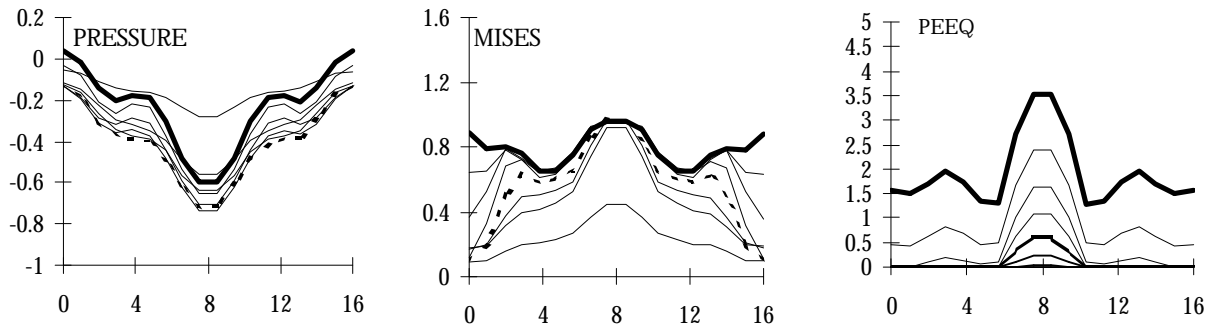
(a) Plasticity vs. Applied Tip Displacement



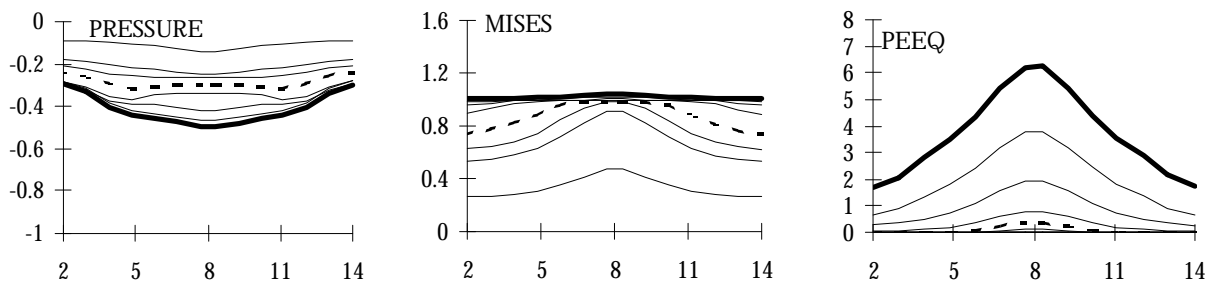
(b) Load vs. Applied Tip Displacement



(c) Pressure, Mises, and PEEQ at interface

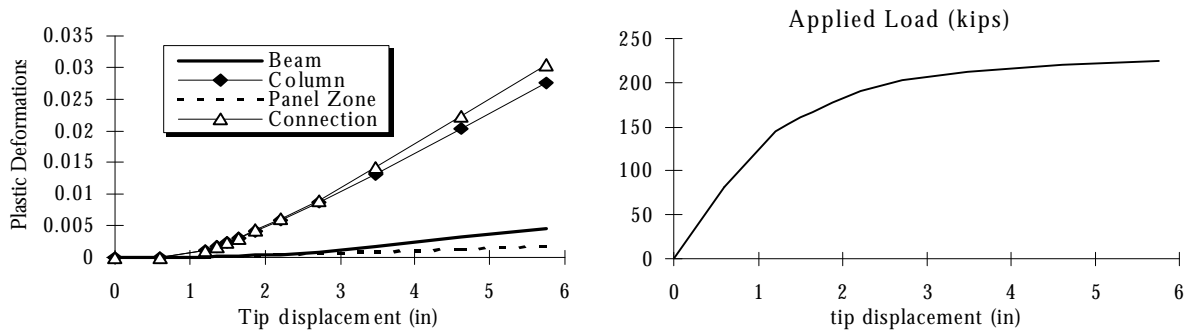


(d) Pressure, Mises, and PEEQ in column flange



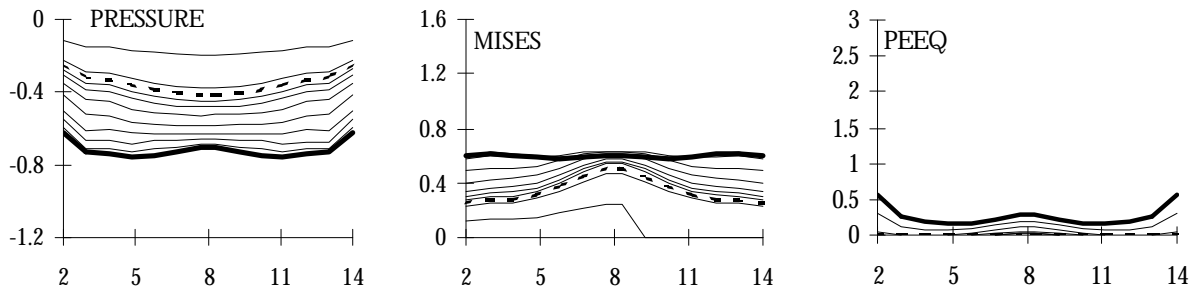
(e) Pressure, Mises, and PEEQ below access hole

FIGURE B.17. SPECIMEN CFS3, ( $f_{yb}=70$  ksi,  $f_{yc}=45$  ksi)

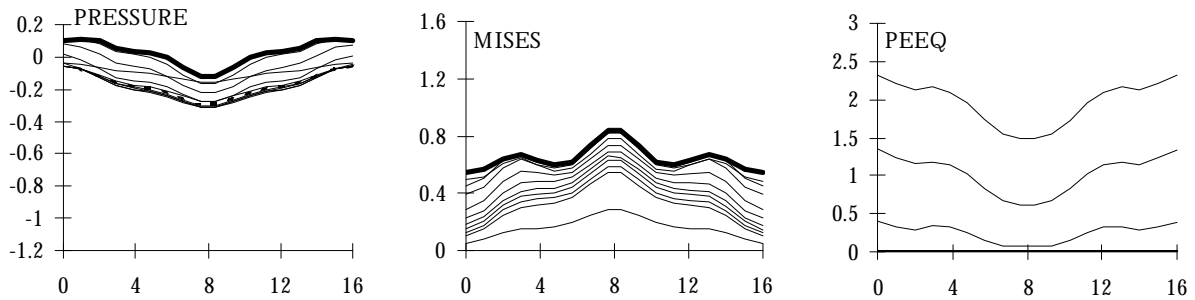


(a) Plasticity vs. Applied Tip Displacement

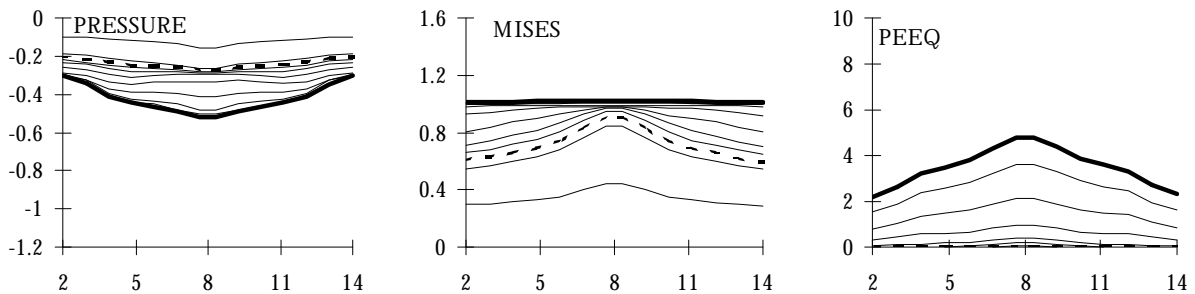
(b) Load vs. Applied Tip Displacement



(c) Pressure, Mises, and PEEQ at interface

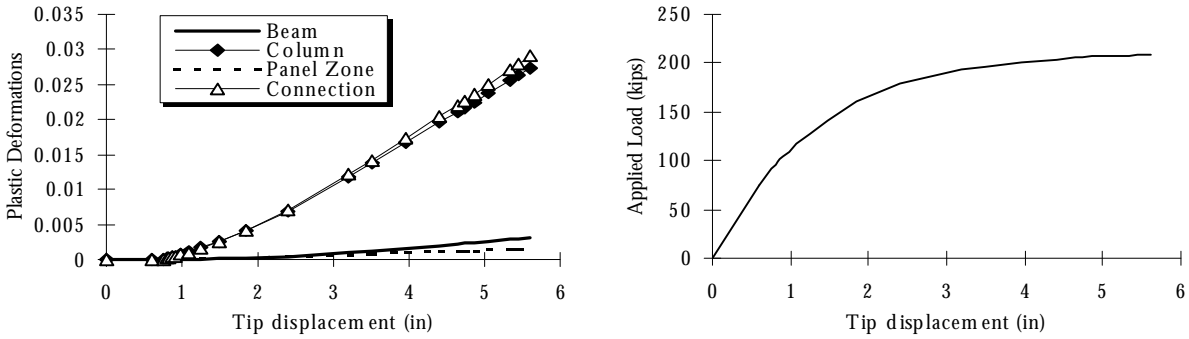


(d) Pressure, Mises, and PEEQ in column flange



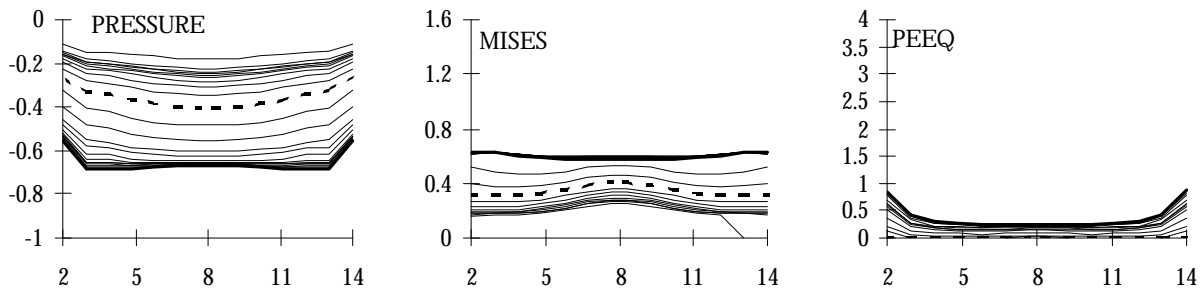
(e) Pressure, Mises, and PEEQ below access hole

FIGURE B.18. SPECIMEN CFS4, ( $f_{yb}=70$  ksi,  $f_{yc}=45$  ksi)

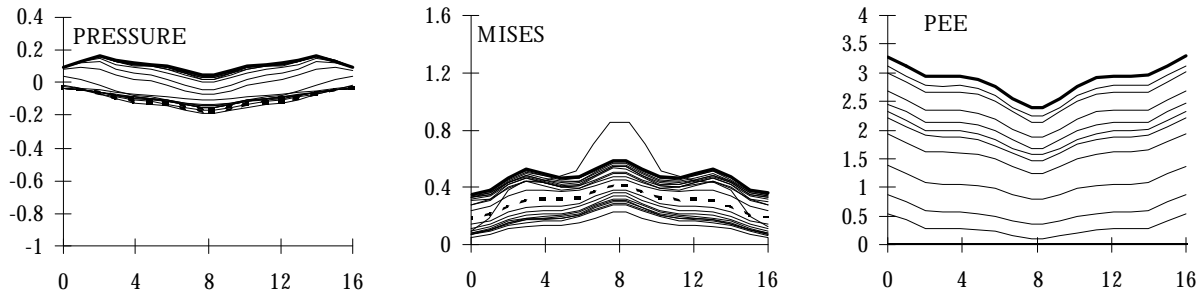


(a) Plasticity vs. Applied Tip Displacement

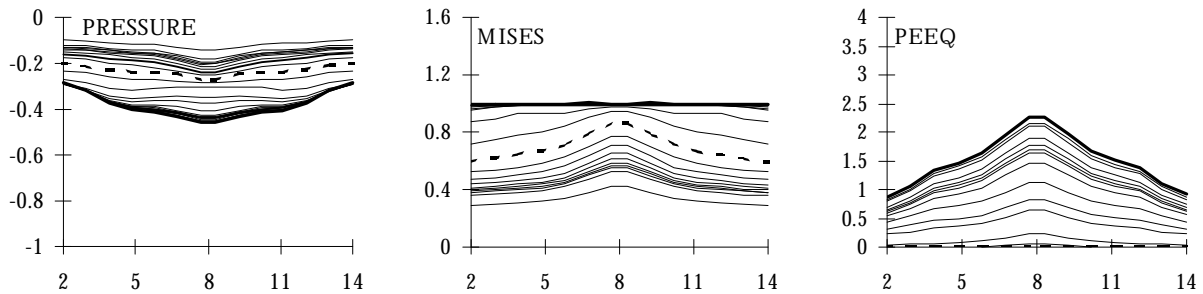
(b) Load vs. Applied Tip Displacement



(c) Pressure, Mises, and PEEQ at interface

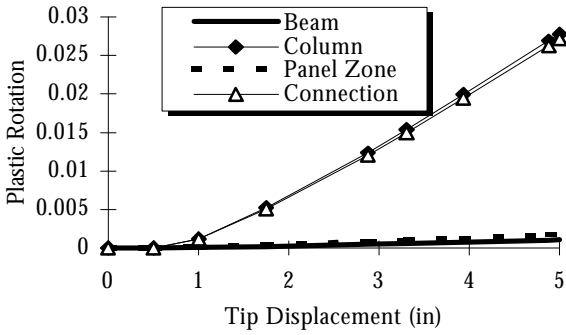


(d) Pressure, Mises, and PEEQ in column flange

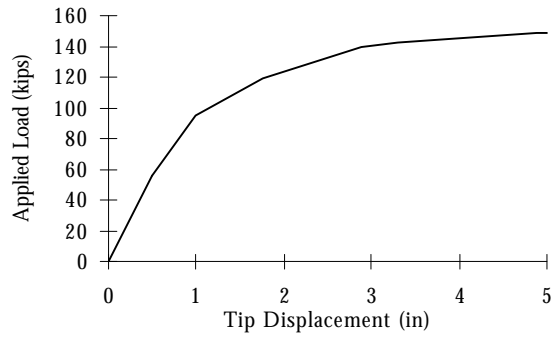


(e) Pressure, Mises, and PEEQ below access hole

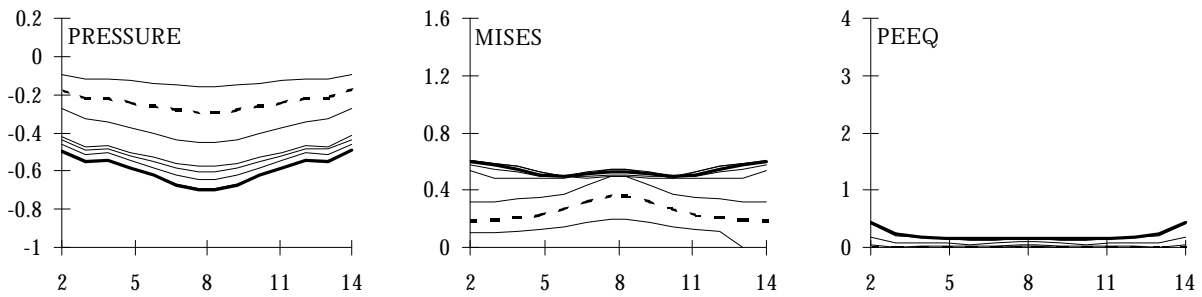
FIGURE B.19. SPECIMEN CWT1. ( $f_{yb}=70\text{ksi}$ ,  $f_{yc}=45\text{ksi}$ ).



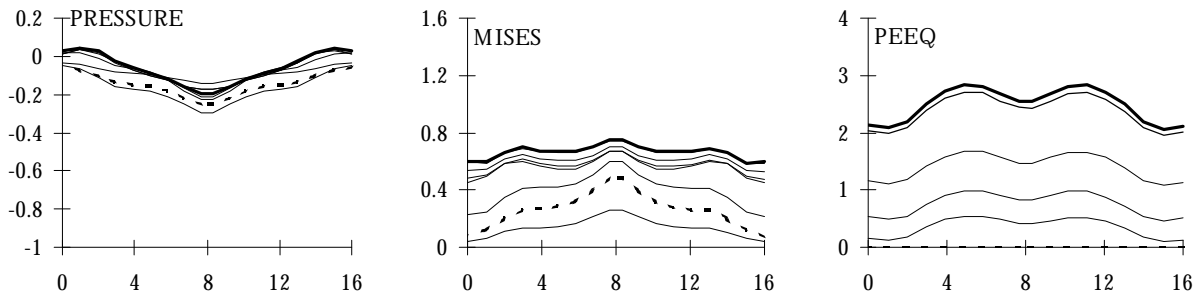
(a) Plasticity vs. Applied Tip Displacement



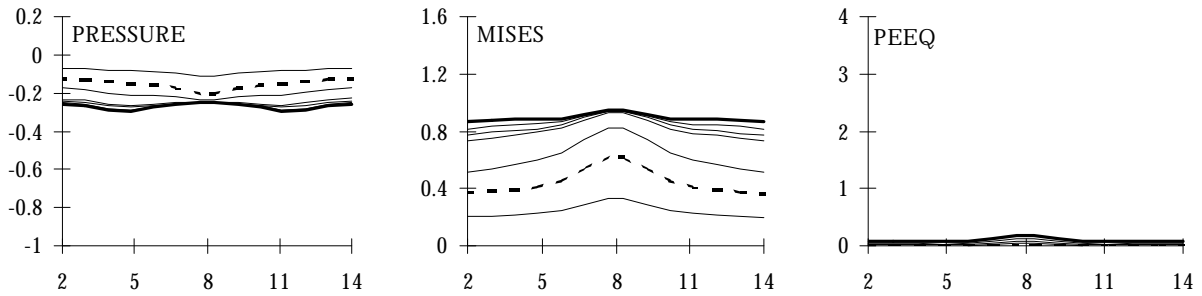
(b) Load vs. Applied Tip Displacement



(c) Pressure, Mises, and PEEQ at interface

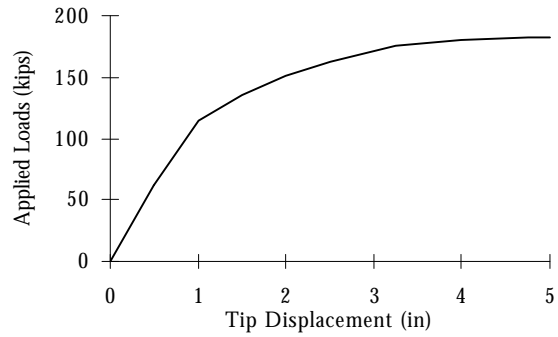
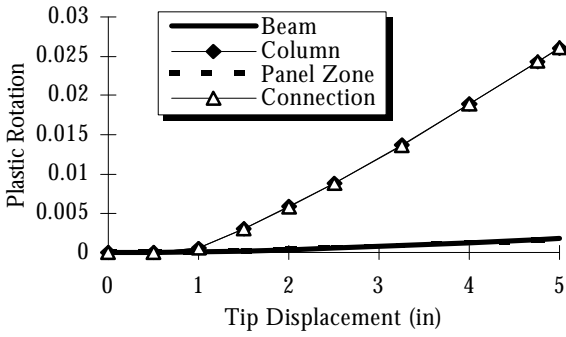


(d) Pressure, Mises, and PEEQ in column flange



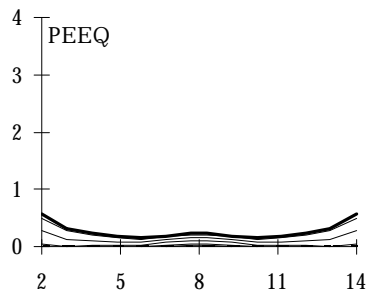
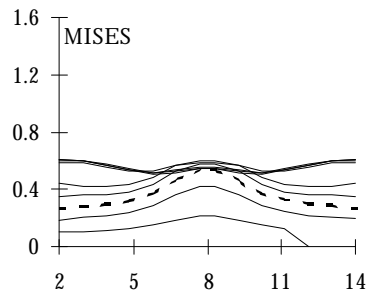
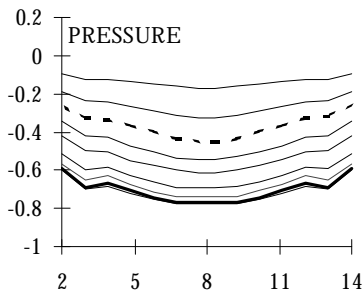
(e) Pressure, Mises, and PEEQ below access hole

FIGURE B.20. SPECIMEN CWT2. ( $f_{yb}=70\text{ksi}$ ,  $f_{yc}=45\text{ksi}$ ).

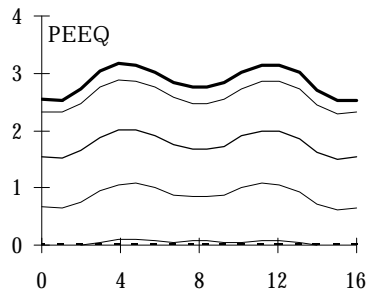
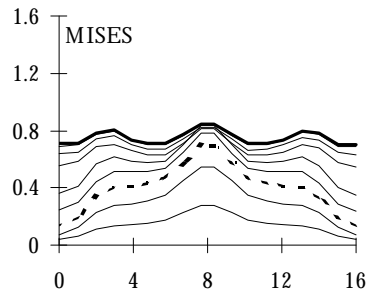
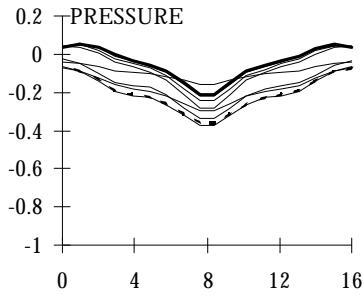


(a) Plasticity vs. Applied Tip Displacement

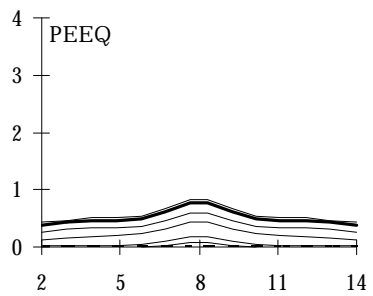
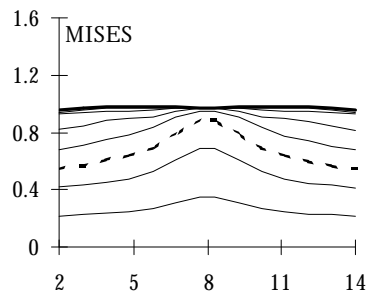
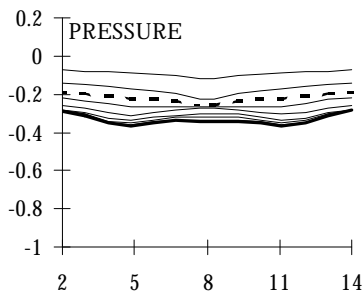
(b) Load vs. Applied Tip Displacement



(c) Pressure, Mises, and PEEQ at interface

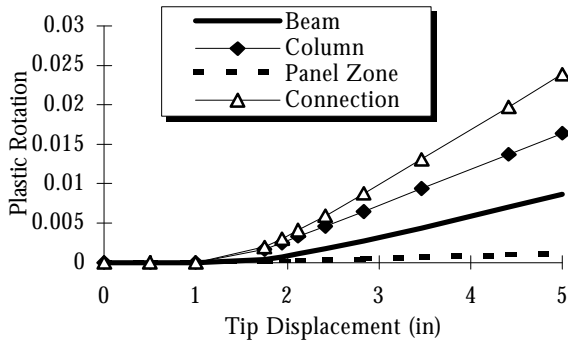


(d) Pressure, Mises, and PEEQ in column flange

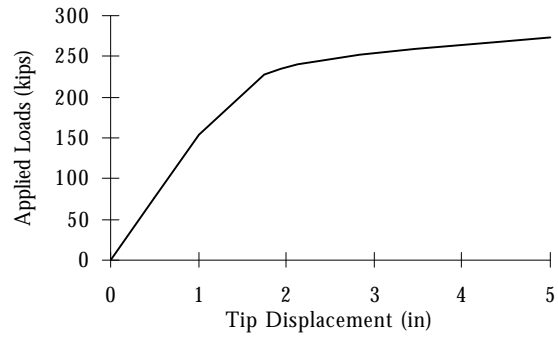


(e) Pressure, Mises, and PEEQ below access hole

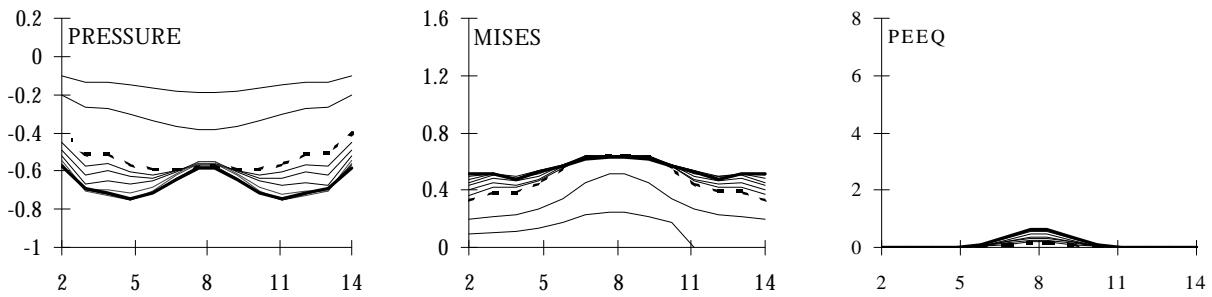
FIGURE B.21. SPECIMEN CWT4. ( $f_{yb}=70\text{ksi}$ ,  $f_{yc}=45\text{ksi}$ ).



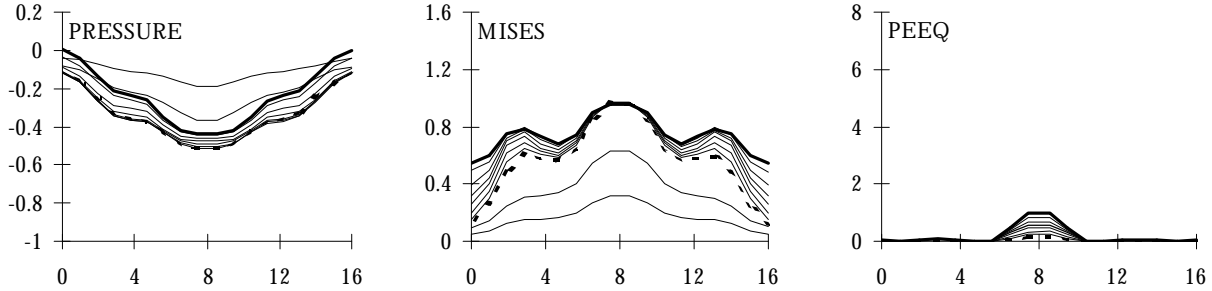
(a) Plasticity vs. Applied Tip Displacement



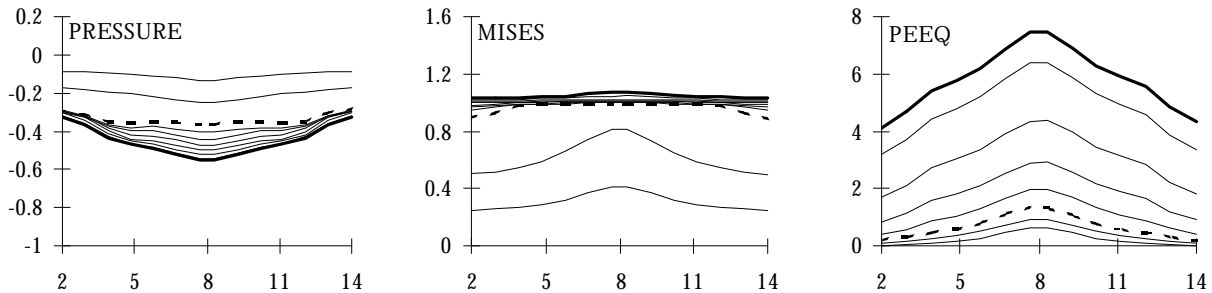
(b) Load vs. Applied Tip Displacement



(c) Pressure, Mises, and PEEQ at interface

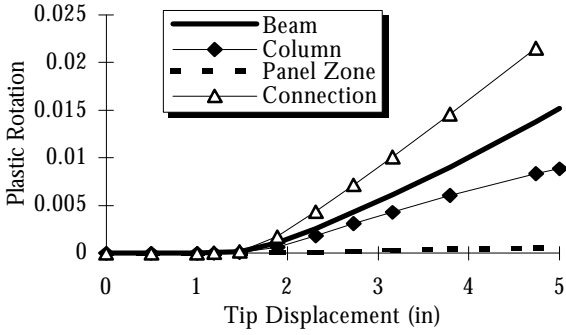


(d) Pressure, Mises, and PEEQ in column flange

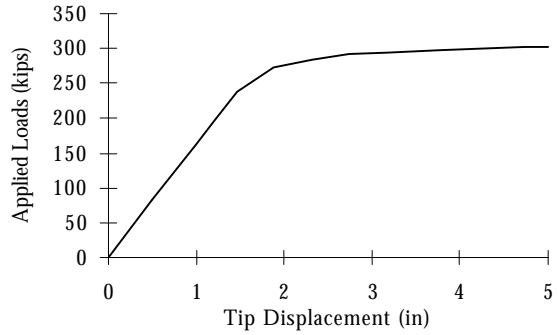


(e) Pressure, Mises, and PEEQ below access hole

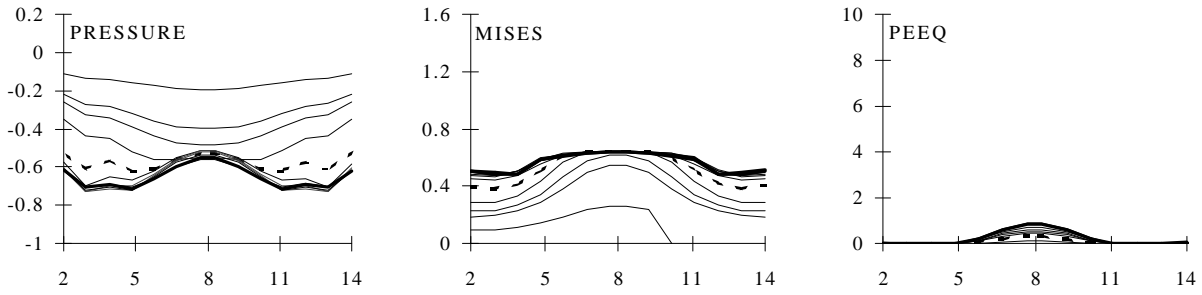
FIGURE B.22. SPECIMEN CWT5. ( $f_{yb}=70\text{ksi}$ ,  $f_{yc}=45\text{ksi}$ ).



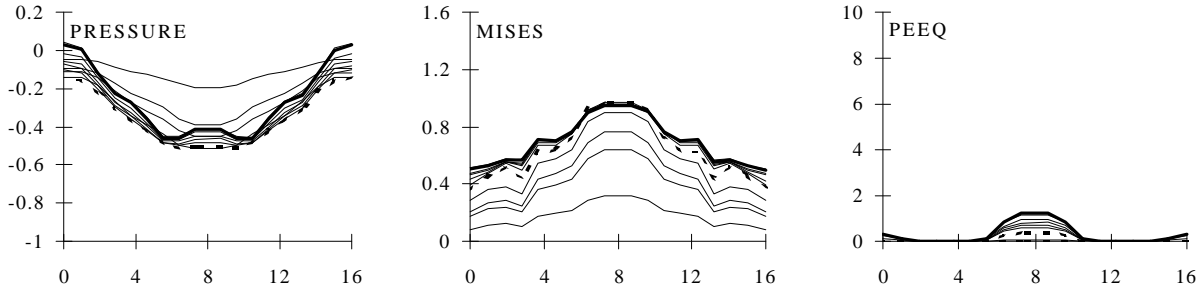
(a) Plasticity vs. Applied Tip Displacement



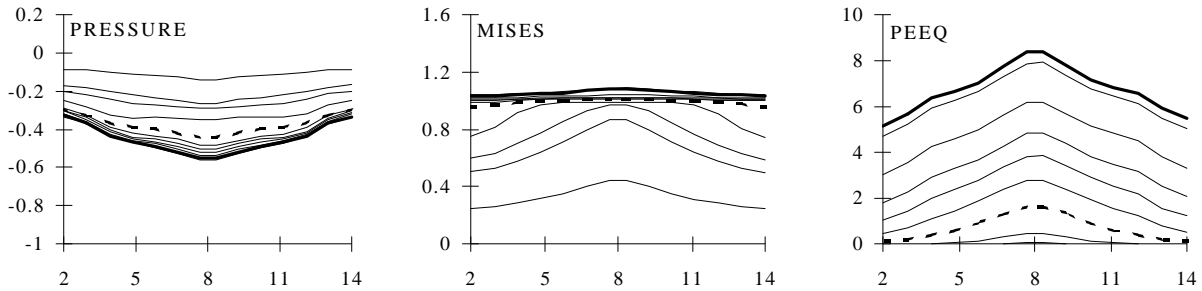
(b) Load vs. Applied Tip Displacement



(c) Pressure, Mises, and PEEQ at interface

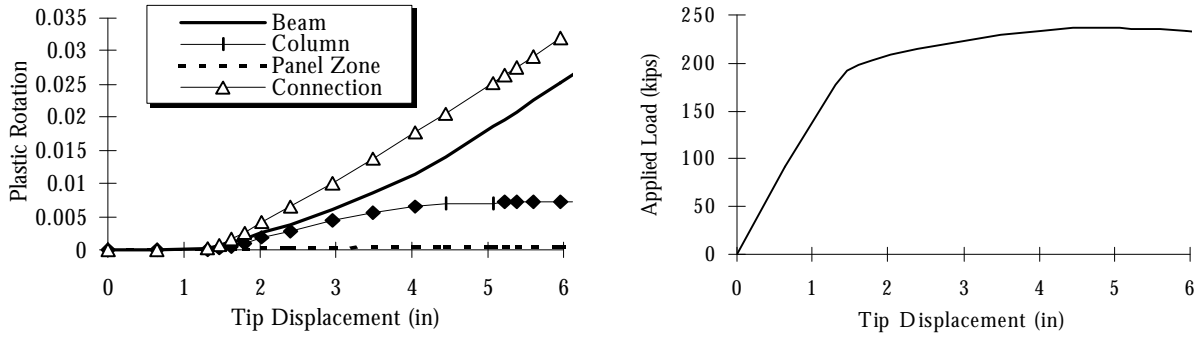


(d) Pressure, Mises, and PEEQ in column flange



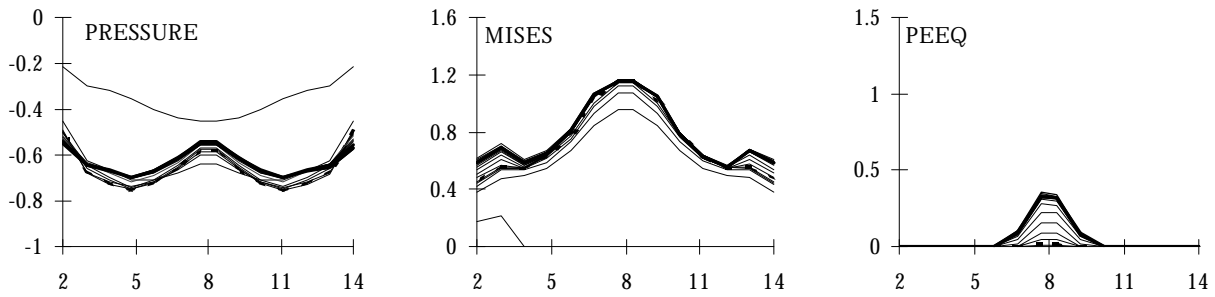
(e) Pressure, Mises, and PEEQ below access hole

FIGURE B.23. SPECIMEN YUSR-65. ( $f_{yc}=60\text{ksi}$ ,  $f_{yb}=50\text{ksi}$ ).

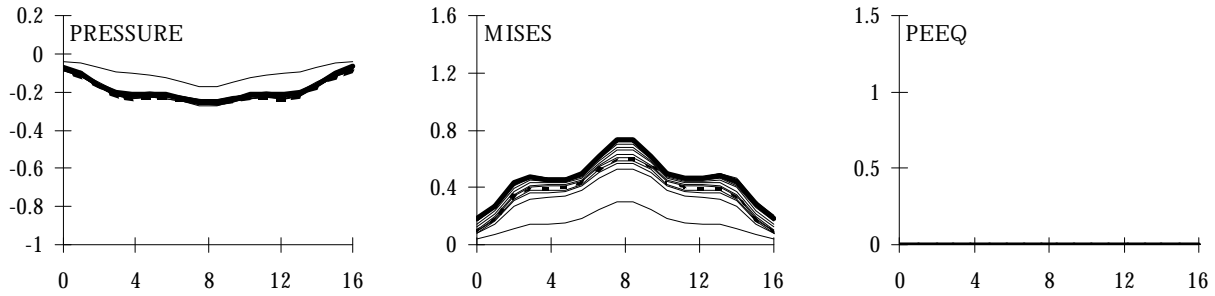


(a) Plasticity vs. Applied Tip Displacement

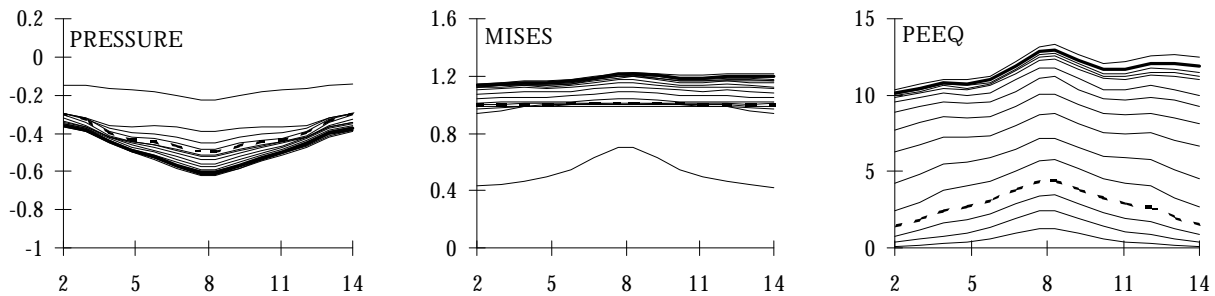
(b) Load vs. Applied Tip Displacement



(c) Pressure, Mises, and PEEQ at interface

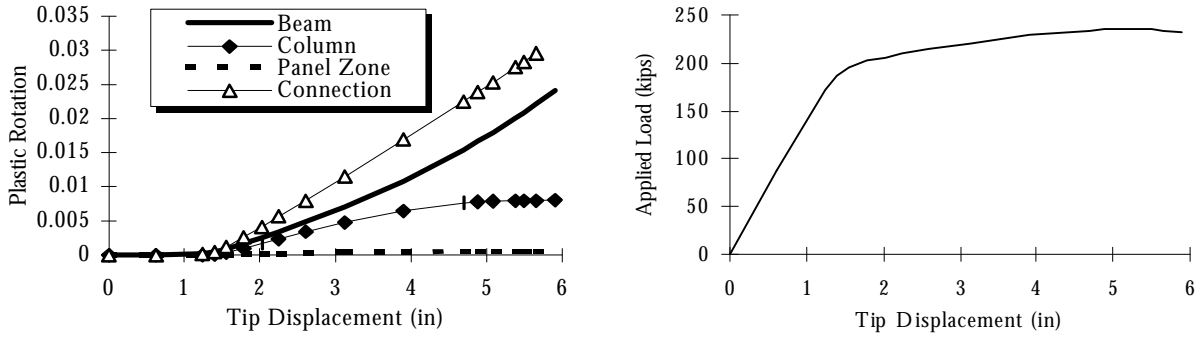


(d) Pressure, Mises, and PEEQ in column flange



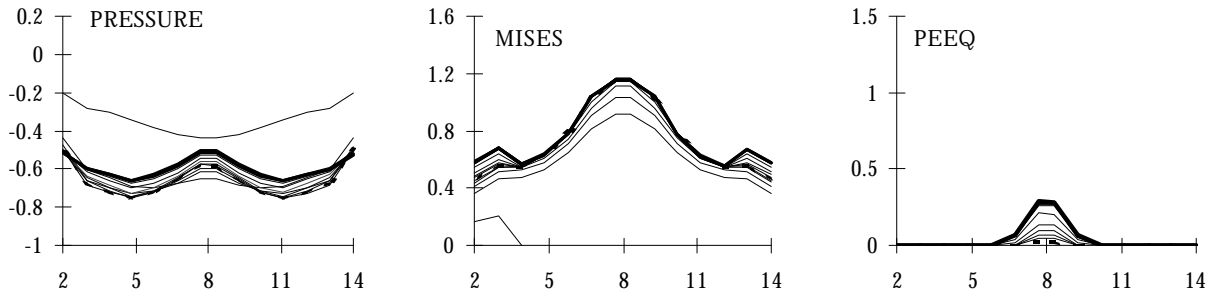
(e) Pressure, Mises, and PEEQ below access hole

FIGURE B.24. SPECIMEN YUSR-80. ( $f_{yc}=60\text{ksi}$ ,  $f_{yb}=50\text{ksi}$ ).

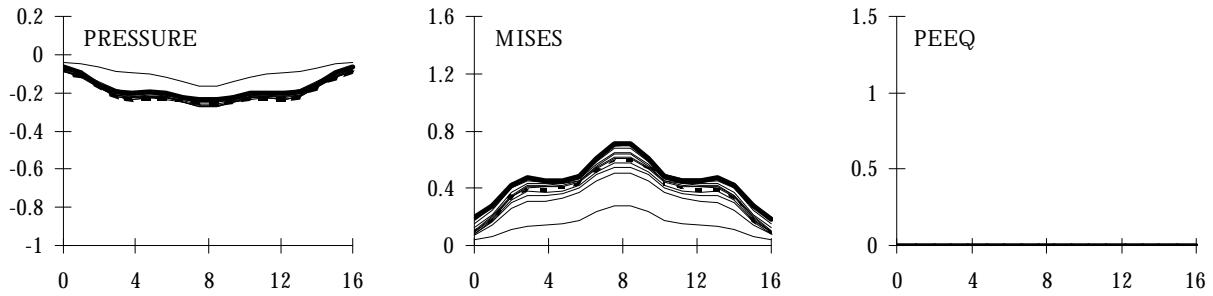


(a) Plasticity vs. Applied Tip Displacement

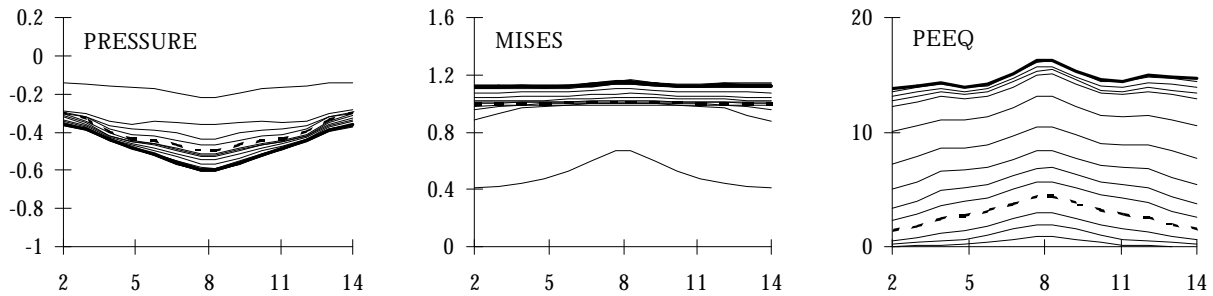
(b) Load vs. Applied Tip Displacement



(c) Pressure, Mises, and PEEQ at interface

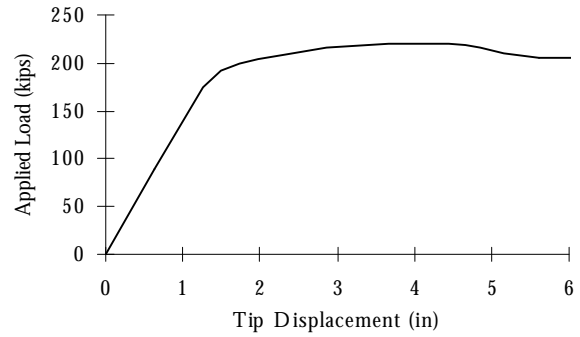
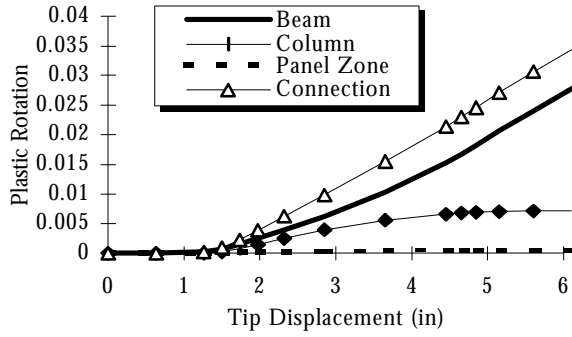


(d) Pressure, Mises, and PEEQ in column flange



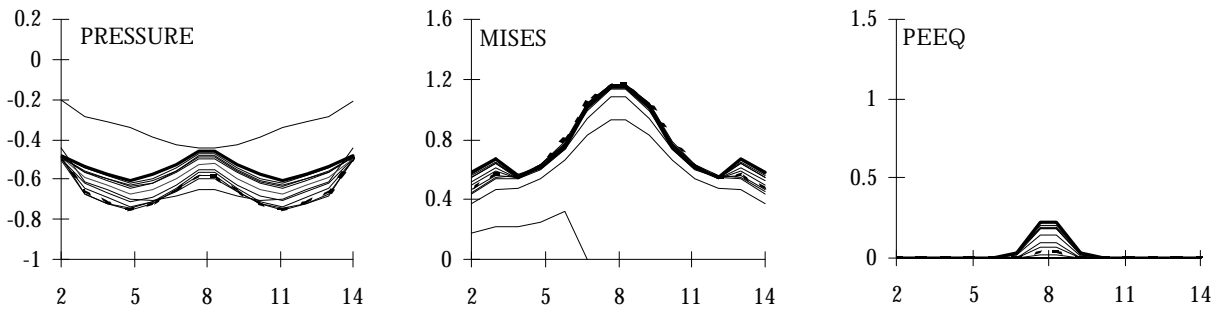
(e) Pressure, Mises, and PEEQ below access hole

FIGURE B.25. SPECIMEN YUSR-95. ( $f_{yc}=60\text{ksi}$ ,  $f_{yb}=50\text{ksi}$ ).

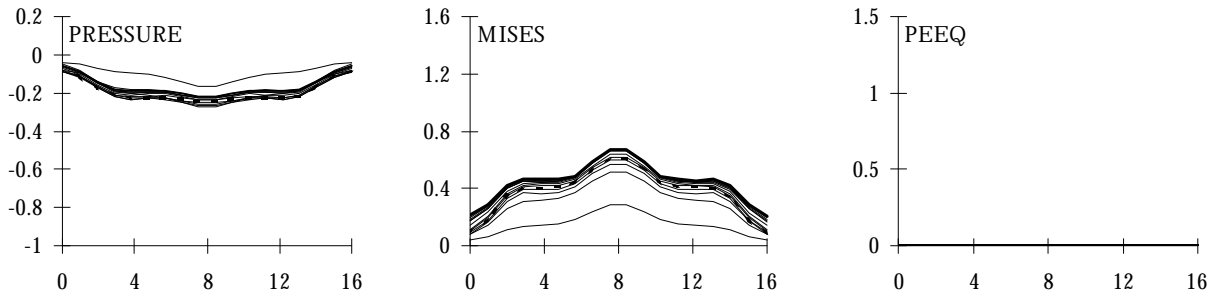


(a) Plasticity vs. Applied Tip Displacement

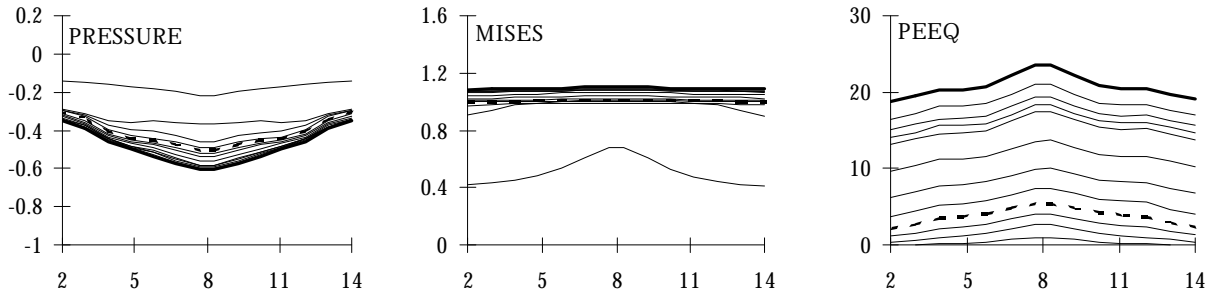
(b) Load vs. Applied Tip Displacement



(c) Pressure, Mises, and PEEQ at interface

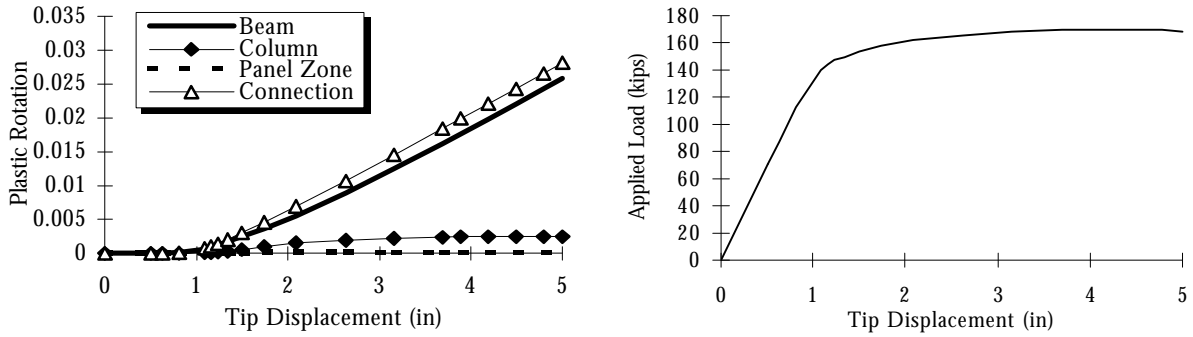


(d) Pressure, Mises, and PEEQ in column flange



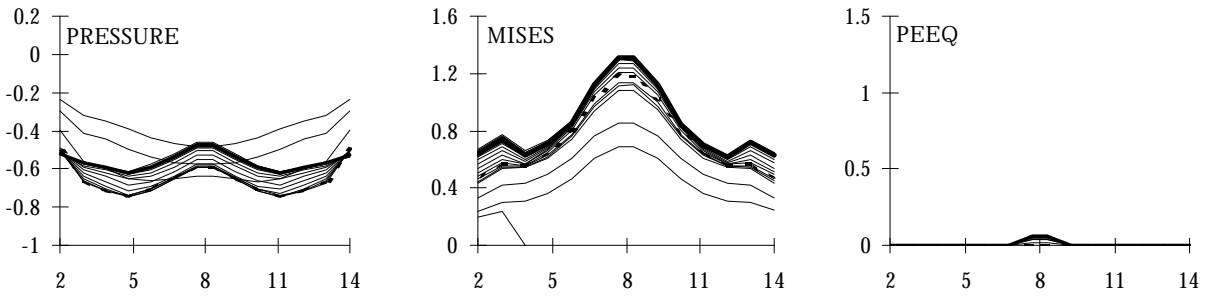
(e) Pressure, Mises, and PEEQ below access hole

FIGURE B.26. SPECIMEN A2. ( $f_{yc}=50\text{ksi}$ ,  $f_{yb}=36\text{ksi}$ ).

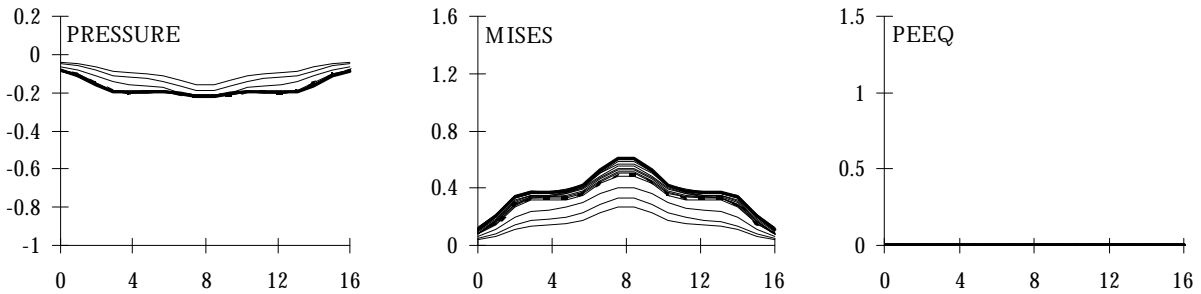


(a) Plasticity vs. Applied Tip Displacement

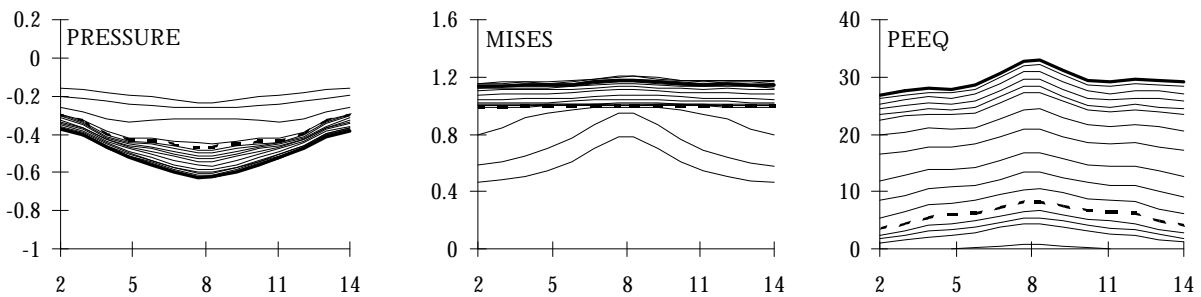
(b) Load vs. Applied Tip Displacement



(c) Pressure, Mises, and PEEQ at interface

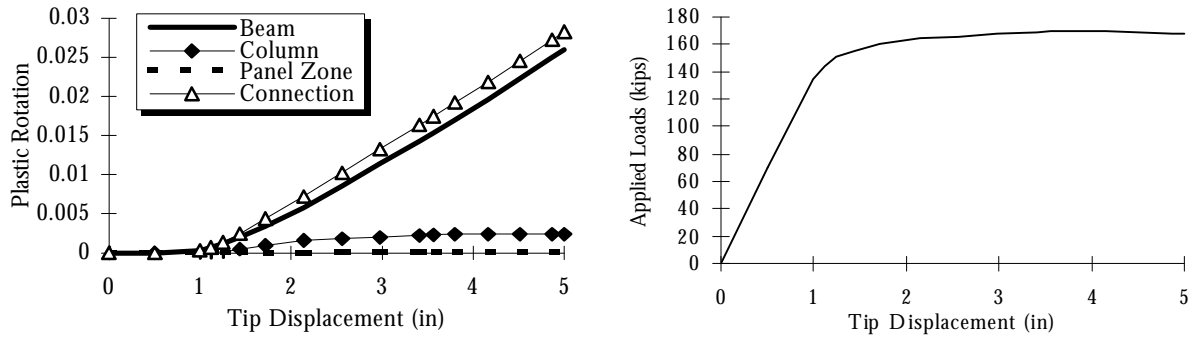


(d) Pressure, Mises, and PEEQ in column flange



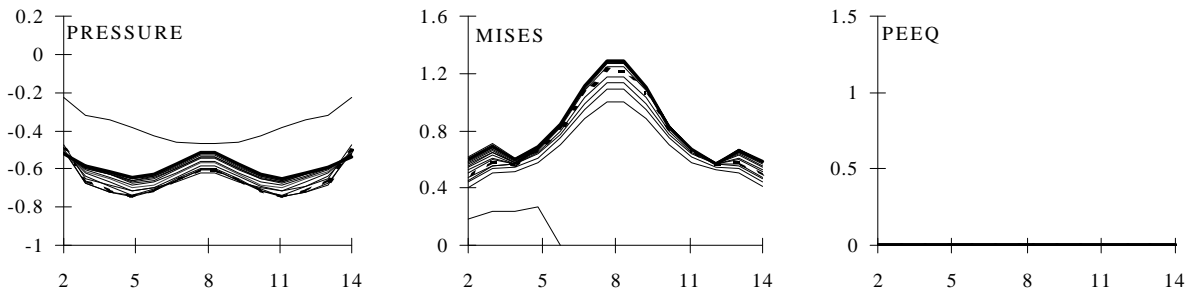
(e) Pressure, Mises, and PEEQ below access hole

Figure B.27. Specimen A3. ( $f_{yc}=50\text{ksi}$ ,  $f_{yb}=36\text{ksi}$ ).

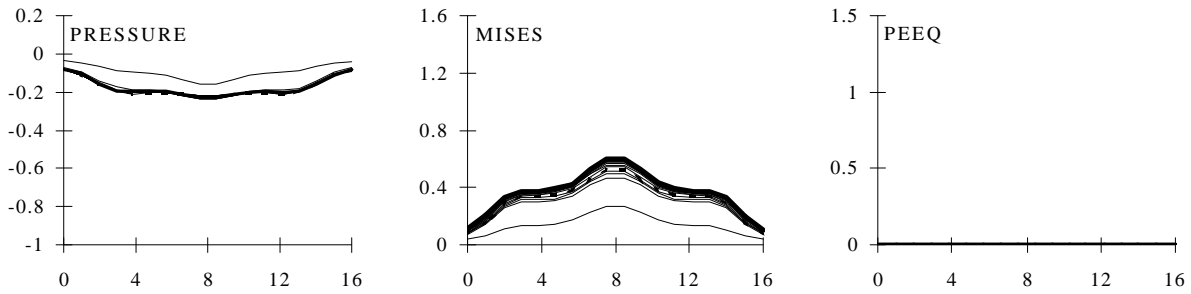


(a) Plasticity vs. Applied Tip Displacement

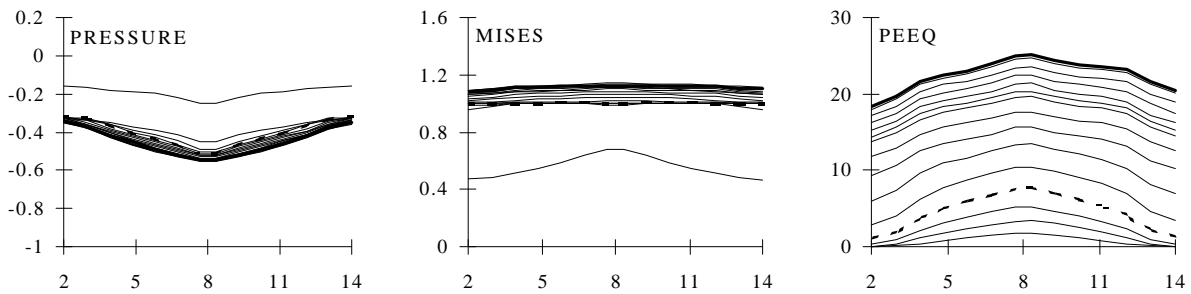
(b) Load vs. Applied Tip Displacement



(c) Pressure, Mises, and PEEQ at interface

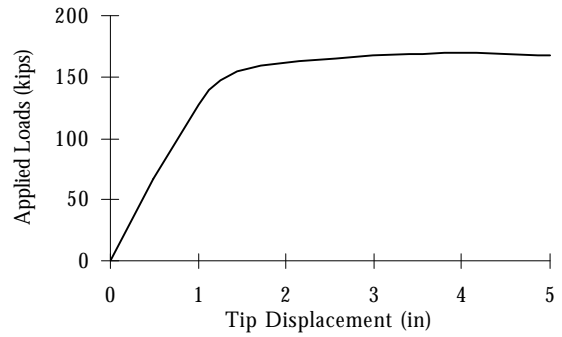
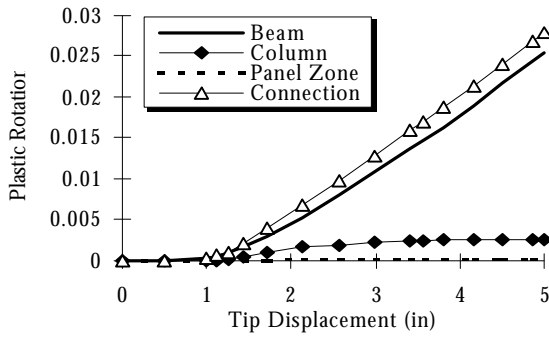


(d) Pressure, Mises, and PEEQ in column flange



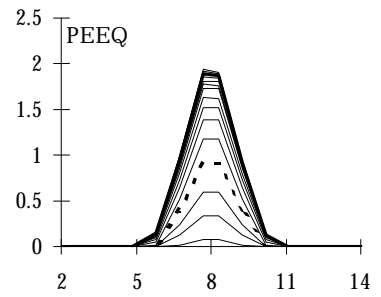
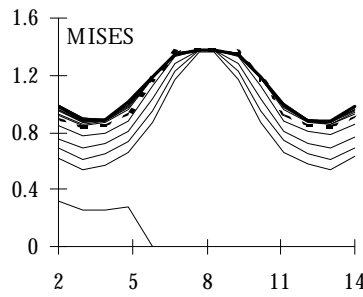
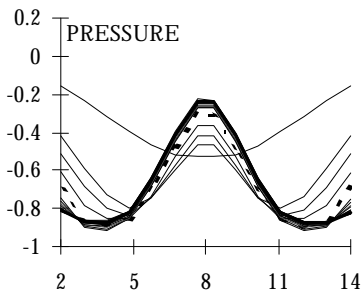
(e) Pressure, Mises, and PEEQ below access hole

FIGURE B.28 SPECIMEN CONT-N (WITHOUT CONTINUITY PLATES)

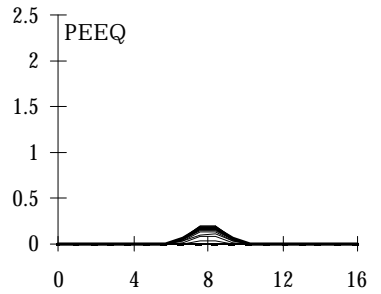
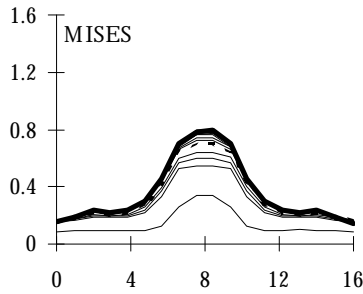
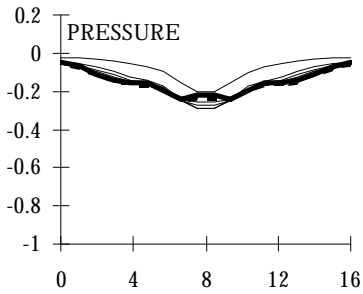


(a) Plasticity vs. Applied Tip Displacement

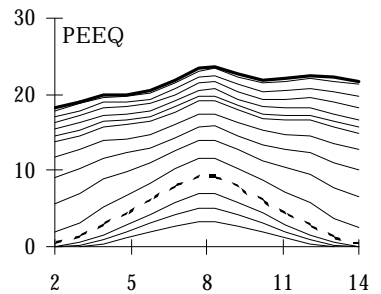
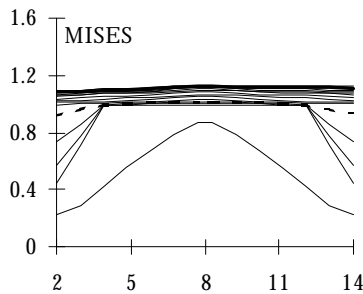
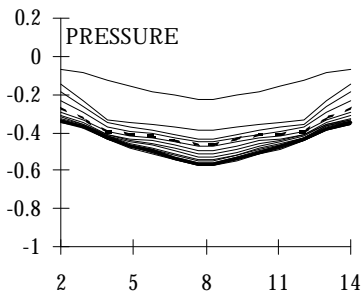
(b) Load vs. Applied Tip Displacement



(c) Pressure, Mises, and PEEQ at interface

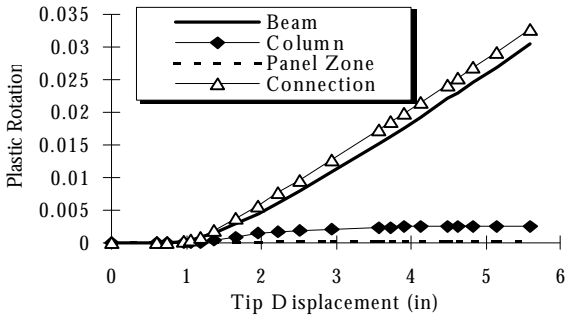


(d) Pressure, Mises, and PEEQ in column flange

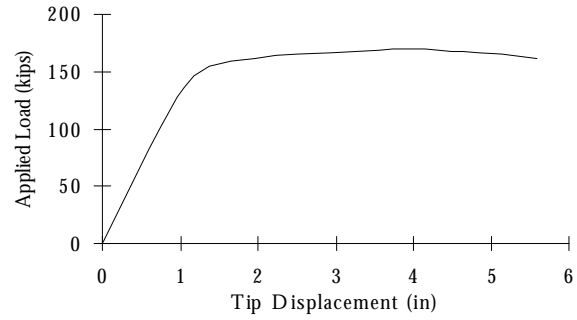


(e) Pressure, Mises, and PEEQ below access hole

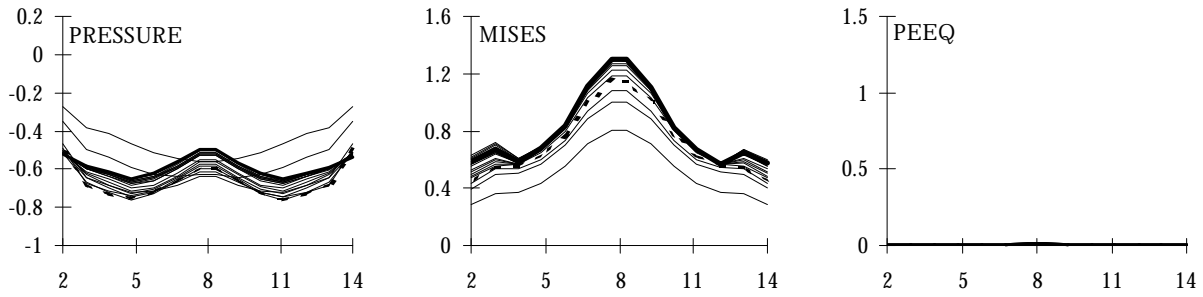
FIGURE B.29. SPECIMEN CONT-0.5



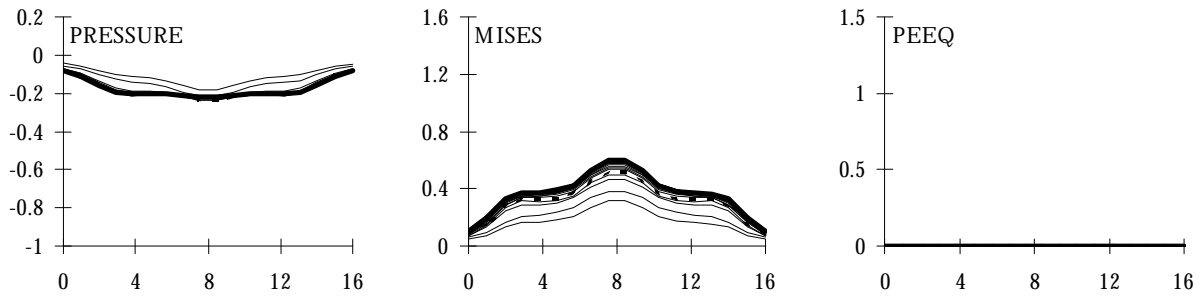
(a) Plasticity vs. Applied Tip Displacement



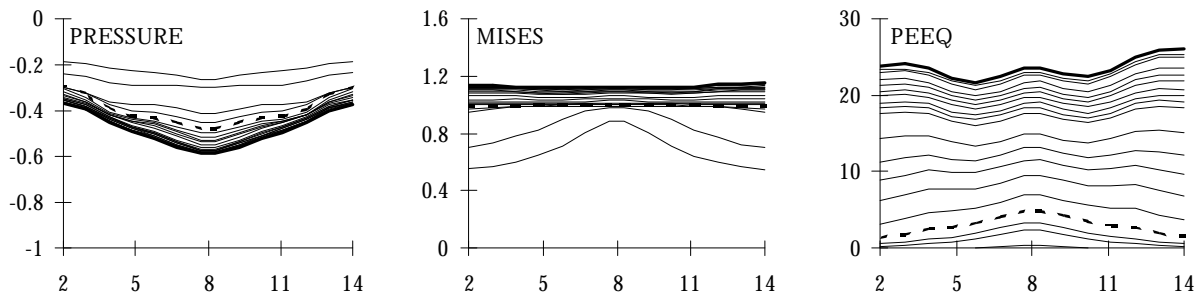
(b) Load vs. Applied Tip Displacement



(c) Pressure, Mises, and PEEQ at interface

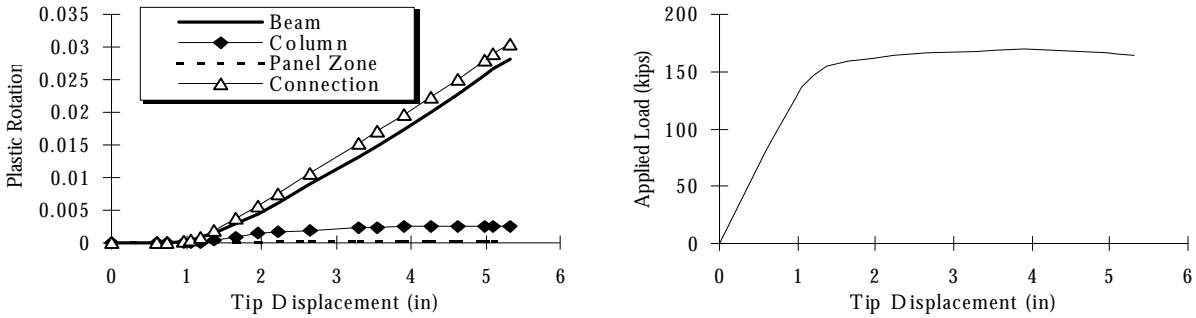


(d) Pressure, Mises, and PEEQ in column flange



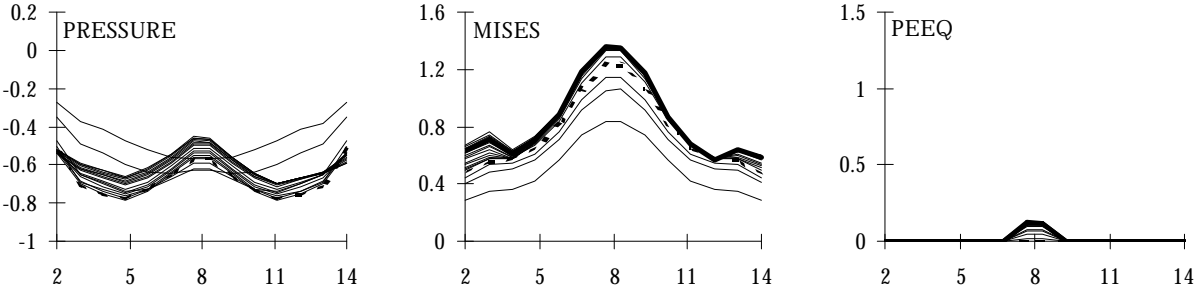
(e) Pressure, Mises, and PEEQ below access hole

FIGURE B.30. SPECIMEN CONT-0.94.

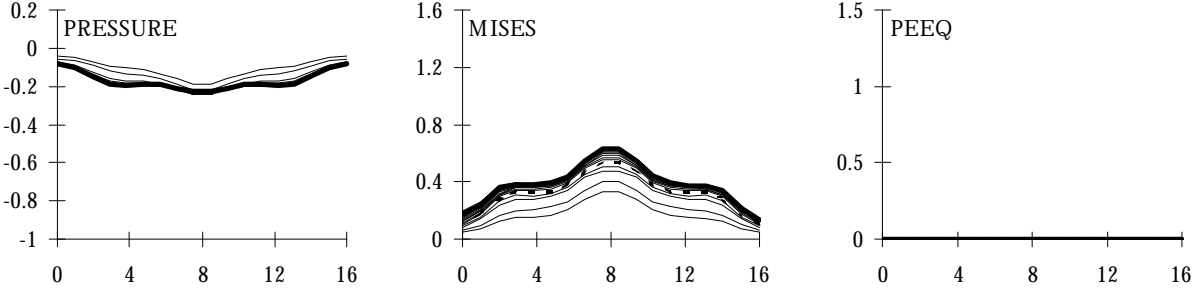


(a) Plasticity vs. Applied Tip Displacement

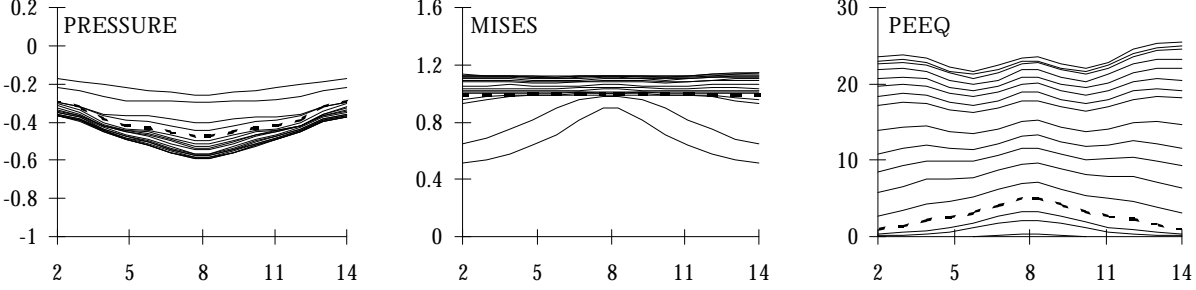
(b) Load vs. Applied Tip Displacement



(c) Pressure, Mises, and PEEQ at interface



(d) Pressure, Mises, and PEEQ in column flange



(e) Pressure, Mises, and PEEQ below access hole